



University  
of Glasgow

Denholme, Saleem J. (2011) *Novel nanostructures in transition metal chalcogenide systems*.  
PhD thesis.

<http://theses.gla.ac.uk/3077/>

Copyright and moral rights for this thesis are retained by the author

A copy can be downloaded for personal non-commercial research or study, without prior permission or charge

This thesis cannot be reproduced or quoted extensively from without first obtaining permission in writing from the Author

The content must not be changed in any way or sold commercially in any format or medium without the formal permission of the Author

When referring to this work, full bibliographic details including the author, title, awarding institution and date of the thesis must be given

# Novel nanostructures in transition metal chalcogenide systems



Thesis submitted to the University of Glasgow for the  
degree of Doctor of Philosophy

By

**Saleem. J. Denholme**

School of Chemistry  
University of Glasgow

July 2011

## Abstract

This thesis discusses the synthesis of transition metal chalcogenide nanostructures (where the chalcogen is either sulfur, selenium or tellurium) through the use of standard chemical vapour transport (CVT) and chemical vapour deposition (CVD) techniques. The resultant structures are characterised with a variety of methods and comparisons of their properties are made with their bulk counterparts. A discussion into how some of these structures form during the reaction is also given.

Highly symmetrical, isotropic, nickel disulfide ( $\text{NiS}_2$ ) nanocubes have been synthesised via a Physical Vapour Transport (PVT) method in which sulfur vapour generated *in situ* is reacted with nickel-coated silica substrates. Systematic studies demonstrate the effect of the reactant ratio, substrate, metal layer thickness and reaction temperature on the synthesis and growth process. The evolution of structure and composition has been followed by diffraction and scanning electron microscopy (SEM). The size of the  $\text{NiS}_2$  cubes can be varied from below 200 nm to 1 -2  $\mu\text{m}$  across. Magnetic properties of the disulfide nanomaterials have been determined using superconducting quantum interference device (SQUID) magnetometry. Initial experiments also demonstrate that related CVT techniques can be exploited to produce alternative compositions in the Ni-S system with varying morphologies that can be controlled via chemical and physical reaction parameters.

Surface Assisted Chemical Vapour Transport (SACVT) methods have been employed to grow flower-like nanostructures of titanium disulfide ( $\text{TiS}_2$ ) and titanium trisulfide ( $\text{TiS}_3$ ) on titanium coated silica substrates. Systematic studies demonstrate the role of the reactant ratio and reaction temperature on the synthesis and growth process. The evolution of structure and composition has been followed by powder X-ray diffraction (PXD) and electron microscopy techniques such as and transmission electron microscopy (TEM). Magnetic properties of the disulfide nanomaterials have been determined using SQUID and Raman spectroscopy has been used to confirm the identity of the sulfides.

Investigations into nanostructured materials of the group IV transition metals zirconium and hafnium resulted in the successful synthesis of nanostructures of zirconium trisulfide/selenide ( $\text{ZrS}_3/\text{Se}_3$ ) and hafnium trisulfide/selenide ( $\text{HfS}_3/\text{Se}_3$ ). The unusual effects on structure that can occur when reactant time and synthesis temperature are varied and when a balance between these two factors is successfully found, nanostructures other than tubes and wires can be formed. Each of these systems were characterised with a variety of techniques including, TEM, PXD and SQUID.

## Acknowledgements

There are a number of people to whom I would like to express my gratitude for their help and support during this research project. First and foremost, I would like to thank my supervisor Professor Duncan Gregory for his guidance and patience during my studies and giving me the opportunity to undertake this project. Next I offer my gratitude to my two second supervisors Dr Phil Dobson and Professor John Weaver for their advice and encouragement over the years.

I would like to thank past and present members of the Gregory group for making the PhD a thoroughly enjoyable experience and in particular Dr Robert Hughes for his invaluable help and support and willingness to do so at the sacrifice of his own time.

A special thanks to Dr Ian MacLaren for his help in collecting and interpreting the transmission electron microscopy data and Helen Kitchen for her time and patience in collecting (the often horrific) magnetic data. Also, the technical staff in both the chemistry and electrical engineering departments, especially Lesley Donaldson for preparing the metal coated silica substrates.

I would also like to thank the EPSRC and WestCHEM for funding during my studies.

Finally I would like to sincerely thank my mum and dad for their understanding, patience and innumerable amount of yummy meals that kept me going for the last six months.

# Contents

Abstract	i
Acknowledgments	ii
Contents	iii
Chapter 1: Introduction	
1.1 Nano-materials	1
1.2 Synthesis	4
1.2.1 Methodology	4
1.2.2 Growth mechanism	5
1.3 Alternative synthetic methods	7
1.3.1 Liquid phase routes	7
1.3.2 Template assisted growth	8
1.3.3 Solvothermal and hydrothermal routes	9
1.3.4 Other methods	10
1.4 Transition metal chalcogenides (overview)	10
1.5 Transition metal dichalcogenides	12
1.5.1 Layered structures	12
1.5.2 Non-layered structure	17
1.6 Transition metal trichalcogenides	19
1.5.1 Group IV trichalcogenides	21
1.5.1.1 Titanium trichalcogenides	21
1.5.1.2 Zirconium trichalcogenides	22
1.5.1.3 Hafnium trichalcogenides	22
Chapter 2: Experimental	
2.1 Synthesis	24
2.1.1 Phase diagrams	25
2.1.2 Experimental parameters: chalcogen	26
2.1.3 Experimental parameters: transition Metal	26
2.2 Scanning Electron Microscopy (SEM)	29
2.2.1 The scanning electron microscope (SEM)	29
2.2.2 Sample preparation and instrumentation	42
2.2.3 Energy dispersive X-ray analysis	42
2.3 Powder X-ray diffraction (PXD)	44
2.3.1 Crystallography	44
2.3.2 Screw axes and glide planes	45
2.3.3 Space groups	47
2.3.4 Interaction of X-rays with crystals	47
2.3.5 Powder X-ray diffraction (PXD)	49
2.3.6 Rietveld refinement	53
2.3.7 Practical aspects of PXD experiments	56
2.4 Magnetic measurements	57
2.4.1 Magnetism in solids	57
2.4.2 Superconducting Quantum Interference Device (SQUID)	59
2.5 Raman spectroscopy	60
5.5.1 Principles	60
5.5.2 Sample preparation	63
2.6 Transmission Electron Microscopy (TEM)	63

## Chapter 3: Nickel Disulfide

3.1	Introduction	66
3.1.1	Nickel Disulfide	67
3.2	Experimental	69
3.3	Characterisation	70
3.4	Results and discussion	71
3.4.1	Trial reactions	71
3.4.2	Metal layer thickness	73
3.4.2.1	25nm nickel layer thickness	73
3.4.2.2	50nm nickel layer thickness	78
3.4.2.2.1	Pyrite-NiS <sub>2</sub> - structural and magnetic data	82
3.4.2.3	100nm Nickel layer thickness	85
3.4.3	Nickel powder and sulfur reaction	90
3.4.4	Trial reactions with patterned substrates	92
3.5	Discussion and conclusions	94

## Chapter 4: The binary titanium - sulfur system

4.1	Introduction	97
4.1.1	Titanium Disulfide	98
4.1.2	Titanium Trisulfide	100
4.2	Experimental	101
4.3	Characterisation	102
4.4	Results and discussion	104
4.4.1	Trial reactions	104
4.4.2	Metal chalcogen powder reactions	106
4.4.2.1	Raman and magnetic measurements	114
4.4.3	Increased reaction ratio	116
4.4.3.1	TEM and Raman spectroscopy studies	121
4.5	Discussion and conclusions	122

## Chapter 5: Zirconium and hafnium trichalcogenides

5.1	Introduction	126
5.2	Experimental	128
5.3	Characterisation	130
5.4	Results and discussion	132
5.4.1	Zirconium trisulfide; structural characterisation	132
5.4.1.1	Zirconium trisulfide; SQUID magnetometer studies	135
5.4.1.2	Zirconium trisulfide; Raman spectra	137
5.4.1.3	Zirconium trisulfide; TEM investigations	140
5.4.1.4	Zirconium trisulfide; quenched reactions	142
5.4.2	Zirconium triselenide	146
5.4.3	Hafnium trisulfide	152
5.4.3.1	Raman Spectra and reaction at 650 °C	154
5.4.3.2	TEM investigations	157
5.4.3.3	HfS <sub>3</sub> reactions with hafnium powder	158
5.4.4	Hafnium triselenide	161
5.4.5	Hafnium and zirconium tellurides	164
5.5	Discussion and Conclusions	167
Chapter 6: Overall conclusions and further work		169



# 1. Introduction

## 1.1 Nano-materials

The field of nanoscience could aptly fill an expanding demand for more power in smaller dimensions and if proven to fulfil its promised potential could revolutionise developments in medicine and technology. The concept of nanoscience was perhaps first publicised by Richard Feynman during a lecture he gave in 1959 at the annual meeting of the American Physical Society entitled 'There's Plenty of Room at the Bottom'. During this talk he proposed that:

"The principle of physics as far as I can see, do not speak against the possibility of manoeuvring things atom by atom"

He saw miniaturisation of science as an 'invitation into a new field of physics' and predicted some of the impacts nanoscience could have. Although he never actually coined the phrase 'nanoscience' he is given recognition for first bringing attention to a new area of science which is now probably one of the most widely studied areas of materials research. <sup>[1]</sup>

Nanomaterials are regarded as having a size intermediate between bulk material and individual molecules (with at least one dimension around the  $1 - 500 \times 10^{-9}$  m scale).<sup>[2]</sup> Reducing a material down to such a scale can create stark contrasts in its standard physical properties; a classic example being gold and silver. Normally considered chemically inert, they become extremely reactive as nanoparticles which has led to applications in fields such as catalysis.<sup>[3,4]</sup> Generally, the observed divergence in physical properties is thought to be a result of numerous factors such as surface exposure, quantum confinement and reduced diffusion lengths. Focusing on the surface to bulk ratio, as the size of the material is reduced the number of atoms exposed on the surface increase exponentially. If one considers a spherical PbS nano lattice as an example, with decreasing diameter the percentage of overall atoms exposed increases until at approximately 5nm the majority of them lie on the lattice surface. <sup>[5]</sup> (Fig 1.1)

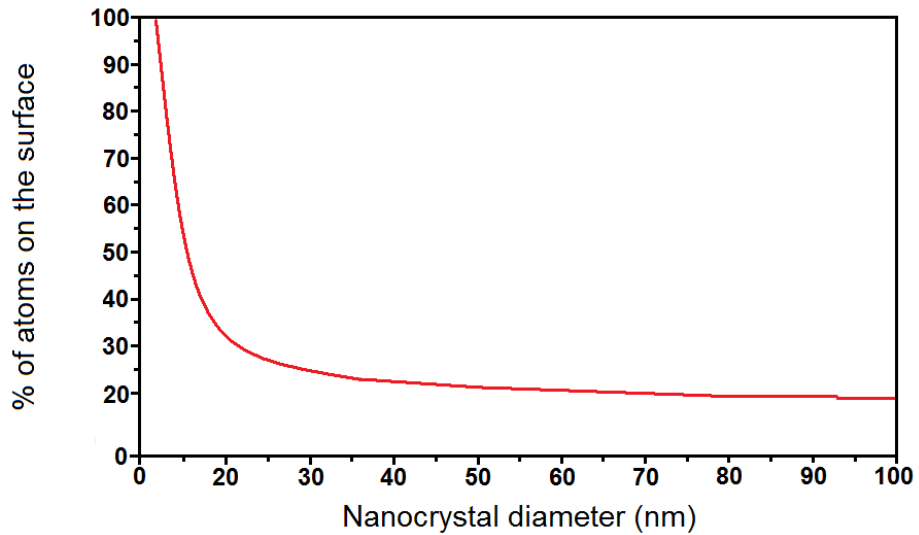


Fig 1.1 Approximate percentage of surface atoms with decreasing nanocrystal size (for a spherical PbS lattice)<sup>[5]</sup>

Typically at the surface atoms are coordinatively unsaturated, revealing ‘dangling bonds’. Usually these atoms demonstrate a partial electric charge, increasing the total energy of the surface. This increase is given as,

$$\gamma = \eta_{db} \left( \frac{\Phi}{2} \right) \quad (1.1)$$

where ( $\gamma$ ) is the surface energy, ( $\eta_{db}$ ) is the surface density of dangling bonds and ( $\Phi$ ) is the energy of the bond.<sup>[5]</sup> From this equation it can be determined that the energy of the surface increases with increasing density of dangling bonds which is decided by chemical composition and other factors such as defects. Therefore the likelihood of a system forming a nanostructure and the physical properties which it exhibits will vary from system to system. Shape can also have a profound affect on the properties either augmenting or diminishing size dependent effects.<sup>[6]</sup> Isotropic spherical gold nanoparticles display a red colour due to the resonant oscillation of electrons at a single frequency. If, however, the structure is anisotropic, e.g. rod shaped, the oscillation occurs at two different frequencies along the transverse and longitudinal dimensions of the particle. This enables the colour to be tuned by changing the aspect ratio (e.g. the longitudinal direction can be adjusted to absorb in the infrared region).<sup>[5]</sup>

Nanomaterials and their development into such an expansive field of research can be traced back to the initial discovery of carbon nanotubes by S. Iijima in 1991 <sup>[7]</sup> which followed the first successful synthesis of fullerenes in 1985 by Kroto *et al.* <sup>[8,9]</sup> Fullerenes were first noticed in the soot formed by arcing graphite electrodes. <sup>[10]</sup> The simplicity of the synthesis breathed new life into carbon research <sup>[11]</sup> and led to the discovery of carbon nanotubes by Iijima. Studying the electrodes closely in fullerene synthesis, Iijima noticed that the insoluble material of arc-burned graphite rods contained nanotubules that were deposited on the negative electrode during the direct current arcing of graphite. <sup>[7]</sup> These particular nanotubes were concentric graphitic cylinders that were closed at either end due to the presence of five membered rings and hence were classed as fullerenes. Carbon nanotubes generated a great deal of interest because of their fascinating properties and structure. They have the potential to play an integral role in future nanoelectronic devices, their mechanical properties have also attracted interest, such as being used as reinforcers in composite materials. <sup>[9]</sup>

The first reported synthesis of inorganic nanotubes was that of WS<sub>2</sub> by Tenne *et al* in 1992. <sup>[12]</sup> Inorganic nanotubes are essentially geometrically similar to carbon nanotubes but from the many compositions that can exist, have the potential for an expansive range of chemical and physical properties. Due to their cylindrical geometry, low mass, high porosity and massive surface area to weight ratio, uses such as highly porous catalytic and ultra light anticorrosive materials, electron field emitters and non-toxic strengthening fibres have been proposed. <sup>[13]</sup> Research on nanomaterials has predominantly focused on oxides, one of the most examples being TiO<sub>2</sub> nanoparticles whose photocatalytic properties have led to the production of self-cleaning coatings on glass, for example. <sup>[14]</sup> There is however a vast scope of work on layered inorganic compounds such as transition metal dichalcogenides, section (1.5), halides and elemental metals. <sup>[11]</sup>

## 1.2 Synthesis

Solid state synthesis is a distinctive area of chemistry which differs from other areas such as organic and co-ordination chemistry. These are understood through the principle that reactions involve distinct molecules with associated ligands and functional groups. Solid state chemistry on the other hand does not concern the interaction of single bonds but rather the construction or modification of entire lattices and therefore needs to be approached with a more appropriate methodology.<sup>[15]</sup>

Solids can be synthesised in many different ways and in many different forms; fibres, films, foams, ceramics, powders, nanoparticles and single crystals for example. To accomplish the optimum result the method must be carefully considered; preparation is dependent upon numerous factors and particular attention must be paid to the stoichiometric quantities and purity of the materials. The stability of the end product under particular reaction conditions is also an important factor to consider.<sup>[16]</sup> Solid state synthesis tends to be a slow process and for it to be successful high temperatures (500°C - 2000°C) are generally needed. For many of the reaction schemes used during this project, the temperatures employed did not exceed the melting point of at least one of the reactants (mainly in the case of the transition metal). It can be challenging to predict resultant phases and for this reason phase diagrams are often utilized.

### 1.2.1 Methodology

The synthesis of chalcogenide nanostructures in the past has been readily achieved through the combination of solids or solids with gases and is an exemplar for the synthesis of anisotropic structures such as nanotubes, nanowires or nanoribbons.<sup>[17,18,19]</sup> Modern solid-state processes can be derived from the ceramic method, one of the oldest and most commonly used practices in synthetic chemistry and still one of the most effective today. A solid-state reaction requires a high level of contact between materials since during a reaction solids can tend to be less reactive than a liquid or gas. Therefore reactants are often ground to increase homogeneity, surface area and hence interaction between the crystal faces. Further interaction can be induced by

having one or more of the reactants in either liquid or gaseous form. A common instance of such a process is chemical vapour transport (CVT) - reactions between reactant powders, which require reaction in the vapour phase or between vapour phase and a substrate, often followed by deposition. The aim of this project was to synthesise non-oxide nanomaterials. Reactions had to be carried out in an inert atmosphere, CVT is a process which can occur under these conditions.

### 1.2.2 Growth mechanism

Crystallisation and growth from solid-gas reactions like CVT are usually understood to proceed via either vapour-liquid-solid (VLS) or vapour-solid (VS) growth mechanisms. VLS growth was first proposed by Wagner *et al.* in 1964. [20] They grew whiskers of Si from a silicon substrate by exploiting gold as a catalyst and  $\text{SiCl}_4/\text{H}_2$  vapour as a source of Si atoms. The VLS mechanism functions through the formation of a catalyst liquid droplet *in situ*, often nucleating crystal growth at one end of the crystal and mediating its propagation. (Fig 1.2)

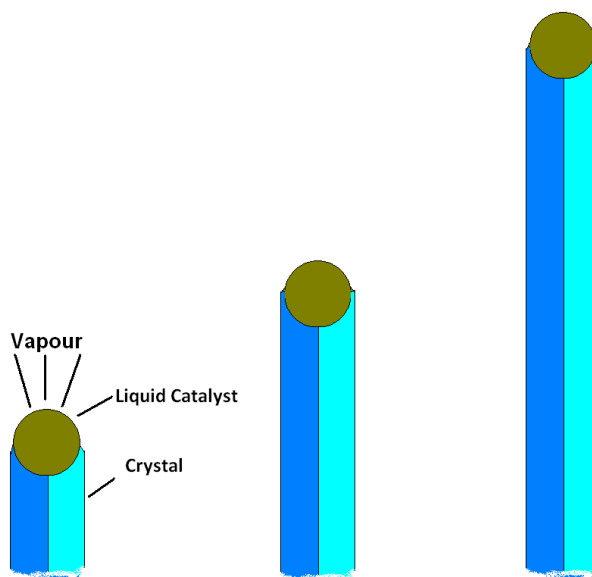


Fig 1.2 Image representing an example of the appearance of a wire forming due to the VLS mechanism with the propagation of the wire as the liquid droplet catalyst sits on top.

The process is reported to proceed via three stages. [21] (1) creation of the participating metal or alloy droplets, (2) subsequent sorption of the vapour phase on and diffusion into the droplet, (3) the supersaturation of the metal (alloy) droplet and the nucleation at the liquid-solid interface leading to

consequent anisotropic crystal growth. The VLS mechanism can be influenced by many factors; surface tension and electronegativity are aspects that directly affect the interaction between catalyst and reactive elements. Composition, rate of development and decomposition are influential features that affect the droplet itself. <sup>[22]</sup> The VS mechanism differs in the fact that it requires no such catalyst. It was first proposed for the growth of SiC whiskers and is usually the most likely to occur for an uncatalysed CVT reaction. <sup>[23]</sup> In comparison to VLS the VS mechanism has been far less reported on. It is generally understood to proceed via self-catalytic or defect-induced growth. Generally, semi-molten droplets form on a surface once critical saturation of the vapour has been reached. These drops, to attain stability and further growth must reach a certain critical size. In one of the first reports, the crystal growth is thought to proceed from this point via screw dislocations at the kink sites of a surface step. This although may not necessarily be the case for other systems. <sup>[24]</sup> In a VLS mechanism, normally one catalytic droplet contributes to the growth of one structure i.e. a nanowire or nanotube. In a VS mechanism a droplet can facilitate the formation of several nanostructures simultaneously. For reactions between chalcogen and substrate the true mechanism may lie between both VLS and VS. Drawing from a scheme theorised for ZnTe nanowire films it may be that crystals can undergo several discontinuous processes, producing multiple layers of nanostructures (Fig 1.3). In this particular case: molten droplets of the zinc condense onto the cooler surface of a substrate (1) forming a solid interface (2). This metal droplet continuously absorbs chalcogen from the surrounding vapour and precipitates out a solid layer of zinc-telluride alloy at the bottom (3) This slowly consumes the metal droplet. Via multiple nucleations, wires of ZnTe form continuously beneath the droplet, solidifying (given their high melting point) and forming a nanolayer film beneath the molten zinc droplet. These layers form discontinuously which results in development of multilayer superstructures of aligned ZnTe nanowire films. <sup>[25]</sup>

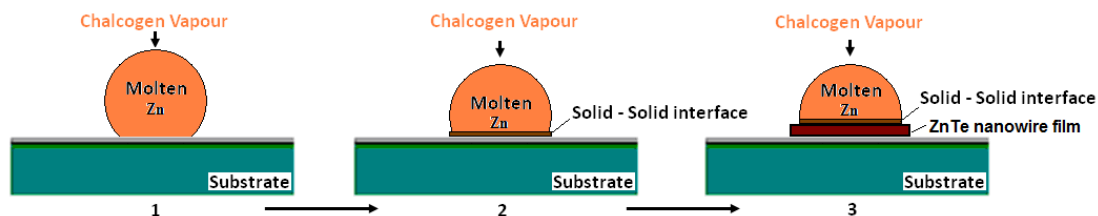


Fig 1.3 Schematic of the proposed VS mechanism

The precise growth mechanism is something which is likely to be dependant on the systems investigated during this project. The explanation in this section is intended simply as a summary and more precise theories of growth with regards to particular systems, will be described in the relevant chapters.

### 1.3 Alternative synthetic methods

The solid-gas phase synthesis approach comprises only a small part of the overall techniques which can be adapted to synthesise transition metal chalcocogenide nanostructures in section 1.3 a few of the other methodologies which can be employed are briefly discussed.

#### 1.3.1 Liquid phase routes

Liquid phase routes are a methodology which offers a plethora of variable parameters to design your reaction: choice of reagents, solvents, concentrations, additives, temperature, pressure, heating and cooling rates are just some of the factors which can have an effect on the chemical composition of the product and its morphology. In some cases it is possible to determine the growth mechanism and link these to the chosen reaction parameters and therefore alter them accordingly depending on the desired outcome. In most cases, however, it is not fully understood how a particular set of reaction parameters can produce certain outcomes and further investigation is needed. Conventional solution methods require separate sources of metal and chalcogen, reacted together in solvent from which the nanomaterials are precipitated. For instance,  $MQ_2$  nanoparticles (where  $M = Mo, W$  and  $Q = S, Se$ ) have been successfully synthesised via a metal carbonyl and chalcogen dissolved in para-xylene solution at a temperature of  $140^\circ C$  for 30 min under a atmosphere of

nitrogen.<sup>[26]</sup> In more complex reactions, structure directing agents (SDA) can be added to influence the product morphology. One of the most clear examples of the impact an SDA can have is in the case PbS nanoparticles. In this example, lead(II)acetate trihydrate ( $\text{Pb}(\text{Ac})_2 \cdot 3\text{H}_2\text{O}$ ) and thioacetamide are reacted at room temperature to produce fern-like crystals of PbS. If on the other hand, SDA poly(vinyl pyrrolidone) (PVP) is added, then the crystal growth switches from anisotropic to isotropic and produces nanocubes of PbS instead.<sup>[27]</sup> Combinations of higher temperature reactions with multiple SDAs can be manipulated to produce nanocrystallites of very small dimensions. For example, nanocrystalline  $\text{Ni}_3\text{S}_4$  with a particle size of ca. 10 nm can be prepared from  $\text{NiCl}_2$  dissolved in an oleylamine (OLA), n-trioctylphosphine (TOP) and sulfur solution. This procedure occurs via two steps with the nickel precursor being first reduced by the OLA and then the resultant nickel nanoparticles reacting with the sulfur to produce  $\text{Ni}_3\text{S}_4$ .<sup>[28]</sup>

### 1.3.2 Template assisted growth

Template-assisted synthesis is generally a convenient and reproducible method for the production of uniform nanowires of varying dimensions and are therefore a useful route for preparing 1D chalcogenide nanostructures with predetermined length and diameter set by the template. In most cases these methods are performed in solution and in the particular case of chalcogenide growth a porous anodic alumina (PAA) template is typically employed.<sup>[29]</sup> These highly ordered PAA membranes are fabricated by the anodization of aluminium foils, either in  $\text{H}_3\text{PO}_4$ ,  $(\text{COOH})_2$  or in  $\text{H}_2\text{SO}_4$  electrolytes. An example of such a method is that of ZnS nanotubes.<sup>[30]</sup> The methodology involves the heating of a volatile precursor dialkyldithiocarbamate,  $\text{Zn}(\text{S}_2\text{CNEt}_2)_2$  in a horizontal tube furnace under a flow of  $\text{N}_2$  gas at a temperature of 200 °C. The PAA itself is held upstream from the reactants at a temperature of 400 °C. Post reaction, the template is further annealed for 5 h at 400 °C. This converts the amorphous nanotubes to the crystalline wurtzite structure and results in the production of well aligned, high density ZnS nanotubes. A major advantage of such a process is that it can easily be scaled up for larger production.

### 1.3.3 Solvothermal and hydrothermal routes

Solvothermal methods (of which hydrothermal methods form a subsection) are generally achieved through the combination of a source of transition metal and chalcogen, a suitable solvent and sometimes a SDA. Reactions are often run in autoclaves at high pressures which are dependent on the reaction temperature used. SDAs are not essential to the growth process but it has been observed in some cases that the inherent crystal structure of a material can act as a guide to the formation of a specific morphology on the nanoscale. For instance, the reaction between  $\text{SbCl}_3$  and  $\text{K}_2\text{TeO}_3$  with tartaric acid, ammonium hydroxide and hydrazine at  $180\text{ }^\circ\text{C}$  for 5 h produces hexagonal platelets of nano- $\text{SbTe}_3$ .<sup>[31]</sup> Bulk  $\text{SbTe}_3$  is rhombohedral (space group  $R\bar{3}m$ ), it comprises of Te and Sb layers, separated by van der Waals interactions between adjacent tellurium layers which stack along the c-axis. For the ab plane of the structure, covalent bonding is found instead. Thermodynamically there is more free energy in a broken covalent bond than a disrupted van der Waals interaction and therefore growth occurs fastest in the ab-plane. For this reason it is suggested that the crystal structure of the inherent material is the driving force behind the observed anisotropic crystal growth of the  $\text{Sb}_2\text{Te}_3$  nanoplatelets. Other than SDA, the choice of solvent is also an equally important prerequisite for the formation of a particular morphology. For example, the formation of CuS nanostructures are achieved using a mixture of copper acetate, citric acid and thiourea. A number of different product morphologies were found to emerge depending on the solvent used.<sup>[32]</sup> Using ethanol for instance, flower-like structures composed of flakes were produced, whereas other solvents such as ethylenediamine and ethylene glycol formed smaller, less regular shapes. In addition, the use of capping agents is sometimes implemented to induce a preferential growth direction and encourage products with low dimensionality. In the synthesis of CuS, reacting copper acetate with  $\text{CS}_2$  in toluene, nano-platelets are formed when hexadecylamine (HDA) is added as a capping agent.<sup>[33]</sup> The hexagonal platelets already exhibit preferential growth in the (110) planes but the HDA also inhibits growth in the 001 direction and it is both these factors which contribute to the overall morphology.

### 1.3.4 Other methods

Other than solution and template directed approaches there are a number of somewhat less conventional methods that are starting to play an increasing role in transition metal chalcogenide nanoscale synthesis. These are techniques such as mechanical processing. For instance FeS<sub>2</sub> and FeS nanoparticles have been produced by high energy ball milling of elemental iron and sulfur bulk powders with the use of NaCl as a dispersion medium.<sup>[34]</sup> Although this can provide a means to produce particle sizes of <10 nm there appears to be little opportunity to manipulate the morphology of the nanostructured products. Another example is sonochemical production which involves a phenomenon termed acoustic cavitation<sup>[35]</sup> whereby the crystal growth is directed by the formation, growth and implosive collapse of bubbles in the solution under sonication. The temperature and pressure of these bubbles can reach up to values as 5000 K and 500 bar but exist on such a short timescale that cooling rates of 10<sup>9</sup>K s<sup>-1</sup> are possible. A number of different nanostructures have been synthesised this way including chalcogenides of mercury<sup>[36]</sup> and copper.<sup>[37]</sup>

## 1.4 Transition metal chalcogenides (overview)

The transition metal chalcogenides are a vast area that has been the subject of extensive studies over the years. For example, McTaggart *et al* in the late fifties conducted a thorough review on the synthesis, structure and properties of the group IV chalcogenides<sup>[38,39,40]</sup> whereas Wilson *et al* have investigated dichalcogenides across the d-block metals.<sup>[41, 42]</sup> Structurally the transition metal dichalcogenides can be split into two categories, layered and non-layered. The layered dichalcogenides (groups IV- VII) are a well defined family of compounds that tend to form at high temperatures and a single compound can exhibit a number of different phases depending on the reaction conditions. For example, the 1T form of TaS<sub>2</sub>/Se<sub>2</sub> forms above 827 °C whereas the 2H-TaS<sub>2</sub> polytype can be synthesised at the lower temperature of 550 °C.<sup>[43]</sup> They encompass a vast spectrum of electrical properties which comprises insulators like HfS<sub>2</sub>, semiconductors such as MoS<sub>2</sub> and metallic conductors like NbS<sub>2</sub> and VSe<sub>2</sub>. Their diversity in properties is thought arise partly from the presence of non-bonding d-bands and the extent to which they are filled.<sup>[41]</sup> Non-layered

dichalcogenides (Group VIII onwards) show an equal diversity in their physical properties. For example, 3d metals have a tendency to be Mott-insulators (e.g. NiS<sub>2</sub>) a characteristic that is no longer present as you travel across to the 4d and 5d metals.<sup>[44]</sup> Again, this diversity arises from filling of the narrow non-bonding d bands but also in conjunction with increasing metal-metal atom orbital overlap going from 3d to 4d and 5d members due to the increasing ionic radius of the cation.

The transition metal trichalcogenides are a more concise collection and cover groups IV - VI. Numerous publications by Kjekshus *et al* in the sixties and seventies covered much of their initial structural work.<sup>[45, 46]</sup> and have helped set the foundations for many future investigations. The group IV and V trichalcogenides typically produce black, needle-like crystals, except for the trisulfides of zirconium and hafnium which are orange (there are no reported examples with vanadium) and are synthesised typically between 400 °C - 700 °C.<sup>[47]</sup> Beyond these ranges they tend to decompose to their dichalcogenide equivalents. The trichalcogenides possess a pseudo one-dimensional structure which gives rise to a high level of anisotropy in their physical properties. Tantalum trisulfide (TaS<sub>3</sub>) for example, (which was first synthesised in 1938 by Blitz and Kocher<sup>[48]</sup> and the structure later determined in 1962 by Jellinek)<sup>[49]</sup> is unusual amongst the group IV and V chalcogenides because other than a monoclinic crystal system it also exhibits an orthorhombic alternative with space group C222<sub>1</sub>, (lattice parameters;  $a = 36.084 \text{ \AA}$ ,  $b = 15.173 \text{ \AA}$  and  $c = 3.340 \text{ \AA}$ ). It is interesting because the monoclinic phase displays a commensurate charge density wave (CCDW) transition at 215 K<sup>[50]</sup> whereas the orthorhombic counterpart has two incommensurate charge density waves (ICDW) at 240 K and 160 K.<sup>[51]</sup> Charge density wave formation is in fact typical of the Group V trichalcogenides. Niobium triselenide (NbSe<sub>3</sub>) for example, (which is probably one of the most widely studied of the compounds) exhibits CDW formations at 145 K and 59 K<sup>[52]</sup> whereas on the other hand tantalum triselenide (TaSe<sub>3</sub>) forms a superconducting state below 2.1 K.<sup>[53]</sup> In general, the sulfides and selenides form more readily than tellurides which have proven elusive for titanium, tantalum and niobium.<sup>[47]</sup> The latter two however form tetratellurides, TaTe<sub>4</sub> and NbTe<sub>4</sub>, which also exhibit a series of CCDW formations.<sup>[54,55,56]</sup> There are some examples of Group VI trichalcogenides such as MoS<sub>3</sub> and WS<sub>3</sub><sup>[57]</sup> but these

are evidently amorphous and have not been synthesised *via* CVT or CVD means and have been the subject of little investigation in comparison to their Group IV and V analogues. The focus of this research is on group-IV trichalcogenides and only this group shall be discussed in more detail in subsequent sections.

Both the dichalcogenide and trichalcogenide families are covered in more detail in the two subsequent sections (1.5) and (1.6).

### 1.5. Transition metal dichalcogenides

As mentioned in section (1.4) Transition metal dichalcogenides ( $TQ_2$ , T= transition metal, Q = chalcogenide) can be characterised into two basic structural categories: layered and non-layered.<sup>[41]</sup> The covalent character of the T-Q bond and the polarizability of the anionic chalcogen result in numerous possible atomic arrangements.

#### 1.5.1 Layered structures

Layered type structures are exhibited by the dichalcogenides of the early transition metals (typically groups IV-VI) and consist of covalently bonded (Q-T-Q) sheets. These sheets propagate along the c-axis and are weakly bound to each other by van der Waals interactions. The metal can have either trigonal prismatic or octahedral coordination, depending on the system i.e.  $MoS_2$  or  $NbS_2$  contain T-S trigonal prisms whereas  $HfS_2$  and  $ZrS_2$  contain octahedral species (Fig 1.4). In general, Group IV-  $MQ_2$  structures adopt octahedral coordination, Group V- $MQ_2$  a combination of both octahedral and trigonal prismatic and Group VI- $MQ_2$  solely trigonal prismatic coordination. This variation in coordination arises from the change in the number of electrons in the d orbitals of the transition metal ( $d^0$ ,  $d^1$  and  $d^2$  respectively). In a transition metal complex there are a total of five d orbitals, three of which have their lobes pointing between the x, y and z axes:  $d_{xy}$ ,  $d_{yz}$  and  $d_{xz}$  and two which are directed along the axes:  $d_z^2$  and  $d_x^2 - y^2$ . In the case of octahedral coordination a populated  $d_z^2$  orbital would point towards axial anions (Fig 1.5) and therefore the band would be higher in energy in comparison to trigonal prismatic coordination. For this

reason,  $d^0$  metals will adopt octahedral coordination whereas  $d^2$  metals will adopt trigonal prismatic coordination.<sup>[58]</sup>

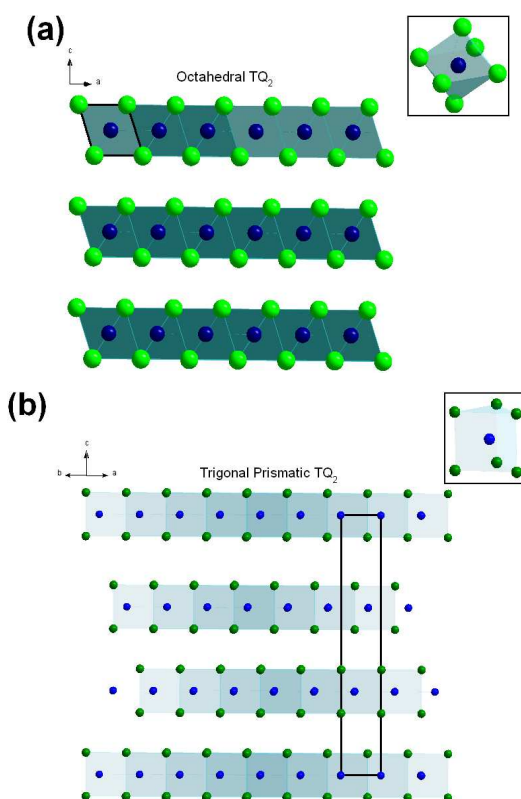


Fig 1.4 a) Schematic representing layered octahedral-  $TQ_2$  structure, blue atoms represent the transition metal, green atoms the chalcogen. Inset octahedral coordination of the transition metal. b) Trigonal prismatic -  $TQ_2$  structure, inset trigonal prismatic coordination of the transition metal. Layers stack along the  $c$ -axis held together by weak van der Waals forces. Unit cells are indicated by black outlines on the structure.

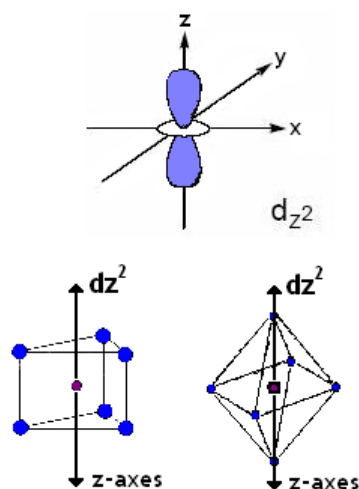


Fig 1.5 Molecular orbital diagram of the  $d_{z^2}$  orbital in conjunction with trigonal prismatic and octahedral coordination.

The crystal symmetry of  $TQ_2$  structures is determined by the stacking of the layers of these units along the c-axis. In the case of group V and VI metals, stacking sequences can differ giving rise to various *polytypes*. A specific example is tantalum disulfide where the central cation is surrounded by six anions in either trigonal prismatic or octahedral coordination. The stacking sequences in these structures can vary creating multiple polytypes which retain the same chemical composition. The 1T polytype of  $TaS_2$  for example consists of purely octahedral units, 2H solely consists of trigonal prismatic  $MQ_6$  species and 4H<sub>b</sub> contains layers of each type<sup>[59]</sup> (Fig 1.6). In regards to nomenclature, the letter part of this polytype classification system represents the crystallographic symmetry, for instance, H is hexagonal and T is trigonal (but with a hexagonal Bravais lattice). The numeric part represents the stacking periodicity sometimes accompanied by either of three subscript letters (a, b or c respectively) which indicate along which of the three axes of the compound the periodicities occur.<sup>[60]</sup> The stacking sequence of the layers themselves can be identified using ‘ABC’ notation to represent each identical layer of atoms. In accordance with Ramsdell notation the metal layers are usually expressed with lower case letters so they can be differentiated from the anions which are denoted in upper case letters. In the case of the 1T polytype for instance the structure can be denoted as *AbC*, since it composed of solely octahedral units there are only three distinct layers of atoms. The trigonal prismatic coordination of 2H however gives rise to the slightly more complicated *AbACbC* stacking sequence.

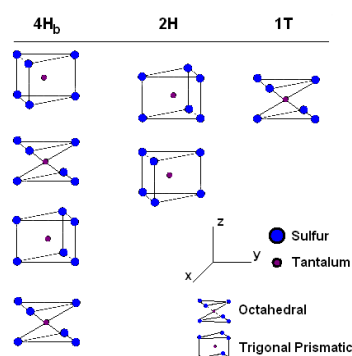


Fig 1.6 Stacking sequence of three polytypes of  $TaS_2$ . Left the 4H<sub>b</sub>-polytype which alternates between octahedral and trigonal prismatic layers, 2H which contains only octahedral layers and 1T which is comprised only of trigonal prismatic layers.

The-TQ<sub>2</sub> compounds of Group IV on the other hand have a preference for the 1T-polytype (*cadmium iodide* structure, hexagonal space group P $\bar{3}$ m1).<sup>[58]</sup> Specific lattice parameters for a range of T(IV) Q<sub>2</sub> compounds are given in Table 1.1 and a plot of *a*, *c* lattice parameters vs. ionic radii is given in (Fig 1.7). Generally, group IV-TQ<sub>2</sub> compounds are semiconductors with the exception of TiSe<sub>2</sub> and TiTe<sub>2</sub> which are considered semi-metals.<sup>[61]</sup>

Table 1.1 Gives unit cell dimensions for known examples of group IV-TX<sub>2</sub>

Group IV- TX <sub>2</sub>	a (Å)	c (Å)
TiS <sub>2</sub> <sup>[58,41]</sup>	3.39	5.70
TiSe <sub>2</sub> <sup>[62, 41]</sup>	3.535	6.004
TiTe <sub>2</sub> <sup>[63, 41]</sup>	3.76	6.48
ZrS <sub>2</sub> <sup>[58, 41]</sup>	3.662	5.813
ZrSe <sub>2</sub> <sup>[58, 41]</sup>	3.770	6.137
ZrTe <sub>2</sub> <sup>[58, 41]</sup>	3.952	6.660
HfS <sub>2</sub> <sup>[58, 41]</sup>	3.635	5.837
HfSe <sub>2</sub> <sup>[58, 41]</sup>	3.748	6.159
HfTe <sub>2</sub> <sup>[64]</sup>	3.957	6.650

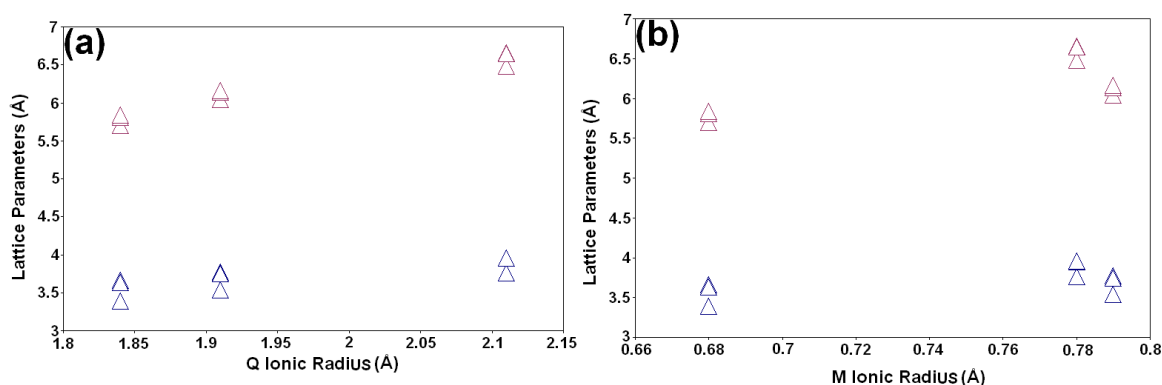


Fig 1.7 Plot of *a* and *c* lattice parameters vs. increasing a) Q ionic radii b) Metal ionic radii. Blue Triangles represent the *a*-lattice parameter and purple triangles the *c*-lattice parameter.

In general, the structure of the TQ<sub>2</sub>-layers results in a behaviour comparable to that of graphene sheets.<sup>[65]</sup> Due to the weak inter-layer forces, the TQ<sub>2</sub> sheets have the propensity to slide over one another. This makes several TQ<sub>2</sub> compounds excellent as solid state lubricants, most notably the sulfur and selenide compounds of molybdenum and tungsten.<sup>[66]</sup>

The electronic properties of layered transition metal dichalcogenides have been the subject of much attention, such as their ability to support charge-density wave (CDW) formation as seen in the cases of  $\text{TiSe}_2$ <sup>[67]</sup> or  $\text{TaSe}_2$ .<sup>[42,68]</sup> Charge-density waves are the name given to an anomalous set of distortions that occur in the electromagnetic properties of a metallic compound whose electronic structure is otherwise highly uniform. It is believed that that these distortions result in the formation of a superlattice.<sup>[68]</sup> They are periodic in nature and tend to be related to the Fermi surface of a structure. Fermi surfaces support charge density wave formation and their size directly affects the periodicity of the CDW. The transition metal dichalcogenides have proven to be an ideal system to study this complex relationship. The number of different polytypes exhibit a number of different band structures creating an abundance of examples which exhibit such periodic distortions. In addition, their electronic concentrations can be easily altered *via* doping to create a wider scope of analysis.<sup>[59]</sup> Further, several examples of layered-TQ<sub>2</sub> materials demonstrate superconductivity. The metal coordination with each layer type and the layer stacking sequence determines the band structure and hence the overall physical properties of a particular polytype.<sup>[69]</sup> For example, 2H polytypes tend to exhibit superconductivity (e.g. 2H-TaSe<sub>2</sub> and 2H-NbSe<sub>2</sub>)<sup>[69,70]</sup> compared to the 1T polytypes which have no reported superconducting transitions under normal conditions. Recent studies have shown however that under high pressure 1T-TaS<sub>2</sub> shows superconductivity with T<sub>c</sub> (critical temperature) < 1.5 K at pressures of 2.5 GPa.<sup>[71]</sup>

To conclude this brief overview, the layered dichalcogenides of V and Cr are now discussed, but as a whole there is a lot less information available on these particular compounds. With the exception of VSe<sub>2</sub>, the vanadium dichalcogenides have received less attention than their group V counterparts since these in comparison are more difficult to prepare.<sup>[72]</sup> VSe<sub>2</sub> and VTe<sub>2</sub> crystallise with a CdI<sub>2</sub> layered structure. In the particular case of VSe<sub>2</sub>, the sheet of vanadium atoms occupies octahedral holes between two sheets of hexagonally close packed selenium atoms. It exhibits metallic behaviour over the range of 1.5 - 300 K and more interestingly it displays the formation of charge density waves at approximately 100 K.<sup>[73]</sup> Other early transition metals however, such as VS<sub>2</sub> (which is also reported to exhibit CDW formation at ca. 308 K.<sup>[74]</sup>), CrS<sub>2</sub> and CrSe<sub>2</sub>

cannot be achieved in a stable state by the direct combination of their elements. Instead they are most easily obtained in a metastable  $\text{Cd}(\text{OH})_2$  type structure by the deintercalation of alkali metal intercalates  $\text{MTQ}_2$  (where M = an alkali metal).<sup>[75]</sup> For instance,  $\text{CrSe}_2$  was eventually prepared by the oxidation of  $\text{KCrSe}_2$  with  $\text{I}_2$  in acetonitrile at room temperature.<sup>[76]</sup>  $\text{CrSe}_2$  was found to be metastable and convert to  $\text{Cr}_2\text{Se}_3$  and Se at around 600 K. It is also rather unique among Group - VI dichalcogenides as it adopts octahedral coordination rather than trigonal prismatic.  $\text{CrSe}_2$  is metallic with enhanced Pauli paramagnetism. On the other hand it is reported that it is not possible, or at least very difficult, to synthesise  $\text{CrS}_2$ .<sup>[59]</sup> Although, one crystal structure has been reported with octahedral layers of  $\text{CS}_6$  as part of a study into misfit layer  $(\text{YS})_x \text{CrS}_2$  compounds.<sup>[77]</sup>

### 1.5.2 Non-layered structures

Examples of non-layered  $\text{TQ}_2$  compounds emerge from group VII and onwards. They can be categorised into four different sub-groups: pyrites, marcasites,  $\text{IrSe}_2$  and  $\text{PdS}_2$  type structures.<sup>[41]</sup> For the purposes of this research only pyrite structures will be discussed. The 3d transition metal sulfides (e.g.  $\text{FeS}_2$ ,  $\text{CoS}_2$ ,  $\text{NiS}_2$ ,  $\text{CuS}_2$  and  $\text{ZnS}_2$ )<sup>[78]</sup> are a common set of systems which crystallise to form the cubic-pyrite structure. They have been of particular interest for their range of semiconducting and metallic behaviour coupled with a wide range of magnetic properties.<sup>[78]</sup> A few examples are; iron disulfide for instance, which has a narrowband gap of 0.95 eV and has been of particular interest since it can be adapted to photochemical and photovoltaic solar cells and as a cathode material for lithium batteries.<sup>[79]</sup> Cobalt disulfide has a higher electronic conductivity and thermal stability when compared to other metal sulfides (such as  $\text{FeS}_2$ ) and has been investigated for its application in secondary lithium-ion batteries.<sup>[80]</sup> The structure of pyrites differs from the layered structures discussed above in that it is essentially 3D in nature (with no van der Waals gaps) and contains complex anions which show strong chalcogen to chalcogen bonds ( $\text{X}_2^{2-}$  pairs).<sup>[58]</sup> They crystallise in a similar fashion to the fcc lattice of the NaCl rocksalt structure where the positions of  $\text{Na}^+$  and  $\text{Cl}^-$  are substituted by the transition metal and  $\text{X}_2^{2-}$  pairs (Fig 1.8).<sup>[81]</sup> Each metal cation is surrounded by six anions in a distorted octahedral environment (Fig 1.9) and each anion is bonded

to one other anion and three cations in a distorted tetrahedral environment.<sup>[82]</sup> Examples along with lattice parameters are given in (Table 1.2), all crystallise with cubic space group  $Pa\bar{3}$ .

Table 1.2 Unit cell dimensions for cubic-pyrite structured  $TS_2$

$TS_2$ pyrite structure	a (Å)
$FeS_2$ <sup>[78]</sup>	5.407
$CoS_2$ <sup>[78]</sup>	5.524
$NiS_2$ <sup>[78]</sup>	5.677
$CuS_2$ <sup>[78]</sup>	5.790
$ZnS_2$ <sup>[78]</sup>	5.954

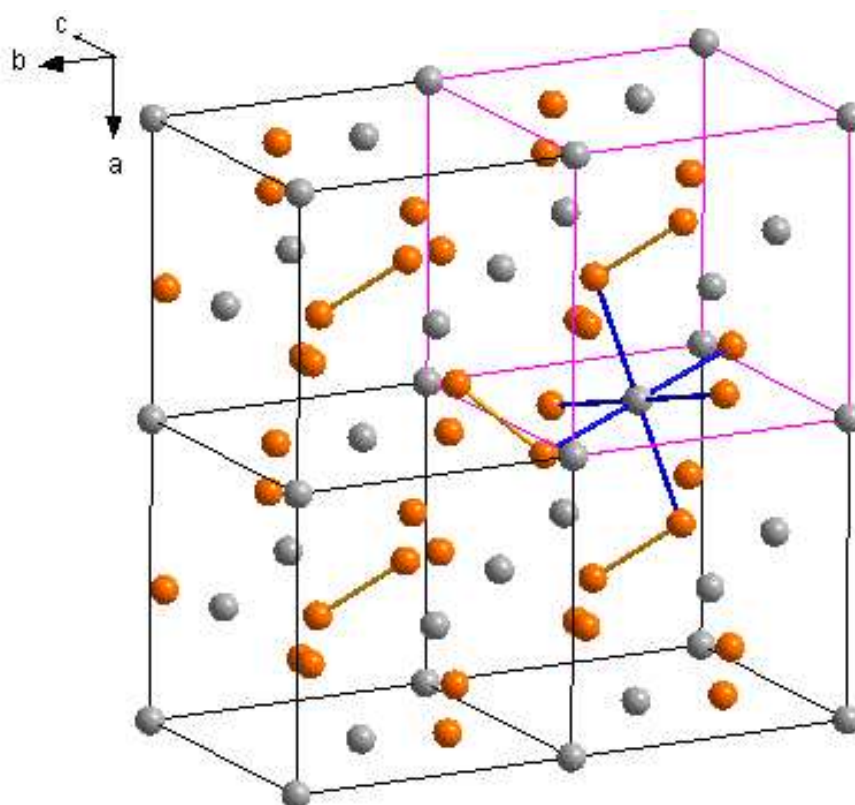


Fig 1.8 Cubic pyrite structure; face centred rocksalt structure with the metal atoms in a distorted octahedral coordination to  $Q_2^{2-}$ , share common corners. Grey spheres represent iron, orange spheres represent sulfur. Sulfur to Sulfur bonds are represented in gold and iron to sulfur bonds in blue. Unit cell edges are highlighted in magenta.

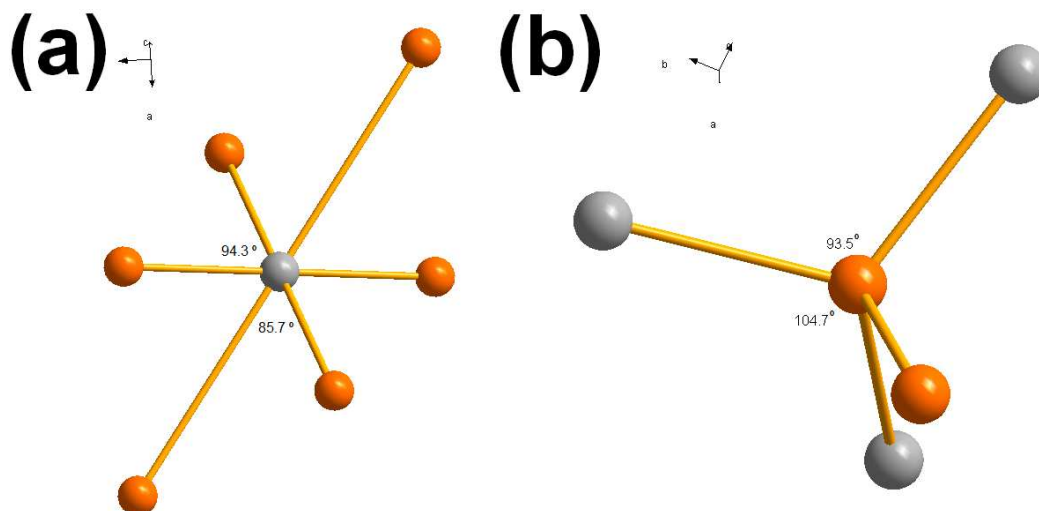


Fig 1.9 a) Distorted octahedral coordination of metal cation to six anions, two angles given show deviation from standard  $90^\circ$  octahedral bond geometry. b) Distorted tetrahedral environment of anion, bonded to one other anion and three cations.

## 1.6 Transition metal trichalcogenides

Transition metal trichalcogenides ( $\text{MQ}_3$ ,  $M$  = transition metal and  $Q$  = chalcogenide) are a class of one-dimensional systems which have been an active area of research for many decades due to their unusual and/or promising range of physical properties. Like  $\text{TQ}_2$  they constitute a structurally and chemically well-defined family of compounds which encompasses the group IV, V or VI transition metals with chalcogens: sulfur, selenium or tellurium. Structurally, their pseudo one dimensional structure is comprised of  $\text{MQ}_3$  trigonal prismatic chains which result from stacking of  $\text{MQ}_6$  trigonal prism units with the metal occupying the centre of the prism (Fig 1.10). The three chalcogen atoms which form the triangular base are non-equivalent with one side much shorter than the remaining two. In the case of  $\text{ZrSe}_3$  for example there are two longer Q-Q distances of  $3.75 \text{ \AA}$  and  $3.79 \text{ \AA}$  compared to the shorter distance of  $2.35 \text{ \AA}$  <sup>[83]</sup> (Fig 1.11). The latter is in good agreement with the expected value for a single elemental Se bond ( $2.32 \text{ \AA} \pm 0.003 \text{ \AA}$ ). <sup>[84]</sup> The formation of these chalcogen-chalcogen bonds means the valence state of  $\text{MQ}_3$  is considered as  $M^{+4/+5/+6}(\text{Q}_2^{2-})\text{Q}^{2-}$  (the oxidation state of the metal centre being dependent on group from which it originates i.e. Group IV, V or VI). The chains are held together by strong ionic, covalent (or sometimes metallic) bonding and expand parallel to the  $b$ -axis. The distance between the chains is comparatively large

exhibiting weak van der Waals bonding. <sup>[47]</sup> Crystals propagate along the (001) plane and are easily cleaved to reveal flat (001) surfaces. <sup>[85]</sup> The anisotropic growth usually produces fibrous ribbon like crystals and has a profound effect on their overall physical properties giving rise to phenomena such as charge density waves (CDW) and superconductivity. The chain-like structure also makes them ideal candidates as intercalation compounds with various investigations carried out with Li as a guest, for example. <sup>[86]</sup>

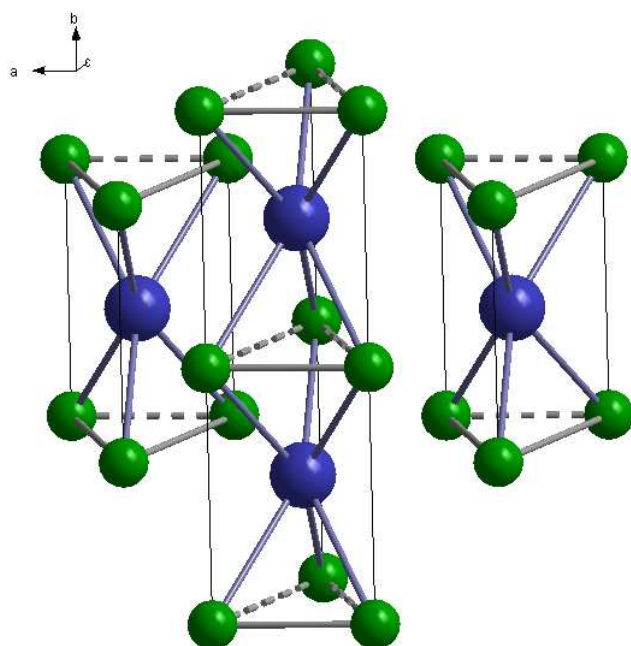


Fig 1.10 Schematic representing typical structure of MQ<sub>3</sub> with the MQ<sub>6</sub> trigonal prisms propagating along the *b*-axis, blue spheres represent the transition metal, green spheres the chalcogen.

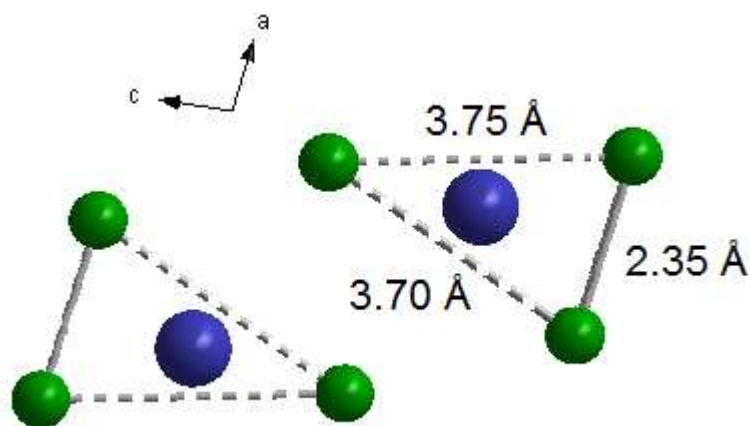


Fig 1.11 Projection down the *b*-axis of the MQ<sub>6</sub> prism, showing the different bond lengths between the chalcogen atoms. Blue spheres represent the metal and green the chalcogen.

### 1.6.1 Group IV trichalcogenides

All known examples of group IV-MQ<sub>3</sub> compounds are considered iso-structural with ZrSe<sub>3</sub> and crystallise monoclinically with space group P2<sub>1</sub>/m. Lattice parameters for each of these M<sup>IV</sup>Q<sub>3</sub> compounds are given in (Table 1.3).

Table 1.3 Unit cell dimensions for known examples of group IV-MQ<sub>3</sub>

Compound	a (Å)	b (Å)	c (Å)	B (°)	V (Å <sup>3</sup> )
TiS <sub>3</sub> <sup>[83,87]</sup>	5.01	3.40	8.80	98.40	146.8
ZrS <sub>3</sub> <sup>[83,88]</sup>	5.06	3.60	8.95	98.40	165.4
ZrSe <sub>3</sub> <sup>[83]</sup>	5.41	3.74	9.44	97.48	189.9
ZrTe <sub>3</sub> <sup>[83]</sup>	5.89	3.92	10.10	97.82	231.5
HfS <sub>3</sub> <sup>[83]</sup>	5.09	3.52	8.96	97.38	162.8
HfSe <sub>3</sub> <sup>[83, 89]</sup>	5.38	3.72	9.40	97.80	187.3
HfTe <sub>3</sub> <sup>[83]</sup>	5.87	3.90	10.05	97.98	228.5

#### 1.6.1.1 Titanium trichalcogenides

Titanium trisulfide is the only reported MQ<sub>3</sub> phase for titanium. To the authors knowledge there are no reported synthesis of either titanium triselenide (TiSe<sub>3</sub>) or titanium tritelluride (TiTe<sub>3</sub>). Reviews by McTaggart<sup>[38]</sup> and Kjekshus<sup>[83]</sup> state that they were unable to produce either phase. A later publication by Kjekshus *et al.*<sup>[45]</sup> however does report the synthesis of TiSe<sub>3</sub> but with no accompanying structural determination. It is noted that the stability of Group IV-transition metal trichalcogenides increases as one goes from titanium through to hafnium. Furthermore, the sulfur based equivalents tend to be more covalent in their chemical behaviour in comparison to their relatively metallic tellurium counterparts.<sup>[39]</sup> The structure of titanium trisulfide like ZrSe<sub>3</sub> contains three sulfur sites, S<sub>I</sub>, S<sub>II</sub> and S<sub>III</sub>, which at the base of the MQ<sub>6</sub> prism have bond lengths 3.29 Å, 3.76 Å and 2.04 Å respectively. The latter again implies strong S-S bonding and the formula of TiS<sub>3</sub> is given as Ti<sup>+4</sup> (S<sub>2</sub><sup>2-</sup>)S<sup>2-</sup> with oxidation states confirmed by X-ray photoelectron spectroscopy (XPS).<sup>[90]</sup> It is an example of n-

type semiconductor with a band gap of 0.9 eV <sup>[91]</sup> and exhibits largely temperature independent diamagnetism (between the ranges of 100 K and 573 K). <sup>[92]</sup> Recent interests have involved fabricating TiS<sub>3</sub> (or TiS<sub>2</sub>) on metal or semiconducting substrates as they can be used for electronic field emission functional blocks. <sup>[93]</sup> They have also been investigated for their potential application in copper oxide based cathodes for non-aqueous alkali metal batteries. <sup>[94]</sup>

#### 1.6.1.2 Zirconium trichalcogenides

One of the first studies of the zirconium-sulfur system was conducted by Strotzer, Blitz and Meisel in 1939. <sup>[95]</sup> Further investigations were made by McTaggart <sup>[41]</sup> and Ness <sup>[96]</sup> in the late fifties and a full structural analysis of zirconium trisulfide was established by Kjekshus *et al.* in 1975. <sup>[45]</sup> Studies on single crystals of ZrS<sub>3</sub> have shown a typical resistance of a approximately 10-12 MΩ at room temperature a value which decreases with increasing temperature to about 2 MΩ. At room temperature, an increase in pressure causes the resistivity to increase with a rise from 1 MΩ to 18 MΩ at pressures of ca. 5 to 90 x 10<sup>8</sup>Pa. <sup>[97]</sup> Zirconium triselenide is also a semiconductor, and exhibits temperature independent diamagnetism. <sup>[83]</sup> Zirconium tritelluride (ZrTe<sub>3</sub>) on the other hand is a metallic conductor <sup>[40]</sup> and exhibits a plethora of phenomena such as CDW <sup>[98,99]</sup>, a resistivity/structural anomaly at 63 K <sup>[100]</sup> and superconductivity below 2 K. <sup>[101]</sup>

#### 1.6.1.3 Hafnium trichalcogenides

Hafnium Trisulfide (HfS<sub>3</sub>) is one of two examples where an MQ<sub>3</sub> exhibits dichroism (the other being ZrS<sub>3</sub>). <sup>[87]</sup> A dichroic material is one which splits visible light into distinct beams of different wavelengths. HfS<sub>3</sub> is another example of an n-type semiconductor with a very high specific resistivity (approximately 10x10<sup>11</sup> Ωcm at 80 °C); it therefore borders on being an insulator with a band gap of 3.1 eV. <sup>[88,40]</sup> It has a low magnetic susceptibility displaying temperature independent diamagnetism from 90 K - 573 K. <sup>[92]</sup> Hafnium Triselenide (HfSe<sub>3</sub>) is a p-type semiconductor <sup>[97]</sup> (the only example in group IV-

$\text{MQ}_3$  compounds) and like  $\text{HfS}_3$  exhibits temperature independent diamagnetism but with a slightly higher magnetic susceptibility ( $-0.4 \chi_g \times 10^6 \text{ emu g}^{-1}$  compared to  $-0.21 \chi_g \times 10^6 \text{ emu g}^{-1}$  for  $\text{HfS}_3$ ).<sup>[83]</sup> Hafnium tritelluride ( $\text{HfTe}_3$ ) was first investigated by Kjekshus *et al.* who reported that it can be produced via a direct synthesis between the corresponding elements at around  $500 \text{ }^\circ\text{C}$ .<sup>[64]</sup> A later publication claims that single crystals can only be achieved by the thermal decomposition of  $\text{HfTe}_5$ .<sup>[102]</sup>  $\text{HfTe}_5$  itself can be synthesised by reacting the elemental powders at temperatures between  $450 - 500 \text{ }^\circ\text{C}$  for approximately 148 hours and allowing several days for the vessel to cool.<sup>[103,104]</sup>  $\text{HfTe}_3$  decomposes at temperatures  $\geq 600 \text{ }^\circ\text{C}$ .<sup>[97]</sup> There is little reported on the physical properties of  $\text{HfTe}_3$  but it is suggested that the compound could be similar to  $\text{ZrTe}_3$ . One such report combines experimental and theoretical studies to calculate the band structures of  $\text{ZrTe}_3$  close to the Fermi level ( $E_f$ ), given its isostructural relationship to  $\text{HfTe}_3$  similar electronic behaviour is predicted.<sup>[105]</sup> Both structures exhibit a partial overlap between the chalcogen p-block bands and the metal d-block bands so there is considerable charge transfer from the tellurium atoms to the metal and vice versa. Calculations have shown that tellurium to tellurium pairs and excess interstitial tellurium atoms between the trigonal prismatic columns have a tendency to carry a larger charge that increases the Fermi level<sup>[106]</sup> and therefore play a significant role in the phase transition that forms the CDW. In addition, the electronic properties of  $\text{ZrTe}_3$  have been shown to be pressure dependent. Studies have shown that initially, with increasing pressure, the temperature of the CDW formation also increases. At about 2GPa it begins to decrease and disappears altogether by 5 GPa.<sup>[107]</sup> The similarity in the arrangement of tellurium between  $\text{HfTe}_3$  and  $\text{ZrTe}_3$  implies similar pressure dependant behaviour in the hafnium compound.<sup>[105]</sup>

## 2. Experimental

### 2.1 Synthesis

A standard chemical vapour transport (CVT) is where powdered reactants are heated in a sealed reaction vessel (in this case a vessel composed of quartz-silica) and to which a temperature gradient is applied. The difference in temperature from one end of the vessel to the other facilitates the gaseous transport of one or more of the reactants. This can also be aided by the addition of a transport agent, typically iodine or bromine. The vessel can be split into two sections; the charge end (heated zone, containing the reactants) and the growth end (where crystals of the product evolve). The process often involves one of the reactants forming a volatile gas which reacts with the remaining reactants. The product is transported via the vapour phase from the charge to the growth end from which they condense and grow. Silica is a suitable material for the vessel chiefly because of its high melting point, poor conduction of heat and chemical inertness towards the reactants. In the case of this project, prepared ampoules were loaded with the required reactants and attached to a rotary pump. The atmospheric pressure of the reaction vessel was reduced to c.a. 3 mbar and sealed shut (Fig 2.1) with glass blowing equipment - an oxygen/methane gas torch; a process which required the wearing of didymium eyeglasses to protect against the resultant UV light.



Fig 2.1 Typical sealed silica reaction vessel/ampoule with reactants inside

The above process removed any oxygen that could contaminate the reaction. The absence of air is a key feature of a typical CVT reaction process and allows the formation of the chalcogen vapour to play a more determinative role in the reaction between the chalcogen and metal. Generally, the CVT process is reported to proceed via three steps: (1) the evaporation of the solid reactants, (2) transport of the reactants from one end of the reaction vessel to the other whilst in the vapour phase and (3) condensation of the vapour on a surface from

which it grows.<sup>[21]</sup> The reaction is thus conducted within a closed system and the vapour pressure induced within the vessel is dependent upon factors such as temperature and the stoichiometric ratio of the reactants.

### 2.1.1 Phase diagrams

When necessary, phase diagrams were consulted to help choose reaction conditions. Phase diagrams show the behaviour of a multicomponent system as a function of temperature and ratio of reactants. They are used to highlight the stabilities of various phases through the balance of these two factors and are constructed experimentally. A binary phase diagram plots temperature against composition. It illustrates the balance between component A vs. component B at various temperatures and the different phases which can be achieved under a particular set of conditions. Fig 2.2 demonstrates some typical features. For example, it indicates that there are conditions which favour the system to be either entirely liquid or entirely solid. The curves  $A\alpha$  and  $B\alpha$  are calculated by recording the freezing points of the liquid at various ratios of A:B and plotting them against the corresponding composition of the liquid. As the value of B is increased the freezing point of A decreases (curve  $A\alpha$ ), similarly as A is increased the freezing point of B decreases (curve  $B\alpha$ ). If the composition is A-rich and cooled to a temperature below curve  $A\alpha$ , solid A will precipitate and vice versa for curve  $B\alpha$ . At point  $\alpha$  (where the two curves meet), solids A and B are in equilibrium with the liquid. At this point all three phases exist simultaneously and is termed the *eutectic point* and it is the lowest temperature at which a liquid phase can be observed. In this project binary phase alloy diagrams were consulted where available such as in the case of the nickel-sulfur system to help determine the stability of a particular phase and the required conditions to achieve its synthesis.<sup>[108]</sup>

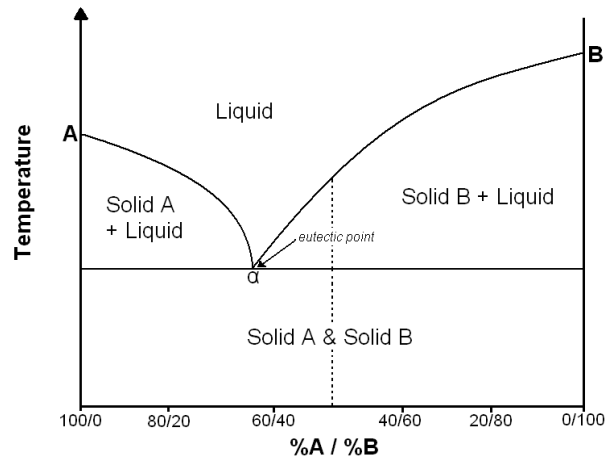


Fig 2.2 Typical features of a binary phase diagram

### 2.1.2 Experimental parameters: chalcogen

A CVT reaction proceeds best under non-stoichiometric conditions although too far a departure will decrease the growth rate as a result of the increased pressure from the vapour. <sup>[109]</sup> A prime example of this is the synthesis  $\text{TaSe}_3$ , which is a good illustration that CVT has the capacity to produce a wide range of alternate morphologies. In this system the selenium creates a vapour with which the tantalum powder reacts. The excess of selenium is essential to the reaction as it functions simultaneously as a carrier gas and template for growth; it is thought that crystals of  $\text{MQ}_3$  condense onto suspended droplets of selenium vapour *in-situ* and grow around the chalcogen spheres to create rings and a whole host of unusual structures including Möbius strips. <sup>[110,111]</sup> An abundant source of chalcogen which readily produces a reactive vapour is a factor that plays an important role in similar tri/dichalcogenide systems investigated in this project.

### 2.1.3 Experimental parameters: transition metal

At the start of every reaction the chalcogen has remained in powdered form. In the case of the transition metal either powder, foil or a specially designed substrate has been exploited. The foil thickness would range from 0.0075mm to 0.1mm and thin strips of metal were cut typically to dimensions of 1 cm x 2 cm. The specially designed substrate was a nanometric metal layer sustained on a silica support. (Fig 2.3)

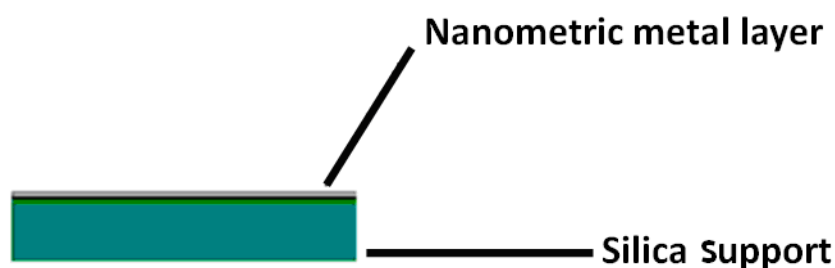


Fig 2.3 Substrate, made up of a silica support with a nanometric layer of a chosen metal evaporated on top.

These metal films were produced by evaporation techniques. The nanoscale layer of metal was deposited on to a ca. 0.4 mm thick silica support using a Plassys MEB 400S electron beam evaporator under a chamber pressure of  $1 \times 10^{-7}$  mbar. Under these conditions, the metal layer was deposited with no particular crystal orientation. Various thicknesses could be determined during deposition via an in-chamber quartz crystal sensor. Three differing thickness were used in this project; 25, 50 and 100 nm.

The foil or substrate is kept separate from the chalcogen by a constriction put in the centre of the ampoule. (Fig 2.4) This separation was necessary to ensure that the interface between the two reactants was of solid-gas phase rather than solid-solid and therefore encourage a vapour liquid solid (VLS) type mechanism.



Fig 2.4 Silica ampoule with chalcogen in one end and metal foil at the other separated by a constriction

In addition, towards the end of the project rather than a uniform layer, patterned substrates consisting of islands of metal of varying sizes were prepared by shadow-masking. Shadow-masking is a simple procedure where the silica substrate is partially covered preventing evaporation of the metal onto a particular area. Masks with a specific design can be prepared with electron beam lithography such as the pattern shown in (Fig 2.5).

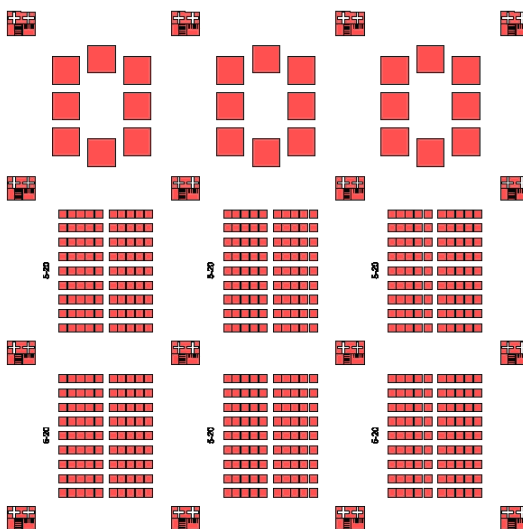


Fig 2.5 Design of a particular patterned substrate with different sizes of metal islands

The primary purpose of such a design was to investigate the reactivity of the chalcogen and the strength of its interaction with the metal as opposed to the silica with the motivation to use this selectivity to develop further competency in pre-determining the position of a structure on the substrate surface and later expand this to direct control over size and morphology. The ultimate aim was to use these patterned substrates for property measurements. In the semiconductor industry for example, patterned thin films are frequently used to create small electrodes to investigate the electrical properties of a nanostructure. <sup>[112]</sup> These metal features can be altered (such as *via* oxidation or sulfurisation) to make use of their corresponding electronic and optical properties. <sup>[113]</sup> The benefits of such a study would help tackle the dilemma of manipulating these structures once they have been produced. The measurement of electrical resistivity on individual nanostructures, for example, is a notable challenge compared to equivalent measurements performed on crystals or compacts on the bulk scale simply because they become much more difficult to handle.

## 2.2 Scanning Electron Microscopy (SEM)

Scanning electron microscopy (SEM) is a technique that has played a key role in the development of this project. The capability of the SEM to produce high magnification, high resolution topographical images makes it an ideal mode of analysis to determine whether nanostructures have been produced. In addition, the SEM offers a mode of sample characterization known as Energy Dispersive X-ray analysis (EDX). A technique which can quantitatively determine elements present and thus determine their stoichiometric ratio.

### 2.2.1 The scanning electron microscopy (SEM)

Put simply, the SEM uses a beam of electrons to form an image. These electrons are produced by an electron gun with an energy ranging from 0.1 eV to 30 keV and are accelerated down a column towards the specimen. The history and development of the SEM spawns from the origins of the transmission electron microscope (TEM). This machine was initially developed by two research groups in Berlin following studies in 1926 which showed that electric and magnetic fields could function as lenses to charged particles. <sup>[114]</sup> There was a desire to further this research and in 1935 the first example of a scanning electron microscope was built. <sup>[115]</sup> It was based on the principle whereby a focused beam of electrons passes through several lenses and is deflected by a current generated through coils by a sawtooth generator causing the probe to ‘zig-zag’ across the surface of a sample. In parallel, the same principle is applied to a beam of electrons within a cathode ray tube. The two beams are controlled by the same current and hence move in conjunction with one another. Secondary and backscattered electrons from the sample are collected via a detector and the resulting current directs the potential of the grid at the base of the cathode ray-tube. (Fig 2.6)

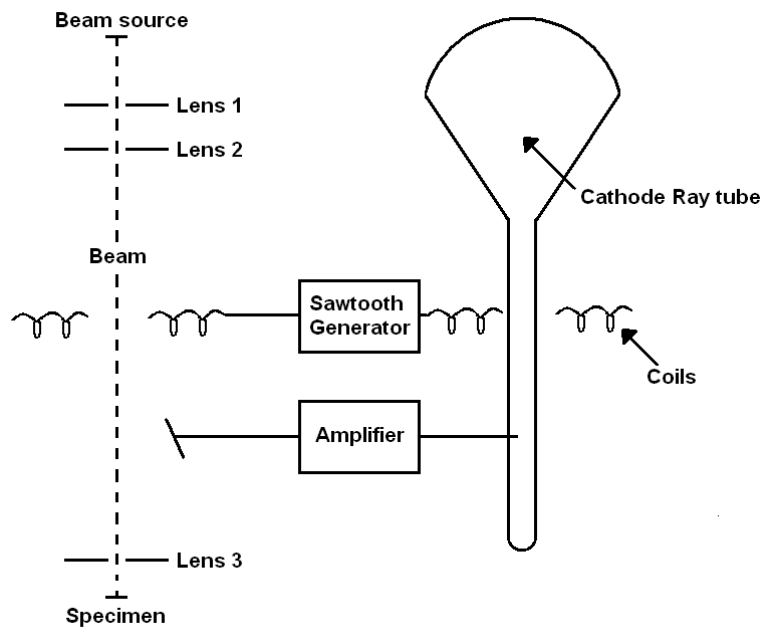


Fig 2.6 Schematic of the basic set-up on a SEM

Therefore the picture formed is a direct correlation of the electrons removed from the surface of the sample. A good control of this current enables the development of greatly magnified images. Further theoretical studies were covered by two subsequent publications by von Ardenne in 1938.<sup>[116]</sup> In the late forties Oatley drew from the previous investigations made in America and Germany and produced the first machine for general use in 1965 by Cambridge instruments.<sup>[117]</sup>

The beam must be treated by various lenses to correct aberrations and ensure that a spot size of normally less than 10 nm is maintained. At the same time an appropriate current is required to produce the necessary signal strength and form a decent image. There are several types of electron gun available each with their own particular benefits. The main features to consider are the balance between spot size and current strength, the stability of the beam and finally the gun's lifetime. Of the two machines employed during this project, one used a tungsten thermionic emitter whereas the other had a cold field emission (CFE) gun. These types of instrument are addressed briefly below.

The tungsten hairpin gun is the most common variety amongst older machines and is made up of three individual parts.<sup>[118]</sup> The filament or cathode, the grid cap or Wehnelt cylinder and the anode (Fig 2.7).

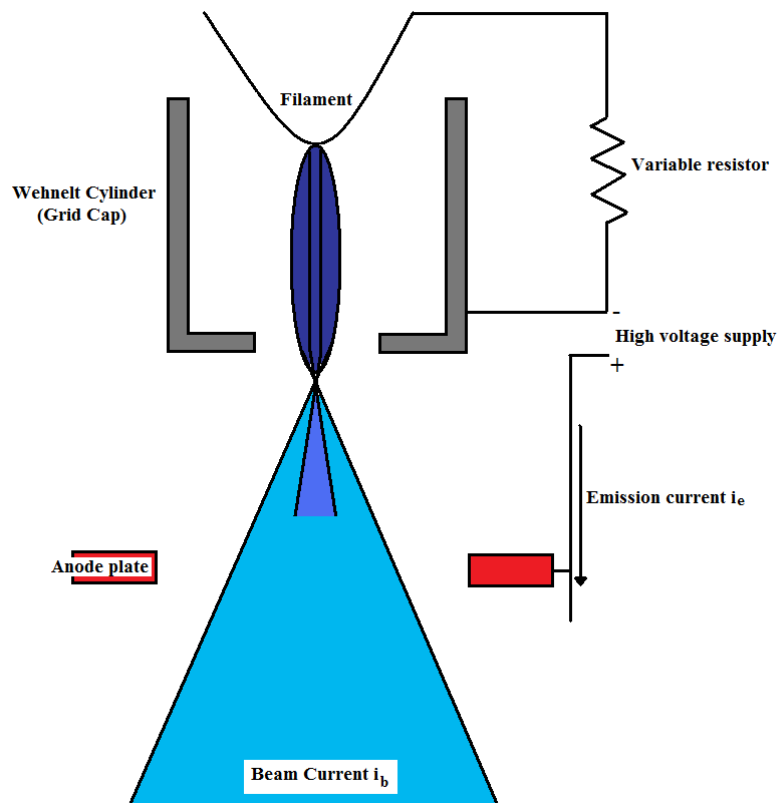


Fig 2.7 Simplified schematic of a tungsten hairpin gun

The filament is a thin piece of wire bent in a similar way to the filament found in the common light bulb. It is heated to a temperature between 2000 and 2700 K by the resistance generated when the filament heating current ( $i_f$ ) is pushed through it. This causes the emission of thermionic electrons from its tip. This emission is mediated by the grid cap and helps focus the electrons. The grid cap and filament are connected by a variable resistor. This variable resistor generates a negative bias by supplying an equivalent current to the tungsten hairpin to replace that which is lost as a result of the emission. This negative field focuses the emitted electrons and forces them into a cross-over point from which they diverge towards the anode; a circular plate with an opening that allows a percentage of the electrons down to the column. During the journey from cathode to anode the initial emission current ( $i_e$ ) is reduced to beam current ( $i_b$ ). This beam current is further concentrated down the column as it passes through each lens and aperture until it is measured as probe current ( $i_p$ ) once it reaches the specimen. The SEM records images over an extended period of time, therefore the probe current must be maintained at a constant level to produce data of a decent quality. This is achieved via a process known as

saturation, whereby any small fluctuations in  $i_f$  will not alter  $i_b$ . In this state electrons are only discharged from the tip of the filament and are tightly focused by the negative bias. This system is successful due to its self regulatory nature. Any increase in electron emission has a proportional effect on the negative bias of the grid cap which in turn resists the increase in emission and hence any knock on effect on  $i_p$ . The major advantage of a thermionic emitter such as the tungsten hairpin gun is its relative cheapness in comparison to a field emission gun and the fact that it does not need such a high vacuum to operate.

A field emission gun (in contrast to the method of producing electrons by thermal emission) adopts a cold-field technique and encourages electrons to directly tunnel through the filament by lowering the work potential for electrons to enter the vacuum. This filament is a wire filed into a sharp point of 100 nm or less and attached to a tungsten hairpin. In the case of the Hitachi S-4700 the filament is composed of mono-crystalline tungsten. A negative potential is applied and concentrated at the tip of the cathode. The electrons spread out from a point of origin of a few nanometres and form a cone. For a CFE gun, the total  $i_e$  is small and independent of temperature but due to the minute size of the source and confinement of the beam, the brightness is orders of magnitude greater than that of a thermionic emitter. Another strong advantage is the lifetime of cold field emitters. Due to the diminutive size of the CFE gun tip, the area of emission must be kept clean to an atomically high level. After several hours of use the cathode becomes contaminated with layers of gas molecules eventually causing destabilisation. These layers must be removed by a process known as flashing. The filament is heated to around 2500 K, which eradicates any organic layers present. After this process the tip emits at top capacity for about a quarter of an hour until a monolayer reforms stabilising the output for several hours. The build up will eventually increase to the point where the flashing needs to be repeated. Each flash blunts the tip until eventually the filament can no longer produce a sufficient current. This however takes several thousand flashes and therefore the lifetime of the filament can be more than a thousand hours. A lifetime hugely in excess when compared to the 40-100 hour span of the tungsten filament.

As the electrons travel down the column the beam must be treated with several electromagnetic lenses, the purpose of which is to reduce spot size before reaching the sample. A lens is constructed of a wire coil inside an iron shell casing. A gap within this casing separates two polepieces which house a magnetic field generated by a current flowed through the wire (Fig 2.8).

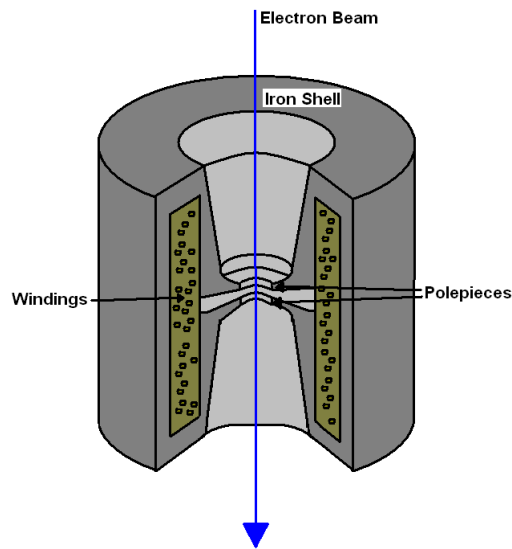


Fig 2.8 A cylindrical electron lens, composed of an iron shell which encases the wire coil. The electron beam passes through the centre, across the field generated by the two polepieces

Travelling electrons are bent towards the optical axis and eventually cross it. The difference between this interaction and the cross-over point is known as the focal length ( $f$ ) and is determined by the current flowing through the wire. An SEM has two types of lenses. The first is the condenser lens and its purpose is to control the amount of demagnification. Sometimes an SEM can contain two condenser lenses but they are normally controlled simultaneously. The second type is an objective lens and this holds the stigmator, scanning coils and beam-limiting aperture. Below is a schematic of the Hitachi S-4700 (Fig 2.9), which employs a variation of the objective lens known as the **snorkel lens**. The advantage of such a design is that it has low aberrations and can accommodate large specimens for observation. The design also enables a strong magnetic field to extend from the polepiece onto the specimen and therefore allows greater control of the beam and resultant image.

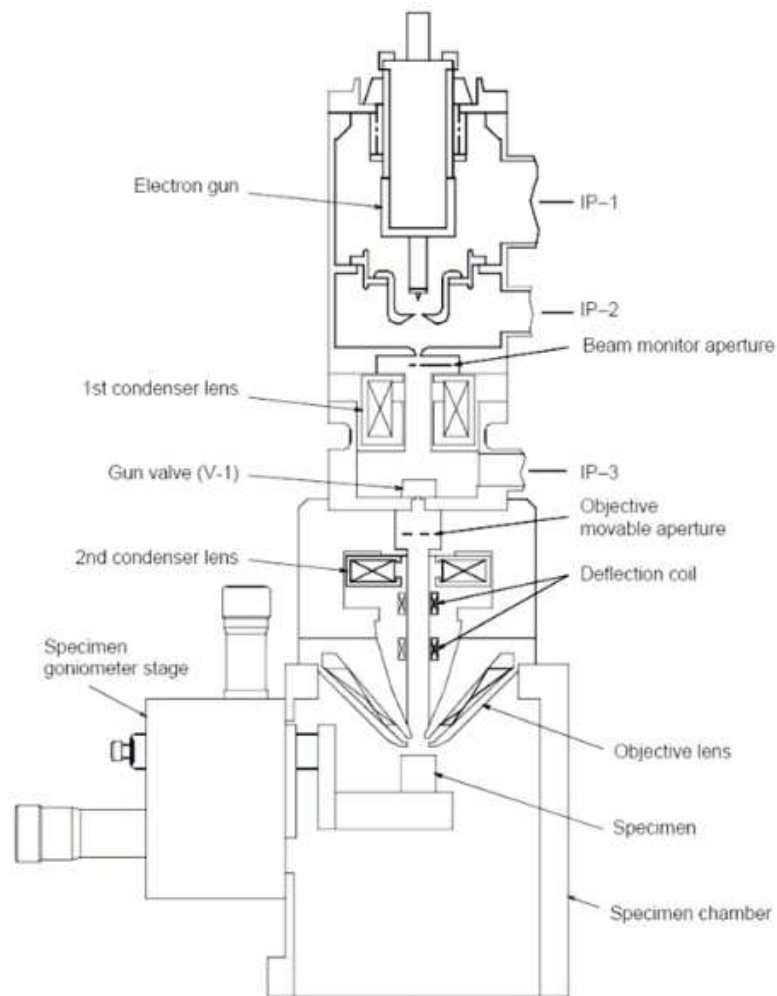


Fig 2.9 Schematic of the S-4700 Hitachi scanning electron microscope. <sup>[119]</sup>

All lenses suffer from defects or aberrations which degrade their performance. An example of this is spherical aberration. Spherical aberration is a result of electrons that are further from the optic axis and therefore interact more strongly with the magnetic field of the lens than those that are closer (Fig 2.10). Electrons that follow the path from P to A form an image that would be expected if no error were to exist. Those electrons that have a stronger interaction with the magnetic field follow path P to B.

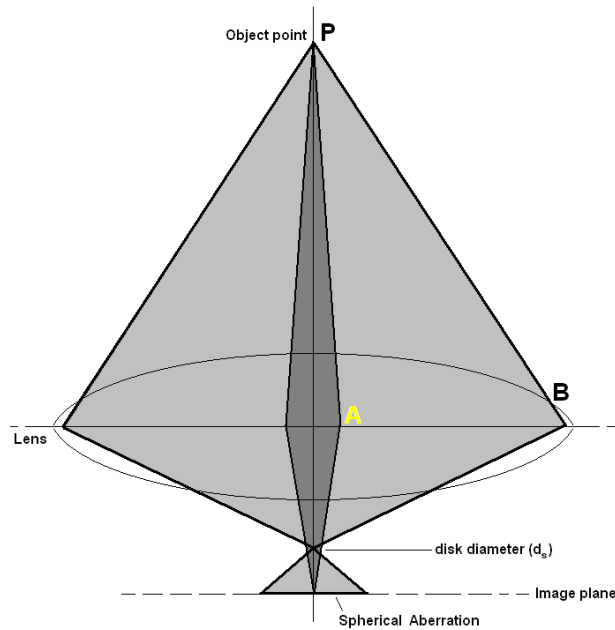


Fig 2.10 Diagram representing spherical aberration and the different paths which electrons follow to cause this.

Those in the latter category require a greater deal of focusing and as a result cross the optic axis closer to the lens. The overall result is that rather than the electrons converging at a specific and narrow point, a disk of diameter ( $d_s$ ) is created instead. Reducing the angle of divergence of path PB can help reduce the influence ( $d_s$ ) has on the spot size of the final beam. Another common form of aberration is astigmatism. Astigmatism is a consequence of a lens which is not perfectly cylindrical. This can be due to numerous factors from inhomogeneities in the polepieces to dirt on the apertures. It causes diverging electrons to create separate lines of focus which travel at right angles to one another. This is represented in the final image as streaking in a particular direction, making objects appear stretched. This effect can be corrected by using a device called the stigmator. This apparatus applies a weak magnetic field to the lens to make it appear symmetrical to the electron beam. This is controlled manually by adjusting X and Y stigmator controls in conjunction with the focus control until a sharp image is acquired.

When the electron beam interacts with the sample, the majority of electrons from the beam penetrate the sample creating what is called the “region of

primary excitation”. This produces many different signals not all of which are necessary in determining the resolution of the image formed. (Fig 2.11)

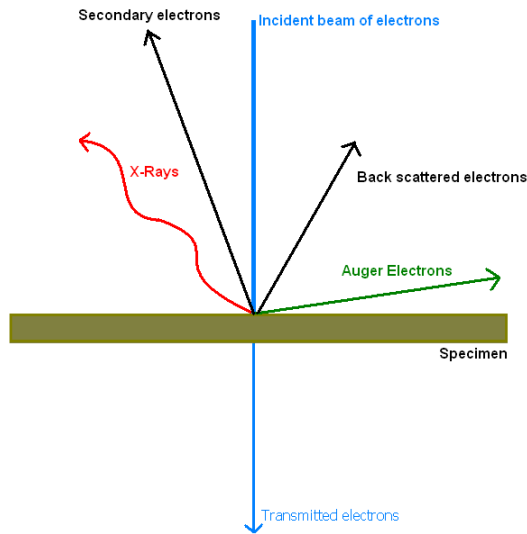


Fig 2.11 Simplified diagram showing the major excitations caused by the interaction of the electron beam with the sample. Those indicated in black are the most relevant signals.

The most important signals produced are those concerned with elastic and inelastic scattering. From a graph displaying the entire energy distribution of electrons emitted from the sample from  $E_0 - E$  keV (where  $E_0$  is the total incident beam energy), it can be seen that the emission chiefly consists of backscattered electrons (Fig 2.12)

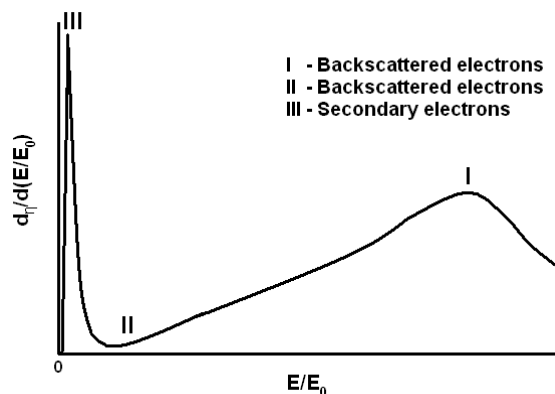


Fig 2.12 Energy distribution diagram showing the regions of backscattered and secondary electrons as a fraction of the beam energy <sup>[118]</sup>

In short, secondary electrons are loosely bound outer shell electrons which receive a sufficient amount of kinetic energy from the incident beam to be ejected from the atom and set into motion. These electrons spread throughout the sample intersecting and leaving its surface. They move at a slow enough rate to be attracted to a positively charged secondary electron detector which draws electrons from a wider range of areas. Detection in this manner allows the SEM to build its topographical images.

Secondary electrons are defined simply by their kinetic energy and hence the total secondary electron coefficient ( $\delta$ ) can be calculated using the following,

$$\delta = \frac{n_{SE}}{n_B} = \frac{i_{SE}}{i_B} \quad (2.1)$$

Where,  $n_{SE}$  is the number of secondary electrons emitted when a sample is struck with  $n_B$  electrons and  $i$  relates to the corresponding currents.

Therefore as the beam energy rises,  $\delta$  will decrease. Below 5 keV their contribution to the emitted signal increases significantly. This is because typically the depth at which secondary electrons are produced from the sample is shallow, metals have an escape depth in the order of  $\lambda = 0.5-1.5\text{nm}$  for example. Electrons are subject to energy loss as they travel through the specimen and to reach the detector they must overcome the work function of the surface to escape into the vacuum. Since these electrons already have such low kinetic energies the probability for a secondary electron produced at distance ( $X$ ) from the surface decreases at the rate

$$P = e^{-\frac{X}{\lambda}} \quad (2.2)$$

where  $\lambda$  is the mean escape depth. <sup>[120]</sup> As the beam energy is lowered an increasing amount of secondary electrons are produced near the surface of the sample achieving larger values for  $\delta$ . The yield for secondary electrons is therefore dependent upon the type of material and its topography (since these can effect the depth at which secondary electrons are produced). This makes

them most adequate to analyse the surface of a sample compared to any other region.

Backscattered electrons are a result of those electrons from the incident beam which intercept the sample surface and undergo sufficient enough deflection from their initial pathway to exit the surface once again. They are an example of elastic scattering and directly interact with the atoms of the sample. Backscattered electrons remove a significant portion of energy from the incident beam (Fig 2.12). The backscatter coefficient  $n$  is given as

$$n = \frac{n_{BSE}}{n_B} = \frac{i_{BSE}}{i_B} \quad (2.3)$$

where  $n_B$  is the number of incident beam electrons and  $n_{BSE}$  is the number of backscattered electrons and  $i$  is their corresponding currents. Typically electrons of the incident beam undergo several elastic scattering events before their pathway deviates adequately enough to escape the sample surface. Monte Carlo trajectory plots have revealed the increasing number of beam electrons which achieve this trajectory with increasing atomic size and it is understood that the number of backscattered electrons increases proportionally with atomic number (Fig 2.13). This is because with an increase in atomic number the electrons undergo more elastic scattering and typically have a higher scattering angle. As a result electrons have a tendency to deviate from the incident beam pathway at a rate which increases their overall contribution to backscattering. The correlation with atomic number ( $Z$ ) tends to plateau around  $Z \geq 50$  (Fig 2.14).

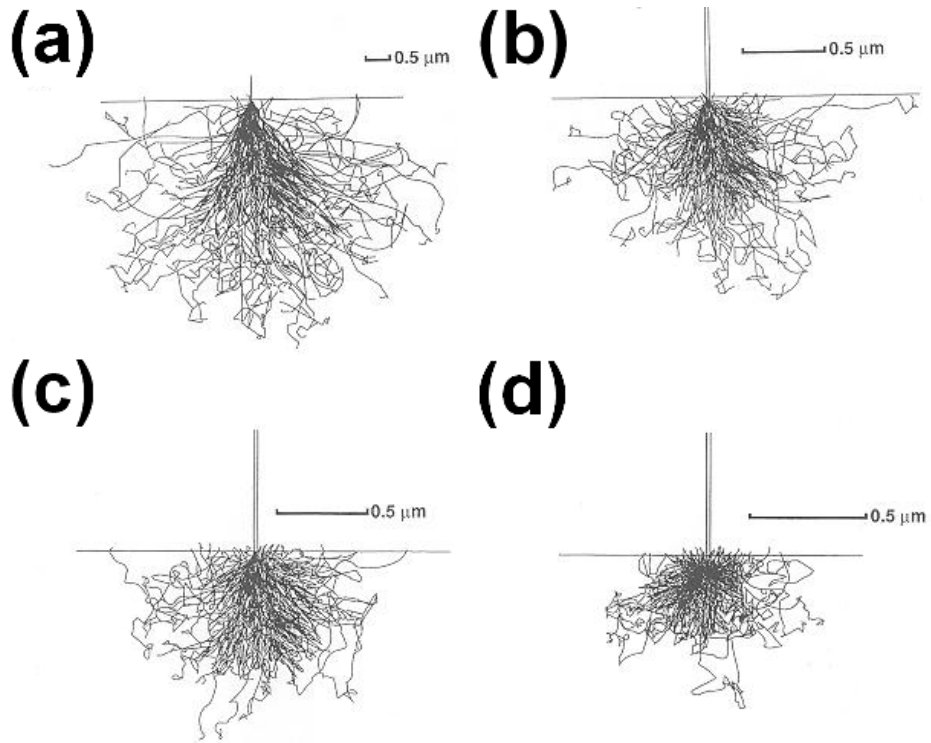


Fig 2.13 Monte Carlo trajectory plots of (a) carbon ( $Z=6$ ) (b) iron ( $Z=26$ ) (c) silver ( $Z=47$ ) (d) uranium ( $Z=92$ ) at a constant beam energy of 20 KeV. The number of electrons with a trajectory that allows them to breach the surface of the sample increases with increasing atomic number. [118] Figure reproduced with kind permission of Springer Science and Business Media, Springer, Scanning Electron Microscopy and X-ray Microanalysis, 3<sup>rd</sup> Ed, 2003, pages 70 and 71, chapter 3, J. Goldstein, D. Newbury, D. Joy, C. Lyman, P. Echlin, E. Lifshin, L. Sawyer and J. Michael, Figs 3.5 and 3.6.

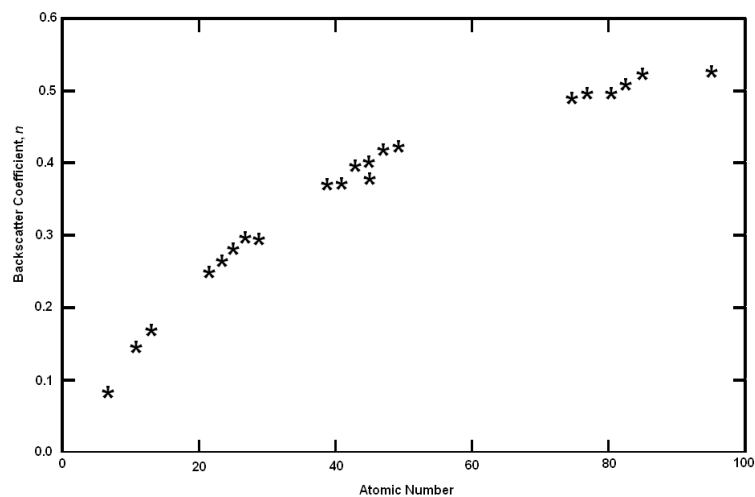


Fig 2.14 Graph showing the relationship of the number backscattered electrons with increasing atomic number.

Conversely the beam energy dependence of backscattered electrons is shown to be markedly less than that of secondary electrons with as little as 10% of backscattered electrons being affected by increasing beam energy. From the range of 5-50 KeV with a specific element, the energy dependence of the backscattered electrons behaves sporadically by increasing, decreasing or showing almost no change at all. The apparent lack of proportionality between the two factors is due to a large proportion of electrons retaining a constant possibility of scattering and escaping the sample surface despite a change in incident beam energy. This is because according to the Bethe energy loss expression with increasing energy of a charged particle the rate loss decreases. [121],

$$-\frac{dE}{dx} = \frac{4\pi}{m_e c^2} \cdot \frac{nz^2}{\beta^2} \cdot \left(\frac{e^2}{4\pi\epsilon_0}\right)^2 \cdot \left[ \ln\left(\frac{2m_e c^2 \beta^2}{I \cdot (1-\beta^2)}\right) - \beta^2 \right] \quad (2.4)$$

Where  $B = v/c$ ,  $v$  is the velocity of the particle,  $E$  is the energy of the particle,  $x$  the distance travelled by the particle,  $c$  is the speed of light,  $z$  is the particle charge,  $e$  is the charge of the electron,  $m_e$  is the rest mass of the electron,  $n$  is the electron density of the target,  $I$  is the mean excitation potential of the target and  $\epsilon_0$  is the vacuum permittivity.

For example, consider an electron of incident energy ( $\alpha$ ) and another at double the energy ( $\beta$ ). These two electrons have both travelled the same depth into the sample, electron ( $\alpha$ ) may dissipate its energy and be unable to leave the specimen whereas the electron at higher energy according to the afore mentioned Bethe energy loss expression loses energy at a decreased rate and therefore retains enough energy to leave the sample. A large percentage of electrons at different depths in the sample always maintain sufficient energy to scatter and therefore despite beam energy the quantity of backscattered electrons remains stable. A backscattered electron detector is placed in the pathway of these electrons. It is only backscattered electrons that follow this pathway that will be picked up by the detector as it does not use any form of electronic attraction. It is therefore common that more than one detector is present near the sample. These signals are used to build a topographical image

of the sample but one differing from that of the secondary electrons as the electrons can originate deeper from within the sample.

Detectors convert the emitted electrons to electronic signals which are further processed to create the final SEM image. Detectors are positioned at a place termed the take-off angle ( $\psi$ ) which is the angle from the specimen surface where a line can be drawn direct to the centre of the detector face (Fig 2.15) The detector size ( $\Omega$ ) is determined by the ratio between the area of the detector face ( $A$ ) and the square of the radial distance ( $r$ ) to the beam impact point

$$\Omega = \frac{A}{r^2} \quad (2.5)$$

An SEM typically has two electron detectors as the differing energy characteristics of secondary and backscattered electrons makes it difficult to design a detector which can measure both.

In addition, backscattered electrons sometimes collide with neighbouring atoms of the specimen and produce, cathodoluminescence, X-rays (which are important for EDX) and Auger electrons. Auger electrons are the secondary emission of an electron which can occur when another electron from a higher energy level drops down to fill an inner-shell vacancy. The subsequent emission of excess energy can sometimes transfer to a neighbouring electron which results in its ejection from the atom.

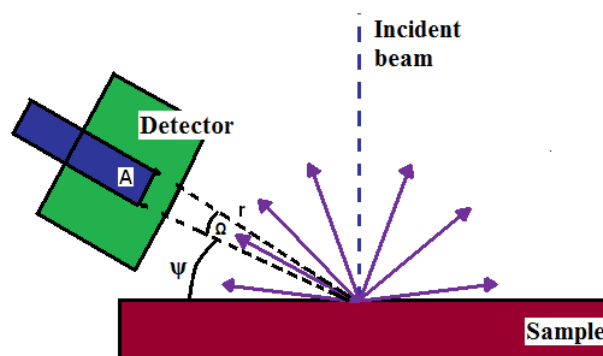


Fig 2.15 Typical set up for an electron detector with the detector relative to the take-off angle  $\psi$  measured from the surface plane. The size of the area detected ( $A$ ) is given by  $\Omega r^2$ .

### 2.2.2 Sample preparation and instrumentation

Microscopy work was performed using two instruments: a Philips XL30 ESEM and a Hitachi S4700 cold field emission gun SEM (Fig 2.9). Typically, samples were loaded onto aluminum stubs using adhesive carbon tabs and run in high vacuum mode with an applied accelerating voltage of 10 kV and a working distance of 12.5 mm for imaging and 20 kV and a working distance of 10 mm for energy dispersive X-ray analysis, (EDX). EDX analysis was performed within the Philips instrument using an Oxford Instruments 7200 EDX spectrometer in order to determine elemental compositions (which can be obtained with accuracy for elements of atomic number from carbon upwards).

### 2.2.3 Energy Dispersive X-ray Analysis

As stated earlier the interaction of the electron beam with a sample produces numerous emissions other than secondary electrons (Fig 2.11). The high electron energy beam is able to knock out core electrons of an atom leaving behind electron vacancies that must be filled by electrons from a higher energy level (Fig 2.16).

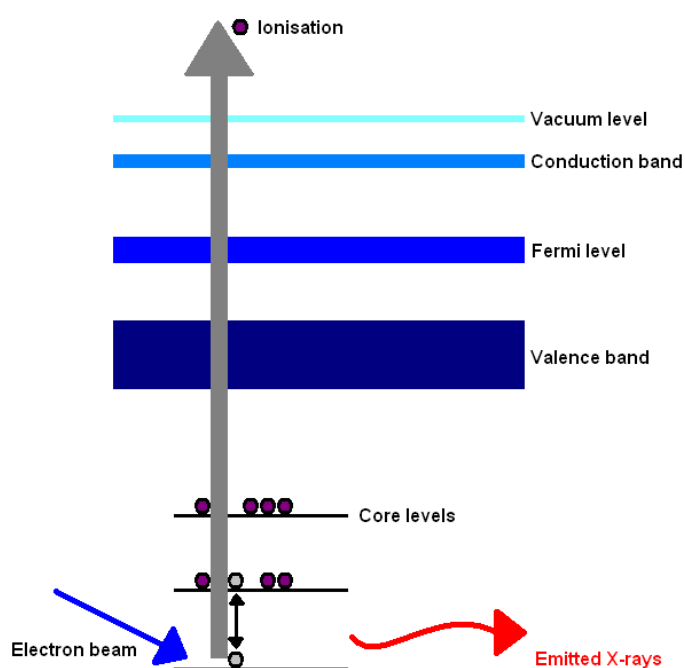


Fig 2.16 Diagram representing the process which takes place to produce for X-rays for EDX <sup>[118]</sup>

This results in a quantum of excess energy being released from the atom in the form of an X-ray. The wavelength of this X-ray will be dependent upon the energies of the individual energy levels and therefore unique from one atom of an element to another. The electrons of an atom occupy electron shells which have specific energies. Closest to the core is the K-shell, followed by M and L which can be further divided into sub-shells. Ionisation of an electron from the K-shell would increase the energy of the atom until the vacancy is replaced by a L-shell electron which is then replaced by a lower energy electron and so on. These transitions between the sub shells produce characteristic X-rays of particular energies. The energy and number of these X-rays can be counted by an energy dispersive X-ray (EDX) detector. This apparatus is constructed around a crystal typically consisting of *p*-type silicon doped with a *n*-type dopant in most cases lithium. The lithium diffuses through the crystal to create a micrometer thick *p-n* junction making it behave essentially like an intrinsic semiconductor. The Si(Li) crystal absorbs each incident X-ray photon with energy  $h\nu$  which stimulates the ejection of an inner shell electron of energy  $(h\nu - E_c)$ , where  $E_c$  for a silicon atom is 1.84 KeV. Ideally the number of charges ( $n$ ) created in the detector per incident photon with energy  $E$ (eV) is given by,

$$n = \frac{E}{\epsilon} \quad (2.6)$$

Where ( $\epsilon$ ) is the electron hole pair creation energy and is equal to 3.86 eV for Si at 77 K. For example, a photon of energy 5 KeV would produce a charge of  $2 \times 10^{-16}$  C. This is a very small charge and therefore to make accurate measurements the detector crystal is kept close to liquid nitrogen temperatures to reduce contributions from thermal noise. The charge pulse then is converted by a charge to voltage converter to a voltage pulse. This signal is amplified and shaped by linear amplifier and passed onto a computer X-ray analyzer (CXA) and represented as a spectrum of X-ray counts against energy by a technique called digital pulse processing (Fig 2.17). N.B. When the bias is applied it is imperative that EDX detector is kept at liquid nitrogen temperatures to prevent diffusion of the lithium through the crystal. The data can be quantified to give a ratio of percentages of the elements detected and therefore an approximate stoichiometry of the elements concerned. <sup>[118]</sup>

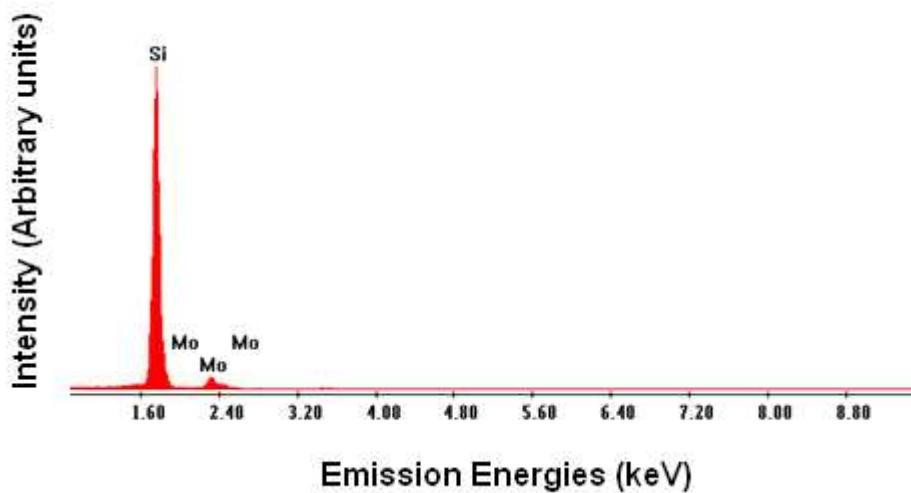


Fig 2.17 Typical EDX spectrum with X-ray counts (y-axis) against X-ray energies (x-axis)

EDX analysis was performed with an Oxford instruments 7200 EDX spectrometer with a working distance of 10 mm and a typical beam energy of 10 keV. Prior to usage, the EDX was calibrated and during analysis, measurements were compared to standard values of KeV for elemental identification. The computer then quantified results to calculate the atomic percentages. Typically, per sample, an average of around 10-15 measurements were taken (both spot and selected area scans) and an average calculated from the sum of these measurements.

## 2.3 Powder X-ray Diffraction (PXD)

### 2.3.1 Crystallography

A crystal exhibits a typically faceted shape which is a reflection on the periodicity of its atomic array. This can be simplified to a singular repeating component known as a *unit cell*. A unit cell is the basic ‘building block’ from which you can build the whole crystal structure. Seven possible crystal systems exist; cubic, tetragonal, trigonal, orthorhombic, hexagonal, monoclinic and triclinic (Fig 2.18). <sup>[122]</sup>

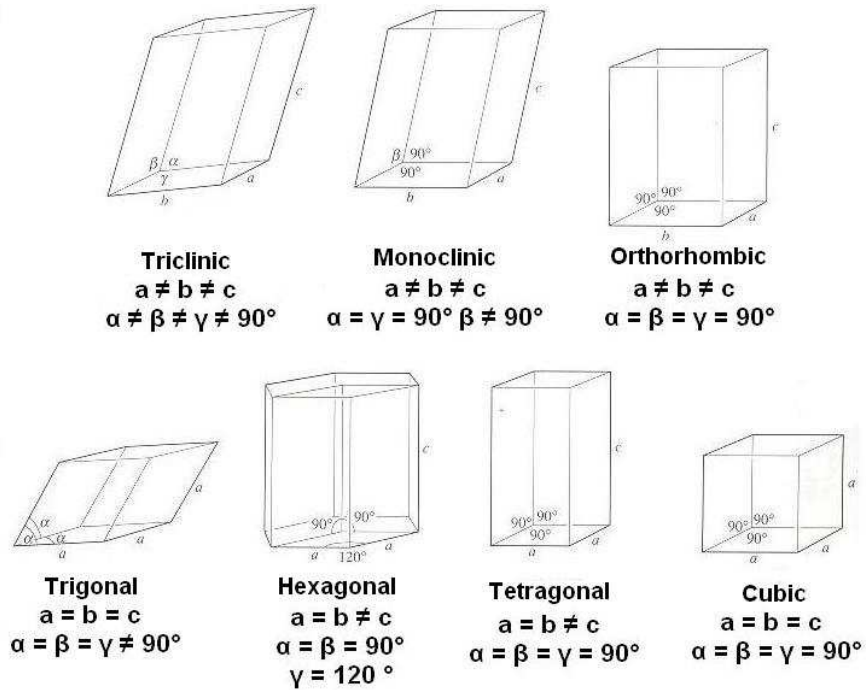


Fig 2.18 The seven crystal systems [16]

The unit cell itself has up to four lattice types depending on the position of the lattice points; primitive (P), body-centred (I), face-centred (F) and end-centred ABC. The four lattice types in combination with the seven crystal systems create 14 possible alternatives known as Bravais lattices which adhere to the minimum symmetry requirements. Bravais lattices represent the arrangement of lattice points in real space. At any specific point within a crystal certain symmetry operations can be performed, giving rise to *three-dimensional point groups*. These symmetry operations are: the identity, an inversion centre, mirror planes, axes of rotation and improper rotation axes and in total they form 32 permissible point groups. In the solid state, the number of symmetry operations is expanded by translational symmetry as discussed below.

### 2.3.2 Screw axes and glide planes

Screw axes and glide planes are examples of translational symmetry which also form an integral part of a space group (see below). A glide plane is a combination of translation with reflection Fig 2.19. shows a cross section of a crystal. There is a mirror plane of symmetry along the xz-direction. A glide plane consists of reflection across this plane and simultaneous translation along the x-

axis. The translation is equal to half of the repeat distance of the lattice parameter, in this case  $a$ , so it can be written as  $a/2$ . [123]

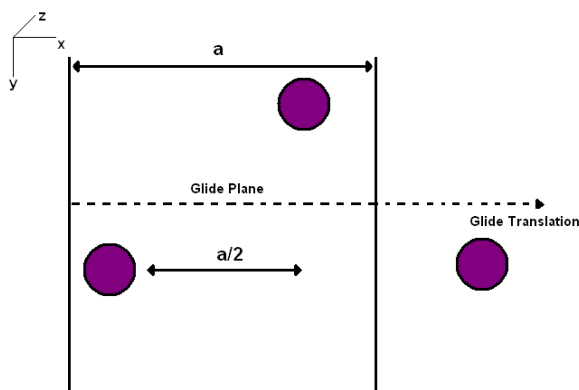


Fig 2.19 An example of an 'a' glide plane perpendicular to b

A screw axis is a single symmetry element which occurs in monoclinic and higher symmetry crystal systems. Typically a screw axis is denoted as  $(n_i)$ , where  $n$  is an angle of rotation ( $360^\circ/n$ , where  $n = 2, 3, 4, 6$ ) and  $(i)$  is the degree of translation across the lattice vector (given by the ratio  $n/i$ ). This leaves an atom in a crystal indistinguishable from its position prior to performance of the symmetry operation. For example,  $2_1$  is a twofold screw axis whereby a  $180^\circ$  rotation is followed by translation of  $1/2$  across the lattice vector (Fig 2.20). [123]

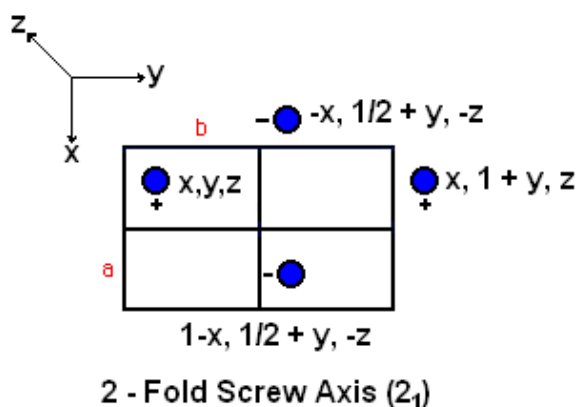


Fig 2.20 An example of a two-fold screw axes, c axes is perpendicular to the page and blue spheres represent atomic positions.

In Fig 2.20, it can be seen that a  $2_1$  operation can be used to relate each of the atomic positions to one another. For instance, by rotating atom  $(x, y, z)$  by  $180^\circ$  about the  $b$  - axis (in either direction) and then translating it half of the unit cell distance, its new position becomes either  $(-x, 0.5 + y, -z)$  or  $(1 - x, 0.5 + y, z)$ .

These positions are equivalent by translation of one unit cell length long the  $a$  - axis.

### 2.3.3 Space groups

The 14 Bravais lattices in conjunction with the 32 point groups, create 230 possible *space groups*. Space groups contain information not just about the lattice type but also regarding the symmetry operations that can be performed on the structure which it represents. It is thought around 90% of known crystal substances crystallise with low symmetry in either the triclinic, monoclinic or orthorhombic crystal systems. <sup>[124]</sup>

### 2.3.4 Interaction of X-rays with crystals

Crystallography, the identification and classification of a crystal species began as a subsection of mineralogy and traces its roots back to the discovery of the diffraction of X-rays in 1912 by Bragg <sup>[125]</sup>. The wavelength of the incident X-ray beam must be of the same order of magnitude as the spacings of the crystal lattice planes, which function like a diffraction grating towards a beam of light (Fig 2.21). The atomic planes can ‘reflect’ the incident beam when the crystal is at particular orientations to the source allowing *constructive interference* to occur.

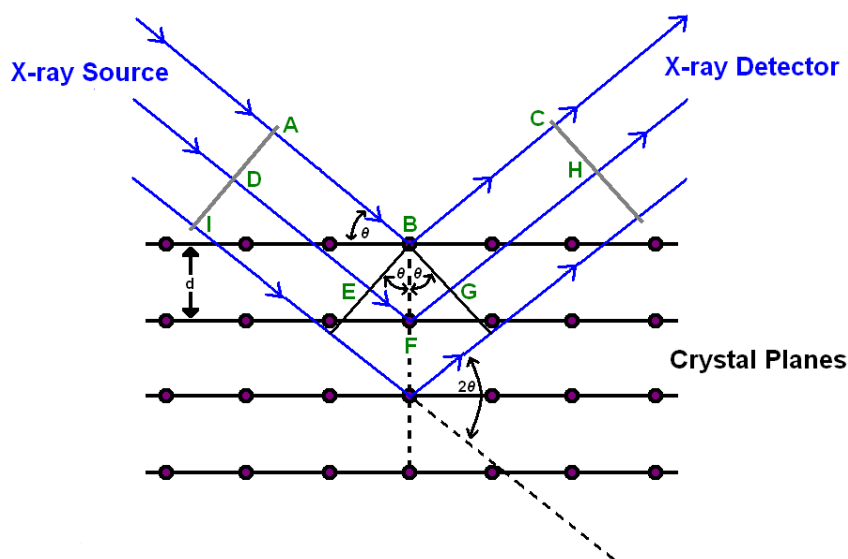


Fig 2.21 A set of crystal planes which show Bragg reflection of an X-ray beam

The first beam, beam **A**, interacts with the top plane at atom **B**. The second beam (**D**), travels a greater distance to interact with the plane below at atom **F**. This increase in distance between beams **A** and **D** is equal to **EF + FG**. From (Fig 2.21) it can be determined,

$$EF = FG = d \sin \theta \quad (2.7)$$

Therefore the total path difference,

$$EF + FG = 2d \sin \theta \quad (2.8)$$

Finally, for the reflected beams to travel in phase, the total path difference must be an integer (**n**) of the incident beam wavelengths (**λ**). This constitutes *Bragg's Law* <sup>[125]</sup>.

$$n\lambda = 2d \sin \theta - \text{Bragg's Law} \quad (2.9)$$

The faces and planes of a crystal can be defined in three dimensions with Miller indices. Fig 2.22 gives a basic example, the unit cell is defined along the crystallographic axis **x**, **y**, **z** and **a**, **b**, **c** are fractional coordinates (where **a**, **b** and **c** = 1), which originate at the point of origin (**o**). The plane **ABC**, intercepts the crystallographic axes at points **A**, **B** and **C** respectively so the Miller indices would be defined as,  $h = 1/A$ ,  $l = 1/B$ ,  $k = 1/C$ . For instance, for an intercept of  $x = 1/2$ ,  $y = 1/2$ ,  $z = 1/2$ ,  $h = 1/A$ ,  $l = 1/B$ ,  $k = 1/C$ , so  $h = 1/1/2$ ,  $l = 1/1/2$ ,  $k = 1/1/2$  and therefore the Miller indice would be defined as (222). Bragg's law shows the relationship between successive crystallographic planes (**h**, **k** and **l**) and a specific Bragg angle  $\theta_{hkl}$  where **hkl** represents the Miller indices. These values are particular to a crystal and therefore different structures give rise to different diffraction patterns. <sup>[123]</sup>

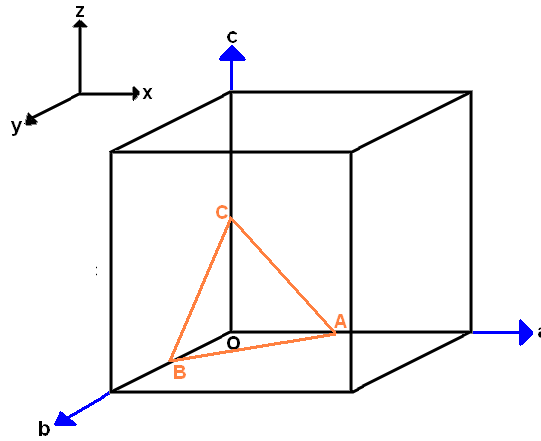


Fig 2.22 Example of Miller indices of crystal planes

### 2.3.5 Powder X-ray diffraction (PXD)

In terms of a single crystal, X-ray diffraction can be used to determine exact atomic positions, bond lengths and molecular angles. A powdered sample will contain an innumerable amount of randomly orientated crystallites. This displays all the possible orientations which fit Bragg's law and hence a unique pattern for that particular structure. For a powder X-ray diffractometer, an X-ray source of copper is usually utilized. This creates an emission of *white X-rays* at lower wavelengths but two very prominent peaks of  $K_{\alpha}$  and  $K_{\beta}$  radiation at higher values of  $\lambda$  (Fig 2.23).

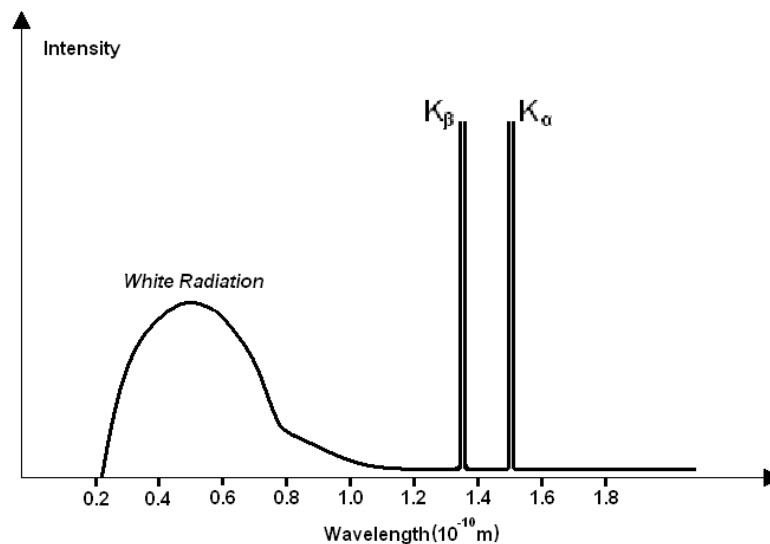


Fig 2.23 Spectrum of the X-ray emission of a copper source.

These lines are a result of the bombarding electrons knocking electrons from the innermost K shell of the copper source. Subsequent vacancies are then filled by

other electrons dropping down from the above shells (L shell for  $K_{\alpha}$ , M shell for  $K_{\beta}$ ). PXD utilises monochromatic X-rays, normally  $K_{\alpha}$ , (since these are the most intense) by use of a monochromator which filters out the unwanted wavelengths. The sample is rotated in the path of the source and the diffracted beam leaves the sample at an angle of  $2\theta$  to the incident beam. This is collected by a detector adjacent to the X-ray source (Fig 2.24).

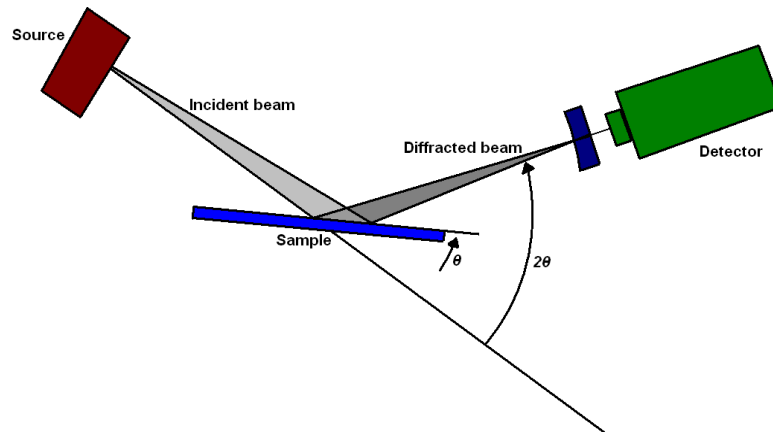


Fig 2.24 Simplified schematic of a typical powder X-ray diffractometer.

The incident beam diffracts from the planes of crystallites orientated at the correct angle to fulfil the Bragg condition. This produces a cone of diffracted X-rays, which was originally recorded as arcs on a photographic film wrapped around the sample (a technique known as the Debye-Scherrer method). The distance between these arcs,  $y$ , and the angle between them as they meet at the sample ( $4\theta$ ) can be used to calculate the Bragg angle and therefore the  $d_{hkl}$  spacings for each reflection using the equation

$$\frac{y}{2\pi r} = \frac{4\theta}{360} \quad (2.10)$$

where  $2\pi r$  is the circumference of the photographic film. The challenge lies in determining the appropriate  $hkl$  plane for each reflection, a process termed indexing and is most easily achieved for high symmetry systems.

The greater the Bragg angle determined by equation (2.8) the smaller the associated d-spacing will be (according to Bragg's law). In a primitive cubic

crystal system for example the (100) reflections have the largest separation ( $y$ ), therefore the smallest Bragg angle and hence the largest  $d$ -spacings. Given that in a cubic crystal system  $a = b = c$  the (100), (010) and (001) planes will reflect in the same position so the spacings of the reflecting planes can be written as,

$$d_{hkl} = \frac{a}{h^2 + k^2 + l^2} \quad (2.11)$$

combining (y) with Braggs law gives,

$$\lambda = \frac{2a \sin \theta_{hkl}}{h^2 + k^2 + l^2} \quad (2.12)$$

which can be rearranged as,

$$\sin^2 \theta_{hkl} = \left( \frac{\lambda^2}{4a^2} \right) (h^2 + k^2 + l^2) \quad (2.13)$$

Using equation (2.12) the Bragg angle can be determined for a specific set of lattice planes and each peak assigned the appropriate plane given that the unit cell dimension  $a$  is equal to the spacing of the (100) planes. For example, if one considers the possible  $hkl$  values for a face centred cubic system (e.g. (111), (200), (220), (311)) and substitute these into equation (2.12) the values of ( $\sin^2 \theta_{hkl}$ ) would be given in the order of an increasing ratio (3:4:8:11) with ( $\lambda / 4a^2$ ) as a common factor.

Depending on the symmetry of the structure, peaks can be missing due to destructive interference between some reflections. These are known as *systematic absences*. If one considers the translational symmetry of a body centred cubic lattice, for every atom at position ( $x, y, z$ ) there is an equivalent at ( $1/2 + x, 1/2 + y, 1/2 + z$ ). The structure factor for an arbitrary  $hkl$  reflection can be calculated for these two atom contributions using the following:

$$\begin{aligned} F_c(hkl) &= f \cos[2\pi(h \cdot 0 + k \cdot 0 + l \cdot 0)] + f \cos[2\pi(h/2 + k/2 + l/2)] \\ &= f + f \cos[\pi(h + k + l)] \end{aligned} \quad (2.14)$$

The sum of the  $h + k + l$  must be an integer, if this value is even then the cosine has a value of +1 and if it is odd, -1. It can therefore be determined that for a reflection to be observed the indices must be all odd or all even, otherwise they cancel each other out and  $F_c(hkl)$  will equal zero. Therefore, for a body-centred cubic structure, half of the possible reflections are absent. It is thus possible to identify the Bravais lattice by the particular systematic absences.

Intensity is dependent upon which atom (element) is present on a certain site. X-rays interact with the electrons of each individual atom and therefore the more electrons an atom has the stronger it will scatter the X-rays (so the heavier the higher the atomic number greater the intensity). This ability is termed the scattering factor or form factor ( $f_o$ ) and is dependent upon atomic number, Bragg angle and wavelength on the incident X-ray beam. The finite size of the atom means that with increasing Bragg angle, scattered X-rays from electron clouds are increasingly out of phase and  $f_o$  decreases so as  $\theta$  increases intensity decreases and higher intensity peaks are often found at lower angles. The resultant of the waves scattered by all the atoms in a unit cell at a particular  $hkl$  reflection are called the structure factor ( $F_{hkl}$ ) and are given by

$$F_{hkl} = \sum_j f_j e^{2\pi i(hx_j + ky_j + lz_j)} \quad (2.15)$$

where ( $f_j$ ) is the scattering factor of atom ( $j$ ) and ( $x_j, y_j, z_j$ ) are the corresponding fractional coordinates. The intensities of the  $hkl$  reflections ( $I_{hkl}$ ) are proportional to the square of  $F_{hkl}$  and undergo a set of corrections before being processed (2.14).

$$|F_{hkl}| = \sqrt{\frac{KI_{hkl}}{Lp}} \quad (2.16)$$

Where  $L$  is the Lorentz correction which relates geometry to the mode of collection  $p$  is the polarisation correction which recognises that non-polarised X-ray beam can become slightly polarised when reflected and  $K$  is the scaling factor. From equation (2.13) it can be seen that the structure factor is related to atom position and the magnitude of the scattering and therefore so is

intensity. This data are then used to calculate the particular intensities for each reflection. <sup>[126]</sup>

In some cases intensity can represent a bias to the orientation of the crystallites on the scanned surface rather than a representation of its growth behaviour. In the case of silica substrates for example, patterns would be composed of a high intensity singular peak simply because the surface has been manufactured to expose only one crystal plane. If the substrate were ground up and reanalysed it is likely that more planes would become exposed giving rise to more reflections.

Powder X-ray diffraction was mainly used in this work to identify the structure, phase purity and cell dimensions. This was accomplished primarily by comparison of obtained data to previously published structural analyses and then indexing of the pattern. Patterns can be indexed using a series of programmes such as Cellref or Dicvol<sup>[127, 128]</sup> for example. Indexing and subsequent least squares refinement allows one to obtain cell parameters from diffraction data. For a small number of samples, further structural analysis was carried out by Rietveld refinement (see below).

#### 2.3.6 Rietveld refinement

A PXD pattern is a section taken from rings of diffracted X-rays, therefore peaks tend to overlap and it is relatively difficult to extract their structure factor information. To address this problem the Rietveld method was developed. <sup>[129]</sup> To overcome the overlapping of peaks Rietveld created a method in 1967 which uses a structural model similar to the final solution as a basis for comparison. The positions of Bragg reflections are determined through a combination of sample displacement parameters, lattice parameters and zero-point corrections. This is followed by fitting peak intensities to peak shape functions, atomic positions and temperature factors to represent the thermal motion of the constituent atoms.

Refinement is performed using software such as GSAS. <sup>[130]</sup> It uses a least squares, best fit method that compares the entire experimental profile with that generated from a model structure, where each experimental data point is

compared to the corresponding theoretical data point of the structural model. The concept of refinement is given in the following equation:

$$S = \sum_i w_i (y_i - y_{ci})^2 \quad (2.17)$$

Where  $w_i$  is the weight factor ( $1/y_i$ ),  $y_i$  is the observed intensity (for each  $2\theta$  data point on the PXD pattern),  $y_{ci}$  is the calculated intensity and  $S$  is the residual being minimised. Refinements are repeated to reduce  $S$  as much as possible.

$y_{ci}$  is calculated using the following equation

$$y_{ci} = S \sum_K L_K |F_K|^2 \phi(2\theta_i - 2\phi_K) P_K A + y_{bi} \quad (2.18)$$

Where ( $S$ ) is the scale factor, ( $L_k$ ) is the Lorentz polarisation and multiplicity factors, ( $\phi$ ) the reflection profile function, ( $P_k$ ) preferred orientation function and ( $A$ ) the absorption factor. The calculated intensities ( $y_{ci}$ ) are derived from the  $|F_k|^2$  values which are generated from the structural model by a summation of the calculated contributions from neighbouring Bragg reflections ( $K$ ) including background contributions ( $y_{bi}$ ) for each step.

When performing a refinement, variable parameters fall into two separate categories. The first group involves the unit cell, overall temperature factors and coordinates/occupancies of each atom. The second group contains parameters such as profile scale factor, unit cell parameters, zero-point, asymmetry and preferred orientation parameters which determine peak position and shape.

Observed peak shape is a direct result of the sample (e.g. domain size) and the instrument (e.g. radiation source, slit sizes and geometry) and must be taken into account when considering peak shape. Generally, the symmetrical part of an X-ray diffraction peak can be described by the pseudo-Voigt approximation

$$\eta L + (1 - \eta)G \quad (2.19)$$

where (L) and (G) are the Lorentzian and Gaussian contributions to the peak shape and ( $\eta$ ) is the mixing parameter which can be defined as a linear function of  $2\theta$

$$\eta = N_A + N_B (2\theta) \quad (2.20)$$

where ( $N_A$ ) and ( $N_B$ ) are refinable parameters.

The full width half maximum (FWHM) ( $H_k$ ) of each peak is also accounted for with the variables U, V and W, equation (2.21) <sup>[131]</sup>

$$H_k^2 = U \tan^2 \theta + V \tan \theta + W \quad (2.21)$$

Where ( $\theta$ ) is the scattering angle.

To achieve a good agreement between the observed and calculated profiles, a series of R factors are determined;  $R_{\text{profile}}$  ( $R_p$ ),  $R_{\text{expected}}$  ( $R_{\text{exp}}$ ) and  $R_{\text{weightedprofile}}$  ( $R_{\text{wp}}$ ).

The measurement of the quality of the refinement is achieved by comparison of  $R_{\text{wp}}$  and  $R_e$  which are given by (2.22) and (2.23)

$$R_{\text{wp}} = \sqrt{\left\{ \frac{\sum w_i (y_i(\text{obs}) - y_i(\text{calc}))^2}{\sum w_i (y_i(\text{obs}))^2} \right\}} \quad (2.22)$$

where ( $y_i$ ) is diffraction intensity and ( $w_i$ ) is equal to  $(1/y_i)$ .

$$R_{\text{exp}} = \left\{ \frac{(N - P + C)}{\sum w_i (y_i(\text{obs}))^2} \right\}^{\frac{1}{2}} \quad (2.23)$$

where (N) is the number of observations, (P) is the number of independently refined parameters and (C) is the number of constraints.

The measure of quality is expressed as the goodness of fit ( $\chi^2$ ) and is given by:

$$\chi^2 = \left[ \frac{R_{wp}}{R_{exp}} \right]^2 \quad (2.24)$$

For a good fit ( $R_{wp}$ ) should approach as closely as possible to ( $R_{exp}$ ) (i.e. as close as to 1 as possible). The accuracy of this fit can be observed by a graphical plot of the profile fit. A difference line between the calculated and observed patterns should be as flat as possible to represent an 'ideal'.

### 2.3.7 Practical aspects of PXD experiments

Powder X-ray diffraction analyses were performed using a PANalytical X'pert PRO MPD powder diffractometer with copper source ( $\lambda = 1.54056 \text{ \AA}$ ) in either flat plate or capillary geometry. In the case of flat plate analysis, powdered samples were loaded into the recess of a flat glass holder. Diffraction data were typically collected for  $5^\circ \leq 2\theta \leq 85^\circ$  with a  $0.017^\circ$  step size with scan times from 1 - 12 h.

In the case of substrate reactions (2.1.3) the small sample volumes obtained required that PXD analysis allowed for the high intensity reflections from the underlying silica substrate. Alternative methods of loading samples were attempted to try and reduce or remove substrate effects but best results were obtained by attaching the substrate to a flat plate with double sided sticky tape. In a few cases there was enough sample to sonicate the substrate in iso-propyl alcohol and dropper the solution onto the glass.

For capillaries, finely ground samples were loaded into 0.5 or 0.7 mm glass capillaries and sealed. The capillary is rotated in the path of the X-ray beam and therefore aligned with the aid of a goniometer prior to attaching to the diffractometer to ensure that it spins about one axis and therefore constantly maintains itself within the beam of the X-rays.

Diffraction data were compared to patterns in the ICDD (JCPDS) powder diffraction file (PDF) using the PANalytical High Score Plus software package.

## 2.4 Magnetic measurements

### 2.4.1 Magnetism in solids

Magnetic measurements can reveal information about the arrangement of electrons in an atom or molecule. Given their negative charge, electrons can behave like small magnets but normally the pairing of spins in an orbital result in a cancellation of this effect. Observable magnetic effects can be characterized by the behaviour of a substance towards an applied magnetic field ( $H$ ). For example, para- and diamagnetism are instances of weak magnetic effects and can be differentiated by the contrast in their magnetic susceptibilities ( $\chi$ ); diamagnetism has a negative susceptibility and repels an applied magnetic field whilst paramagnetism is positive and is attracted.

Magnetism is most widely recognised in solids due to the strong cooperative effects which can occur between atoms in close proximity to one another. This interaction can give rise to a number of possible states dependent upon the alignment of their spins. An alignment between magnetic spins results in a state known as *ferromagnetism*. On the other hand anti-alignment between spins is *antiferromagnetism* and the presence of both these states simultaneously is termed as *ferrimagnetism*.

A magnet produces lines of force which can be easily represented by the lines which appear when iron fillings are scattered around a magnet (Fig 2.25).

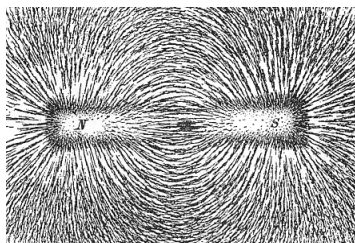


Fig 2.25 Bar magnet placed beneath a sheet of paper and iron fillings scattered across the surface highlight the lines of force produced by the magnetic field.

The density of these lines is called the magnetic flux density ( $B$ ) and can be influenced by a magnetic field. In the case of a diamagnet, the density would decrease whereas for a paramagnet an increase would be observed. The

relationship of  $B$  with  $H$  and influence under the applied field, also known as magnetization ( $M$ ), can be expressed as the following

$$B = \mu_0(H + M) \quad (2.25)$$

Where  $\mu_0$  is the permeability of free space in a vacuum.  $(H + M)$  is known as the Magnetic susceptibility ( $\chi$ )

In a transition metal complex, unpaired electrons on different centres tend to be isolated from one another giving rise to simple paramagnetic behaviour. Normally, these electrons are randomly aligned but under an applied magnetic field, they have a tendency to align with regards to the field and each other. This is opposed by the randomizing effects of thermal energy. The relationship between the applied field and thermal randomization leads to a temperature dependence known as the *Curie Law*:

$$\chi = C/T \quad (2.26)$$

Where  $C$  is the Curie constant and  $T$  is the temperature (K)

Depending on the cooperative behaviour of the spins, different temperature dependences can be observed. In the case of ferromagnetism

$$\chi = \frac{C}{(T - \theta)} \quad (2.27)$$

Where  $\theta$  is the Weiss constant.

For antiferromagnetism it becomes

$$\chi = \frac{C}{(T + \theta)} \quad (2.28)$$

Where  $\theta$  is the Weiss constant.

In the cases of both antiferromagnetism and ferromagnetism the magnetic susceptibility becomes paramagnetic above these respective transition temperatures,  $T_C$  or  $T_N$ . All three behaviours are illustrated in (Fig 2.26) in terms of magnetic susceptibility against temperature. <sup>[16]</sup> The Weiss constant can be calculated from a plot of  $\chi^{-1}$  against  $T$  (K) (Fig 2.26d). The point at which the straight line portion intersects the x-axis is the Weiss constant. In the case of a paramagnetic substance which shows no tendency towards magnetic ordering the graph should extrapolate to the origin.

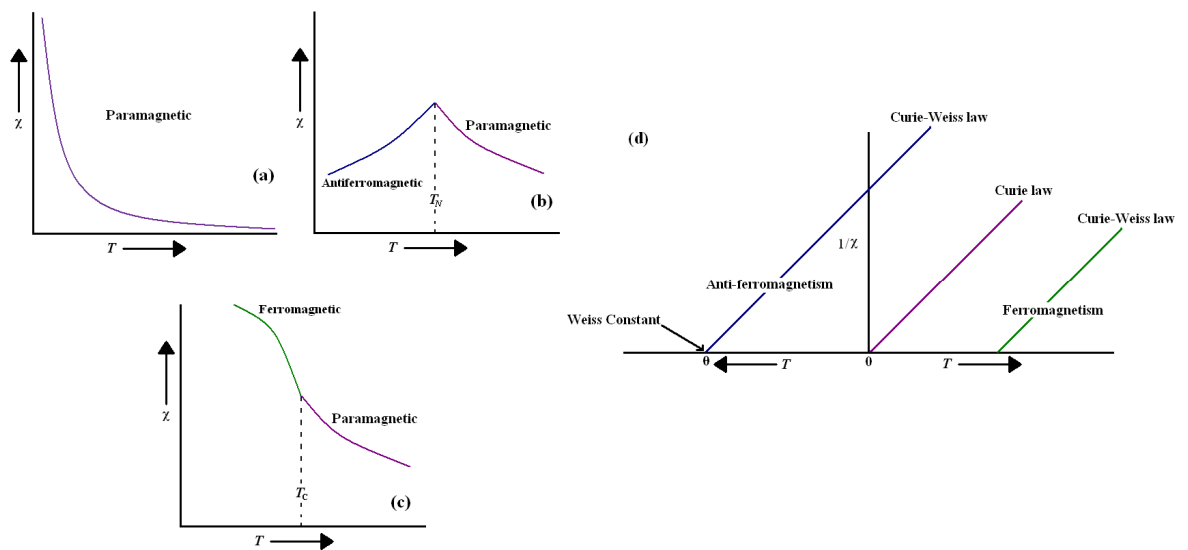


Fig 2.26 Graphs showing the changes of magnetic susceptibility with temperature depending on the types of magnetism, (a) Curie paramagnetism, (b) antiferromagnetism, (c) ferromagnetism (d) Plot of  $\chi^{-1}$  against temperature for paramagnetic substances with either some or no magnetic ordering, from which the Weiss constant can be extrapolated.

#### 2.4.2 Superconducting quantum interference device (SQUID)

A superconducting quantum interference device is designed to detect any change in the applied magnetic flux of a sample. This allows it to measure properties directly affected by this change such as magnetic susceptibility, current and voltage. It is an extremely sensitive piece of equipment and is able to detect fields down to a level of femtoteslas. The SQUID is composed of a superconducting ring which is able to detect small changes in magnetic field and convert these to large electrical signals. It typically consists of two superconducting coils ( $L_1$  and  $L_2$ ) one of which is coupled to a third coil ( $L_3$ ). A sample passed through  $L_1$  produces a current proportional to the magnetisation of the sample which can be displayed as a function of temperature. <sup>[132]</sup>

For this project, materials were investigated to determine their behaviour under a magnetic field at various temperatures and therefore classify the type of magnetism which they exhibited. Magnetic measurements were performed using a Quantum Design MPMS 5T SQUID magnetometer. Depending on the sensitivity of the material to the applied magnetic field, experiments were conducted under either a field of 10, 100 or 1000 Oe at temperatures normally ranging from 2 - 100 K. Due to the minute sample size it was unfortunately not possible to remove samples from the substrate prior to analysis. To account for this, measurements of blank silica substrates were performed and the resulting data subtracted from sample data. Magnetic data given in the thesis are weighted values for the sample itself and does not include the substrate. Since the dimensions of the silica substrate and metal layer were known. The amount of metal present on the substrate could be calculated and the assumption made that the amount of sample produced would be approximate to this value.

## 2.5 Raman spectroscopy

### 2.5.1 Principles

Raman spectroscopy is an analysis technique that was discovered by Raman in 1928 <sup>[133]</sup> and is based upon the interaction of light with the chemical bonds of a material (Fig 2.27). It can provide information about chemical structure, phase, crystallinity and molecular interactions of a substance. It covers a range of inorganic, organic and biological materials and can be used to analyse samples from solids to gases. It is generally thought not to be suitable for metals and their alloys however, given that they tend to exhibit high reflectance, small penetration depths and weaker resonant enhancement. <sup>[134, 135]</sup>

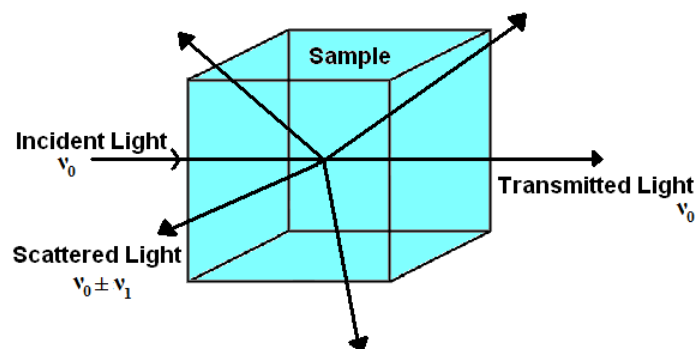


Fig 2.27 Basic interaction of light with a particle utilised by Raman

In principle, a monochromatic beam of light, from a high intensity laser light source, with frequency  $\nu_0$  and energy  $h\nu_0$  (where  $h$  = Planck's constant) is directed at a sample. The majority of photons will elastically scatter and retain  $h\nu_0$  (Rayleigh scattering). A much smaller fraction (around  $1 \times 10^{-7}$  %) will inelastically scatter and gain or lose energy. This results in a change in the internal energy of the targeted molecule. This is a quantized value and therefore frequency shifts from that of the initial beam occur in discrete steps ( $E_0 - E_1$ ). Raman spectroscopy makes it possible to observe photons which have either decreased in frequency ( $\nu_0 - \nu_1$ ) or increased in frequency ( $\nu_0 + \nu_1$ ) with the former being an example of *Stokes radiation* whereas the latter is *anti-Stokes*. Therefore a Raman spectrometer observes frequencies of  $\nu_0$  and  $(\nu_0 \pm \nu_1)$ . It measures these reflections 90 degrees to the incident beam. The scattering process occurs in two steps whereby a photon collides with a molecule raising it to an excited electronic state termed the *virtual* energy level (Fig 2.28). A second photon then leaves the molecule with either an increase or decrease in energy. <sup>[136]</sup>

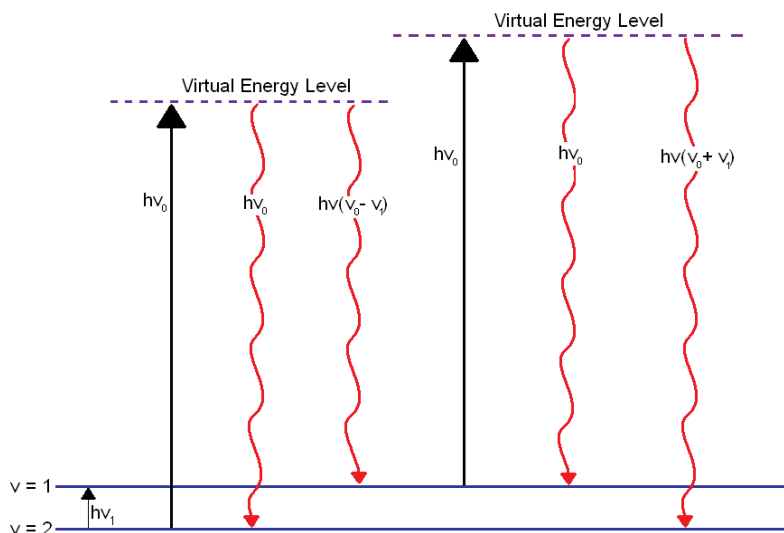


Fig 2.28 Energy level diagram displaying the origin of the vibrational Raman effect

The photon exposes the molecule to an oscillating electric field causing a vibration of its electrons which affects the time dependent electric dipole of the molecule. This is proportional to the oscillation of the electric field. This dipole moment causes electromagnetic radiation to be given off resulting in the emission of a second photon. The magnitude of the induced dipole moment depends on both the polarizability of the molecule and the amplitude of the light wave. The polarizability is a reflection of how readily the electrons are displaced by the light wave and therefore determine the frequency of the field fluctuation ( $\nu_0$ ). For Raman scattering to occur, the interaction of the molecule with the light must cause a change in the polarizability of the molecule ( $\alpha$ ). Whether any scattering is observed will also depend on the magnitude of this change. Therefore a symmetrical molecule such as  $\text{CH}_4$  is not Raman active because its polarizability is identical at any orientation (since it is considered spherical) and the oscillating electric field cannot couple differently to the light wave so only Rayleigh scattering will be observed. <sup>[137]</sup>

A Raman spectrum consists of numerous peaks with varying intensity and wavelength. Each peak is specific to a molecular bond vibration. This can be either a singular molecular bond or a group such as a benzene ring. The figure below (Fig 2.29) is an example of a spectrum of  $\text{CCl}_4$ , the Rayleigh scattering is centred at  $\nu_0 = 22,938 \text{ cm}^{-1}$ . It can be seen from the spectrum that the lower energy side (Stokes radiation) are more intense than those on the higher energy side (anti-Stokes). This is a reflection on the fact that typically for Raman

spectroscopy, energy loss of the incident beam is far more likely to occur than energy gain. It is more common now however for a Raman spectrometer to use *Raman shift* on the x-axis.  $V_0$  is set to  $0 \text{ cm}^{-1}$  and the measurements taken from this as the normal. Therefore there are no observed negative Raman frequencies.

Spectra are often complicated but unique for a particular material therefore libraries of Raman spectra are usually consulted when identifying a substance. In the case of this project, Raman was used either as a means of distinguishing one compound from another or to determine any change in frequency between bulk and nanoscale structures.

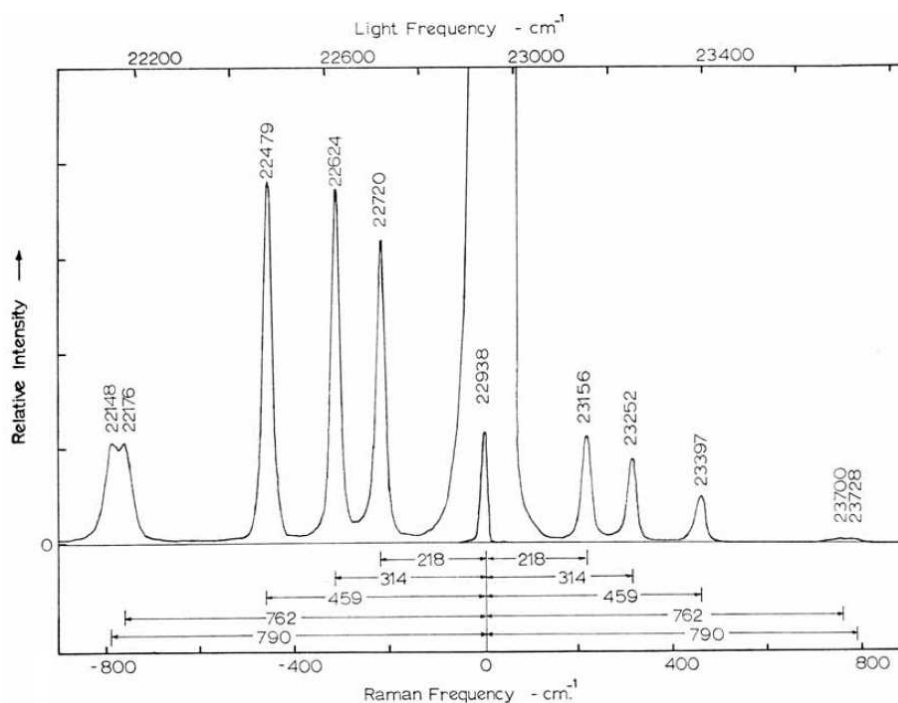


Fig 2.29 Spectrum of carbon tetrachloride <sup>[136]</sup>

### 2.5.2 Sample preparation

Raman spectra were collected at room temperature using a Horiba LabRAM HR confocal microscope system with a 532 nm green laser. A hole aperture of 50  $\mu\text{m}$ , 600 gr/mm grating, 50x objective lens and a Synapse CCD detector were used.

Powdered samples were spread onto a glass slide and observed with an optical microscope. The machine was then calibrated and a spectrum collected over a

period of several minutes from an average of multiple scans, normally at a range of  $0\text{ cm}^{-1}$  to  $800\text{ cm}^{-1}$ .

In the case of substrate reactions, samples could be observed on the silica substrate itself and this posed no interference to the overall pattern other than one band at ca.  $518\text{ cm}^{-1}$  corresponding to the substrate itself (confirmed by running blank silica).

## 2.6 Transmission Electron Microscopy

Transmission electron microscopy (TEM), like scanning electron microscopy utilises a beam of electrons treated with various electromagnetic lenses to create a high magnification image of a specimen. A microscope typically consists of an electron gun and series of lenses named the condenser, objective and projector lens. These are used for probe formation, image or diffraction pattern formation and magnification respectively. Rather than exploit scattered electrons like SEM, TEM mostly utilises transmitted electrons to form an image. The sample itself is situated in the objective lens and generated electrons (typically by thermionic emission of either a tungsten or lanthanum hexaboride filament) are accelerated through the sample at high voltage ca. 100-400 kV. They travel along the optic axis of the microscope under high vacuum hitting either a photographic film, fluorescent screen or CCD (depending on the type of machine used) creating a two dimensional image (Fig 2.30). Specimens must be thin enough to allow sufficient transmission of electrons through the sample. TEM is able to produce extremely high magnification images which can approach the range of Ångströms ( $10^{-10}\text{ m}$ ). The two principal modes of a TEM are bright field imaging and electron diffraction. A diffraction pattern is a reconstruction of the diffracted beam once it has passed through the sample and is formed in the back focal plane of the objective lens. Through the aid of a selected area aperture a selected area electron diffraction pattern (SAED) can be obtained. This limits the total number of contributing electrons to a specific area of interest within the sample. This technique produces a spot pattern from the transmission beam which can give crystallographic information about a certain plane including structure and crystal defects.

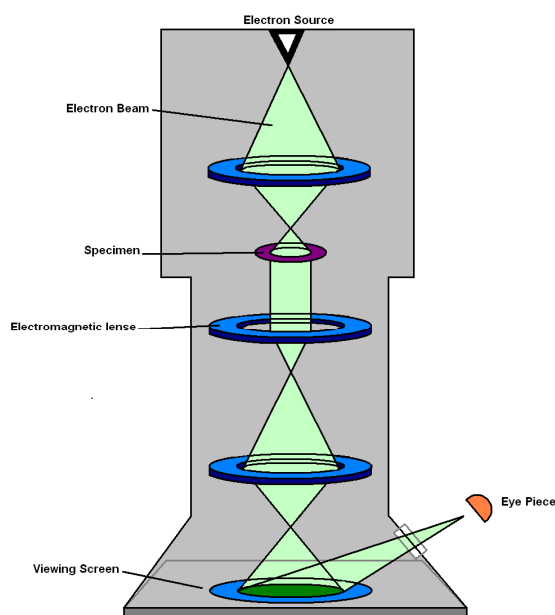


Fig 2.30 Rough schematic of a TEM

By centring the objective aperture on the non-diffracted transmitted beam a bright field (BF) image is produced. Alternatively if the objective lens is centred on a diffracted beam a dark field (DF) image is created instead. Bright field imaging is the standard type of imaging for TEM. It arises from contrast generated from the electron beam and specimen. Areas of low contrast (bright) show the areas with least interaction (i.e. absorption or scattering) whereas areas of high contrast (dark) have had the most interaction. A change in absorption typically indicates a change in thickness of the sample whereas a change in scattering is related to Bragg scattering and therefore an alteration in diffraction. Dark field imaging occurs when the electron beam interacts with the sample at an angle. If a particular angle corresponds to a specific Bragg condition a dark field image is achieved. Dark field imaging therefore highlights any contrast between different areas of the sample which may occur from differences in crystal growth. <sup>[138]</sup>

This project employed the use of a FEI Techni T20 TEM. The machine operated at 200 kV and recorded images and diffraction patterns using a SIS Megaview III CCD camera. TEM was primarily used to provide information about the crystal structure of nanostructures which could not be so readily obtained with XRD. Further details such as specimen thickness and lattice spacings were also clarified. Operation of the TEM was conducted by Dr Ian MacLaren.

### 3. Nickel disulfide

#### 3.1 Introduction

Currently research into hydrothermal and solvothermal reaction schemes provide the widest range of examples of nanostructures and has shown the greatest diversity in morphology and chemical composition. <sup>[139]</sup> They often involve multiple steps which are dependent upon factors such as concentration and pH, features that are not so easy to control without the aid of sometimes deleterious or expensive chemicals. In addition, such a complex methodology can often lead to impure yields which require vigorous purification before obtaining the final product. This research focuses on alternative solid-state methods and is a development of work in the tantalum - sulfur system where a single (CVD) step method was established to produce well defined single-crystalline TaS<sub>2</sub> nanowires on Ta foil. <sup>[140]</sup> By exploiting the relatively low melting and boiling points of the chalcogen, it is possible to overcome the inherent restrictions of the high melting points of many transition metals and adapt *physical vapour transport methods* (PVT) to grow the TaS<sub>2</sub> nanostructures on the tantalum metal surface. For the nickel-sulfur system, thin films where the nickel metal was deposited as a nanometric layer onto a SiO<sub>2</sub> support were used instead of metal foil. Metal layers such as this have been previously manipulated to grow films of the corresponding disulfide or diselenides by a reaction with a gaseous precursor. <sup>[141-144]</sup> A further aspect of this approach is that if the vapour selectively reacts with metal, one, in theory, could design and template the resultant nanomaterials by patterning the metal substrate with high precision.

### 3.1.1 Nickel disulfide

Pyrite structured nickel disulfide,  $\text{Ni}^{2+}(\text{S}_2)^{2-}$  forms an fcc array with  $\text{Ni}^{2+}$  in an octahedral coordination to the S (Fig 3.1).<sup>[82]</sup>

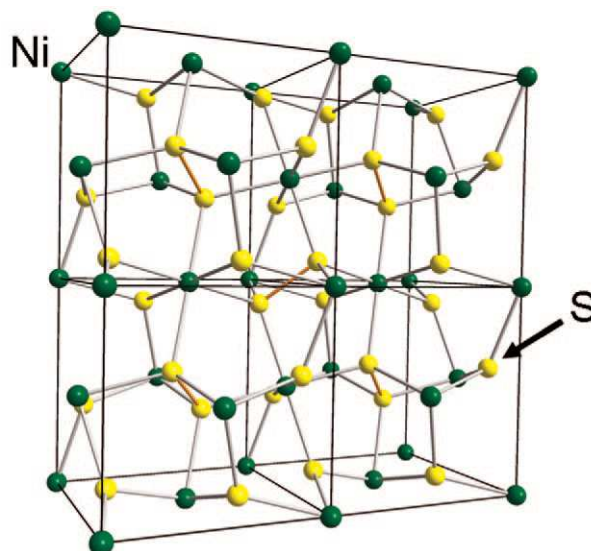


Fig 3.1 Crystal structure of pyrite  $\text{NiS}_2$ , four unit cells with Ni-S bonds in silver and S-S bonds in gold.

Bulk  $\text{NiS}_2$  is an example of a Mott-Hubbard insulator which results from interactions between electrons in the narrow half-filled  $e_g$  band. These interactions cause a localisation of the electrons and open a band gap.<sup>[145]</sup>

It has complicated magnetic behaviour and undergoes two distinct transitions. One between 37-51 K, an antiferromagnetic transition normally labelled  $T_{N1}$  and a weak ferromagnetic state at 30 K,  $T_{N2}$ .

The nickel - sulfur system is exemplar in illustrating the diversity in nano-morphology that can occur with different stoichiometries. For instance, the realisation of nanoprisms and flower like structures of  $\text{NiS}$ <sup>[146,147]</sup> to nanowires of  $\text{Ni}_3\text{S}_2$ <sup>[148]</sup> and nanorods of  $\text{Ni}_9\text{S}_8$ .<sup>[149]</sup> The interest of this chapter however lies with the dichalcogenide equivalents. Crystalline  $\text{NiS}_2$  has been produced in the past using both hydrothermal and<sup>[150, 151]</sup> solid-state methods<sup>[152]</sup> but there is also a plethora of solvothermal examples<sup>[153-155]</sup> such as the reaction between  $\text{NiSO}_4 \cdot 6\text{H}_2\text{O}$  and  $\text{Na}_2\text{S}_3$  to produce cubic nanocrystallites.<sup>[156]</sup>

The purpose of this chapter is to show that an array of nanostructures can be synthesised via a physical vapour transport (PVT) method in which sulfur vapour generated *in situ* is reacted with nickel coated silica substrates. Systematic studies demonstrate the effect of the reactant ratio, metal layer thickness and reaction temperature on the synthesis and growth process. The evolution of growth with temperature and reactant quantity are discussed and analysed with SEM, PXD and SQUID.

### 3.2 Experimental

The nickel sulfides were synthesised using a reaction between the aforementioned SiO<sub>2</sub>-supported Ni thin films (3.1) with chalcogen vapour in sealed silica reaction tubes (Fig 3.2)

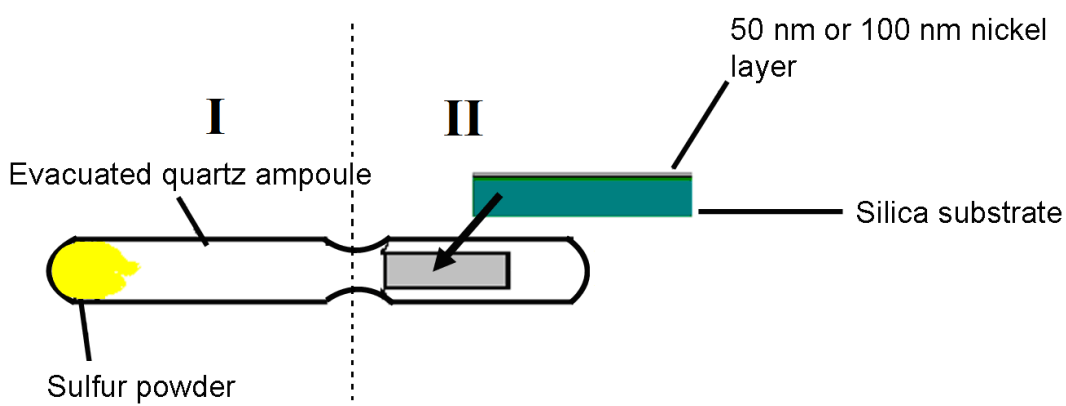


Fig 3.2 Typical experimental set-up for reactions, nickel coated silica substrate (section II) and sulfur powder (section I) are located on opposite ends of an evacuated silica ampoule

Pre-determined amounts of sulfur were placed in one end of the silica ampoule prior to forming the constriction. The nickel coated substrate of a known film thickness (25, 50 or 100 nm) and substrate (typically of around 2cm<sup>2</sup>) was then placed in the opposite end of the silica ampoule and the vessel sealed under vacuum to a pressure of 3 mbar. The ampoules were heated in a box furnace to an initial temperature below the reaction temperature for 3 hrs to allow for the controlled volatisation of sulfur and then to the intended reaction temperature for 60 hrs. The temperature was increased at 125 - 200°C/h for each heating step. Once reactions were complete, samples were allowed to cool in the furnace overnight. Unless stated otherwise, reactions used 0.01g of sulfur. In an alternative reaction, the addition of nickel powder was included at a 1:2 ratio of nickel to sulfur (0.018g : 0.01g) all other conditions were kept identical to the corresponding sulfur reaction. Experiments typically produced dark coloured films with an estimated yield of around 0.5-2 mg.

### 3.3 Characterisation

Products were retained on the substrate for analysis unless otherwise noted. Powder X-ray diffraction (PXD) analysis was performed using a PANalytical X'pert PRO MPD powder diffractometer in flat plate geometry. Samples were loaded onto a flat glass plate and secured with double sided sticky tape. Diffraction data were typically collected for  $5^\circ \leq 2\theta \leq 85^\circ$  with a  $0.017^\circ$  step size with scan times of 1-12 h. The sample displacement error was accounted for by measuring the offset of a standard and then using Highscore software to correct sample scans. Small sample volumes required that PXD analysis allowed for the high intensity reflections from the underlying silica substrate. Alternative methods of loading samples were attempted to try and reduce or remove substrate effects but best results were obtained from the method described above and characterisation of unique sample reflections was possible via this method. Diffraction data were compared to patterns in the ICDD (JCPDS) powder diffraction file (PDF) using the PANalytical High Score Plus software package. Indexing was achieved using the DICVOL software package<sup>[127]</sup> and least squares cell parameter refinement.

Scanning electron microscopy (SEM) was performed using two instruments; a Philips XL30 ESEM and Hitachi S4700 cold field emission gun SEM. Typically, samples were loaded onto aluminium stubs using adhesive carbon tabs and run in high vacuum mode with an applied accelerating voltage of 10 kV and a working distance of 12.5 mm for imaging and 10 kV and a working distance of 10mm for energy dispersive X-ray analysis, (EDX). EDX analysis was performed within the Philips instrument using an Oxford Instruments 7200 EDX spectrometer in order to determine elemental compositions (which can be obtained with accuracy for elements of atomic number from carbon upwards). Samples for SEM of sufficient thickness were prepared by depositing powder onto a carbon tab.

Magnetic measurements were performed using a Quantum Design MPMS 5T SQUID magnetometer. Samples were loaded into gelatine capsules. Field cooled (FC) and zero field cooled (ZFC) measurements were performed with an applied field of 100 Oe between 2 - 300 K. All magnetic data were corrected for the gelatine capsules and for core diamagnetism.

### 3.4 Results and discussion

#### 3.4.1 Trial reactions

There was a range of metals which could be produced in the form described in section (3.2). Therefore preliminary investigations used different metals, namely molybdenum, nickel, titanium and tungsten. It became clear from an early stage that the combination of nickel plus sulfur provided the best reproducible examples of nanostructures and therefore this system was considered a good starting point to begin a more detailed analysis.

To ensure consistency, substrates were kept at a size of roughly 2cm<sup>2</sup> but in early experiments the amount of sulfur was varied. An initial uncertainty of the reactivity of the metal toward the chalcogen led to the assumption that an excess would provide a rich enough vapour to force a reaction. Table 3.1 shows preliminary parameters with a 0.05 g sulfur and different the metallic layers.

Table 3.1 Trial reactions with different metal layers

Sample No.	Powder reactants; mass /g	Metal	Film thickness /nm	Initial T /°C (3 h)	Reaction T /°C (60 h)
1	S; 0.05	Ni	50	300	500
2	S; 0.05	Ti	50	300	500
3	S; 0.05	W	50	300	500

Results indicated that an excess of chalcogen was in fact disadvantageous to successful growth and that reactions resulted in a coating of the substrate with a thick layer of chalcogen. (Fig 3.3)

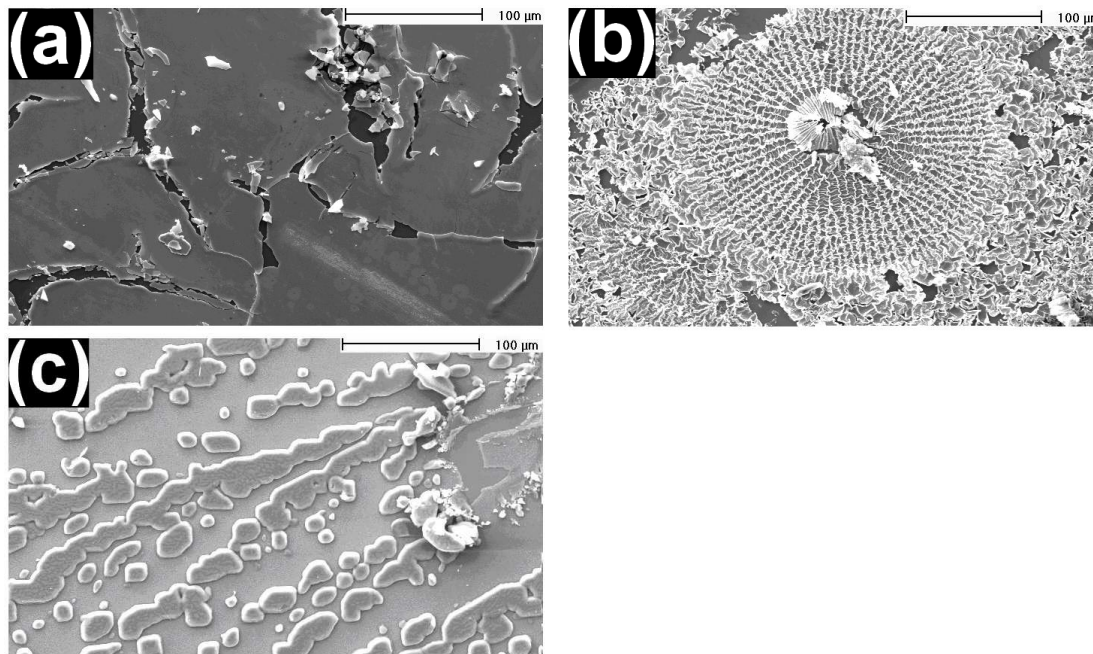


Fig 3.3 SEM Micrographs of products of reactions with 0.5 g sulfur with (a) Ni layer (b) Ti layer (c) W layer

The appearance of the layers however are distinct to each metal. This implies an interaction between the vapour and the surface has occurred leading to sulfide growth followed by coating of the surface with the remaining chalcogen. EDX of samples (1-3) detected solely sulfur in addition to the silica substrate. The idea that the metal is perhaps stripped from the substrate during heating was later discarded by a control reaction where the substrates were heated in the absence of sulfur at temperatures of up to 650 °C. There was no visible change to the substrate surface and EDX still gave an approximate 1:5 ratio of metal: SiO<sub>2</sub>. Further to this, vacuum sublimation performed on samples (1-3) by the cold-finger technique could partially remove sulfur revealing differing nanostructured layers beneath. From these two analyses it could be assumed that the ratio between chalcogen and metal is excessive and that any metal-containing phases are obscured by the sulfur regardless of whether a reaction has taken place to form a chalcogenide or not. Therefore, subsequent study used lower chalcogen masses which did not result in deposition of excess sulfur. Experiments centred

on the relationship between film thickness and temperature and how this contributed to the evolution of growth and composition.

### 3.4.2 Metal layer thickness

Three thicknesses of nickel film were investigated, 25, 50 and 100 nm respectively. Subtle variations in composition and morphology unique to each thickness were observed dependent on the reaction scheme.

#### 3.4.2.1 25 nm nickel layer thickness

Table 3.2 exhibits samples with a 25 nm layer of nickel.

Table 3.2 Reactions at different temperatures with 25 nm of nickel

Sample No.	Powder reactants; mass /g	Ni film thickness /nm	Initial T /°C	Ramp rate /°C h <sup>-1</sup>	Reaction T /°C
4	S; 0.01	25	100	125	250
5	S; 0.01	25	150	125	350
6	S; 0.01	25	225	125	450
7	S; 0.01	25	250	125	550
8	S; 0.01	25	300	200	650
9	S; 0.01	25	300	200	750

Reactions with a 25 nm layer at temperatures of 350 °C and below (4 and 5) produce an unidentifiable structure. The corresponding PXD patterns reveal sharp crystalline peaks at low angles which could not be wholly matched to any currently known nickel - sulfur phases (Fig 3.4).

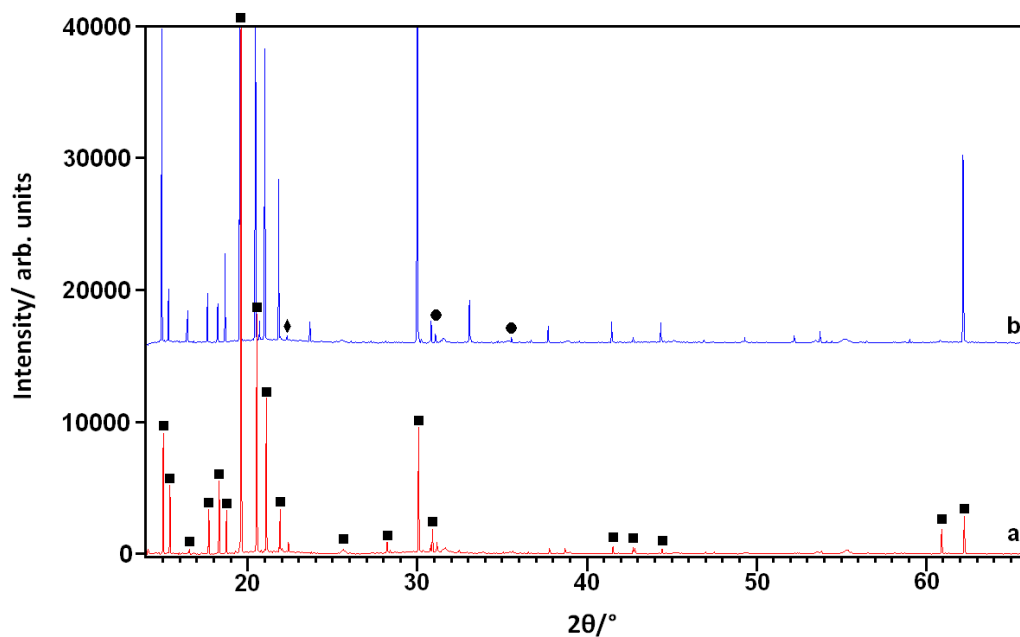


Fig 3.4 PXD patterns of samples prepared at (a) 250 °C (4), (b) 350 °C (5). Filled squares denote the unidentified phase. Filled diamonds represent any reflections from underlying silica substrate and filled circles are provisionally attributed to NiS<sub>2</sub>.

Despite patterns for samples (4) and (5) being near identical, there are some discrepancies between the intensity ratios; the first six peaks for example do not maintain a constant relative intensity ratio. This relationship suggests that the reflections between approximately 14 and 25  $2\theta$  belong to multiple phases rather than one structure. EDX mostly detected sulfur and very small traces of nickel, yet a suitable PXD match to sulfur could not be established. Lower temperature reactions ( $\leq 350$  °C) could suffer from a deposition of excess sulfur, masking any nickel richer phases beneath. At slightly higher angles, a number of the coinciding peaks however can be matched to Ni<sub>9</sub>S<sub>8</sub> Table 3.3 gives a full list of these. Indexing of the relevant reflections to the Ni<sub>9</sub>S<sub>8</sub> phase gave the following parameters;  $a = 9.26(1)$  Å  $b = 11.28(2)$  Å  $c = 9.52(2)$  Å (4) and  $a = 9.17(2)$  Å  $b = 11.30(3)$  Å  $c = 9.46(2)$  Å (5) (Orthorhombic, Space group C222). Sample (5) is in good agreement with literature values ( $a = 9.180$  Å  $b = 11.263$  Å  $c = 9.457$  Å respectively)<sup>[157,158]</sup> whereas (4) shows a slight lattice expansion in the  $a$  and  $b$  parameters, of the order of 0.74 %. Reference to the nickel-sulfur phase diagram confirms that Ni<sub>9</sub>S<sub>8</sub> forms under the given reaction conditions.<sup>[159]</sup>

Table 3.3 Comparison of matching peaks of (4) and (5) to Ni<sub>9</sub>S<sub>8</sub>

Ni <sub>9</sub> S <sub>8</sub> <sup>[157]</sup> (2θ)	Sample 4 (2θ)	Δ (± 2θ)	Sample 5 (2θ)	Δ (± 2θ)
15.398	15.400	(+) 0.002	15.313	(+) 0.085
18.866	18.734	(-) 0.132	18.214	(+) 0.652
21.446	21.082	(-) 0.364	21.807	(-) 0.361
22.607	22.309	(-) 0.298	22.308	(+) 0.299
31.362	31.535	(+) 0.173	31.526	(-) 0.164
35.892	35.553	(-) 0.339	35.896	(-) 0.004
37.934	37.713	(-) 0.221	37.704	(+) 0.23
41.385	41.531	(+) 0.146	41.443	(-) 0.058
42.612	42.783	(-) 0.171	42.706	(-) 0.094
46.764	46.889	(-) 0.125	46.812	(+) 0.048
53.413	53.488	(-) 0.075	53.428	(-) 0.015
55.514	55.265	(+) 0.249	55.212	(+) 0.302
60.854	60.824	(+) 0.030	60.823	(+) 0.031

At 450 °C (6), Ni<sub>9</sub>S<sub>8</sub> and the remaining unidentifiable reflections give way to pyrite-NiS<sub>2</sub> (Fig 3.5)

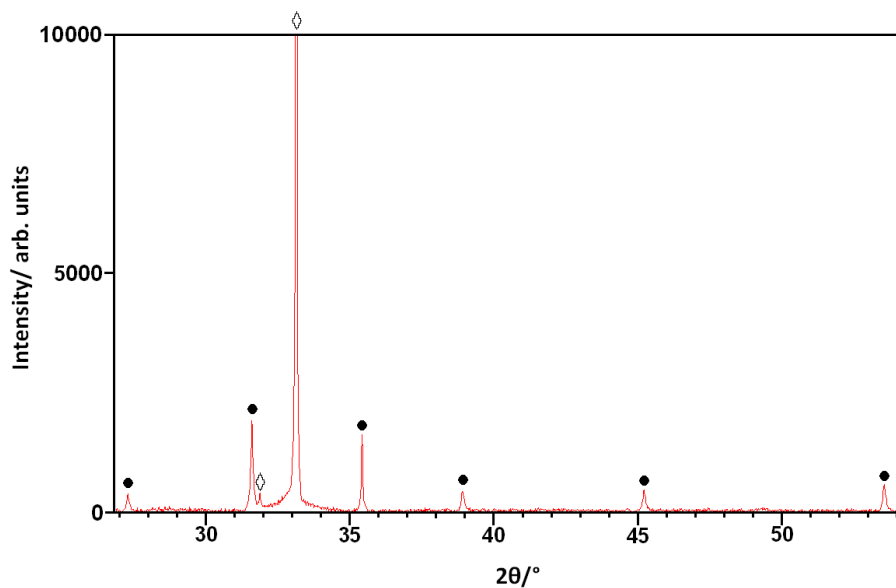


Fig 3.5 PXD pattern of sample (6). Filled circles represent pyrite-NiS<sub>2</sub>. Open diamonds correspond to underlying silica substrate

NiS<sub>2</sub> remains present at other temperatures (7 - 8) and by 650 °C (8) a clear match to pyrite-NiS<sub>2</sub> is produced (Fig 3.6).

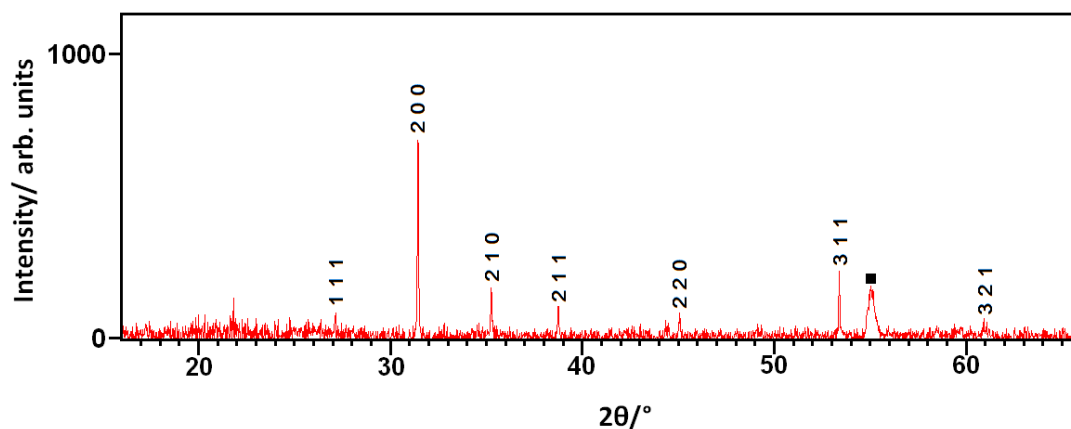


Fig 3.6, PXD pattern of sample (8), indexed peaks represent pyrite-NiS<sub>2</sub>. The filled square marks an unidentified peak tentatively attributed to excess sulfur.

SEM results establish that morphology evolves consistently with reaction temperature (Fig 3.7). At low temperatures, 250 °C (4), an agglomeration of submicron fused particles is formed with some particulates in the nanometre range (Fig 3.7a). At 350 °C (5), the density of coverage of the particles decreases and a slight faceting of the surface of the crystallites becomes apparent (Fig 3.7b). This trend continues at 450 (6) and 550 °C (7).

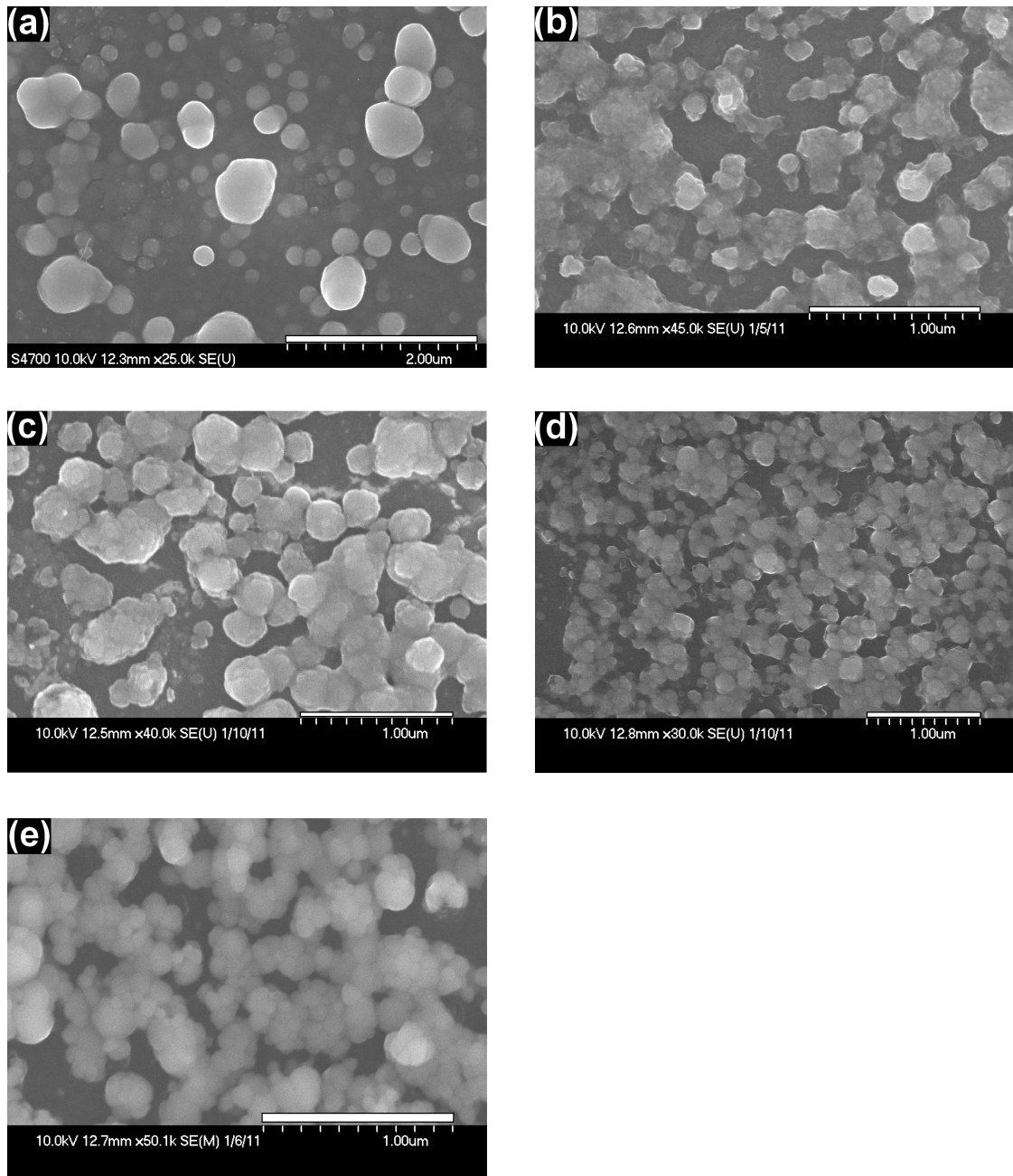


Fig 3.7 SEM micrographs of reactions of S with 25 nm Ni layer on SiO<sub>2</sub> substrate (a) 250 °C (4), (b) 350 °C (5), (c) 450 °C (6) (d) 550 °C (7), (e) 650 °C (8)

Unlike later experiments despite a similarity in crystal structure no cubic-like morphology is observed at higher temperatures. This could be a direct result of the thickness of the nickel layer and is discussed in section 3.5.

### 3.4.2.2 50 nm nickel layer thickness

Table 3.4 displays samples prepared with a 50 nm layer of nickel and their corresponding PXD analysis is given in (Fig 3.8). Reactions at 450 °C and below (10-12) are markedly different from those at higher temperatures. In the case of (10) the pattern contains reflections from the underlying SiO<sub>2</sub> plus several peaks which cannot be suitably matched to any nickel or sulfur containing compound in the literature. These same unidentified peaks occur in (11 and 12) but with diminishing intensity and a slight uniform decrease in their 2θ value (approximately 0.4 2θ), giving way to the then more prominent nickel disulfide phase. It is difficult to make a straightforward interpretation due to the interference of the SiO<sub>2</sub> substrate, but what is clear is that the relative intensities of the five major unassigned reflections (at 2θ ~ 19, 21, 28, 33 and 60 ° respectively) do not alter with temperature. This consistent intensity ratio between the peaks suggests a common phase across these three samples.

Table 3.4 Reactions at different temperatures with 50nm of nickel

Sample No.	Powder reactants; mass /g	Ni film thickness /nm	Initial T /°C	Ramp rate /°C h <sup>-1</sup>	Reaction T /°C
10	S; 0.01	50	100	125	250
11	S; 0.01	50	150	125	350
12	S; 0.01	50	225	125	450
13	S; 0.01	50	250	125	550
14	S; 0.01	50	300	200	650
15	S; 0.01	50	300	200	750

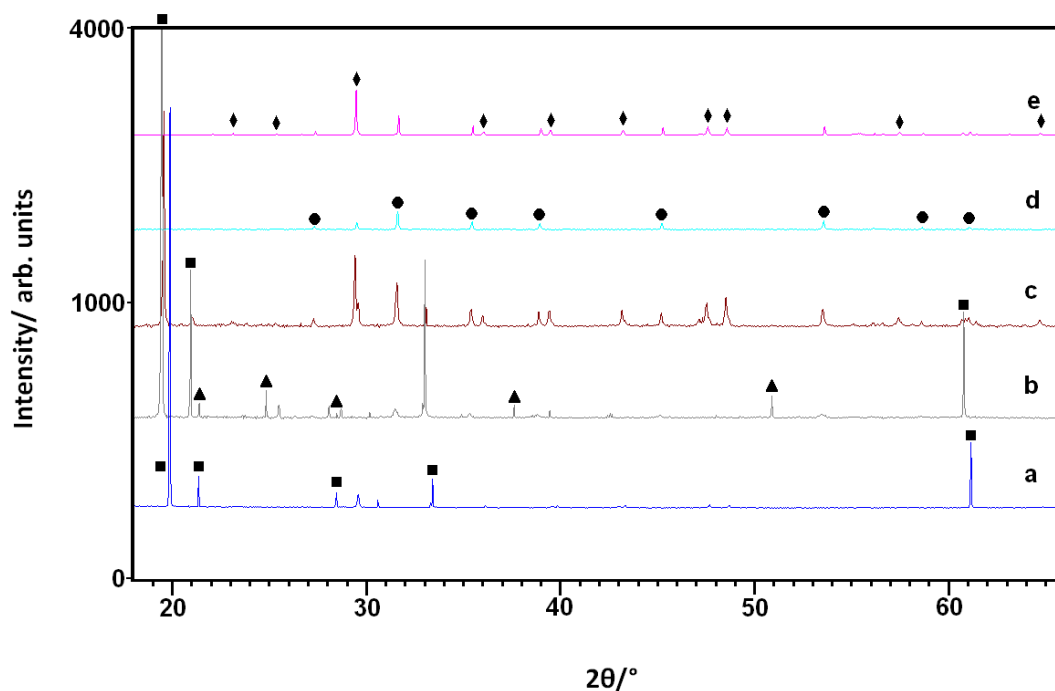


Fig 3.8 PXD patterns of samples prepared at (a) 250 °C (10), (b) 350 °C (11), (c) 450 °C (12), (d) 550 °C (13), (e) 650 °C (14). Filled circles represent reflections corresponding to NiS<sub>2</sub>; filled diamonds denote reflections present in the underlying silica substrate. Filled squares and triangles represent reflections from unidentified phases; the squares represent the four most intense reflections seen across all samples from 250-450 °C.

A comparison of (10) and (11) to (4) and (5) reveal the presence of these same four peaks. Table 3.5 gives a complete list of all the coinciding peaks between samples 4 and 10 and samples 5 and 11. It has already been determined that (4) and (5) are composed of multiple phases, one of which could be matched to Ni<sub>9</sub>S<sub>8</sub>. The correlation in peak position of the remaining unidentified reflections suggests a common phase between all four samples although it did not match to any of the known phases in the nickel-sulfur system. In addition, the increase in reaction temperature from 250 °C to 350 °C increases the number of peaks of the unidentified phase. This suggests that the phase is dependent on temperature as opposed to the thickness of the metal layer.

Table 3.5 Comparison of reflections between samples 4 and 10 and samples 5 and 11

(4) (2 $\theta$ )	(10) (2 $\theta$ ) ( $\Delta\pm 2\theta$ )	(5) (2 $\theta$ )	(11) (2 $\theta$ ) ( $\Delta\pm 2\theta$ )
-	-	16.450	16.506 (+0.056)
19.597	19.863 (+0.266)	19.417	19.597 (+0.180)
-	-	20.519	20.936 (+0.417)
-	-	25.508	25.486 (-0.022)
28.208	28.456 (+0.248)	28.136	28.071 (-0.065)
30.330	30.577 (+0.247)	30.211	30.162 (+0.049)
-	-	31.545	31.470 (-0.075)
-	-	33.061	33.001 (-0.060)
-	-	37.709	37.602 (-0.107)
-	-	42.641	42.758 (+0.117)
-	-	53.482	53.444 (-0.038)
60.929	61.137 (+0.208)	60.911	60.770 (-0.141)

EDX shed some light on the composition the unidentified phase giving average ratios of 2:1 Ni:S implying that it is nickel rich. Although at this stage it can not be ruled out that the excess in nickel is coming from the substrate itself.

At 550 °C (13) it becomes evident from the PXD data that nickel disulfide is favoured at the expense of the unidentified phase. This persists at 650 °C (14) and for both samples 13 and 14, single-phase crystalline NiS<sub>2</sub> was obtained. A suitable pattern for (15) could not be achieved as any diffraction peaks of the product were swamped by scattering from the substrate.

SEM results once again establish that morphology evolves consistently with reaction temperature (Fig 3.9)

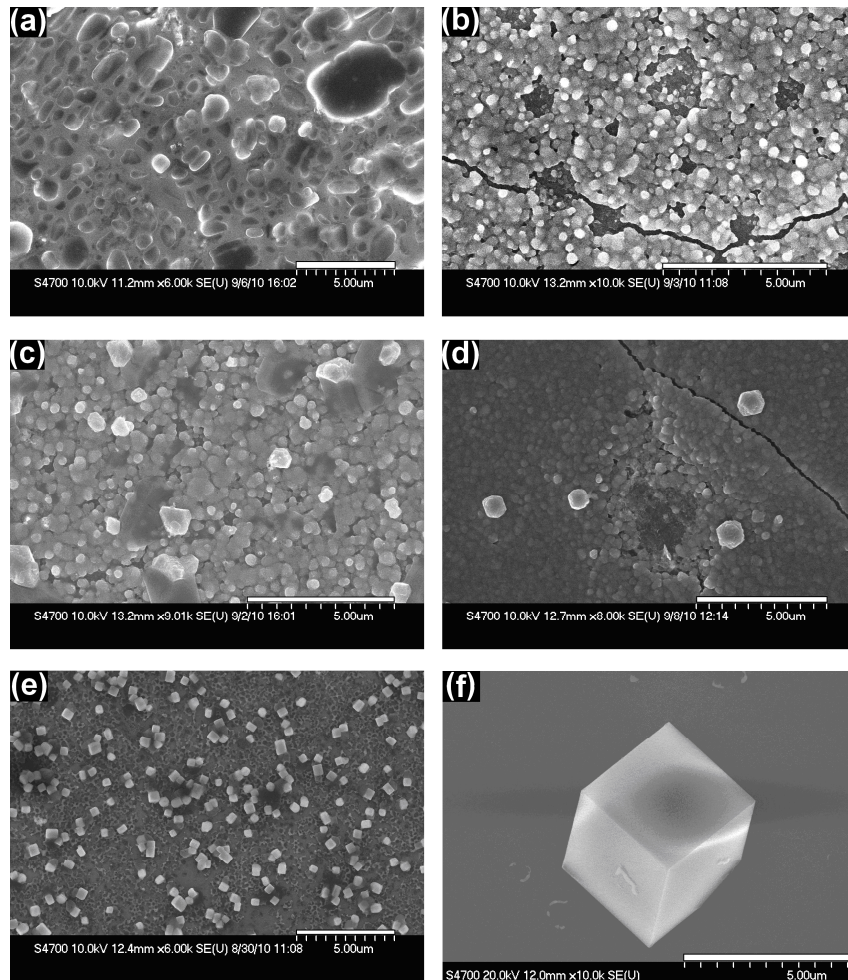


Fig 3.9 SEM micrographs of reactions of S with a 50 nm Ni layer on a SiO<sub>2</sub> substrate at: (a) 250 °C (10), (b) 350 °C (11), (c) 450 °C (12) (d) 550 °C (13), (e) 650 °C (14), (f) 750 °C (15).

Below 550 °C (10-12), the surface of the substrate is coated in a film of irregular fused submicron sized particles (Fig 3.9a-c). The significant change occurs at 550 °C (13) as evidence of faceted structures begin to emerge in the form of larger isolated but irregular particles. The majority of the sample, however, still remains as a mix of fused, ill-defined particles. At 650 °C (14) nanocrystallites of a cube-like nature develop around 200 nm in size. (Fig 3.9e) A further increase in temperature to 750 °C (15) results in crystals that demonstrate additional growth creating well-defined, highly symmetrical, microcubes (Fig 3.9f). The size of the crystallites ranges approximately from 2 - 5 μm. This increment in size occurs at the decrement of the population density of the cubes on the substrate surface (in comparison to 14).

### 3.4.2.2.1 Pyrite-NiS<sub>2</sub> - structural and magnetic data

The onset of nanocubic growth coincides with the NiS<sub>2</sub> phase in the PXD patterns at 650 °C which suggests that the cubes are pyrite-NiS<sub>2</sub>. This is further corroborated with EDX data for (14) and (15). Overnight data (12 h) were collected for (14) and a Rietveld refinement performed. [129] Results are given in (Fig 3.10) and Table 3.6 and 3.7. The data can be matched to the cubic pyrite structure (space group Pa $\bar{3}$ ) of NiS<sub>2</sub>. The interatomic distances, Ni-S (2.4026(8) Å) and S-S (2.066(7) Å) are in good agreement with those from the previously reported structural model (Ni-S (2.3950 Å) and S-S (2.0421 Å)). [160] Magnetic susceptibility data of (14) and (15) were also collected (Fig 3.11). Over the temperature range investigated it can be observed from the magnetic susceptibility vs temperature plot that samples exhibit a broad Curie-Weiss type behaviour. From data collected under zero field cooled (ZFC) and field cooled (FC) conditions a clear divergence in the ZFC and FC data can be identified at around 40 K which is resolved approaching 30 K. This detail can be readily attributed to the two ordering transitions previously reported in the literature. [146,161] When fitting the data above the ordering transition temperature to a Curie-Weiss expression, the Curie constant was calculated as 55 cm<sup>3</sup> K mol<sup>-1</sup> and an effective magnetic moment of 0.33 B.M obtained.

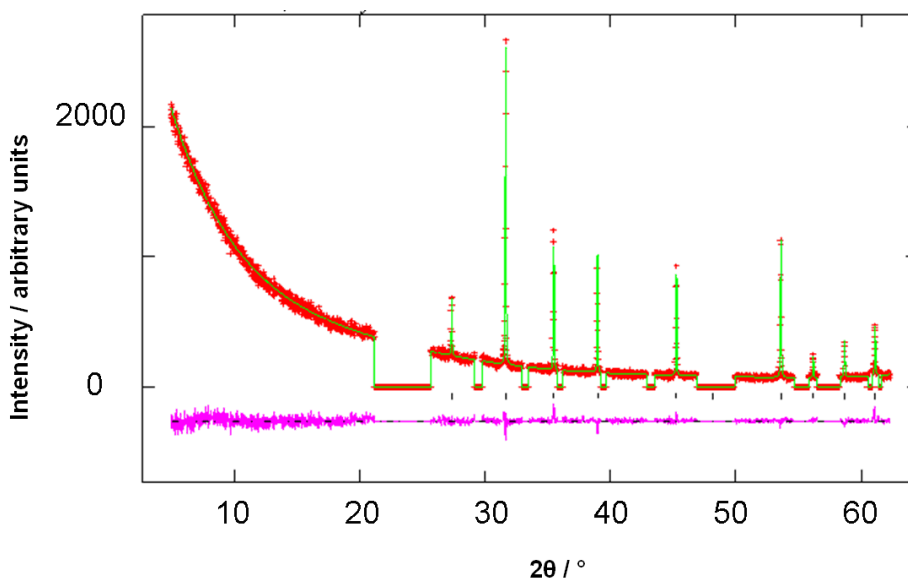


Fig 3.10 Observed, calculated and difference profile plot from the Rietveld refinement of (14) against PXD data. Observed data are indicated by crosses, calculated data by the solid line. The difference profile is shown below and the tick marks denotes the position of NiS<sub>2</sub> reflections. The reflections from the substrate were excluded.

Table 3.6 Crystallographic results from Rietveld refinement against PXD data for (14).

Formula (sample No)	NiS <sub>2</sub> (14)
Crystal system	Cubic
Space group	<i>Pa</i> -3 (No. 1)
<i>a</i> / Å	5.6923 (2)
<i>V</i> / Å <sup>3</sup>	184.44(2)
<i>Z</i>	4
Formula mass, <i>M</i> / g mol <sup>-1</sup>	491.28
Density, $\rho_x$ / g cm <sup>-3</sup>	4.423
Ni; 4 <i>a</i> (0,0,0)	
100 x <i>U</i> <sub>iso</sub> / Å <sup>2</sup>	6.6 (3)
S; 8 <i>c</i> ( <i>x,x,x</i> )	
<i>x</i>	0.3952(3)
100 x <i>U</i> <sub>iso</sub> / Å <sup>2</sup>	4.6 (2)
No. observations, parameters	2600, 21
<i>R</i> <sub>wp</sub>	0.0569
<i>R</i> <sub>p</sub>	0.0386
Goodness of fit, $\chi^2$	1.434

Table 3.7 Bond lengths from Rietveld refinement against PXD data for (14)

Bond length/angle	NiS <sub>2</sub> (14)	NiS <sub>2</sub> (Lit) <sup>[160]</sup>
Ni - S / Å	2.4026(8)	2.3950
S - S / Å	2.066(7)	2.0421
S - Ni - S / ° (x6)	93.51(5)	93.6403
S - Ni - S / ° (x6)	86.49(5)	86.3597
S - Ni - S / ° (x3)	180	180

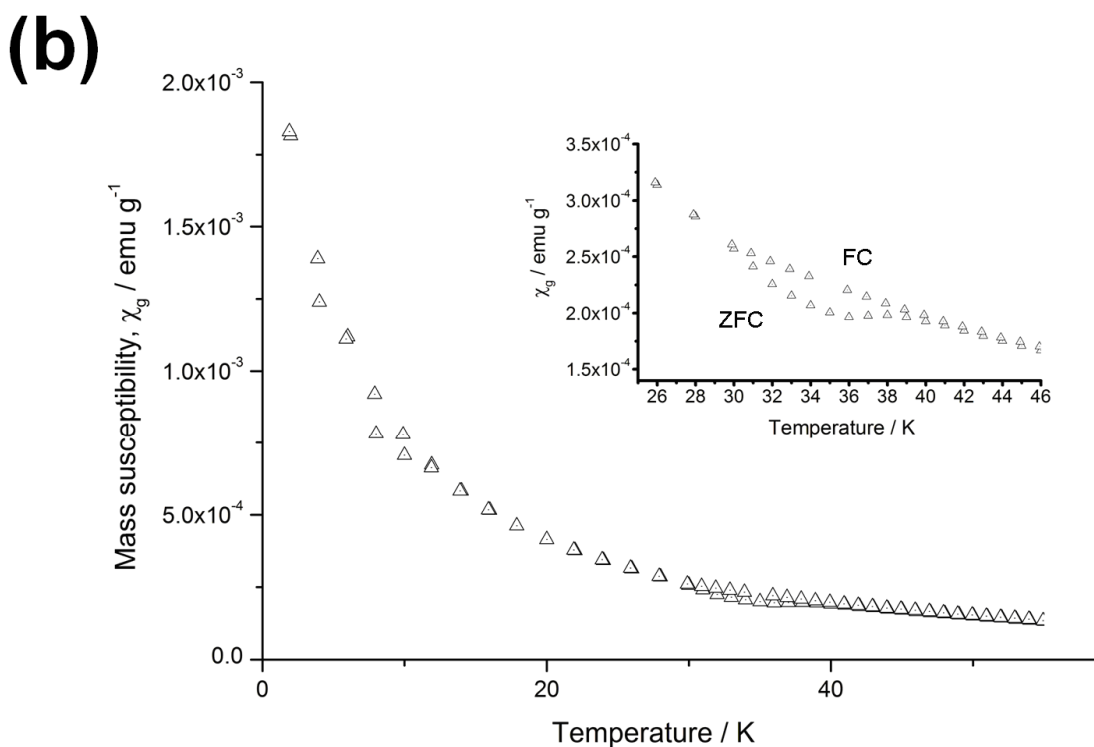
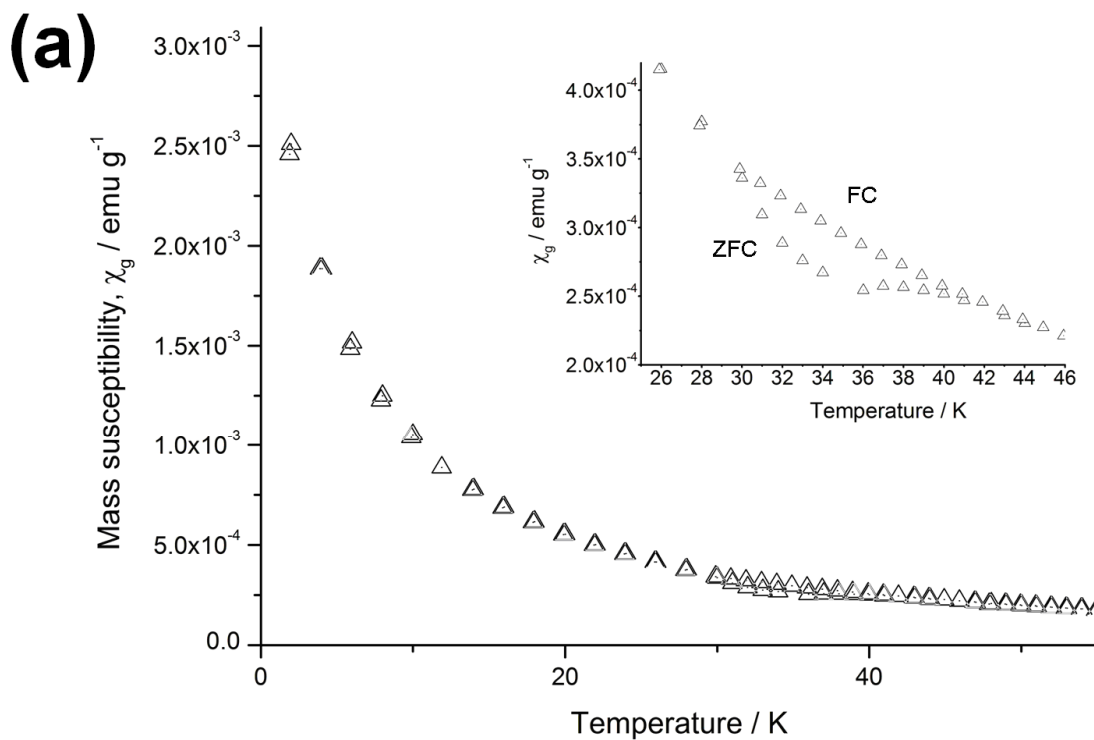


Fig 3.11 Plots of mass susceptibility against temperature (0-55 K) for: (a) 14 (b) 15. The inset in each case is a magnification between 25-46 K to show clearly the two transitions.

It is stated in previous studies that the magnetic transition temperatures are sensitive to stoichiometry and surface effects, i.e. the dimensions of the NiS<sub>2</sub> cubes could have an effect upon their magnetic properties. <sup>[161,162]</sup> The precise stoichiometry of (15) is unknown but the particle size is an order of magnitude greater than (14) and it could be presumed that surface/size effects play a role in their physical properties. The second transition occurs at 30 K (weak ferromagnetic - T<sub>N2</sub>) in both samples but the first transition (antiferromagnetic - T<sub>N1</sub>) occurs at a higher temperature for (14). This coupled with a greater magnitude in the mass susceptibility for (14) supports the assumption that it has stronger ferromagnetic interactions, which may originate from the decrease in cube size. This premise concurs with previous studies where cleaved cubic and dodecahedral crystals of NiS<sub>2</sub> (with a surface:bulk ratio ten times that of the original crystals) exhibited higher susceptibilities and enhanced weak ferromagnetism between the two transition temperatures. <sup>[161]</sup>

#### 3.4.2.3 100nm nickel layer thickness

Table 3.8 details the samples with a 100nm layer of nickel and their corresponding PXD analysis is given in Fig 3.12. Crystallographic results reveal that 100 nm thick nickel samples tend to follow the same trend as that of 50 nm samples with a few notable exceptions in the formation of NiS<sub>2</sub>. For a 50 nm layer, NiS<sub>2</sub> first appears around 550 °C. For 100 nm layers, weak, broad reflections of NiS<sub>2</sub> first become evident at 250 °C (16). These sharpen and intensify with increasing temperature. This type of behaviour can be characteristic of nanocrystalline particles. This assumption is partly confirmed from the supporting SEM micrographs (Fig 3.13). Application of the Scherrer<sup>[163]</sup> equation to sample (16) (using a standard bulk sample as a comparison) calculated an average crystallite size as approximately 65 nm. Although this makes the normal assumption that the particle size and the size of the smallest coherent scattering domain are equivalent.

Table 3.8 Reactions at different temperatures with 100nm of nickel

Sample No.	Powder reactants; mass/g	Ni film thickness/ nm	Initial T /°C	Ramp rate /°C h <sup>-1</sup>	Reaction T /°C
16	S; 0.01	100	100	125	250
17	S; 0.01	100	150	125	350
18	S; 0.01	100	225	125	450
19	S; 0.01	100	250	125	550
20	S; 0.01	100	300	200	650
21	S; 0.01	100	300	200	750

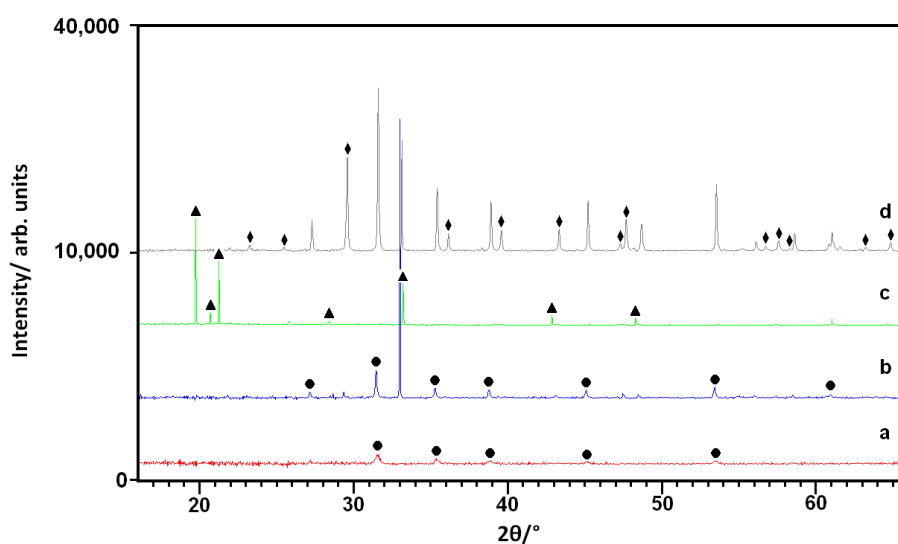


Fig 3.12 PXD patterns of samples prepared at: (a) 250 °C (16), (b) 350 °C (17), (c) 450 °C (18), (d) 550 °C (19). Filled circles represent reflections corresponding to NiS<sub>2</sub>; filled diamonds denote reflections present in the underlying silica substrate. Filled triangles represent reflections from the unidentified phases.

A comparison of the reflections of (18) to (5) and (11) once again reveal a number of coincident peaks (Table 3.9). By these means it can be deduced that (18) produces three phases; Ni<sub>3</sub>S<sub>4</sub>, Ni<sub>9</sub>S<sub>8</sub> and the same unidentified phase seen in samples, 4, 5, 10 and 11.

Table 3.9 Comparisons of reflections between samples 18, 4, 5, 10 and 11.

(18) (2 $\theta$ )	(5) (2 $\theta$ ) ( $\Delta\pm 2\theta$ )	(11) (2 $\theta$ ) ( $\Delta\pm 2\theta$ )	Match (2 $\theta$ ) ( $\Delta\pm 2\theta$ )
14.138	-	-	Unknown
15.457	-	-	Ni <sub>9</sub> S <sub>8</sub>
19.621	19.417 (-0.204)	19.597 (-0.024)	Unknown
20.547	20.519 (-0.028)	20.936 (-0.389)	Unknown
21.107	-	-	Ni <sub>9</sub> S <sub>8</sub> /Ni <sub>3</sub> S <sub>2</sub>
25.638	25.508 (-0.130)	25.486 (-0.152)	Unknown
28.243	28.136 (-0.107)	28.071 (-0.172)	Unknown
30.357	30.211 (-0.146)	30.162 (-0.195)	Ni <sub>3</sub> S <sub>2</sub>
31.161	-	-	Ni <sub>9</sub> S <sub>8</sub> /Ni <sub>3</sub> S <sub>2</sub>
33.048	33.061 (+0.013)	33.001 (-0.047)	Unknown
35.076	-	-	Ni <sub>9</sub> S <sub>8</sub>
41.588	-	-	Ni <sub>9</sub> S <sub>8</sub>
42.827	42.641 (-0.186)	42.758 (-0.069)	Unknown
49.970	-	-	Ni <sub>3</sub> S <sub>2</sub>
50.410	-	-	Ni <sub>3</sub> S <sub>2</sub>
52.475	-	-	Ni <sub>9</sub> S <sub>8</sub>
54.866	-	-	Ni <sub>3</sub> S <sub>2</sub>
55.967	-	-	Ni <sub>9</sub> S <sub>8</sub>

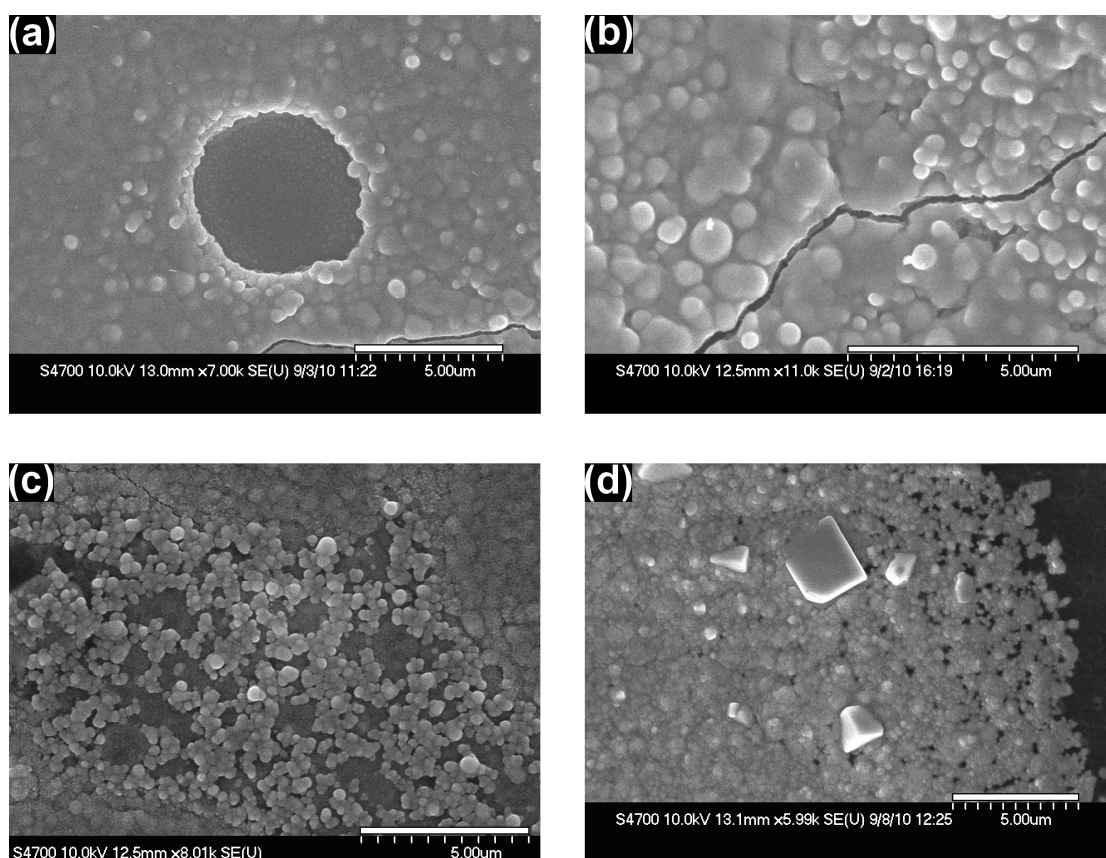


Fig 3.13 SEM micrographs of reactions of S with a 100 nm Ni layer on a SiO<sub>2</sub> substrate at: (a) 250 °C (16), (b) 350 °C (17), (c) 450 °C (18) (d) 650 °C (20).

It can be seen by comparing Fig 3.13 to Fig 3.9 that at low temperatures (below 450 °C) both layer thicknesses produce materials consisting of irregular films (Fig 9a-b) (16 and 17) and by 650 °C faceted cubes on the nano and micron scale are produced (Fig 3.9d) (20). A real contrast, however, is observed on closer inspection of samples synthesised over the temperature range of 450 - 550 °C. This contrast in sample structure at 450 °C (12 vs. 18) and at 550 °C (13 vs. 19) is illustrated in Fig 3.14. The thinner 50 nm layer produces a faceting of nanoparticles and the formation of cubes and cuboids at a lower reaction temperature (Fig 3.14 a and c) whereas the thicker 100 nm Ni layer favours sub-micron sphere like particles composed of agglomerations of smaller, near isotropic nanoparticles (Fig 3.14b and d). The spheres themselves have diameters of 200-300 nm, while the smaller particles of which they are composed measure approximately 20-50 nm across.

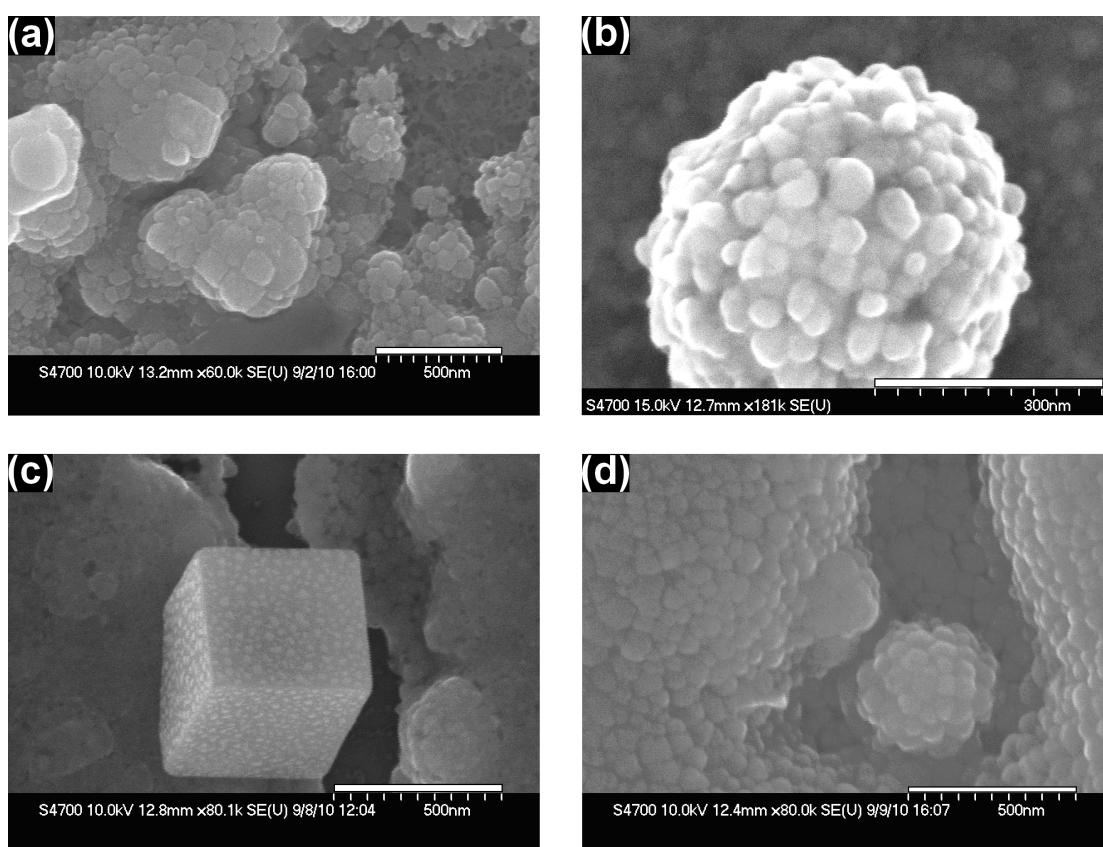


Fig 3.14 SEM micrographs at high magnification of (a) 450 °C, 50nm Ni (12), (b) 450 °C, 100nm (18), (c) 550 °C, 50nm Ni (13), (d) 550 °C, 100nm Ni (19).

EDX data for (18) and (19) yield 1:2 ratios of (Ni:S) implying that the spherical nanoparticles are also pyrite-structured nickel disulfide. This is supported by the corresponding PXD data (Fig 3.12d). Despite this, an increase in thickness would

appear to inhibit the growth rate of the NiS<sub>2</sub> cubes. There is some evidence however, that these smaller spherical particles do exist at lower temperature in the 50 nm Ni reactions (Fig 3.15).

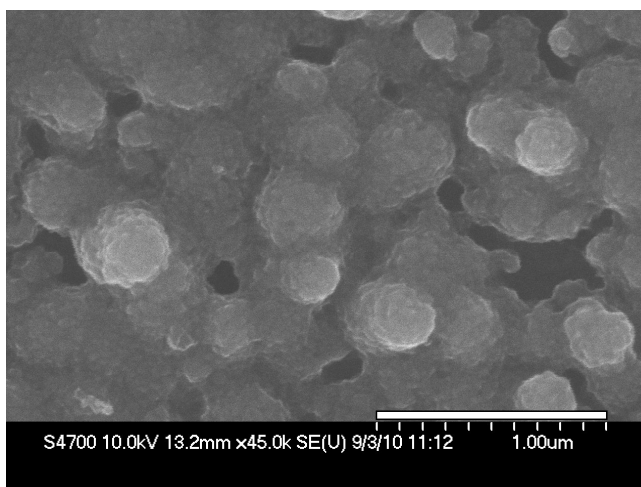


Fig 3.15 SEM Micrograph at high magnification of 350 °C, 50nm Ni (11) which shows evidence of spherical nanoparticles.

In addition both the spherical and cubic structures would appear to have the same ‘residue’ on their surface (Fig 3.16).

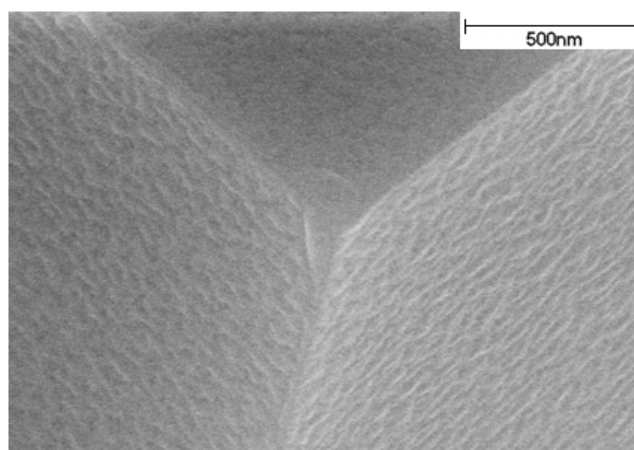


Fig 3.16 High resolution SEM micrograph of the typical topology of a pyrite-NiS<sub>2</sub> cube from sample (14).

This coverage could signify an excess of sulfur on the surface. Equally it could be interpreted as a “growth history” of the cubes from the spherical agglomerates. The latter theory is supported by EDX spot scans of the “mottling” features which show no deviation from a 1:2 (Ni:S) ratio. It is fair therefore to assume that these features are associated with the NiS<sub>2</sub> itself rather than excess sulfur.

### 3.4.3 Nickel powder and sulfur reactions

A surface assisted chemical vapour transport (SACVT) synthesis was performed to investigate the effects of physically adding and mixing nickel powder to the sulfur at the end of the tube (Fig 3.2, Section I). A 1:2 ratio (Ni:S) (0.018:0.01g) was heated under the same conditions as samples (14) and (20) (Table 3.2 and 3.4). In addition, for this particular experiment, a sapphire substrate was used rather than silica (due to constraints on availability). From earlier experiments, using SiN, Al<sub>2</sub>O<sub>3</sub> and SiO<sub>2</sub> substrates it had already been confirmed that under the same reaction conditions, a difference in support has no effect on reaction outcome. The reaction produced differences in both product phases and morphology. PXD revealed that these conditions promote the nickel rich compound heazlewoodite (Ni<sub>3</sub>S<sub>2</sub>) (Fig 3.17). An indexing of the reflections corresponding to Ni<sub>3</sub>S<sub>2</sub> gave values;  $a = 5.74(3) \text{ \AA}$   $c = 7.11(7) \text{ \AA}$  (rhombohedral, space group R32). These are in fairly good agreement with reported literature values ( $a = 5.7311 \text{ \AA}$  and  $c = 7.1188 \text{ \AA}$ ).<sup>[164]</sup>

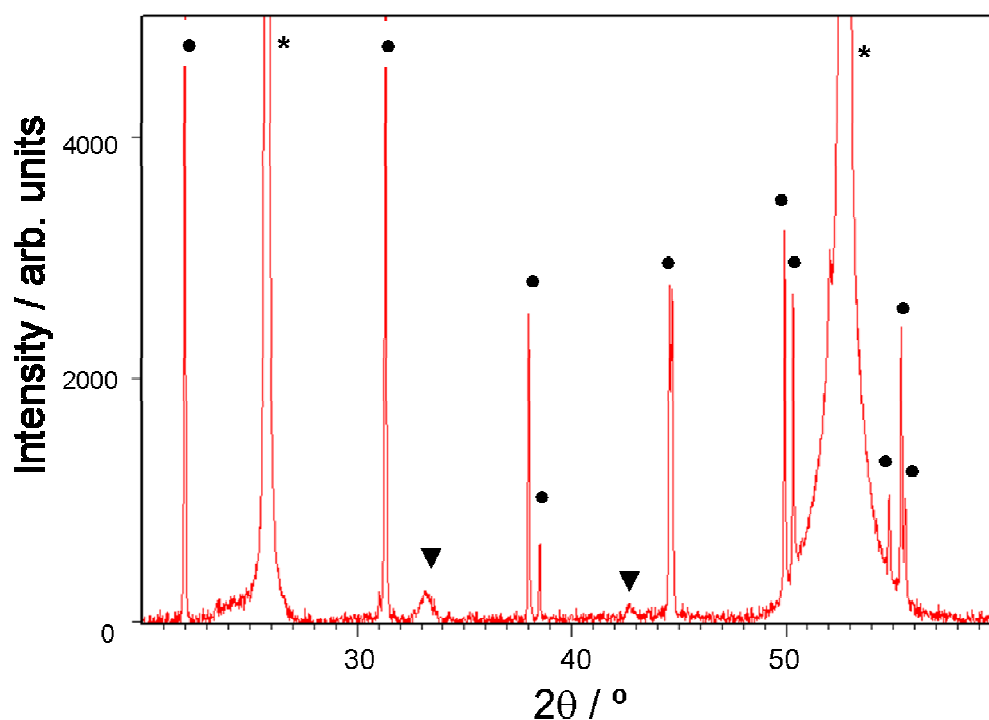


Fig 3.17 PXD pattern of the sample prepared from nickel and sulfur powders. Filled circles represent reflections corresponding to Ni<sub>3</sub>S<sub>2</sub> filled triangles indicate possible excess sulfur and asterisks denote reflections from the sapphire substrate.

The morphology of this product is no longer the cubic crystallites typical of previous NiS<sub>2</sub> samples, but one of spherical particles whose size varies from 10 μm (Fig 3.18a) in diameter to smaller micron sized equivalents. (Fig 3.18b)

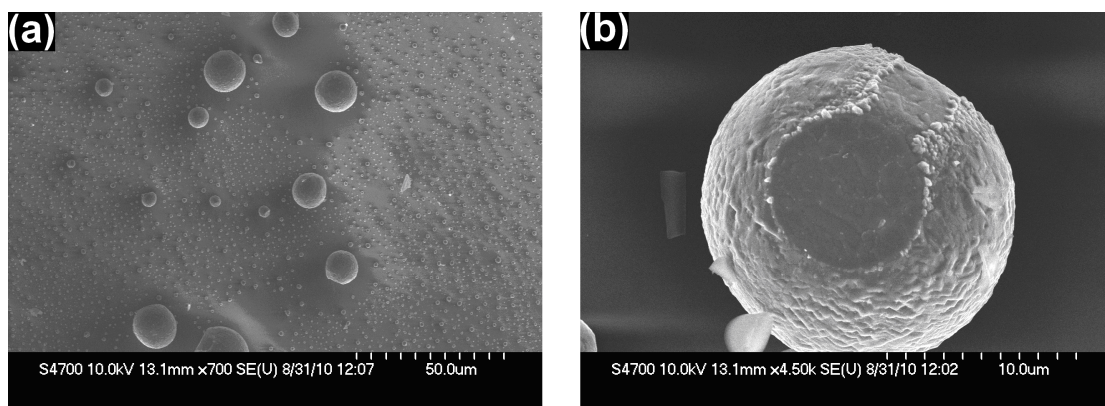


Fig 3.18 SEM micrographs of the sample prepared from nickel and sulfur powders, (a) at low magnification showing size distribution, (b) illustrates surface detail of a larger sphere.

These structures are unique in comparison to other instances in the literature of Ni<sub>3</sub>S<sub>2</sub>. Previous realisations have centred on using solution/solvothermal methods. Examples include “echinus-like” structures templated by PVP [165], sponge like porous structures when templated with L-cysteine [166] or nanowires produced from confined growth between gaps of SiO<sub>2</sub> nanospheres. [146] The outcome of this reaction is that the resultant phase is more nickel rich than the corresponding reaction with solely sulfur (14). This suggests that the Ni deposited on the substrate is reacting with nickel present in the chalcogenide vapour i.e. the sulfur functions as a carrier gas and produces a Ni-S gaseous phase. By further experimentation with the stoichiometric ratios of the reactants one should be able to gain a greater understanding of how to control stoichiometry, structure and morphology of the final product by manipulating the identity and composition of the gaseous phase.

### 3.4.4 Trial reactions with patterned substrates

A complementary experiment was performed to investigate the feasibility of a selective reaction between the deposited metal layer and chalcogen, sample 21. A patterned substrate was designed with an array of rectangles of nickel each (5 mm x 2 mm) on a silica support (Fig 3.19). The substrate was reacted under the same conditions as samples (8), (14) and (20) (Table 3.10).

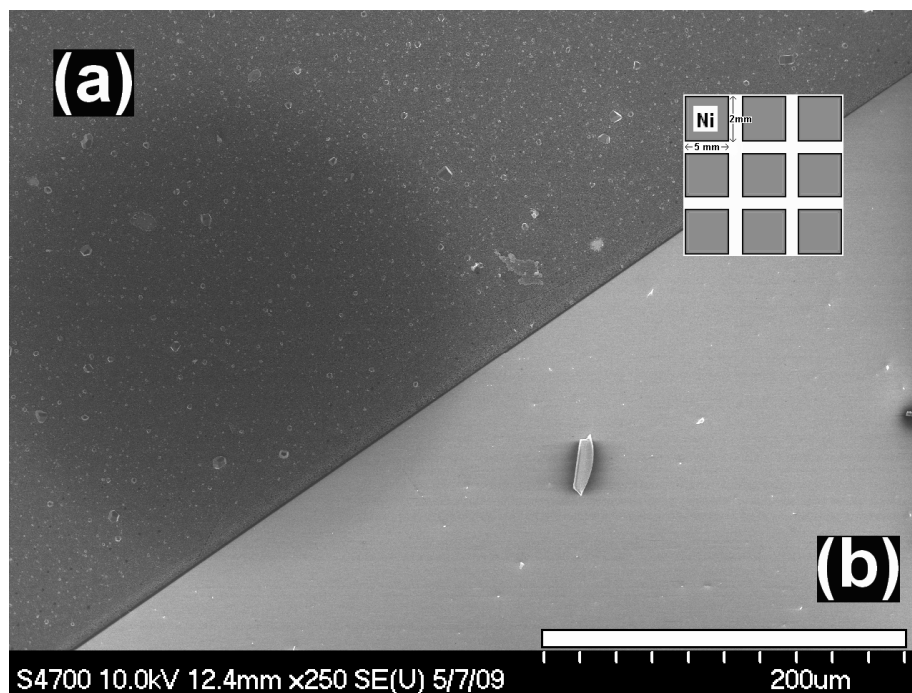


Fig 3.19, Low magnification SEM micrograph of patterned substrate (a) reacted nickel layer (b) underlying silica support. Inset: crude outline of the patterned substrate; shaded squares represent nickel islands and white grid the silica support.

Table 3.10 Reaction conditions for sample 21

Sample No.	Powder reactants; mass /g	Ni film thickness /nm	Initial T /°C	Ramp rate /°C h <sup>-1</sup>	Reaction T /°C
21	S; 0.01g	50nm	300	200	650

From the SEM results below (Fig 3.20) it can be seen that the sulfur does indeed react selectively with the metal leaving a distinct barrier between the two surfaces (Fig 3.20b). The few isolated particles scattered on the surface of the silica by EDX were assigned to sulfur and are therefore likely to be resultant

fragments from the chalcogen vapour. PXD of the patterned substrate revealed a match to NiS<sub>2</sub> (Fig 3.21). The reflections indexed to  $a = b = c = 5.661(8)$  Å (cubic, space group Pa $\bar{3}$ ) and are in good agreement with the literature values ( $a = b = c = 5.6873$  Å).<sup>[160]</sup> This is the same phase exhibited by samples 14 and 20 but without the same cubic morphology. Instead the metal rectangles are covered in a layer of submicron sized particles EDX of which gave average values of (At% 35.31 % Ni 64.69% S  $\pm$  1.70), values, which match well to 1:2 ratio nickel to sulfur. If this sample was annealed (to increase particle size) a more cubic like morphology could be perhaps obtained.

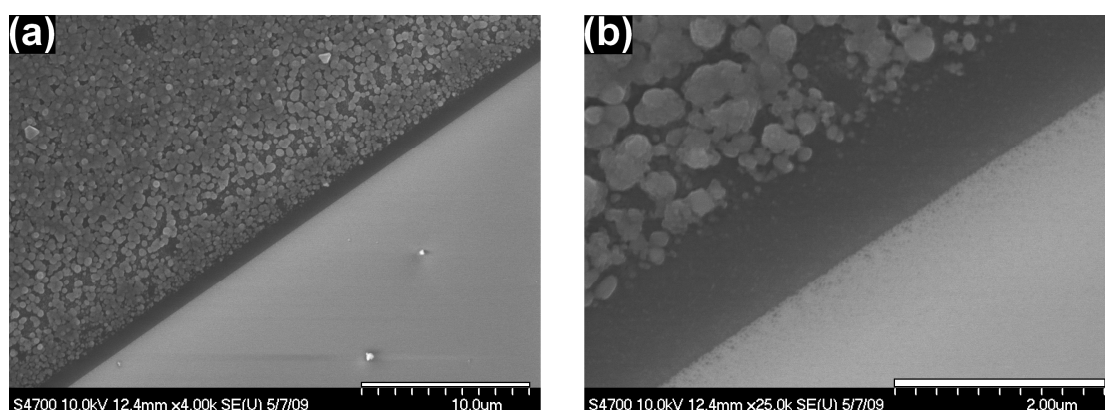


Fig 3.20, SEM micrographs, showing morphology of nickel layer and sharp separation between the metal layer and the silica.

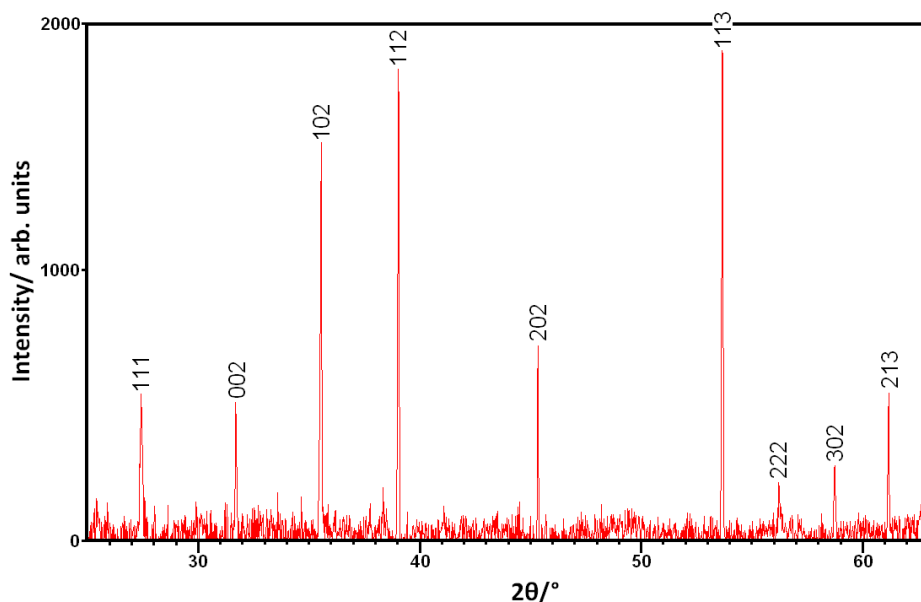


Fig 3.21 PXD of a sample 21, indexed reflections correspond to pyrite - NiS<sub>2</sub>

This is a very important result. Further designs to form patterned metal surfaces could be successful in creating separated individual nanostructures on the substrate surface. This would be advantageous to develop since it helps towards solving the dilemma of manipulating nanostructures once they have been produced. For example, the measurement of electrical resistivity on individual nanostructures is a notable challenge. If one can pre-position structures, i.e. over electrical contacts, then one could in theory move from synthesis to analysis in one step.

### 3.5 Discussion and conclusions

It is difficult to determine from the limited information available, exactly by what means the Ni-S nanostructures form. A typical 1 cm x 2 cm wafer has around  $3.75 \times 10^{-5}$ g of Ni metal on its surface. According to the nickel-sulfur binary phase diagram, nickel disulfide exists from 56-66 At % sulfur. <sup>[159]</sup> If the total amount of sulfur (0.01g) were to fully react with the metal, then the Ni:S molar ratio would be c.a. 1:2500. It is evident post-reaction, however, that sulfur remains not only in its initial starting position but often there is a significant mass of transported sulfur at the opposite end of the ampoule. It is therefore safe to assume from both these observations that not all the sulfur reacts with the metal. For this particular reaction set up if one were to use a precise 1:2 ratio of Ni:S (and thus a much lower mass of sulfur powder) it is unlikely that at a pressure of 3 mbar there would be enough chalcogen present to form a rich enough vapour to sufficiently react with the metal. Conversely, too great a mass of chalcogen can be equally detrimental to crystal growth as has been seen with samples 1 - 3.

It can be supposed that the processes described in the above text are more complex than the three-step vapour transport process described in section (1.2.2). It is likely that the reaction occurs after transport of the chalcogen to the surface of the substrate, likely by a VS or VLS type mechanism and therefore the temperature of the substrate is also a factor to consider. A box furnace approximately uniformly heats the reaction vessel and so the substrate will be at the same temperature as the reactants. It would be interesting to introduce a

temperature gradient and see how a difference in precise substrate temperatures can effect the reaction outcome.

A point of interest for these reactions is the low temperature formation of NiS<sub>2</sub> unique to the 100 nm films. (250 °C; 16). Pyrite-NiS<sub>2</sub> does not become evident for the 25 nm and 50 nm films until 450 °C (6 and 12). Previous studies on the deposition of NiS<sub>2</sub> films have demonstrated that polycrystalline NiS<sub>2</sub> can be grown at 350 °C. [167] It is not until higher temperatures however (550 °C and above) that the NiS<sub>2</sub> samples show the first signs of faceting and formation of cubes with the exception of the 25 nm layers where no faceting occurs at all. It could be theorised that that a VLS growth process is likely since the Ni-S binary eutectic lies at 637 °C. [159] Such a process has been seen before in the growth of WS<sub>2</sub> films on a Ni surface at 650 °C in the presence of NiS<sub>x</sub> where the precursor to sulfide growth is the fragmentation of an Ni substrate (typically 5-50 nm thickness) into islands. [142] Therefore it is possible that sulfur vapour reacts with islands of NiS<sub>x</sub> liquid to form solid NiS<sub>2</sub>, which crystallises from the melt. This latter growth process is a viable theory when one considers that single crystals of NiS<sub>2</sub> can be grown at temperatures between 700 and 750 °C by a reaction of NiS with sulfur vapour. [168] In turn this could explain the absence of faceted structures at higher temperatures with a 25 nm layer of nickel despite their presence for both 50 nm and 100 nm. Perhaps 25 nm nickel does not provide enough metal to produce the proposed NiS<sub>x</sub> island formation which in effect inhibits the formation of a cubic morphology.

In regards to the physical properties, the observed magnetism was shown to be size (surface: bulk ratio) dependent. Samples grown at 650 °C (1) and 750 °C (2) produced profiles which revealed a divergence in the ZFC and FC at approximately the 25 - 46 K range (Fig 3.11). Although ostensibly the samples display Curie-Weiss type behaviour beyond the transition temperatures at 50 K. This is in accordance with the literature which has described NiS<sub>2</sub> exhibiting temperature dependent paramagnetism of the Curie-Weiss law type in the range of 4 - 900 K. [160] Data collected under zero field cooled (ZFC) and field cooled (FC) conditions displayed a clear divergence in the ZFC and FC data at approximately 40 K, which resolves approaching 30 K. The nanoscaled structures of 1 exhibited a mass susceptibility higher than that of the micro structures of 2

and the antiferromagnetic transition occurs at a higher temperature. These observations support the suggestion that surface/size ratio can have an overall effect on the magnetic properties of nickel disulfide.

There is a great deal more synthetic and characterisation research that could be conducted to help gain an understanding of the Ni-S system. This could involve simple methods such as quenching reactions at pre-determined stages to help analyse the development of composition and structure and developing more challenging synthetic set-ups; establishing temperature gradients across a reaction vessel or the substrate itself. More importantly, if a suitable scheme can be devised to remove structures from the substrate intact (of appropriate thickness), TEM coupled with SAED could also play a considerable role in further elucidating the growth mechanism of the nanometric Ni-S phases.

## 4. The binary titanium - sulfur system

### 4.1 Introduction

In Chapter 3 it has been shown that Surface Assisted Chemical Vapour Transport (SACVT) can be exploited to grow structures of nickel disulfide ( $\text{NiS}_2$ ). The following chapter continues this study but adapts and develops this technique for the titanium - sulfur system. Similar themes are discussed; the evolution of growth with regards to temperature and reactant stoichiometry and the structure and physical properties of the resultant phases are investigated with a combination of SEM, SQUID, TEM and Raman spectroscopy. It became clear from an early stage that products resembling either titanium disulfide ( $\text{TiS}_2$ ) or titanium trisulfide ( $\text{TiS}_3$ ) were produced and as a result this chapter is structured around these two systems.

The experimental setup employed in this work is not so dissimilar to studies conducted within the research group on  $\text{TaS}_2$  wires, i.e. a metal foil is reacted with powdered chalcogen under anaerobic chemical vapour deposition (CVD) conditions. <sup>[140]</sup> The possibility to grow nanostructures in such a fashion suggested it was a suitable system to try an experimental setup analogous to that of section (3.2).

Previous examples of  $\text{TiS}_2$  nanomaterials have been realised by precursor reduction-sulfurisation techniques such as in the case of the above mentioned  $\text{TiS}_2$  nanotubes where a  $\text{TiCl}_4$  precursor is reacted with a mix of  $\text{H}_2\text{S}$  and  $\text{H}_2$  gas. <sup>[169]</sup> It is in the interest of this research to simplify reaction conditions and where possible avoid the use of deleterious chemicals such as  $\text{H}_2\text{S}$  gas. Therefore trials with elemental sulfur as a source of chalcogen and a metal substrate as opposed to a halogenated precursor were investigated. There are currently only a small number of instances where CVD or CVT techniques have been successfully adopted to synthesise nano- $\text{TiS}_2$  but encouragingly they have produced some startlingly unique results, some of which allude to the unusual plethora of structures later discovered in the course of this research. Examples include dendritic crystals and flower-like formations, <sup>[170-171]</sup> the latter of which have also been achieved by wet-chemical synthesis. <sup>[172]</sup> The dendritic crystals

[170] are formed from stoichiometric quantities of the powdered elements whereas the nanoflower arrays [171] require the addition of a titanium foil substrate to enable growth. Investigations have identified optimum temperatures and reaction times to achieve the best results for consistent morphology, crystallinity and purity of phase. More specifically, there is an example of TiS<sub>2</sub> whiskers being successfully grown from a nickel-coated silica wafer. [173] The substrate was placed between separate sources of elemental sulfur and titanium and reacted under a stream of argon. It is reported that the nickel functions as a catalyst which mediates the growth of the whiskers via a vapour liquid solid (VLS) mechanism. This leads to the growth of TiS<sub>2</sub> whiskers with diameters ranging from 100 - 200 nm.

#### 4.1.1 Titanium disulfide

TiS<sub>2</sub> has a layered CdI<sub>2</sub>-type structure with close-packed Ti atoms octahedrally coordinated to adjacent sulfur atoms (Fig 4.1). The octahedral units form layers of chalcogen-metal-chalcogen sandwiches with weak van der Waals forces between them. For a more detailed analysis of layered transition metal dichalcogenides see section (1.4.1). [41] The weak bonding results in a mobility between the TiS<sub>2</sub> layers, allowing them to slide over one another, very similar to that of graphite. (Fig 4.2) This signifies the structure is an ideal candidate for intercalation and for years titanium disulfide (TiS<sub>2</sub>) has been extensively studied as a candidate for host intercalation and investigations subsequently carried out on the many resultant properties which are exhibited with different host-species. [174-181] This analysis has now expanded into the nano-regime. For example, TiS<sub>2</sub> nanotubes with inner diameters of 10 nm and lengths up to 5 μm have been investigated for both their hydrogen storage and lithium intercalation capabilities. [182-183]

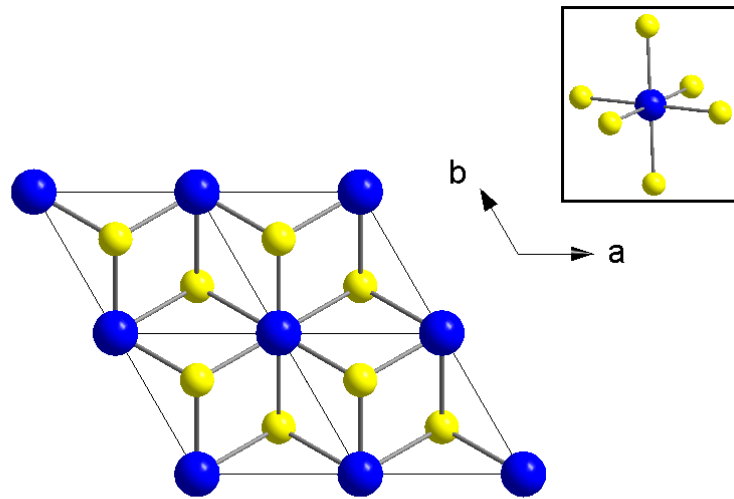


Fig 4.1 Structure of titanium disulfide, blue atoms represent titanium, yellow sulfur. The schematic is projected down the c-axis showing the hexagonal close packing of the titanium layers. Inset: octahedral coordination of the titanium atom to six sulfur atoms.

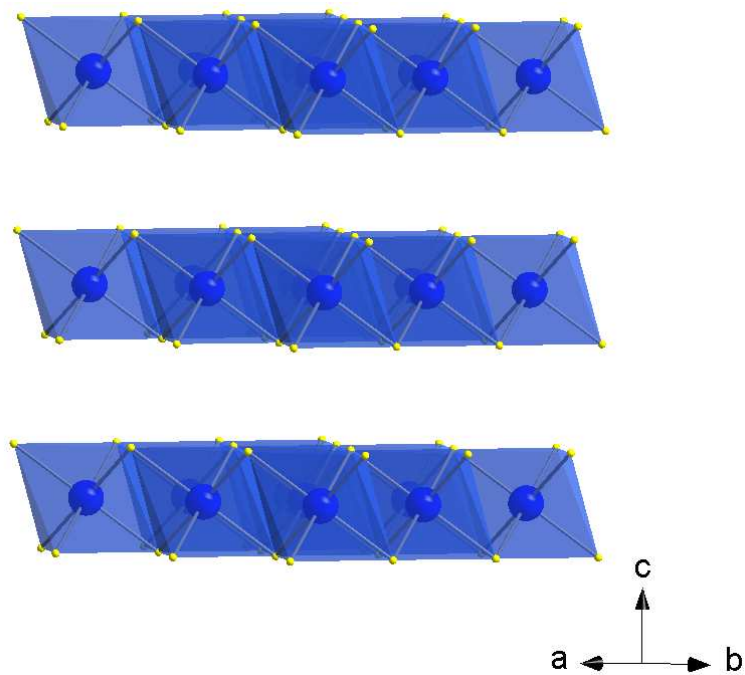


Fig 4.2 Schematic projected along the ab plane showing the two-dimensional layered structure of  $\text{TiS}_2$  with the layers held together along the c direction by weak van der Waals forces.

#### 4.1.2 Titanium trisulfide

TiS<sub>3</sub> on the other hand has been relatively unexplored since original work which investigated its crystal and electronic structure. [83,45] TiS<sub>3</sub> forms a monoclinic structure (space group P2<sub>1</sub>/m) and is iso-structural with ZrSe<sub>3</sub> - a compound considered representative of many of the group IV trichalcogenides. Like ZrSe<sub>3</sub> it contains infinite chains of distorted trigonal metal-chalcogen prisms aligned parallel to the monoclinic *b*-axis. (Fig 4.3) It is semiconducting with a band gap of 0.9 eV.

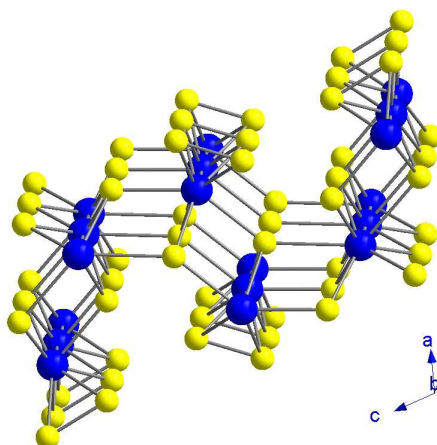


Fig 4.3 Structure of titanium trisulfide, Blue atoms represent titanium, yellow sulfur. Schematic is projected along the *b*-axis showing the infinite chains of the distorted trigonal prisms.

TiS<sub>3</sub> has in the past been synthesised on the nano-scale with previous studies producing bundles of TiS<sub>3</sub>-nanobelts and ribbons which demonstrate both high tensile strength and field emission properties. [184-185]

The purpose of this chapter is to show that nanostructures of TiS<sub>2</sub> and TiS<sub>3</sub> can be synthesised via a surface assisted chemical vapour transport (SACVT) method in which sulfur vapour generated *in situ* is reacted with titanium coated silica substrates. Systematic studies demonstrate the effect of the reactant ratio, metal layer thickness and reaction temperature on the synthesis and growth process. The evolution of growth with temperature and reactant quantity are discussed and analysed with SEM, PXD, SQUID and TEM.

## 4.2 Experimental

In Chapter 3 it has been shown that a thin metal surface can be employed successfully as a growth medium in modified chemical vapour transport CVT and CVD reactions. Analogous to the nickel-sulfur system, investigations of titanium-sulfur were approached as a function of temperature which enabled the production of various titanium-sulfur compositions and morphologies.

A similar experimental set up was employed for synthesis as described in section (3.2) but employing Ti thin films rather than Ni (Fig 4.4) and with the addition of titanium powder to the chalcogen for the majority of the reactions.

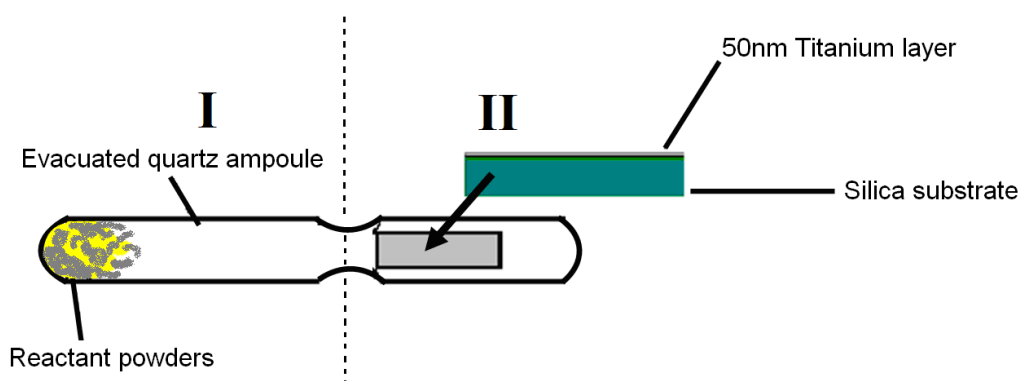


Fig 4.4 Typical experimental set-up. Titanium coated silica substrate and sulfur/titanium powder are located on opposite ends of an evacuated silica ampoule (sections II and I respectively)

Pre-determined amounts of sulfur and titanium powder were placed in one end of the silica ampoule prior to forming the constriction. The titanium coated substrate of 50 nm layer thickness (no variation in thickness was investigated) and typically of around 2 cm<sup>2</sup> in area was then placed in the opposite end of the silica ampoule and the vessel sealed under vacuum to a pressure of 3 mbar. The ampoules were heated in a box furnace to a set reaction temperature for varying amounts of time. The temperature was increased at 200 °C/h. Once reactions were complete, reaction tubes were either quenched in air or allowed to cool in the furnace overnight. Unless stated otherwise reactions used a stoichiometric 1:2 ratio of titanium to sulfur

(0.014g : 0.02 g ). In two alternative reactions, a higher ratio of titanium to sulfur was investigated; 1:3 (0.014g : 0.03g) and 1:4 (0.014g : 0.04g). All other conditions were kept identical to the corresponding 1:2 ratio reactions. Once again experiments typically produced dark coloured films with an estimated yield of around 0.5-2 mg.

#### 4.3 Characterisation

Products were retained on the substrate for analysis unless otherwise noted. Powder X-ray diffraction (PXD) analysis was performed using a PANalytical X'pert PRO MPD powder diffractometer in flat plate geometry. Samples were loaded onto a flat glass plate and secured with double sided sticky tape. Diffraction data were typically collected for  $5^\circ \leq 2\theta \leq 85^\circ$  with a  $0.017^\circ$  step size with scan times of 1-12 h. The sample displacement error was accounted for by measuring the offset of a standard and then using Highscore software to correct sample scans. Small sample volumes required that PXD analysis allowed for the high intensity reflections from the underlying silica substrate. Alternative methods of loading samples were attempted to try and reduce or remove substrate effects but best results were obtained from the method described above and characterisation of unique sample reflections was possible via this method. Diffraction data were compared to patterns in the ICDD (JCPDS) powder diffraction file (PDF) using the PANalytical High Score Plus software package. Indexing was achieved using the DICVOL software package <sup>[127]</sup> and least squares cell parameter refinement.

Scanning electron microscopy (SEM) was performed using two instruments; a Philips XL30 ESEM and Hitachi S4700 cold field emission gun SEM. Typically, samples were loaded onto aluminium stubs using adhesive carbon tabs and run in high vacuum mode with an applied accelerating voltage of 10 kV and a working distance of 12.5 mm for imaging and 10 kV and a working distance of 10mm for energy dispersive X-ray analysis, (EDX). EDX analysis was performed within the Philips instrument using an Oxford instruments 7200 EDX spectrometer in order to determine elemental compositions (which can be obtained with accuracy for elements of atomic number from carbon upwards). Transmission electron microscopy was performed using a FEI Tecnai T20 (FEI, Eindhoven, Netherlands)

operated at 200 kV acceleration voltage using a LaB<sub>6</sub> filament with images recorded using a Megaview II CCD camera (Olympus SIS GmbH, Garching, Germany). Conventional bright field and dark field diffraction contrast imaging was used in combination with selected area diffraction to characterise the nanostructure and relate this to the crystallography of the materials. Samples for SEM of sufficient thickness were prepared by depositing powder onto a carbon tab. Samples for TEM were prepared by sonicating the powders in ethanol and then pipetting drops of the suspension onto holey carbon film Cu grids.

Raman spectra were collected at room temperature using a Horiba LabRAM HR confocal microscope system with a 532 nm green laser. A hole aperture of 50  $\mu\text{m}$ , 600 gr/mm grating and a Synapse CCD detector were used.

Magnetic measurements were performed using a Quantum Design MPMS 5T SQUID magnetometer. Samples were loaded into gelatine capsules. Field cooled (FC) and zero field cooled (ZFC) measurements were performed with an applied field of 100 Oe between 2 - 300 K. All magnetic data were corrected for the gelatine capsules and for core diamagnetism.

## 4.4 Results and discussion

### 4.4.1 Trial reactions

Table 4.1 Reactions with solely chalcogen in section I

Sample No.	Powder reactants; mass (g)	Ti film thickness (nm)	Reaction T (°C)	Reaction time (hrs)	Rate of cooling (°C/h)
1	S; 0.01	50	650	60	50
2	S; 0.01	50	650	60	50

It was shown in the nickel - sulfur system (Chapter 3), that a stark variation in morphology occurred at a temperature range of 450 - 500 °C, culminating in the formation of individual nickel disulfide nanocubes at 650 °C. Therefore the initial study of the titanium-sulfur system employed an analogous set of parameters.

It became apparent after preliminary reactions (1-2) (Table 4.1) that the outcome was not as easy to control as for the nickel - sulfur system. Under these particular conditions, despite nano-particulates, the low coverage of the substrate surface and remaining chalcogen found in section I of the ampoule, indicated that the reaction had possibly not yet reached completion.

(Fig 4.5)

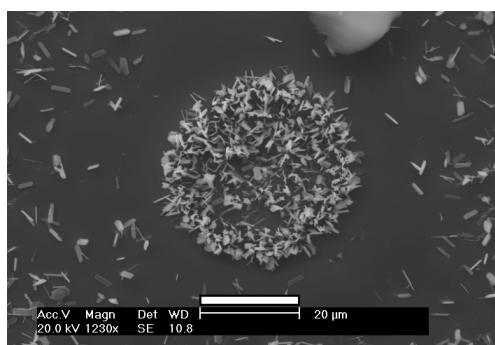


Fig 4.5 SEM micrograph (1) shows rod-like flakes broadly scattered across the substrate surface.

The nano-structures had average dimensions of 100-300 nm in width and ca. 2.5  $\mu\text{m}$  in length. EDX of (1) suggested that they are composed of  $\text{TiS}_2$  (At% 36% Ti, 64% S  $\pm$  1.79%). Sample 2 conversely produced no evidence of any reaction or growth occurring with only micro-particles of sulfur scattered on the metal surface. In the (SAPVT) method, the sulfur is transported as a reactive vapour and the resultant chalcogenide structures are formed post-transport on the surface of the substrate likely *via* a vapour-solid (VS) or VLS type mechanism. If one considers the rather small quantities of metal present; approximately  $3 \times 10^{-4}$  g or  $6.26 \times 10^{-6}$  moles Ti, which equates to roughly a 1 to 50 Ti : S mole ratio, even a very small change in the substrate surface, such as defects or impurities could have a profound influence on nucleation and growth behaviour. This leads to unpredictable outcomes for these SAPVT and related reactions. Therefore for the titanium-sulfur system other options were considered to improve reliability. A possible solution to this problem was to provide another source of the metal analogous to the approach adopted in the Ta-S system <sup>[140]</sup>. Subsequent reactions therefore combined stoichiometric ratios of titanium and sulfur powders in addition to the metal substrate.

#### 4.4.2 Metal chalcogen powder reactions

It was in the initial interests of the project to synthesise titanium disulfide and therefore a 1:2 ratio Ti:S was employed. Considering the small amount of metal on the substrate it was considered to be negligible to the overall stoichiometric ratio of the reactive powders. Conditions for samples 3-8 led to reproducible results. (Table 4.2)

Table 4.2 Reactions with a 1:2 ratio of powdered Ti:S

Sample No.	Powder reactants; mass (g)	Ti film thickness (nm)	Reaction T (°C)	Reaction time (hrs)	Rate of cooling T (°C/h)
3	Ti,S; 0.014, 0.02	50	650	60	50
4	Ti,S; 0.014, 0.02	50	300	24	Air Quenched
5	Ti,S; 0.014, 0.02	50	400	24	Air Quenched
6	Ti,S; 0.014, 0.02	50	500	24	Air Quenched
7	Ti,S; 0.014, 0.02	50	600	24	Air Quenched
8	Ti,S; 0.014, 0.02	50	700	24	Air Quenched

Sample 3 used the same set of parameters as samples 1 and 2 and produced a layer of irregular fused sub-micron particles (Fig 4.6a). EDX gave ratios for  $\text{TiS}_2$  (At% 35% Ti, 65% S  $\pm$  1.25%) and the corresponding PXD pattern provided a strong match to  $\text{TiS}_2$  (Fig 4.6b).

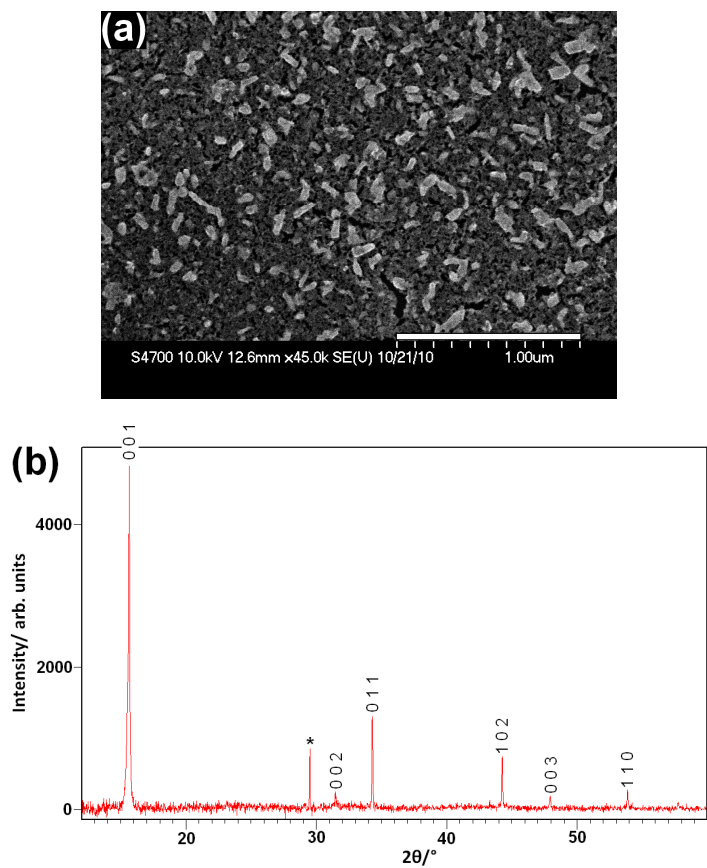


Fig 4.6 (a) SEM micrograph of sample 3 showing sub-micron fused particles (b) corresponding XRD pattern of 3. Labelled reflections match to TiS<sub>2</sub>. The peak marked with an asterisk originates from the underlying silica substrate.

The reflections were indexed to  $\text{TiS}_2$ , (hexagonal space group  $P\bar{3}m$ ) with  $a = 3.411(2) \text{ \AA}$   $c = 5.707(4) \text{ \AA}$ . A SQUID analysis of **3** between 2 - 100 K revealed temperature independent diamagnetism (Fig 4.7). Analysis observed a number of high scatter points resulting from the very low quantity of sample available. This made it difficult to achieve very clear patterns.

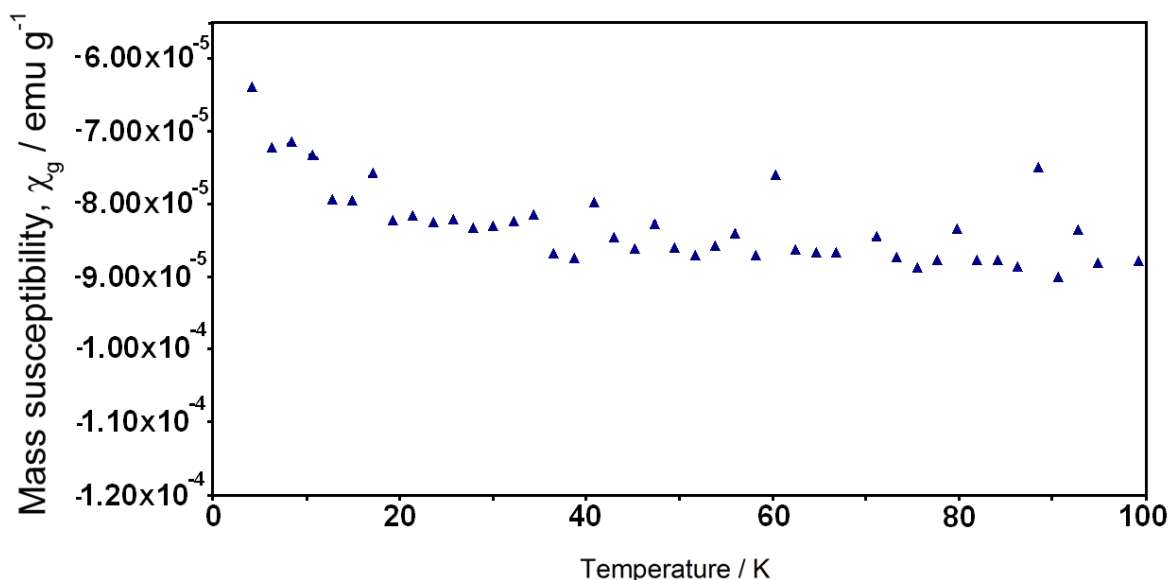


Fig 4.7 Plot of mass susceptibility against temperature (0 - 100 K) sample **3** showing its largely temperature independent weak diamagnetism.

Despite the fact that the synthesis conditions for sample **3** could reproducibly produce  $\text{TiS}_2$ , there was no evidence of nano-sized particulates. As a result, a systematic synthetic investigation was engaged as a function of both temperature and time to elucidate as to whether it was indeed possible to find conditions where nano-structures are favoured. Samples **4** to **8** are the most revealing of this study; at  $300 \text{ }^\circ\text{C}$  (**4**) only *S* was deposited on the substrate surface (Fig 4.8a). This was confirmed by EDX. But an increase in temperature ( $\geq 400 \text{ }^\circ\text{C}$ ) (samples **5-8**) uncovered a dramatic change in the morphology of the products (Fig 4.8b-e). Between  $400$  and  $500 \text{ }^\circ\text{C}$  (**5** and **6**) flower-like structures are formed. These are tentatively characterised as  $\text{TiS}_2$ , on the basis of EDX results (At% 35% Ti, 65% S  $\pm$  2.13%). Unfortunately it was not possible to achieve any suitable PXD patterns because, as was seen in Chapter 3, there was a tendency for product peaks to be swamped by the underlying silica substrate. A closer analysis by SEM showed the flowers to consist of thin veil-like sheets which at high magnification appeared to be electron transparent (Fig 4.9). A

SQUID analysis of sample (6) revealed temperature independent, weakly paramagnetic behaviour from 10 - 300 K with slight evidence of a Curie tail below 10 K (Fig 4.10). A reciprocal plot for (6) (Fig 4.11) also shows weak paramagnetism, most of which is temperature independent, it is likely that;

$$\chi = \chi_0 + \frac{C}{T - \theta} \quad (4.1)$$

where, the first term ( $\chi_0$ ) represents Pauli paramagnetism (temperature independent) and the second term represents Curie - Weiss (localised) magnetism. Where, (C) is the Curie constant and ( $\theta$ ) is the curie temperature  $T_c$ . Calculation of the Curie constant from the data given in Fig 4.11 produced a value of  $6.042 \text{ cm}^3 \text{ K mol}^{-1}$  and an effective magnetic moment of 0.5 B.M. This does not match well with the expected literature values.<sup>[186]</sup> Although it is reported that the effective magnetic moment is highly sensitive to the stoichiometry of  $\text{TiS}_2$  it is most likely due to the poor quality of the sample data owing to extremely low sample quantity.

Another increase in temperature ( $\geq 600^\circ\text{C}$ ) samples (7 and 8) and  $\text{TiS}_2$  becomes the primary phase. The PXD pattern of 7 indexes to  $\text{TiS}_2$  (hexagonal space group  $P\bar{3}m1$ ) with  $a = 3.405(7) \text{ \AA}$   $c = 5.699(4) \text{ \AA}$  whereas  $a = 3.414(7) \text{ \AA}$   $c = 5.702(8) \text{ \AA}$  for sample (8). (Fig 4.12) These values agree well with those parameters reported for bulk  $\text{TiS}_2$  -  $a = 3.407 \text{ \AA}$   $c = 5.695 \text{ \AA}$ .<sup>[187]</sup> A Rietveld refinement was performed on (8) and the results are given in (Fig 4.13) and Table (4.3). The data can be fitted to hexagonal structure (space group  $P\bar{3}m1$ ) of  $\text{TiS}_2$ . The interatomic distances Ti-S ( $2.342(5) \text{ \AA}$ ) and S-S ( $3.205(11) \text{ \AA}$ ) (Table 4.4), show a slight decrease from the previous structural model (Ti-S  $2.429 \text{ \AA}$  and S-S  $3.407 \text{ \AA}$  respectively)<sup>[187]</sup> which is a result from a reduction in the overall size of the unit cell. The X-ray pattern shows extreme preferred orientation leading to an enhancement of  $00l$  reflections in comparison to other reflection classes.

It should also be noted that although samples 7 and 8 have the same crystal structures (according to PXD), sample 7 to an extent retains the flower-like morphology whereas for (8) it is lost completely and replaced by platelet crystallites of around 5 - 10  $\mu\text{m}$  in size. (Fig 4.8e) Application of the Scherrer<sup>[163]</sup>

equation to samples (7) and (8) (using a standard bulk sample as a comparison) calculated an average crystallite size as approximately 80 nm for (7) and 220 nm for (8). Although this is just an approximation as noted previously the results show that particle size increases with increasing temperature and that that nanoscale particles are preferred at lower temperatures as might be expected.

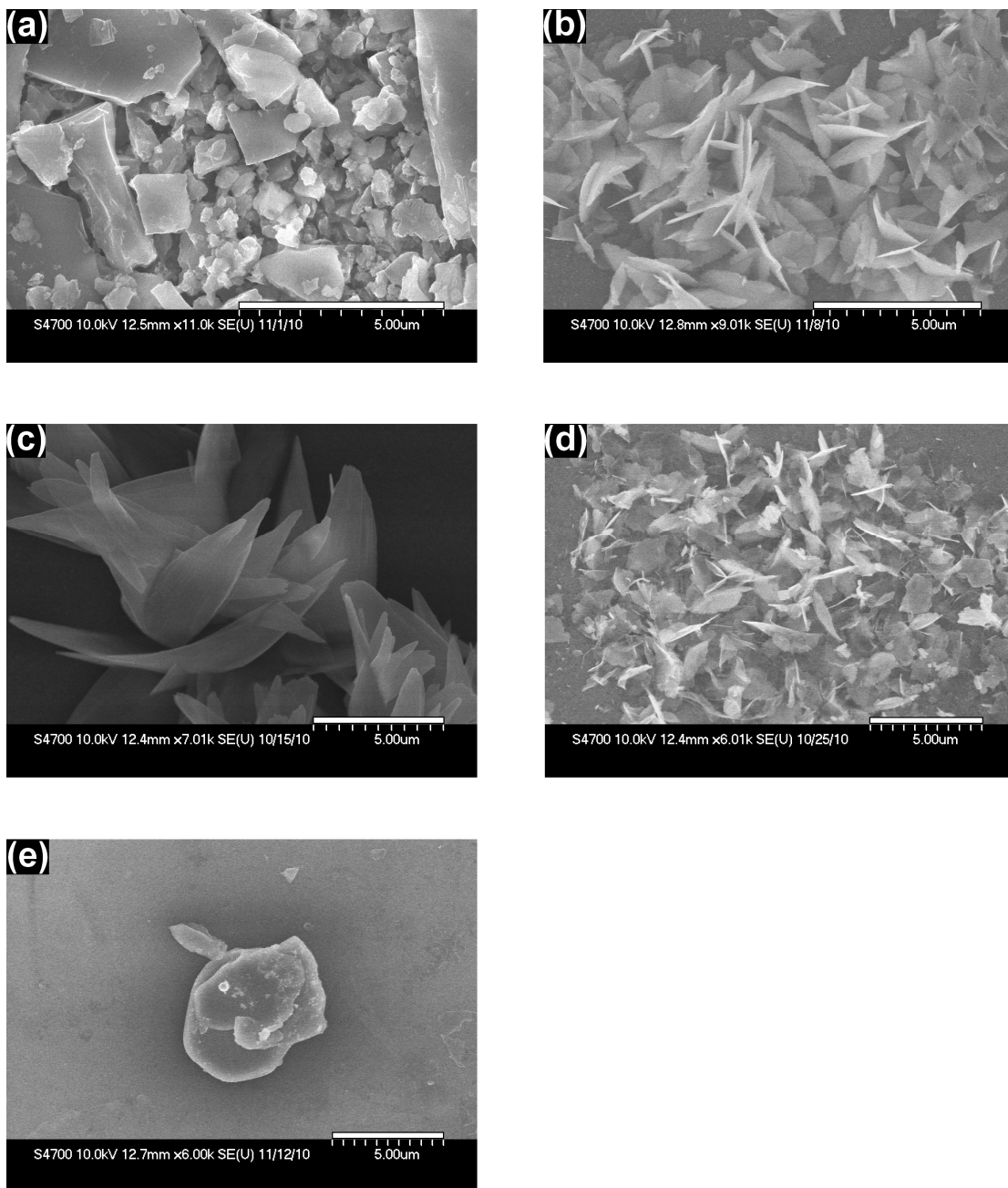


Fig 4.8 SEM micrographs of products from reactions over 24 hrs, quenched in air. (a) 300 °C (4) (b) 400 °C (5) (c) 500 °C (6) (d) 600 °C (7) (e) 700 °C (8)

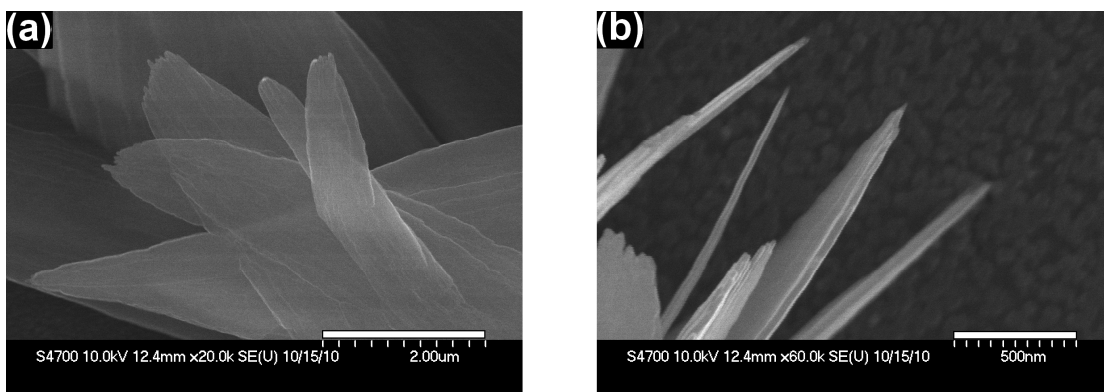


Fig 4.9 High magnification SEM micrographs of (6) which shows (a) the electron transparent sheets that constitute individual petals and (b) the thickness of the edges of those sheets.

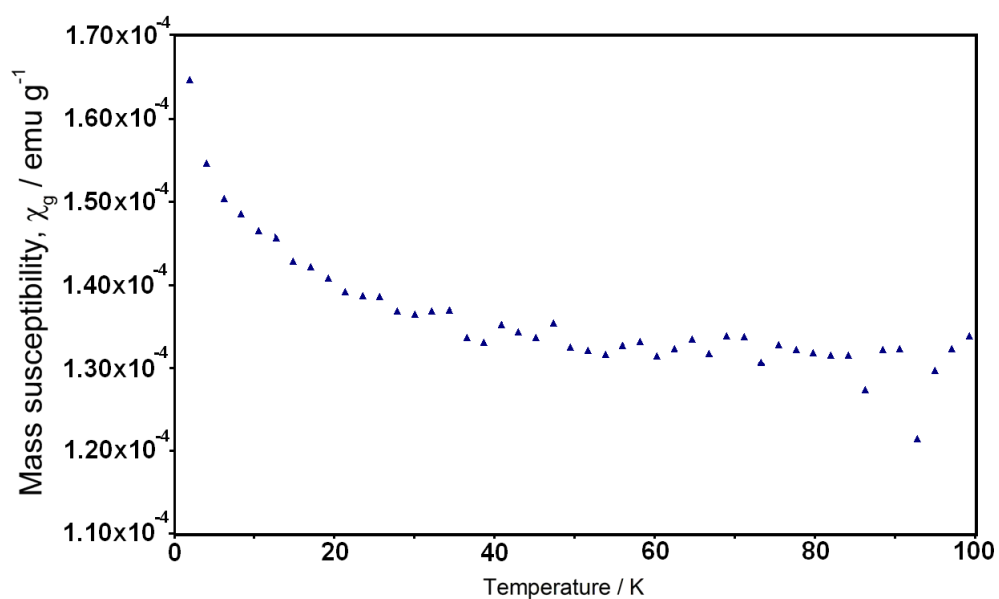


Fig 4.10 Plot of mass susceptibility against temperature (0 - 100 K) sample (6) showing its weakly paramagnetic behaviour.

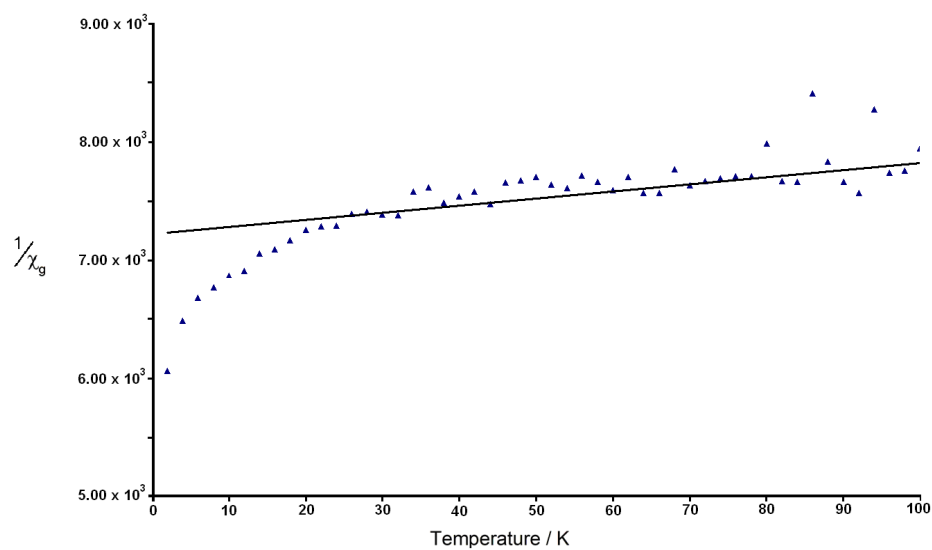


Fig 4.11 Curie-Weiss plot of (6)

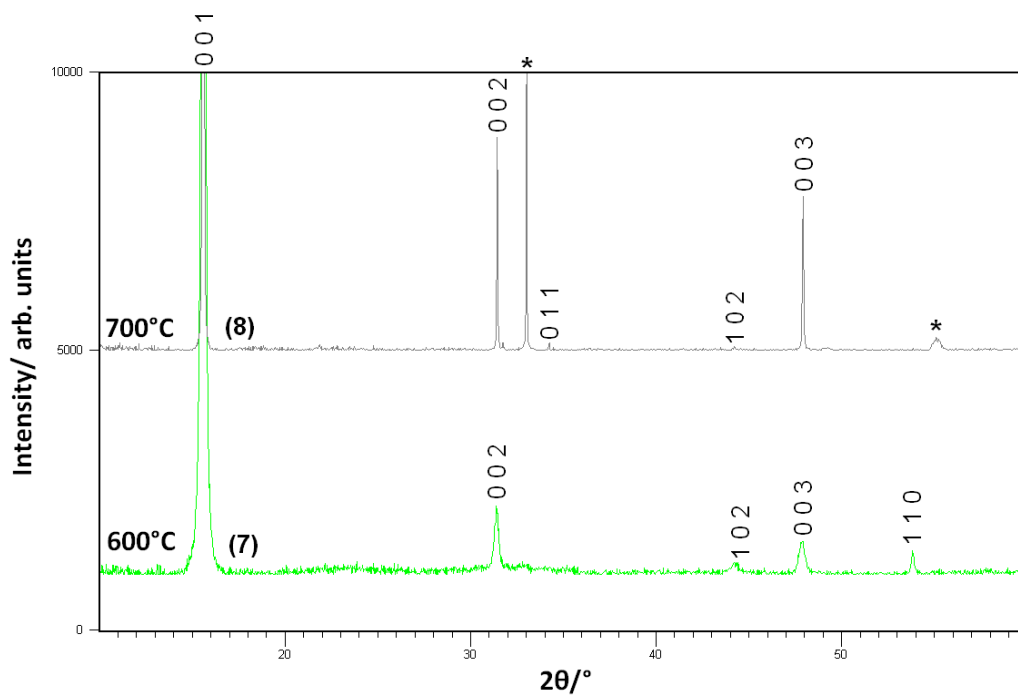


Fig 4.12 Comparison of PXD patterns for samples **7** and **8**. Despite a difference in morphology the crystal structures are effectively the same. Labelled peaks represent  $\text{TiS}_2$  and those marked with an asterisk are from the underlying silica.

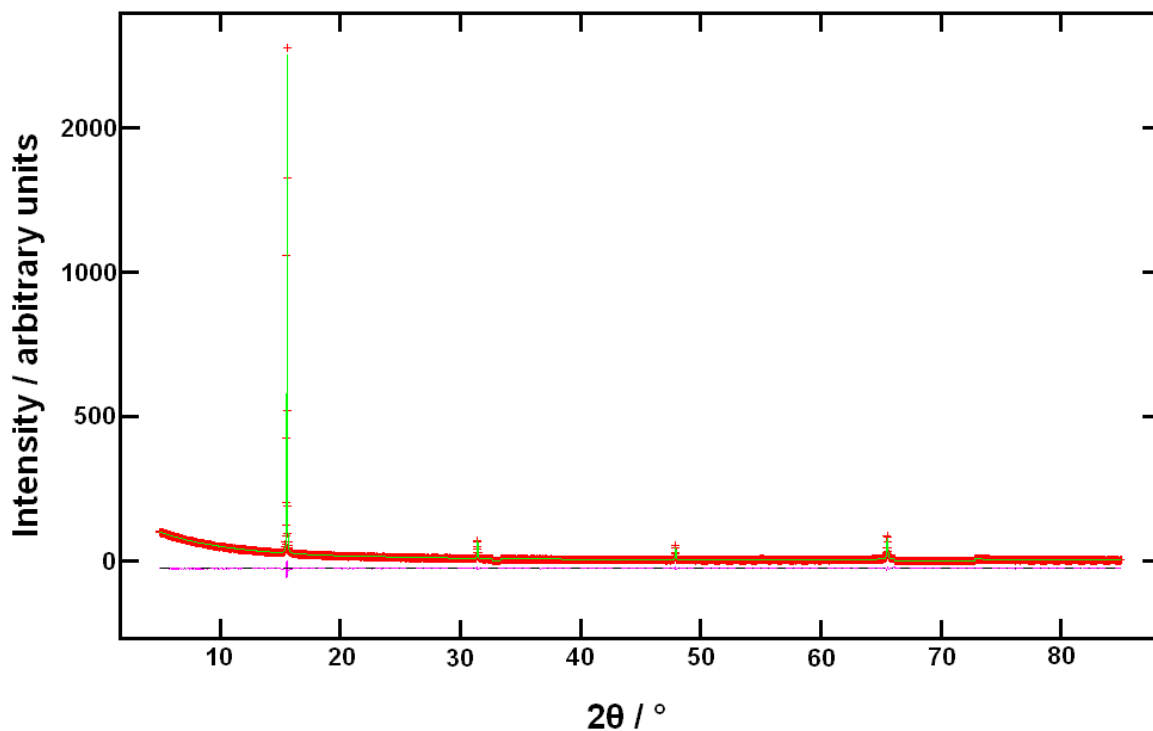


Fig 4.13 Observed, calculated and difference plot from the Rietveld refinement of **8** against PXD data. Observed data are indicated by crosses, calculated data by the solid line. The difference profile is shown below and the tick marks denotes the position of the  $\text{TiS}_2$  reflections. The reflections from the substrate were excluded.

Table 4.3 Crystallographic results from Rietveld refinement against PXD data for (8).

Formula (sample No)	TiS <sub>2</sub> (8)
Crystal system	Hexagonal
Space group	$P\bar{3}m1$ (No. 164)
$a / b$ / Å	3.2049(3)
$c$ / Å	5.6981(1)
$V$ / Å <sup>3</sup>	50.6(2)
Formula mass, $M$ / g mol <sup>-1</sup>	112.020
Density, $\rho_x$ / g cm <sup>-3</sup>	3.670
March - Dollase $R_0$ ( $00l$ )	0.332
Ti; $1a$ (0,0,0)	
$100 \times U_{\text{iso}}$ / Å <sup>2</sup>	3.7 (1)
S; $2d$ ( $\frac{1}{3}, \frac{2}{3}, z$ )	
$z$	0.2521(3)
$100 \times U_{\text{iso}}$ / Å <sup>2</sup>	0.18 (7)
No. observations, parameters	4347, 19
$R_{\text{wp}}$	0.0585
$R_{\text{p}}$	0.0314
Goodness of fit, $\chi^2$	5.305

Table 4.4 Bond lengths from Rietveld refinement against PXD data for (8).

Bond length (Å)	TiS <sub>2</sub> (8)	TiS <sub>2</sub> (Lit) <sup>[187]</sup>
Ti - S / Å	2.342(5)	2.429 Å
S - S / Å	3.205(11)	3.407

#### 4.4.2.1 Raman spectroscopy and magnetic measurements

Raman spectroscopy provides an excellent complementary method of characterising these materials, particularly in the cases where scattering is relatively weak from samples leading to ambiguous powder patterns.

For example, in the case of sample **8** (Fig 4.14) the spectrum exhibited two broad bands at  $230\text{ cm}^{-1}$  and  $330\text{ cm}^{-1}$ . These correspond to the  $E_g$  and  $A_{1g}$  phonon modes of  $\text{TiS}_2$  and are very close to reported values;  $232$  and  $336\text{ cm}^{-1}$  respectively. <sup>[188]</sup>

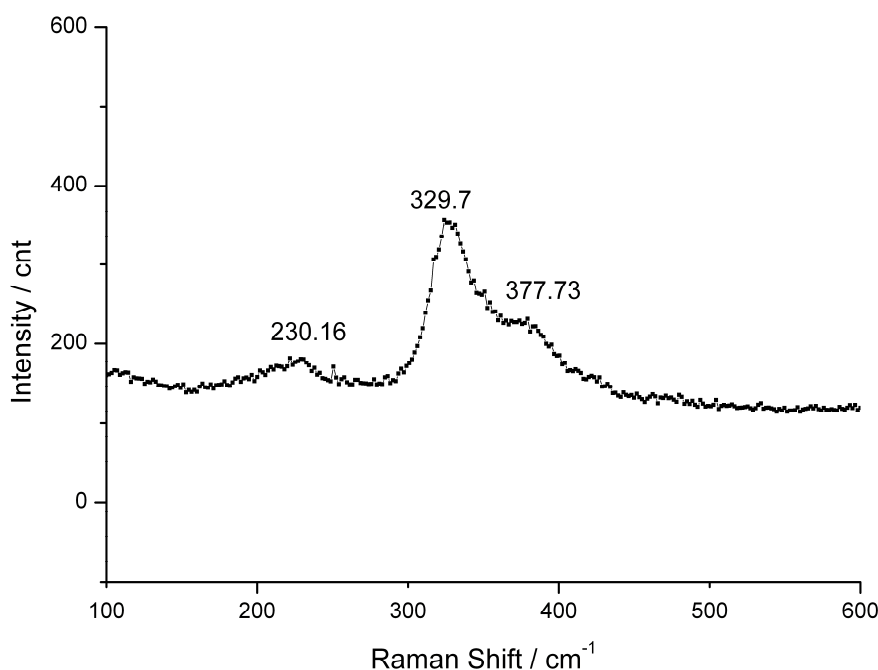


Fig 4.14 Room temperature Raman spectrum of sample **8** with a wavelength of exciting light of 532 nm.

An additional band is detected as a shoulder at ca.  $378\text{ cm}^{-1}$ . Previous reports have stated that this peak is also observable in the spectra of intercalated  $\text{TiS}_2$  samples. <sup>[189]</sup> It is reported in the literature that this peak is temperature dependent. <sup>[189]</sup> In Ag intercalated species for example, a reduction in temperature ( $>150\text{ K}$ ) and the shoulder peak gives way to two additional peaks;  $G_1$  and  $G_2$  (approximately  $380$  and  $415\text{ cm}^{-1}$  respectively). <sup>[188]</sup> The temperature dependence of these two modes are of first order phonons and are attributed to

outcomes of Brillouin zone folding in the superlattice present in intercalated compounds such as  $\text{Ag}_x\text{TiS}_2$ .<sup>[189]</sup> It would be interesting as a basis for future work to run Raman spectra at varying temperatures of these low-dimensional  $\text{TiS}_2$  structures and determine if their behaviour adheres to that of unintercalated  $\text{TiS}_2$  or is something more akin to  $\text{Ag}_x\text{TiS}_2$ , for example. A closer inspection of the Raman spectra for sample **8** reveals the hint of a second maximum close to ca.  $420\text{ cm}^{-1}$ , like that reported for the  $G_1$  and  $G_2$  first order phonon modes. This could be evidence for the possibility of the formation of a superlattice in these low dimensional structures. Further to this, magnetic susceptibility data for (**7**) revealed weak paramagnetic behaviour which was largely independent of temperature and there was no evidence of any magnetic ordering transitions (Fig 4.15). Unintercalated  $\text{TiS}_2$  is expected to be diamagnetic.<sup>[190]</sup> The observed behaviour could be a result of low level impurities but if one considers the Raman spectrum of sample **8**, the SQUID analysis could represent an alteration in electronic structure of samples **7** and **8** in comparison to bulk stoichiometric  $\text{TiS}_2$  (a diamagnetic 0.2eV gap semiconductor which becomes metallic for  $\text{Ti}_{1.05}\text{S}_2$ ).<sup>[189]</sup> Additional selected area electron diffraction (SAED) studies could help determine if there is any evidence for the formation of a superlattice. Alternatively, the observed paramagnetic behaviour could be a result of Ti cations intercalated within the layers of a non-stoichiometric structure. Often titanium disulfide is formed with some excess Ti found within the inter-layer planes, which can cause a partial filling of the Ti d band and can result in it exhibiting uncharacteristic behaviour such as extrinsic semiconductor. Additionally, this ‘self intercalated’  $\text{TiS}_2$ , ( $\text{Ti}_{1.05}\text{S}_2$  for instance) can change the typically diamagnetic behaviour of stoichiometric  $\text{TiS}_2$  to exhibit paramagnetic behaviour. In both cases the susceptibility is weakly dependent on temperature.

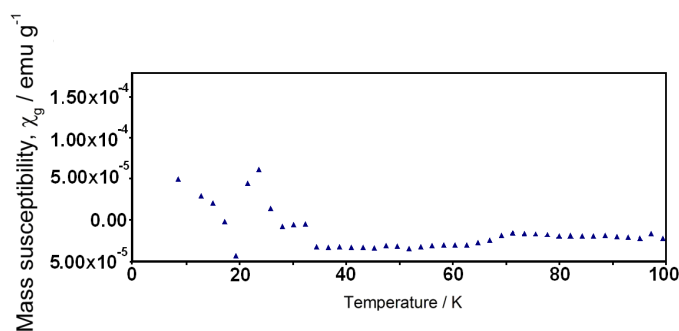


Fig 4.15 Plot of mass susceptibility against temperature (0 - 100 K) sample (**7**) showing its weakly paramagnetic behaviour.

#### 4.4.3 Increased reactant ratio

Table 4.5 displays two additional reactions which studied the effects of a higher stoichiometric ratio between titanium and sulfur.

Table 4.5 Reactions with a 1:3 (9) and 1:4 (10) ratio of Ti:S

Sample No.	Powder reactants; mass / g	Ti film thickness / nm	Reaction T / °C	Reaction time / hrs	Rate of cooling / °C h <sup>-1</sup>
9	Ti,S; 0.014, 0.03 (1:3)	50	500	24	Air Quenched
10	Ti,S; 0.014, 0.04 (1:4)	50	500	24	Air Quenched

For samples 9 and 10 the temperature was maintained at 500 °C since this is the value where the flower-like growth was previously observed (6). All other reaction conditions were kept the same to previous samples. In both cases the flower-like morphology is preserved, to the extent that the veil-like sheets appear to proliferate from a central core. (Fig 4.16a) The widths of these ribbons can range from tens of nm to several μm across. Despite their width, the nanoribbons maintain electron transparency with thicknesses ranging from approximately 10-30 nm.

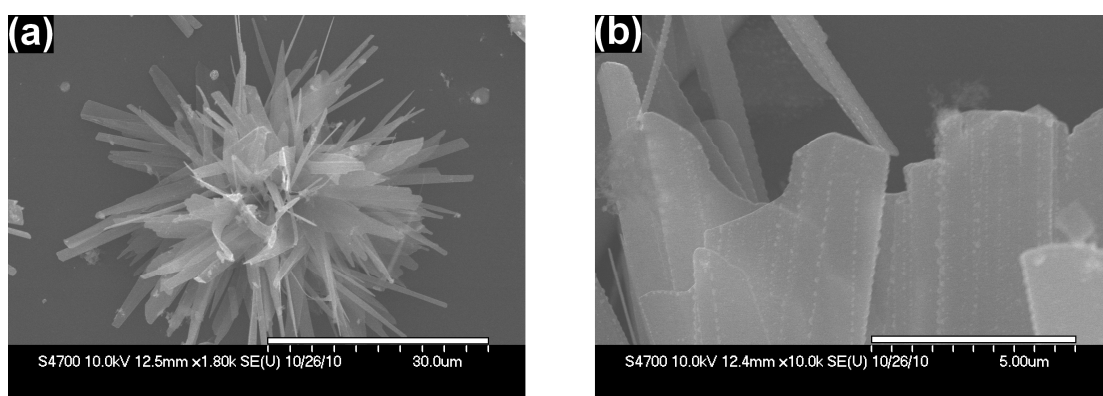


Fig 4.16 SEM micrographs of sample 10 which shows (a) the cluster like growth from a central nucleation point and (b) the electron transparency of the ribbons which is representative of the contrast between the nanometre scale thickness and micron scale widths.

A closer comparison reveals subtle differences in structure with lower stoichiometric ratios. For example, there is a rigidity to the sheets of (10) not seen in (6) (Fig 4.17).

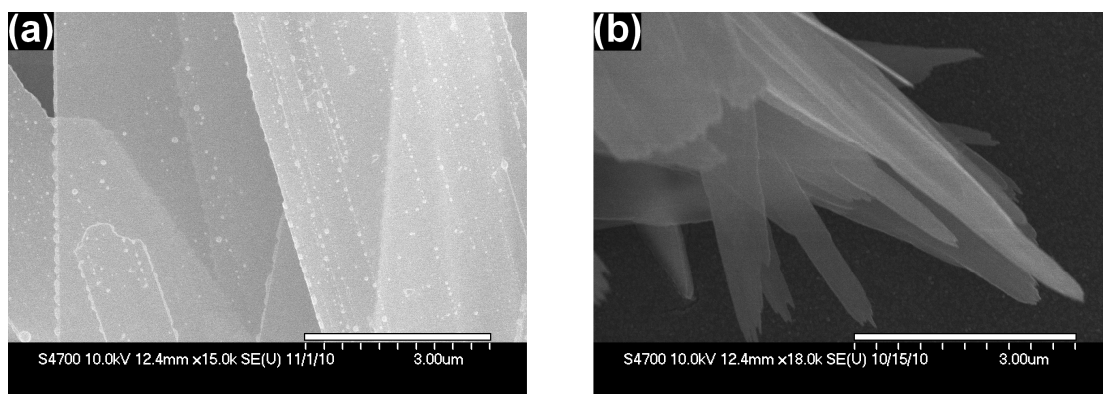


Fig 4.17 SEM micrographs of (a) (10) and (b) (6) showing that (10) is composed of primarily micro-wide tape-like structures whereas (6) has the appearance of torn cloth with widths on the nanoscale.

In fact, the morphology of the petals of the clustered nanostructures of (9) is more akin to the 1D nanostructures previously reported for transition metal trichalcogenides ( $\text{MQ}_3$ ) which were prepared at similar temperatures<sup>[184]</sup> and indeed PXD of (10) revealed that these structures are a closer match to  $\text{TiS}_3$  rather than  $\text{TiS}_2$ , (Fig 4.18), The patterns obtained for samples (9) and (10) have a strong similarity to those of the previously reported  $\text{TiS}_3$  nanobelts<sup>[183]</sup> and the PXD patterns of (9) and (10) can be tentatively indexed to the monoclinic cell ( $P2_1/m$ ) of  $\text{TiS}_3$  with values of;  $a = 5.00(4) \text{ \AA}$   $b = 3.35(1) \text{ \AA}$   $c = 8.73(7) \text{ \AA}$  and  $\beta = 96.59^\circ$  (9) and  $a = 4.97(1) \text{ \AA}$   $b = 3.44(2) \text{ \AA}$   $c = 8.76(8) \text{ \AA}$  and  $\beta = 98.30^\circ$  (10). Both are in good agreement with literature values<sup>[45]</sup> with the exception of the  $b$ -lattice parameter of (9) which shows a slight expansion of c.a. 1%. EDX data would also broadly support these results but with a slight discrepancy in ratios. Values were consistently observed as (At% 30% Ti, 70% S  $\pm$  1.17%) compared to the expected (At% 25% Ti, 75% S). Whether these data however reflect a genuine departure from the ideal stoichiometry of  $\text{TiS}_3$  i.e.  $\text{TiS}_{3-x}$  or  $\text{Ti}_{1+x}\text{S}_3$  remains uncertain. As stated earlier in section (4.1.2),  $\text{TiS}_3$  and related  $\text{MQ}_3$  chalcogenides crystallise in monoclinic, space group  $P2_1/m$  forming structures where chains of  $\text{MQ}_6$  polyhedra propagate along the  $b$ -axis and this often results in profound anisotropic crystal growth. This growth is often manifested in the

microstructures of the trichalcogenides as elongated ribbons and needles of  $\text{MQ}_3$ . [83, 87]

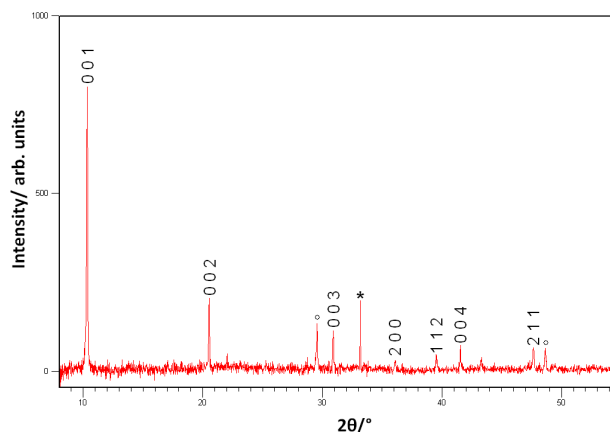


Fig 4.18 PXD pattern of sample **10**. Labelled reflections are those from monoclinic  $\text{TiS}_3$ , whereas open circles represent peaks from the underlying silica. Reflection marked by asterisk is tentatively assigned to excess sulfur.

A Rietveld refinement was performed on (**10**) and the results are given in Fig 4.19 and Table 4.6. The data can be fitted to the monoclinic structure (space group  $P2_1/m$ ) of  $\text{TiS}_3$ . It was unfortunately not possible to refine the atomic coordinates for the structure as any attempt to do so would result in a negative  $U_{\text{iso}}$  and a divergence of the refinement. This unfortunately limits discussion to simply a comparison of cell parameters. It was extremely difficult to achieve a good quality refinement of sample **10** due to numerous factors, primarily the minute sample quantity and low surface coverage across the silica substrate surface. Transparency effects are also likely to have played a significant role; the nanometric thickness of the structures can make them transparent to the X-ray beam and therefore hard to model. The greatest hindrance to a suitable refinement however is likely the preferred orientation. Although the March - Dollase model can be used to account for this (4.1), it is limited in cases of extreme orientation. The best way to improve the refinement would therefore be to remove this preferred orientation which is unfortunately also extremely difficult.

$$P_{k,j} = \frac{1}{m_k} \sum_{n=1}^{m_k} \left( R_0^2 \cos^2 \alpha_n + \frac{\text{Sin}^2 \alpha_n}{R_0} \right)^{\frac{3}{2}} \quad (4.1)$$

where  $R_0$  is the March Dollase parameter,  $m_k$  is the summation of all equivalent hkl reflections and  $\alpha_n$  is the angle between the preferred orientation vector and the crystallographic plane generating the peak. [191]

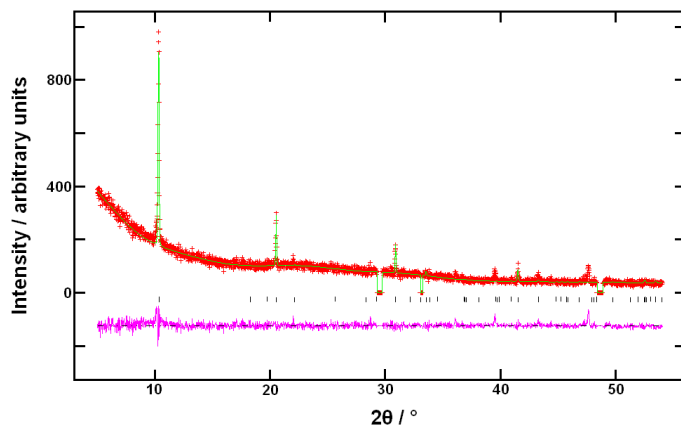


Fig 4.19 Observed, calculated and difference plot from the Rietveld refinement of **10** against PXD data. Observed data are indicated by crosses, calculated data by the solid line. The difference profile is shown below and the tick marks denotes the position of the  $\text{TiS}_3$  reflections. The reflections from the substrate were excluded.

Table 4.6 Crystallographic results from Rietveld refinement against PXD data for (10).

Formula (sample No)	TiS <sub>3</sub> (10)
Crystal system	Monoclinic
Space group	<i>P</i> 2 <sub>1</sub> / <i>m</i> (No. 11)
<i>a</i> / Å	4.980(7)
<i>b</i> / Å	3.405(2)
<i>c</i> / Å	8.813(2)
$\beta$ / °	97.46(8)
<i>V</i> / Å <sup>3</sup>	148.167
Formula mass, <i>M</i> / g mol <sup>-1</sup>	288.160
Density, $\rho_x$ / g cm <sup>-3</sup>	3.233
Ti; 2 <i>e</i> ( <i>x</i> , $\frac{1}{4}$ , <i>z</i> )	
<i>x</i>	0.7152
<i>z</i>	0.6524
100 x <i>U</i> <sub>iso</sub> / Å <sup>2</sup>	5.2 (10)
S; 2 <i>e</i> ( <i>x</i> , $\frac{1}{4}$ , <i>z</i> )	
<i>x</i>	0.2392
<i>z</i>	0.5505
100 x <i>U</i> <sub>iso</sub> / Å <sup>2</sup>	5.7(8)*
S; 2 <i>e</i> ( <i>x</i> , $\frac{1}{4}$ , <i>z</i> )	
<i>x</i>	0.5320
<i>z</i>	0.1762
100 x <i>U</i> <sub>iso</sub> / Å <sup>2</sup>	5.7(8)*
S; 2 <i>e</i> ( <i>x</i> , $\frac{1}{4}$ , <i>z</i> )	
<i>x</i>	0.1205
<i>z</i>	0.1737
100 x <i>U</i> <sub>iso</sub> / Å <sup>2</sup>	5.7(8)*
No. observations, parameters	2819, 12
<i>R</i> <sub>wp</sub>	0.1765
<i>R</i> <sub>p</sub>	0.0725
Goodness of fit, $\chi^2$	1.028

\* Sulfur atoms were constrained

#### 4.4.3.1 TEM and Raman spectroscopy studies

TEM studies have shown that the  $\text{TiS}_3$  ribbons are micron size single crystals of nm scale thickness (Fig 17). They yield well-defined diffraction patterns that can be matched to monoclinic  $\text{TiS}_3$  <sup>[45]</sup> (Inset Fig 4.20). From the diffraction pattern, lattice parameters could be determined as  $a = 5.252 \text{ \AA}$  and  $b = 3.57 \text{ \AA}$ . However  $c$  could not be calculated due to the orientation of the crystallites (in the  $a$ - $b$  plane). These are somewhat larger than the literature values ( $a = 4.958 \text{ \AA}$  and  $3.401 \text{ \AA}$ ). <sup>[45]</sup> No adequate calibration was performed whilst recording the diffraction patterns and therefore this is not convincing evidence to suggest a shift of the lattice parameters from the literature values. In fact, if one compares the  $b/a$  ratio of the diffraction patterns, 0.6797 to the literature value of 0.6859, a clearer match is obtained. The long axis of the ribbon is parallel to (010) and the thinnest direction is parallel to (001). This reveals that the lowest energy surface of the crystal is the (001) face. This is as expected since the  $\text{MQ}_3$  structure typically contains  $\text{MQ}_6$  trigonal prisms connected by weaker  $M$ - $Q$  interactions to form sheets parallel to the (001) planes (Fig 4.3). Hence in the case of  $\text{TiS}_3$ , the fastest rate of growth on the most unstable surface must be happening along the (010) direction, which corresponds to the propagation direction of the Ti - S chains. These observations are in agreement with the growth of  $\text{TiS}_3$  nanobelts reported previously. <sup>[185]</sup>



Fig 4.20 Bright field TEM micrograph of a  $\text{TiS}_3$  ribbon-like sheet, inset Selected area diffraction pattern from the same particle.

TiS<sub>3</sub> was first reported in 1937 by Blitz, Ehrlich and Meisel <sup>[192]</sup> and its crystal structure later determined in 1975. <sup>[45]</sup> The trisulfide apparently decomposes at 560 °C and TiS<sub>2</sub> is favoured above this temperature. <sup>[38]</sup> Previous investigations of powders and single crystals have established that TiS<sub>3</sub> has weak magnetic susceptibility (and is probably intrinsically diamagnetic) it is a semiconductor, which can become extrinsically n-type. <sup>[83, 92, 193]</sup>

The Raman spectrum of **(10)** (Fig 4.21) displays four bands; 171, 296, 363 and 553 cm<sup>-1</sup> respectively. These bands match well to the characteristic bands seen for bulk TiS<sub>3</sub>. Each peak corresponds to A<sub>g</sub> k = 0 phonon modes. <sup>[194]</sup>

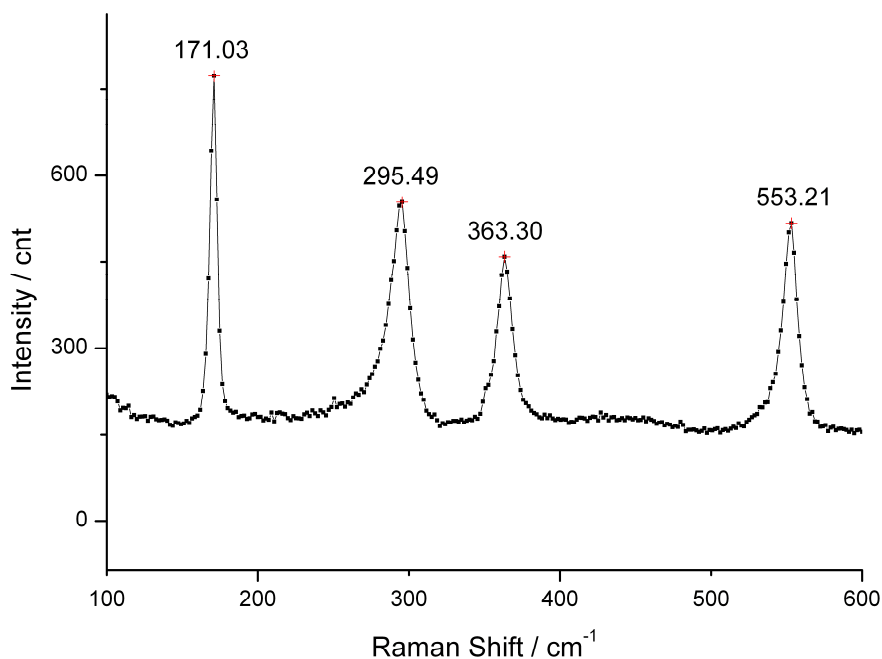


Fig 4.21 Room temperature Raman spectrum of **10** with a wavelength of exciting light of 532nm

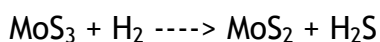
#### 4.5 Discussion and conclusions

Summarising the results for section (4.4) it can be concluded that at low temperatures - 300 °C (**4**) - no reaction occurs between the starting materials and the conditions only result in the transport and deposition of sulfur on the substrate surface. For intermediate temperatures of 400 - 500 °C, (**5**) and (**6**), EDX consistently suggests that the obtained products match best to TiS<sub>2</sub>. At

temperatures above 500 °C (7-8), EDX, PXD and Raman data agree that the sole product obtained is hexagonal CdI<sub>2</sub>-type TiS<sub>2</sub>. As the temperature is increased the TiS<sub>2</sub> flower-like structures become agglomerated platelets of increasing size. In terms of stoichiometry, if the temperature is maintained at 500 °C but the ratio between Ti:S decreased i.e. from 1:2 to 1:4, TiS<sub>3</sub> is the favoured product with a morphology distinct from the TiS<sub>2</sub> structures grown at the same temperature. A distinctive characteristic of transition metal dichalcogenides is the high presence of dangling bonds due the systematic absence of either metal or chalcogen atoms at the edges of the layered structure. As the size of the molecular sheets shrink, the number of unsaturated bonds increases (compared to the bulk) and the layers become unstable, tending to bend and roll into curved structures. In the case of sample 6 (Fig 8c) a curvature in the structure is quite clear and given the nature of the layered MQ<sub>2</sub> compounds could be a result of an increasing number of dangling bonds as the sheets decrease in thickness. Sample 10 (Fig 4.16) on the other hand has a very rigid structure in comparison, possibly due to the absence of the layer like structure typical of MQ<sub>2</sub> compounds.

From the Ti-S phase diagram, at ambient pressure it is expected that TiS<sub>3</sub> would decompose to TiS<sub>2</sub> + S at a temperature of 632 °C. [195] The formation and stability of TiS<sub>3</sub> however is not solely dependent on temperature but a combination of both sulfur partial pressure and reaction temperature. [196] Previous studies with similar experimental parameters to those used in this study (in terms of pressure and configuration), revealed that the partial pressure of sulfur (from a 1:2 ratio; Ti:S) was not sufficient to inhibit the decomposition of TiS<sub>3</sub> to TiS<sub>2</sub> at 400 °C. [197] These previous observations would appear to agree with the reported data. EDX data of the nanostructures grown at 400 °C (5) and 500 °C (6) imply that the synthesised sulfides are in terms of stoichiometry closer to TiS<sub>2</sub> than TiS<sub>3</sub>. Using a 1:3 (9) or 1:4 (10) ratio of Ti:S increases the amount of sulfur present in the system. Therefore at 500 °C it would appear that there is sufficient partial pressure to prevent decomposition of the trichalcogenide. If one considers sample 1 where an estimated ratio of 50:1 (S:Ti) was employed, at elevated temperatures of 650 °C TiS<sub>2</sub> formation was favoured as a result of TiS<sub>3</sub> decomposition which is consistent with previously reported analysis of trichalcogenide stabilities. [38, 47]

Previous studies on the formation of TiS<sub>3</sub> nanobelts from Ti foil and sulfur vapour had proposed that the trisulfide nanostructures grow via a VS mechanism in which gaseous TiS<sub>x</sub> that forms between the sulfur vapour and solid Ti foil are the crucial species in nucleation and subsequent growth. <sup>[180]</sup> This study would support this theory. In the case of sample 9, TiS<sub>x</sub> in the vapour phase is probably transported prior to deposition and further reaction on the substrate surface. It is not currently clear however for samples 1-8 as to whether TiS<sub>3</sub> is formed *in-situ* prior to the growth of the TiS<sub>2</sub> structures. This would require reduction and evolution of S as a result from decomposition. From the SEM results it can be seen that morphologies of the TiS<sub>2</sub> and TiS<sub>3</sub> structures differ and therefore if such a reduction does take place it is not a pseudomorphic process. Previous studies on trisulfide precursors undergoing a pseudomorphic reduction to the disulfide <sup>[198]</sup> suggest that such a reduction can be observed in the Ti-S system but at higher temperatures. In turn this offers the prospect of exerting further control over the dimensions of the tri and disulfide structures by tailoring reaction temperature and partial pressure (via reactant ratios). An investigation of the literature shows that the prospect of a trisulfide intermediate producing a disulfide product parallels with the mechanism of formation for MoS<sub>2</sub>, first proposed by Tenne *et al* <sup>[199]</sup> and is true for many other dichalcogenides. In fact, the use of trichalcogenide intermediates has provided a common route for the synthesis of several disulfide nanotubes; NbS<sub>2</sub>, HfS<sub>2</sub>, MoS<sub>2</sub> and WS<sub>2</sub> <sup>[200-201]</sup> and also in the case of some selenides; WSe<sub>2</sub> and MoSe<sub>2</sub>. <sup>[202]</sup> This is achieved most commonly by direct decomposition of the trichalcogenide under a reducing atmosphere. For example, the decomposition of MoS<sub>3</sub> under a stream of H<sub>2</sub> at 1200 - 1300 °C produces MoS<sub>2</sub> nanotubes of diameter 20-30 nm *via* the following reaction <sup>[203]</sup>



It is interesting to speculate if a similar result could be achieved with TiS<sub>3</sub>. Considering that large activation energies that are required to overcome the activation barrier to bend otherwise flat 2D layers, <sup>[204]</sup> it is a characteristic feature of inorganic fullerene - structures (IF) to form at high reaction temperatures (> 800 °C). <sup>[205]</sup> Therefore it is not unprecedented to presume that it is possible to produce tubule-like nanostructures of TiS<sub>2</sub> by reacting pre-

prepared  $\text{TiS}_3$  nanoribbons under hydrogen at this temperature range. Indeed the curved flower-like structures of sample **6** could be induced to roll into cylindrical structures simply by increasing the reaction temperature. It is also possible to use other precursors, such as an ammonium salt  $(\text{NH}_4)_2\text{MQ}_4$  (where  $M = \text{Mo}, \text{W}$  and  $Q = \text{S}, \text{Se}$ ) or oxides.<sup>[198]</sup> For instance,  $\text{MoO}_3$  under  $\text{H}_2\text{S}$ , where an amorphous  $\text{MoS}_3$  intermediary is still thought to play a fundamental role in the formation of  $\text{MoS}_2$  nanotubes.<sup>[201]</sup>

To briefly summarise the observed magnetic properties, sample **(3)** exhibited temperature independent diamagnetism, which is expected for stoichiometric  $\text{TiS}_2$ <sup>[190]</sup> whereas samples **6** and **7** displayed weak temperature independent paramagnetic behaviour but with a hint of Curie-Weiss like behaviour for **(6)**. An extrapolation of the data for **(6)** (Fig 4.11) also suggested weak, largely temperature independent paramagnetism. Previous magnetic studies on intercalated  $\text{TiS}_2$  have observed paramagnetic, Curie-Weiss behaviour for  $\text{V}_x\text{TiS}_2$  and a ferromagnetic ordered phase in  $\text{Cr}_x\text{TiS}_2$  (where  $x \leq 0.75$ ).<sup>[206]</sup> Given that in some systems, like  $\text{TaS}_2$  for instance, the nanoscaled structure can reflect the effects of doping on structure<sup>[140]</sup>. The paramagnetic behaviour of samples **6** and **7** might be expected given the tendency for nanostructures to sometimes mimic the effect of doped structures or those applied under pressure.

## 5. Zirconium and hafnium trichalcogenides

### 5.1 Introduction

The Group IV trichalcogenides are a class of isostructural compounds which are composed of  $MQ_6$  structural units. These units stack to form  $TQ_3$  prismatic chains, which propagate parallel to the  $b$ -axis of a monoclinic cell (Fig 5.1). The result of which is that these structures tend to possess one-dimensional characteristics that are often exhibited in their crystal growth. <sup>[47]</sup> For a more detailed structural analysis please see section (1.5.1) and a discussion of the group IV-trichalcogenide  $TiS_3$  has already been presented in Chapter 4.

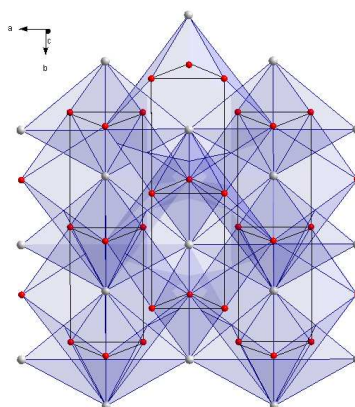


Fig 5.1 Stacking of  $MQ_6$  prismatic units along the  $b$ -axis, grey atoms are the transition metal and red the chalcogen,  $c$ -axis is perpendicular to the page.

A thorough review of these compounds was initially conducted by McTaggart *et al* in the late fifties <sup>[38-40]</sup> and much of the preliminary structural investigations were covered by Kjekshus *et al* in the sixties and seventies who also briefly reported on their magnetic and electrical properties. <sup>[45,83]</sup> Further studies have mainly focused on their optical properties, especially those of  $HfS_3$  <sup>[207]</sup> and  $ZrS_3$ , <sup>[208, 209]</sup> but other than an interest in  $ZrTe_3$  (due to its capacity to exhibit charge density wave formation (CDW) and superconductivity) <sup>[98,99,101]</sup> little has been investigated regarding these compounds.

To the author's knowledge there are currently only two reported examples of nanostructured- $MQ_3$ . Firstly,  $ZrS_3$  which was obtained solvothermally. A 50ml autoclave filled with 2.33g  $ZrCl_4$ , 3.90g thiourea and  $n$ -hexane are heated to 230 °C for 48hours. The resultant product is washed with  $CS_2$ , acetone and

distilled water and left to dry at 60 °C. This produced regular sheets of monoclinic ZrS<sub>3</sub> 4.5 to 6.7 μm in length and up to 100 nm in width. [210] Secondly, TiS<sub>3</sub> which was obtained *via* reacting titanium foil with sulfur powder at 650 °C under standard chemical vapour deposition (CVD) conditions. [183] The interest lay in fabricating TiS<sub>3</sub> (or TiS<sub>2</sub>) nanowires on metal or semiconducting substrates to be used as electronic field emission functional blocks due to their strong local electric field at the tip and unique direction of electron emission. A second publication by Ma *et al* tested the potential application of TiS<sub>3</sub> for copper oxide based cathodes of non-aqueous alkali metal batteries and investigated the tensile strength of TiS<sub>3</sub>-nanobelts. [184] They found that the maximum stress of a bundle of TiS<sub>3</sub> fibres is almost the same as that of aluminium, roughly 100 MPa. [211] Additionally, in the process of writing this thesis, a further report was published on nanostructures of ZrS<sub>3</sub> and HfS<sub>3</sub> by means of a CVT reaction between the elemental metal and chalcogen powders. They were heated at 600 °C over a period of 15 days. They had a thickness ranging from 60 - 120 nm and a length of 2 - 5 mm. [212]

The purpose of this chapter is to illustrate that trichalcogenides of the group IV transition metals (MQ<sub>3</sub>) are prime examples of one-dimensional structures which can be realised on the nanoscale through facile chemical vapour transport and deposition (CVT, CVD) techniques. Studies have been undertaken in the zirconium/hafnium - sulfur/selenium/tellurium systems. As in Chapters 3 and 4, evolution of growth with temperature and time is discussed and analysed with SEM, SQUID, TEM and Raman spectroscopy. Unfortunately, unlike in Chapters 3 and 4, it was not possible to perform any Rietveld refinements. This was due to numerous factors, namely peaks from the underlying foil swamping out those of the sample. Removal of the sample from the foil and onto a different surface for analysis would often result in extreme preferred orientation since their ribbon-like structure often meant they would lie flat across the surface exposing the same (001) plane. Additionally, peaks were often very broad and this made it difficult to determine a precise 2θ value for some peaks as they covered a range of several 2θ. The combination of these three features made it impossible to achieve a suitable refinement of the structures.

## 5.2 Experimental

The transition metal trichalcogenides are synthesised by reacting chalcogen powder and metal foil, sealed in silica reaction tubes. Predetermined amounts of powdered chalcogen (sulfur, selenium or tellurium) are placed in one end of the silica reaction tube (Fig 5.2, section I) in a 1:3 stoichiometric ratio with the corresponding metal foil, (zirconium or hafnium). The foil however, is placed in the opposite end, separated from the chalcogen by a constriction (Fig 5.2, section II). The ampoule is then sealed under vacuum (to a pressure of 3 mbar).

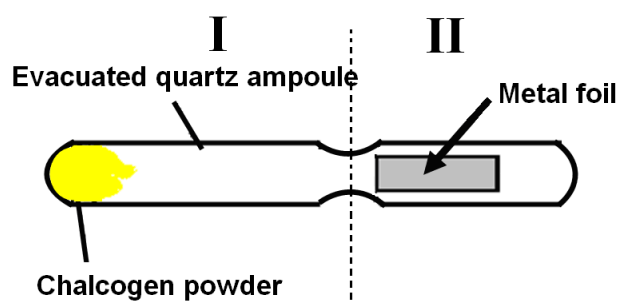


Fig 5.2 Typical experimental setup for reactions; chalcogen powder and metal foil are located on opposite ends of an evacuated silica ampoule

Reactions are performed in a box furnace to elevated temperatures (typically between 200 °C - 1100 °C) for 24 h. The furnace is heated at a rate of 200 °C h<sup>-1</sup> and upon completion samples are left to cool in the furnace at a rate of 50 °C h<sup>-1</sup>. Unless stated otherwise, experiments did not deviate from these parameters (Tables 5.1, 5.2 and 5.3). All samples employed metal foil with one exception, where the foil was replaced with metal powder. This sample is highlighted in grey in Table 5.2.

In the particular case of the Zr-S system, some samples were removed from the furnace mid reaction and quenched in air (Table 5.1). This was done to study the development of crystal growth over the chosen reaction time.

Table 5.1 Synthetic conditions for Zr-Q reactions, where Q = sulfur or selenium .

Sample No.	Reactant powders,foil; mass / g	Ramp rate / °C h <sup>-1</sup>	Reaction T / °C	Reaction time / hrs	Rate of cooling / °C h <sup>-1</sup>
1	S,Zr; 0.112,0.11	200	200	24	50
2	S,Zr; 0.175,0.16	200	900	24	50
3	S,Zr; 0.120,0.12	200	1100	24	50
4	S,Zr; 0.125,0.11	200	400	24	50
5	S,Zr; 0.118,0.10	200	600	24	50
6	S,Zr; 0.122,0.12	200	800	24	50
7	S,Zr; 0.168,0.17	200	450	24	50
8	S,Zr; 0.121,0.12	200	450	1	Air Quenched
9	S,Zr; 0.110,0.11	200	450	2	Air Quenched
10	S,Zr; 0.090,0.09	200	450	10	Air Quenched
11	S,Zr; 0.105,0.10	200	450	16	Air Quenched
12	S,Zr; 0.175,0.18	200	450	20	Air Quenched
13	Se,Zr; 0.48,0.18	200	500	24	50
14	Se,Zr; 0.54,0.21	200	700	24	50
15	Se,Zr; 0.50,0.19	200	900	24	50
16	Se,Zr; 0.28,0.11	200	650	60	50

Table 5.2 Synthetic conditions for Hf-Q reactions, where Q = sulfur or selenium, sample highlighted in grey used metal powder instead of foil.

Sample No.	Reactant powders,foil; mass / g	Ramp rate / °C h <sup>-1</sup>	Reaction T / °C	Reaction time / hrs	Rate of cooling / °C h <sup>-1</sup>
17	S,Hf; 0.180,0.09	200	450	24	50
18	S,Hf; 0.100,0.05	200	650	24	50
19	S,Hf; 0.330,0.25	200	450	24	50
20	Se,Hf; 0.11,0.08	200	450	24	50
21	Se,Hf; 0.13,0.17	200	450	60	50
22	Se,Hf; 0.09,0.07	200	450	120	50

Table 5.3 Synthetic conditions for M-Te reactions, where M = zirconium or hafnium.

Sample No.	Reactant powders,foil; mass / g	Ramp rate / °C h <sup>-1</sup>	Reaction T / °C	Reaction time / hrs	Rate of cooling / °C h <sup>-1</sup>
23	Te,Hf; 0.11,0.23	200	450	24	50
24	Te,Hf; 0.12,0.25	200	450	60	50
25	Te,Hf; 0.09,0.19	200	450	120	50
26	Te,Hf; 0.11,0.23	200	600	24	50
27	Te,Zr; 0.13,0.48	200	450	60	50
28	Te,Zr; 0.12,0.50	200	450	120	50
29	Te,Zr; 0.76,0.18	200	700	24	50
30	Te,Zr; 0.89,0.21	200	900	24	50

### 5.3 Characterisation

Products were retained on the foil for analysis unless otherwise noted. Powder X-ray diffraction (PXD) analysis was performed using a PANalytical X'pert PRO MPD powder diffractometer in flat plate geometry. Samples were loaded onto a flat glass plate and secured with double sided sticky tape. Diffraction data were typically collected for  $5^\circ \leq 2\theta \leq 85^\circ$  with a  $0.017^\circ$  step size with scan times of 1-12 h. The sample displacement error was accounted for by measuring the offset of a standard and then using Highscore software to correct sample scans. Small sample volumes required that PXD analysis allowed for the high intensity reflections from the underlying metal foil. Alternative methods of loading samples were attempted to try and reduce or remove these effects. Sonication of the foil in *iso*-propyl alcohol and the resultant suspension dropped onto a glass slide in some cases proved effective and from this method characterisation of unique sample reflections was possible. Diffraction data were compared to patterns in the ICDD (JCPDS) powder diffraction file (PDF) using the PANalytical High Score Plus software package. Indexing was achieved using the DICVOL software package<sup>[127]</sup> and least squares cell parameter refinement.

Scanning electron microscopy (SEM) was performed using a Hitachi S4700 cold field emission gun microscope. Typically, samples were loaded onto aluminium stubs using adhesive carbon tabs and run in high vacuum mode with an applied accelerating voltage of 10 kV and a working distance of 12.5 mm for imaging and 10 kV and a working distance of 10 mm for energy dispersive X-ray analysis, (EDX). EDX analysis was performed within the Philips instrument using an Oxford Instruments 7200 EDX spectrometer in order to determine elemental compositions (which can be obtained with accuracy for elements of atomic number from carbon upwards). Transmission electron microscopy was performed using a FEI Tecnai T20 microscope (FEI, Eindhoven, Netherlands) operated at 200 kV acceleration voltage using a LaB<sub>6</sub> filament with images recorded using a Megaview II CCD camera (Olympus SIS GmbH, Garching, Germany). Conventional bright field and dark field diffraction contrast imaging was used in combination with selected area diffraction to characterise the nanostructure and relate this to the crystallography of the materials. EELS spectra were recorded using a

convergent probe in diffraction mode and a GIF Gatan Image Filter, (Gatan Inc., Pleasanton, CA), at a dispersion of 0.5 eV / channel.

Samples for SEM of sufficient thickness were prepared by depositing powder onto a carbon tab. Samples for TEM were prepared by sonicating the powders in ethanol and then pipetting drops of the suspension onto holey carbon film Cu grids.

Raman spectra were collected at room temperature using a Horiba LabRAM HR confocal microscope system with a 532 nm green laser. A hole aperture of 50  $\mu\text{m}$ , 600 gr/mm grating and a Synapse CCD detector were used.

Magnetic measurements were performed using a Quantum Design MPMS 5T SQUID magnetometer. Samples were sonicated from the metal foil in iso-propyl and dropped into gelatine capsules. Field cooled (FC) and zero field cooled (ZFC) measurements were performed with an applied field of 100 Oe between 2 - 300 K. All magnetic data were corrected for the gelatine capsules and for core diamagnetism.

## 5.4 Results and discussion

### 5.4.1 Zirconium trisulfide; structural characterisation

Trial reactions investigated a range of temperatures, samples 1-3 (200-1100 °C; 24h), (Table 5.1). At 200 °C (1), PXD suggests that no reaction takes place as a match was only found to zirconium. Conversely at high temperatures of 900 °C (2) or 1100 °C (3) reaction conditions favoured hexagonal  $ZrS_2$  ( $P\bar{3}m1$ ) and  $Zr_3S_4$  (cubic,  $Fd\bar{3}m$ ) respectively. This agrees with previous studies where it is reported that at high temperatures ( $> 800$  °C) the  $MQ_3$  phase typically decomposes to the dichalcogenide equivalent <sup>[38, 47]</sup> and at  $> 1000$  °C a phase which incorporates more metal into the structure is favoured, such as,  $Zr_3S_4$ ,  $Zr_9S_2$  or  $Zr_2S$ . <sup>[213]</sup>

At a temperature range of 400 °C - 800 °C (all 24 h)  $ZrS_3$  is readily produced, samples 4-6, (Table 5.1). SEM performed on samples 4-6 reveal differences in the morphology (Fig 5.3). At 400 °C (4) nodule like structures are produced with no apparent wire or ribbon like growth (Fig 5.3a). EDX of the nodule like structures gave average ratios of (At% 32.01% Zr and 67.99 % S) and PXD of (4) revealed broad low intensity peaks which correspond to  $ZrS_3$ . These however are largely swamped by reflections belonging to the underlying zirconium foil. On increasing the temperature to 600 °C (5), ribbon structures are formed (Fig 5.3b). On average, these ribbons were hundreds of nanometres across and electron transparent with thicknesses approaching the range of 10 nm (Fig 5.4). PXD data for sample 5 matches to  $ZrS_3$  (Fig 5.5). The reflections were indexed to  $ZrS_3$ , (monoclinic space group  $P2_1/m$ ) with  $a = 5.13(2)$  Å,  $b = 3.61(1)$  Å,  $c = 8.94(9)$  Å and  $\beta = 97.1(2)$  °. This is in good agreement with reported lattice parameters;  $a = 5.124$  Å,  $b = 3.624$  Å,  $c = 8.98$  Å and  $\beta = 97.3$  °. <sup>[92]</sup> EDX results gave average ratios of (At% 32% Zr, 68% S  $\pm$  4.70%). Values which, given the associated error, match well to what would be expected for a 1 to 2 ratio. It is likely that this result is due to interference from the foil since PXD data strongly suggests  $ZrS_3$  and no peaks relating to  $ZrS_2$  were observed. Application of the Scherrer <sup>[163]</sup> equation to sample 5 (using a standard bulk sample as a comparison) calculated an average crystallite size as approximately 43.6 nm.

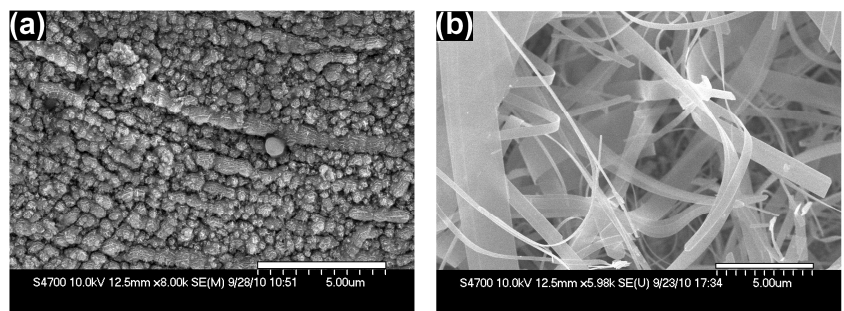


Fig 5.3 SEM Micrographs of products from reactions performed between the range of 400 °C - 800 °C; (a) 400 °C (4) (b) 600 °C (5).

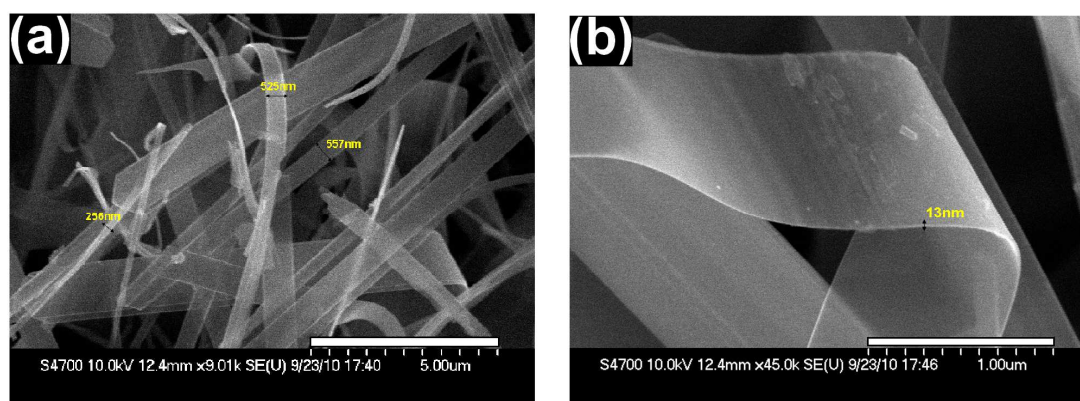


Fig 5.4 SEM Micrographs of sample 5 showing average dimensions of ZrS<sub>3</sub>-ribbons (a) width is several hundred nanometres across (b) thickness approaching the range of 10 nm.

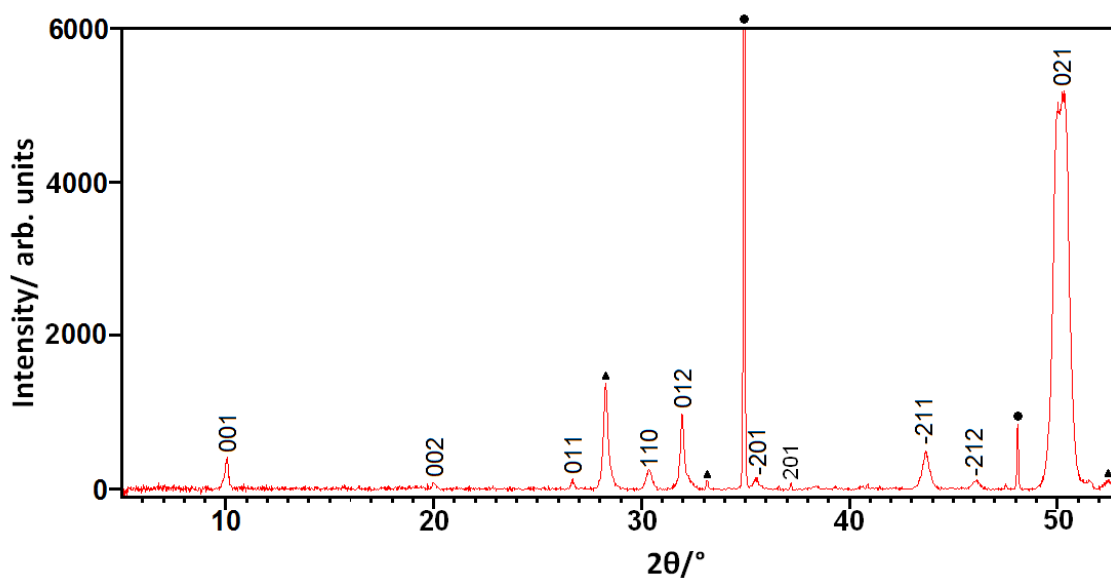


Fig 5.5 PXD pattern of sample 5. Labelled reflections match to zirconium trisulfide. Reflections labelled with filled circles correspond to the underlying zirconium foil and the peaks designated by a filled triangle are tentatively attributed to excess sulfur.

By 800 °C (6) the dimensions of the structures have increased from the nano to micro scale (Fig 5.6). PXD of (6) suggests a mixed phase (Fig 5.7) and the reflections were indexed to  $ZrS_3$ , (monoclinic space group  $P2_1/m$ );  $a = 5.11(2)$  Å,  $b = 3.627(2)$  Å,  $c = 8.99(3)$  Å and  $\beta = 97.65^\circ$  and  $Zr_3S_4$ , (cubic space group  $Fd\bar{3}m$ );  $a = b = c = 10.257(7)$  Å. Both are in good agreement with previously reported values ( $a = 10.250$  Å for  $Zr_3S_4$ ).<sup>[92,96,214]</sup> From the SEM micrographs it can be seen that the wires are sitting upon a denser layer (indicated by the yellow circle in Fig 5.6). EDX of the rod structures using spot diffraction gave average values of (At% 29% Zr, 71% S  $\pm$  2.12%) and EDX of the surface underneath gave average values of (At% 43% Zr, 57% S  $\pm$  1.25%). These results imply that the rods are  $ZrS_3$  whereas the layer underneath is  $Zr_3S_4$ . The fact that the sulfur rich phase grows nearer the surface also suggests that it has a direct interaction with the sulfur vapour.

Past studies have revealed a great deal of ambiguity associated with Zr-S phases with a number of known non-stoichiometric monosulfides that crystallise with different structures.<sup>[215]</sup> For example, those in the range of  $1.20 \leq S/Zr \leq 1.49$  crystallise with the NaCl structure<sup>[216]</sup> whereas those of the order of  $0.5 \leq S/Zr \leq 0.8$  exhibit a defect WC-type structure.<sup>[96]</sup> In the past, this has led to difficulty in structure determination.  $Zr_3S_4$  for example, has been assigned cubic ( $Fd\bar{3}m$ ) symmetry<sup>[214]</sup> but a later study has speculated that this could actually arise from a microtwinned hexagonal ( $R\bar{3}m$ ) structure which simply produces average cubic ( $Fd\bar{3}m$ ) symmetry in an X-ray pattern.<sup>[215]</sup>

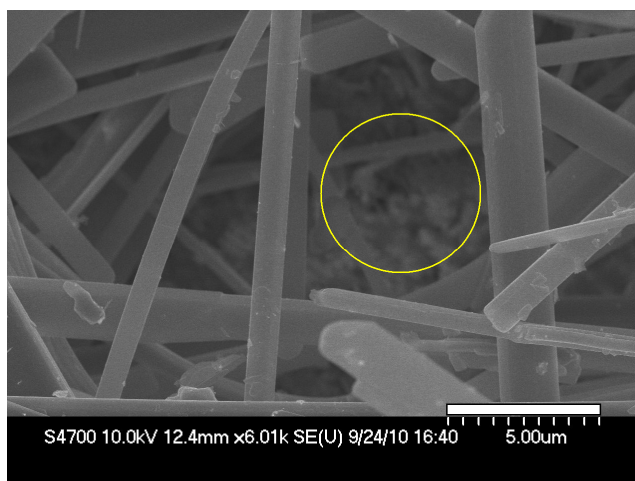


Fig 5.6 SEM Micrographs of sample 6. Yellow circle highlights denser surface beneath the rods.

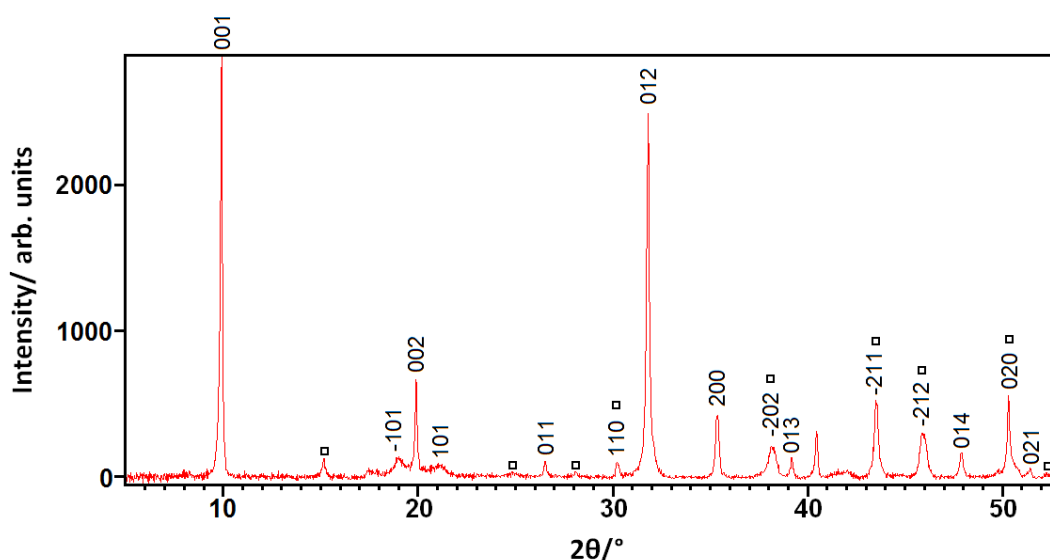


Fig 5.7 PXD sample 6; labelled reflections match to  $ZrS_3$ . Clear squares represent peaks belonging to  $Zr_3S_4$ .

#### 5.4.1.1 Zirconium trisulfide; SQUID magnetometer studies

Bulk-  $ZrS_3$  is diamagnetic with almost zero magnetic susceptibility (in the order of  $\chi_g = -0.19 \times 10^{-6} \text{ emu mol}^{-1}$ ).<sup>[83, 92]</sup> It also has a typical resistance of a few  $M\Omega$  at room temperature. This value decreases with increasing temperature and decreases with increasing pressure with a rise from 1  $M\Omega$  to 18  $M\Omega$  at pressures of ca. 5 to 90  $\times 10^8$  Pa.<sup>[217]</sup> A magnetic susceptibility vs. temperature plot of (5) reproduced the previously observed magnetic behaviour (Fig 5.8). A SQUID analysis of (6) on the other hand shows diamagnetic behaviour becoming paramagnetic at  $T \leq 16$  K (Fig 5.9). A SQUID measurement performed on zirconium foil alone shows paramagnetic behaviour which displays a sharp increase in susceptibility at  $T \leq 20$  K. Studies have shown that Zr deficient structures with a NaCl-structure,  $(Zr_{1-x}S)$  are superconducting with the critical temperature ( $T_c$ ) reaching its maximum at c.a.  $Zr_{0.83}S$ . This is thought to occur with, and therefore thought to be related to, an increase in vacancies on Zr sites.<sup>[218]</sup> Therefore the deviation from diamagnetic behaviour of (6) could be a result of a signal from the zirconium foil or another Zr-containing compound on the foil with a greater ratio of Zr to S than  $ZrS_3$ .

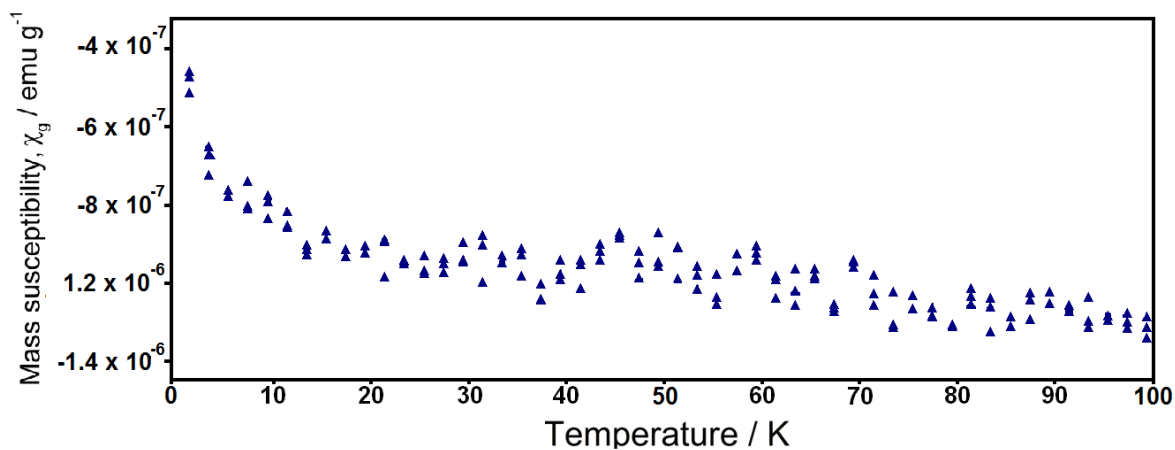


Fig 5.8 Plot of mass susceptibility against temperature (0-100 K) shows temperature independent diamagnetism of sample 5.

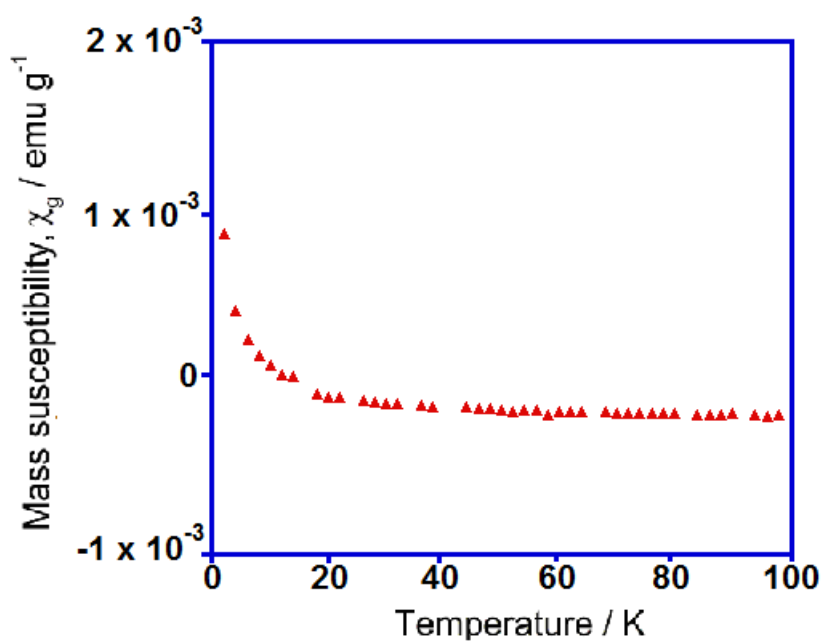


Fig 5.9 Plot of mass susceptibility against temperature (0-300 K) for sample 6, shows diamagnetism and switch to paramagnetism below 16 K, likely resulting from a paramagnetic impurity.

### 5.4.1.2 Zirconium trisulfide; Raman spectroscopy

A Raman spectrum of (6) is in accordance with previously reported results for bulk  $ZrS_3$ ,<sup>[219, 220]</sup> with two low frequency modes  $A_g$  and  $B_g$  at  $146.6\text{ cm}^{-1}$  and  $239.5\text{ cm}^{-1}$  respectively and three high frequency  $A_g$  modes at  $277.2\text{ cm}^{-1}$ ,  $316.9\text{ cm}^{-1}$  and  $525.4\text{ cm}^{-1}$  (Fig 5.10).

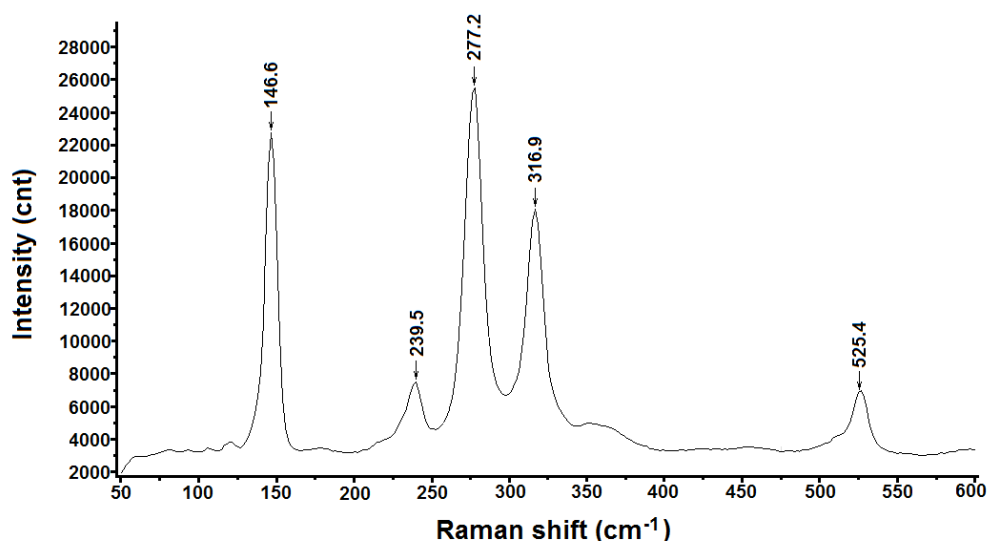


Fig 5.10 Room temperature Raman spectrum of sample 6 with a wavelength of exciting light of 532 nm.

$ZrS_3$  has twenty four normal modes at the centre of the Brillouin zone, twelve of which are Raman active ( $8A_g$  and  $4B_g$ ).<sup>[208]</sup> A previous study detected four phonons with irreducible representations  $A'$ ,  $2E'$  and  $E''$ .<sup>[209]</sup> It is hypothesised that the remaining eight phonons give weak scattering, undetectable in the spectrum because the degree of distortion which they exhibit is rather small.<sup>[209]</sup> It is also reported that at temperatures  $\leq 180\text{ K}$  the three most dominant  $A_g$  modes ( $146.6\text{ cm}^{-1}$ ,  $277.2\text{ cm}^{-1}$  and  $316.9\text{ cm}^{-1}$ ) shift to higher frequencies.<sup>[221]</sup> Interestingly, Raman spectra collected at 300 K on nanorods of  $ZrS_3$  obtained peaks at 147, 240, 277, 318 and  $524\text{ cm}^{-1}$ .<sup>[210]</sup> If one compares this to bulk  $ZrS_3$  ( $150, 243, 280, 320, 527\text{ cm}^{-1}$  respectively)<sup>[219]</sup> there is a slight shift of the peaks to a lower wavenumber. They found that the broadening and shifting of the peaks increased as the particle size decreased and therefore was attributed to the nanosized effect of the crystallites. The Raman spectrum of (6) shows a slight deviation of ca.  $4\text{ cm}^{-1}$  (a redshift) from the reported values<sup>[209]</sup>. Sample 6 was prepared by sonication of the foil in isopropyl alcohol and the resultant

solution was dried on a glass slide. Given that: 1) SEM micrographs (Fig 5.6) show the  $ZrS_3$  phase is sitting atop the  $Zr_3S_4$  (which appears to be fused to the metal surface) and sonication has therefore probably not removed  $Zr_3S_4$  from the foil surface, and 2) using an optical microscope solely crystals of a ribbon-like morphology could be isolated for analysis, one could assume therefore that the Raman spectrum is of solely  $ZrS_3$ . Therefore the deviation in wavelength of the recorded spectrum from the bulk literature values may be a result of the reduced dimensions of the structure.

A Raman spectrum of sample 5 reveals a very similar spectrum to that of (6) (with a uniform deviation of approximately  $-2\text{cm}^{-1}$  for each reading). There is however an additional peak found at  $355\text{ cm}^{-1}$  (Fig 5.11). A band at this value is not reported in any room temperature Raman studies of  $ZrS_3$  but is established in low temperature spectra (77 K). It is attributed to second order scattering and classified as an  $A_g$  phonon mode. [220] Sample 7 (Table 5.1) ( $450^\circ\text{ C}$ , 24h), PXD and SEM of which confirmed transparent nano sheets of  $ZrS_3$  (Fig 5.12) has the same additional peak present in its Raman spectrum (Fig 5.13).

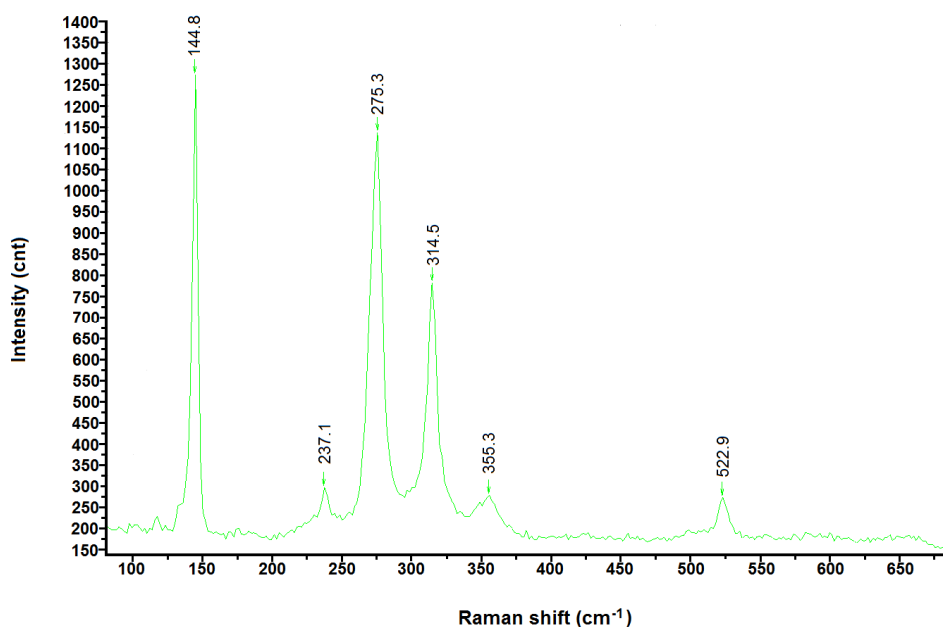


Fig 5.11 Room temperature Raman spectrum of sample 5 with a wavelength of exciting light of 532 nm.

Referring to the synthesis of nano- $ZrS_3$  ribbons [210] the authors associate their observed redshift in frequency of nano- $ZrS_3$  to a phonon confinement effect. The

phonon confinement effect states that in a bulk sample (and therefore crystals of infinite dimensions), only phonons near the centre of the Brillouin zone contribute to the Raman spectrum. In a finite crystal however (such as nanoparticles), the phonons are more likely to be constrained by crystal boundaries and/or defects allowing phonons other than those from the Brillouin centre to add to the Raman Spectrum. This manifests in the spectrum as a broadening of peaks and downshift in observed frequency. This is a feature which is seen to increase with decreasing particle size. <sup>[222, 223]</sup> In all three Raman spectra taken (5,6 and 7) there is an observed deviation in frequency from the bulk-ZrS<sub>3</sub> literature values (around 4 cm<sup>-1</sup>) and this shift could be a result of the reduced dimensions of the samples. The additional peak at approximately 355 cm<sup>-1</sup> could also be related to phonon confinement or possibly surface optical (SO) phonon modes. Surface phonon modes arise from defects in nanostructures, their size distribution and their coupling with the surrounding medium. It is the roughness of the imperfect surface of a nanocrystal which is necessary to disturb the surface potential in order to make (SO) phonon modes observable. This is a phenomenon which has been previously studied in ZnS nanowires<sup>[224]</sup> and GaN nanoribbons.<sup>[225]</sup> The additional peak at 355 cm<sup>-1</sup> could be a result of (SO) phonon modes arising from defects present on the surface of the ZrS<sub>3</sub> nanoribbons of (5) and (7) not present in the bulk.

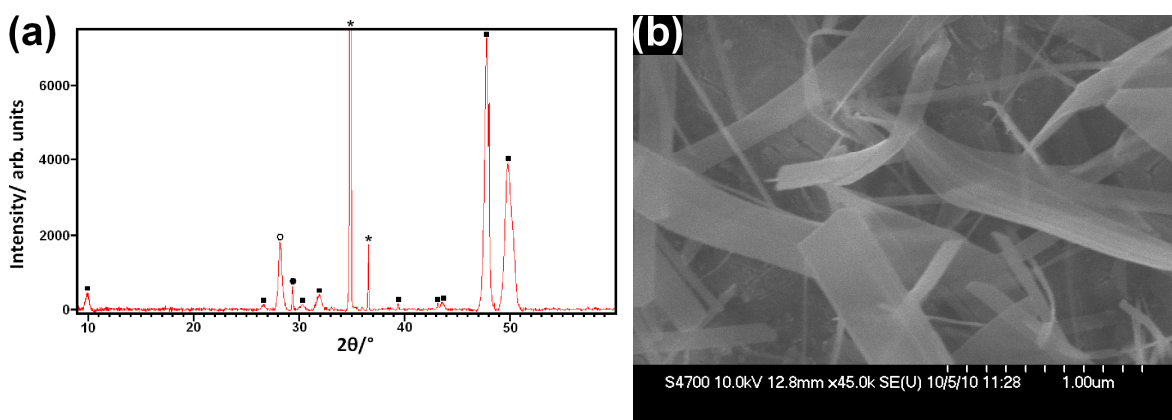


Fig 5.12 a) PXD pattern of (7), squares denote ZrS<sub>3</sub>, open circle represents ZrS<sub>2</sub>, asterisks correspond to underlying Zr foil and the circle is an unidentifiable peak. b) SEM Micrograph of sample 7 showing sheet-like nanostructures.

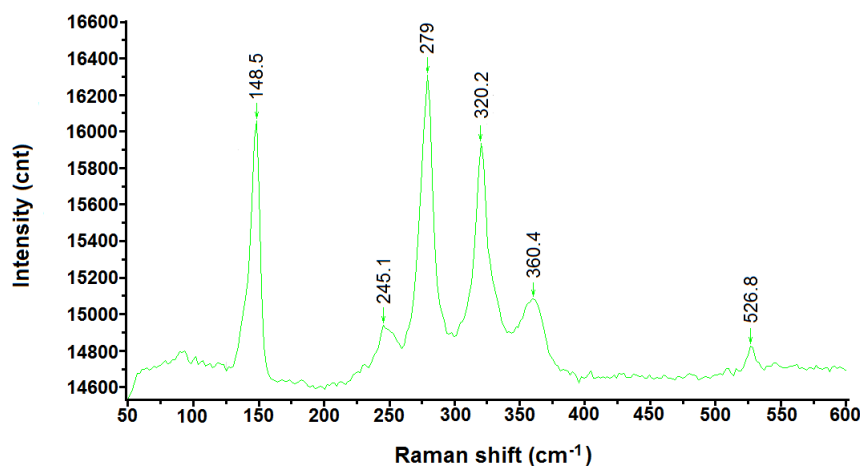


Fig 5.13 Room temperature Raman spectrum of sample 7 with a wavelength of exciting light of 532 nm.

#### 5.4.1.3 Zirconium trisulfide TEM investigations

TEM studies have shown that (6) is composed of  $\text{ZrS}_3$  single crystal micron sized ribbons of nm scale thickness (Fig 5.14). They yield well-defined diffraction patterns that can be matched to monoclinic  $\text{ZrS}_3$ .<sup>[45]</sup> From the diffraction pattern, lattice parameters could be determined as  $a = 5.08(1) \text{ \AA}$  and  $b = 3.65(2) \text{ \AA}$ ,  $c$  could not be calculated due to the orientation of the crystallites (in the  $a$ - $b$  plane). These are in good agreement with the literature values ( $a = 5.1243(11) \text{ \AA}$  and  $b = 3.6244(10) \text{ \AA}$ ).<sup>[45]</sup>

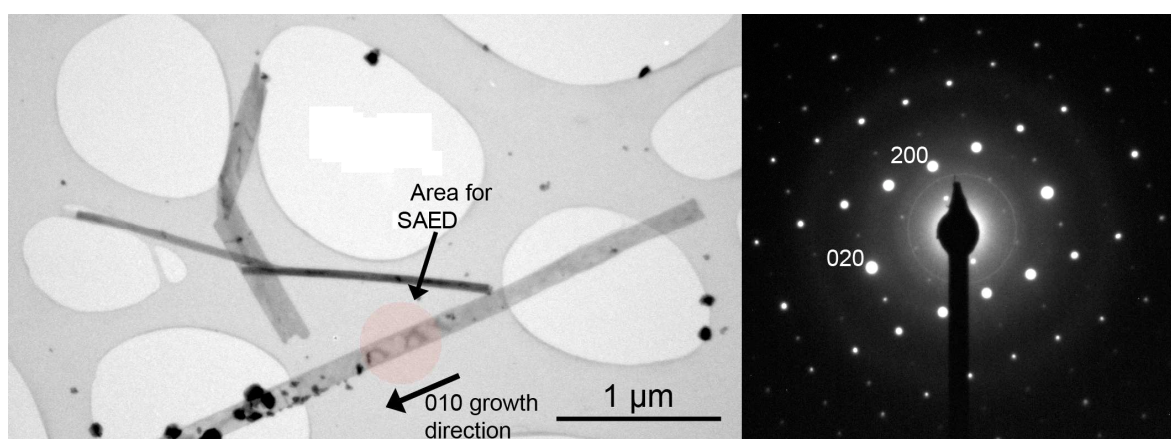


Fig 5.14 Bright field TEM micrograph of a  $\text{ZrS}_3$  ribbon, inset selected area electron diffraction (SAED) pattern from area of particle highlighted by the red circle. Image has been rotated 90 degrees to align with the  $[010]$  growth direction.

The long axis of the ribbon is parallel to (010) and the thinnest direction is parallel to (001). This is expected since the  $MQ_3$  structure typically contains  $MQ_6$  trigonal prisms connected by weaker M-Q interactions to form sheets parallel to the (001) planes. TEM also revealed that as a result from exposure to air over a period of several months, the ribbons had become prone to surface oxidation (Fig 5.15). Alternating between bright field and dark field images it could be seen oxidation had consumed almost the entirety of ribbons at the tips. Dark field image 1, shows a portion of single crystalline  $ZrS_3$  whereas dark field image 2, highlights the surrounding oxide layer. These results were confirmed by electron energy loss spectra (EELS) which revealed peaks belong to zirconium and sulfur (Fig 5.15a) and oxygen (Fig 5.15b).

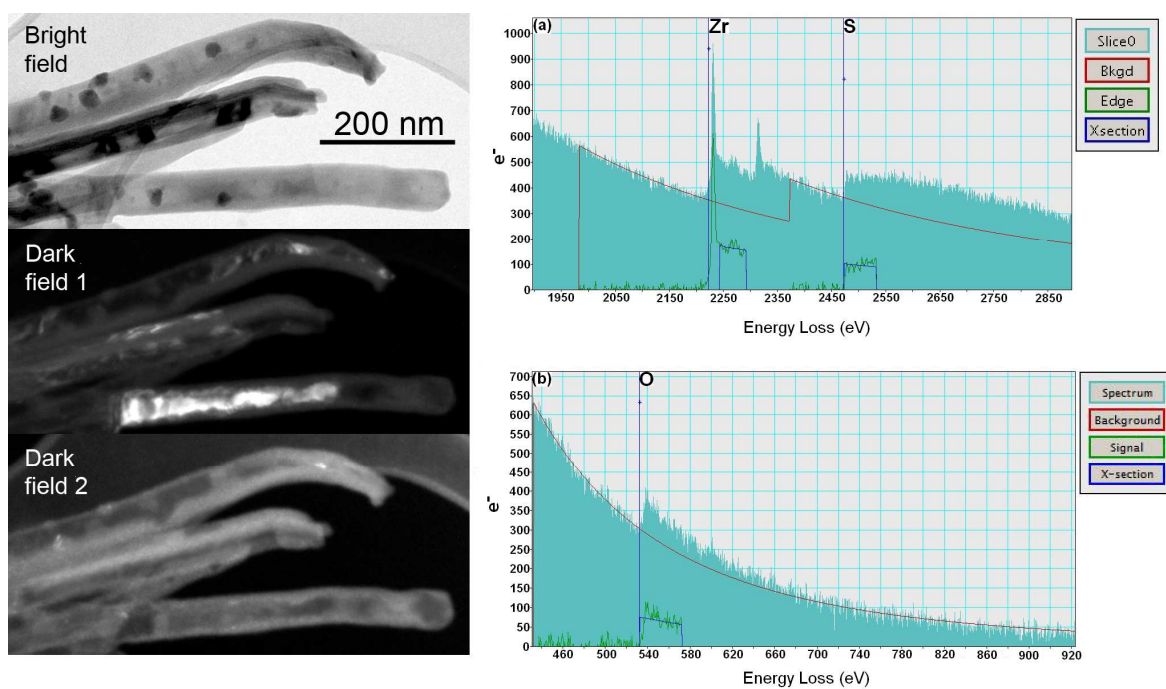


Fig 5.15 TEM (bright field) BF and (dark field) DF images of  $ZrS_3$  nanoribbons and the corresponding EELS spectra.

#### 5.4.1.4 Zirconium trisulfide; quenched Reactions

A series of quenched reactions were performed to help study the observed crystal growth. Samples **8-12**, (450 °C 1-20h) were air quenched at designated times during the reaction, (Table 5.1). High resolution SEM micrographs (Fig 5.16) show the progression of crystal growth on the foil surface from 1 - 20 hrs (**8-12**) and indicate that the onset of crystal development occurs as early as one hour into the reaction (Fig 5.16a). Previous studies of MQ<sub>3</sub> have implemented far lengthier reaction times (in the order of days) but in many cases this is to achieve the growth of large single crystals. <sup>[38]</sup> PXD of sample (**8**) reveals a broad hump at ca. 10 ° 2theta (Fig 5.17) relating to the (001) crystal plane of ZrS<sub>3</sub> which is the preferred direction of crystal growth for MQ<sub>3</sub> (along the b-axis) <sup>[47]</sup> and commonly the (001) peak is the most prominent. There are also a few peaks relating to ZrS<sub>2</sub> and ZrS phases. EDX of the platelet like crystals however gave average ratios of (At% 30 % Zr, 70 % S ± 0.73), values which are approximate to what is expected for either ZrS<sub>3</sub> or ZrS<sub>2</sub>. At 1h the substrate surface is probably not as well covered as for samples **9-12** and values obtained from EDX are likely to suffer from interference from the foil. At 2 h (**9**) nodules form with needle like structures protruding from the centres (Fig 5.16b). Samples **10 - 11** (Fig 5.16c-5.16d) show an evolution in the growth of these structures until 20 h (**12**) where they develop into electron transparent sheets (Fig 5.16e). A comparison of the PXD patterns of samples **8-12** show an increasing intensity of the peaks belonging to ZrS<sub>3</sub> but also an increasing presence of ZrS<sub>2</sub> (Fig 5.18). An indexing of reflections for sample **12** gives values;  $a = 5.10(2) \text{ \AA}$ ,  $b = 3.60(1) \text{ \AA}$ ,  $c = 9.03(4) \text{ \AA}$  and  $\beta = 98.2(9)^\circ$  corresponding to monoclinic ZrS<sub>3</sub> (P2<sub>1</sub>/m). These lattice parameters are in good agreement with the literature values ( $a = 5.1243(11) \text{ \AA}$ ,  $b = 3.6244(10) \text{ \AA}$ ,  $c = 8.980(3) \text{ \AA}$  and  $\beta = 97.28(2)^\circ$ ). <sup>[92]</sup>

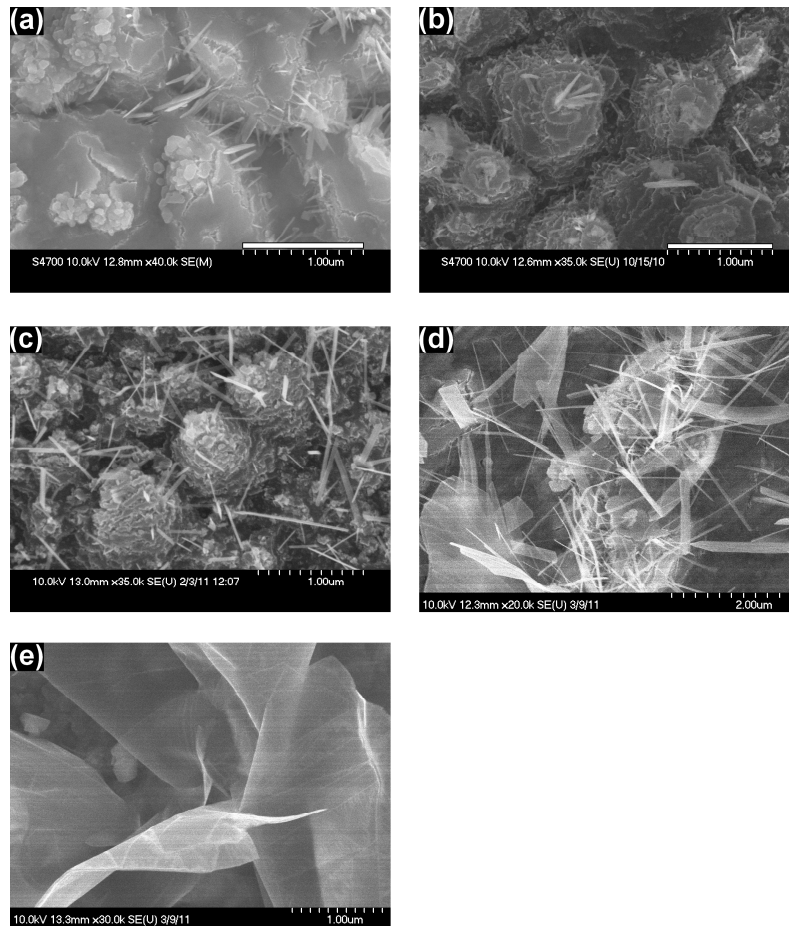


Fig 5.16 SEM micrographs showing the growth behaviour in quenched samples over a period of time (a) 1 hr (8) (b) 2 hrs (9) (c) 10 hrs (10) (d) 16 hrs (11) (e) 20 hrs (12).

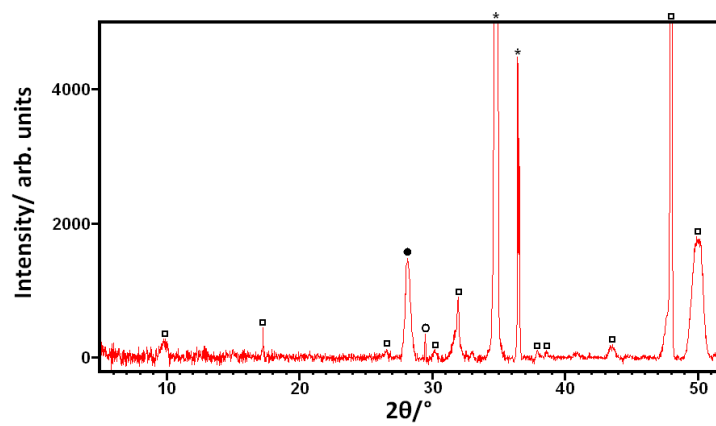


Fig 5.17 PXD Sample 8, Squares correspond to  $ZrS_3$ , filled circles to  $ZrS_2$ , open circle to  $ZrS$  and asterisks to underlying zirconium foil

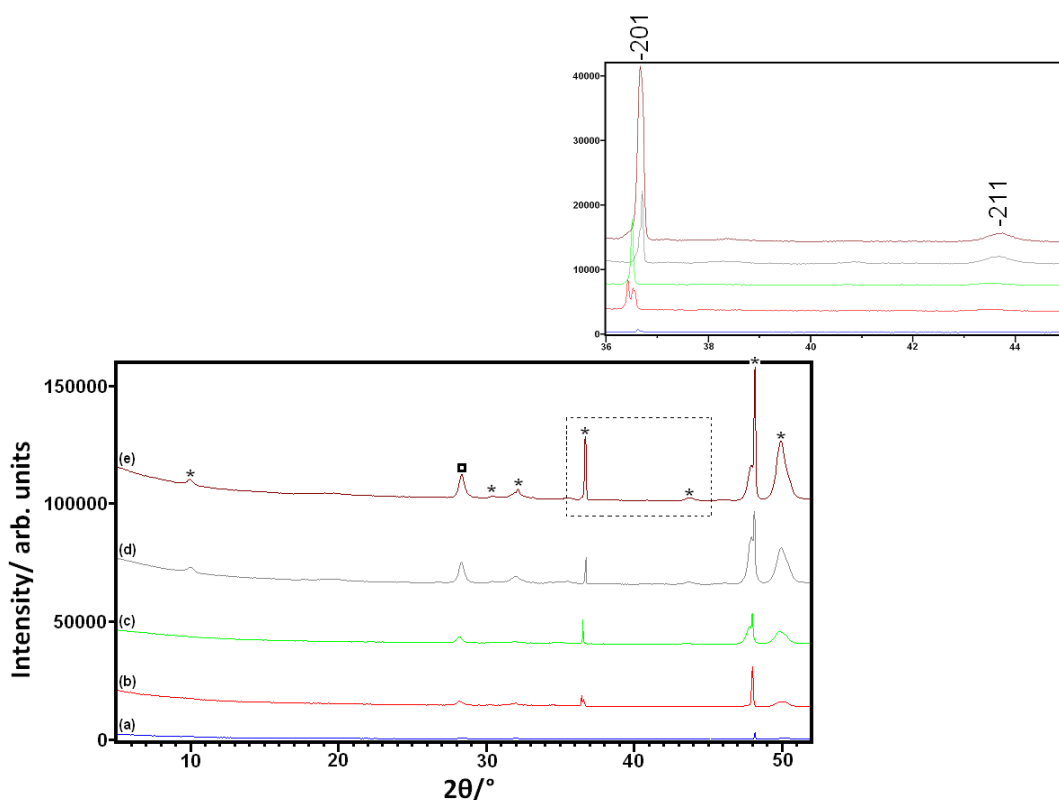


Fig 5.18 Evolution of PXD patterns over time (a) 1 hr (**8**) (b) 2 hrs (**9**) (c) 10 hrs (**10**) (d) 16 hrs (**11**) (e) 20 hrs (**12**). Zirconium foil peak at c.a. 35  $2\theta$  has been omitted for clarity. Asterisks correspond to  $ZrS_3$  and the square represents  $ZrS_2$ . Inset, shows increase in peak intensity more clearly.

A previous investigation by Zhang *et al* into  $ZrS_2$  nanobelt arrays, produced by the pyrolysis of  $ZrS_3$  nanobelts suggested a modified vapour-solid (VS) mechanism behind the crystal growth whereby reactive  $ZrS_x$  particles react with the sulfur vapour and condense onto a zirconium substrate to form stable  $ZrS_2$  seeding sites.<sup>[226]</sup> A similar hypothesis is given for the study into the growth of  $TiS_3$  nanobelts on the surface of titanium foil, where sulfur powder and titanium foil are reacted at 450 °C for 8 h to produce nanobelt films 0.1-12  $\mu\text{m}$  in width and 20-250 nm in thickness.<sup>[184]</sup> It is proposed that the nanobelts form *via* unstable  $TiS_x$  particulates reacting with sulfur in the vapour phase. These particulates condense onto the foil surface creating seeding sites from which the  $TiS_3$  nanobelts grow. It is likely that the growth of the  $ZrS_3$  nanobelts occurs via a similar mechanism. Indeed, the quenched reactions, samples **8-12**, clearly show seeding sites from which the  $ZrS_3$  nano-ribbons originate (Fig 15b), these sites absorb sulfur from the surrounding vapour and via the VS mechanism increase their size and proliferate across the foil surface. This would differ from other

metal foil/chalcogen reactions such as in the tantalum-sulfur system where analysis of TaS<sub>2</sub> nanobelts grown on the surface of tantalum foil suggested a cooperative growth mechanism.<sup>[140]</sup> An indefinite number of nanowires nucleate from the same point and grow along the same crystallographic direction simultaneously. This creates bundles of nanowires which have a tendency to fracture and split apart. Evidence of this was not observed by TEM or SEM for ZrS<sub>3</sub> and it is therefore likely that the ribbons grow independently of one another. The growth of ZnO nanobelts, where zinc powder is evaporated under a constant flow of Ar/O<sub>2</sub> and transported down stream to a silica substrate from which the structures evolve, may occur *via* a similar mechanism. Given the absence of a catalyst it is reported that growth of the ZnO nanostructures cannot occur *via* a VLS process (supported by the noticeable absence of any droplet-like formations on the ends of the nanostructures) and is instead dominated by a VS mechanism.<sup>[227]</sup> The VS mechanism could be manipulated to alter the resultant morphology by control of the gas flow rates and partial pressures of the argon, oxygen and zinc vapour. This is applicable to the Zr-S system; sulfur partial pressure likely determines the rate at which sulfur absorbs on the foil surface to form seeding sites of ZrS<sub>2</sub>/Zr<sub>x</sub>S<sub>y</sub>, from which the ZrS<sub>3</sub> nanobelts grow by further reaction with the sulfur vapour. EDX of the nodules procured by quenching samples mid reaction (samples **8-10**), suggest they are indeed composed of ZrS<sub>2</sub> (At% 36% Zr, 64% S), whereas the nanobelts themselves match to ZrS<sub>3</sub>. No droplet like formations were observed on the ends of the ZrS<sub>3</sub> structures which further support the likelihood of a VS as opposed to VLS mechanism. Sulfur partial pressure in the CVD reactions employed for this study are controlled by sulfur mass and reaction temperature. If reaction conditions analogous to those employed in the ZnO study are applied to the Zr-S (or similar) systems, greater control over factors such as the flow rate of the sulfur vapour could be obtained and therefore further variability in the resultant nanostructures could be observed.

### 5.4.2 Zirconium triselenide

Similar reaction conditions were applied as in section (5.4.1) (Table 5.1), PXD patterns of (13) (500 °C) could be matched to  $\text{ZrSe}_3$ . Reflections indexed to a monoclinic structure, space group  $P2_1/m$ ;  $a = 5.40(4) \text{ \AA}$   $b = 3.738(6) \text{ \AA}$   $c = 9.46(6) \text{ \AA}$  and  $\beta = 97.54^\circ$  and cell parameters agreed well with those for the bulk material in the literature ( $a = 5.410 \text{ \AA}$   $b = 3.748 \text{ \AA}$   $c = 9.444 \text{ \AA}$  and  $\beta = 97.48^\circ$  respectively).<sup>[45]</sup> SEM analysis of (13) revealed tubule like structures originating from clusters scattered on the surface of the foil (Fig 5.19). EDX of the particle clusters gave average ratios of (At% 41% Zr, 59% Se  $\pm$  0.58%) whereas EDX of the nanostructures gave a closer match to a 1:2 ratio (At % 31% Zr, 69% Se  $\pm$  0.47).

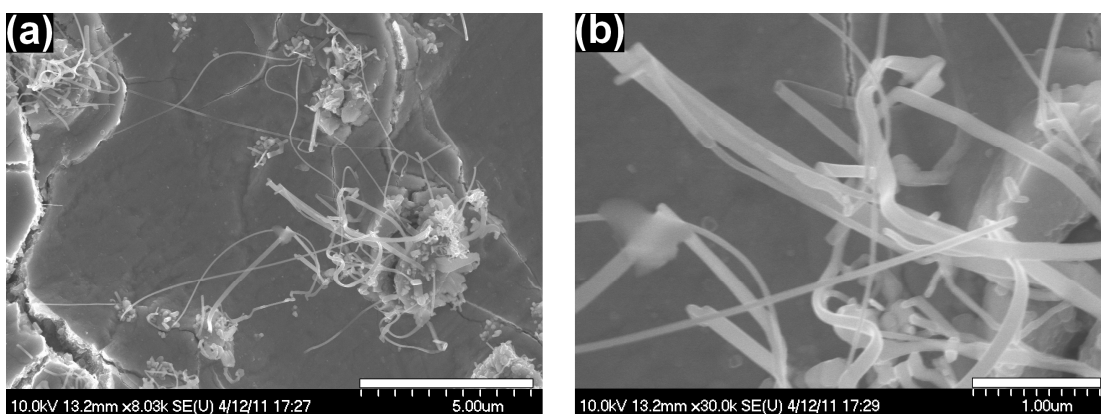


Fig 5.19 SEM Micrographs of sample 13; a) clusters from which tubule like structures are originating b) higher magnification of the nanostructures.

PXD of (14) (700 °C) matched to both  $\text{ZrSe}_2$  and  $\text{ZrSe}_3$  (Fig 5.20). Reflections indexed to hexagonal  $\text{ZrSe}_2$ , space group  $P\bar{3}m1$ ;  $a = b = 3.7733(7) \text{ \AA}$  and  $c = 6.1327(2) \text{ \AA}$  and monoclinic  $\text{ZrSe}_3$ , space group  $P2_1/m$ ;  $a = 5.407(7) \text{ \AA}$   $b = 3.755(2) \text{ \AA}$   $c = 9.45(1) \text{ \AA}$  and  $\beta = 97.86^\circ$ , both are in excellent agreement with the literature values (expected literature values for  $\text{ZrSe}_2$  are  $a = b = 3.798 \text{ \AA}$  and  $c = 6.192 \text{ \AA}$ ).<sup>[228, 45]</sup> SEM of (14) revealed ‘mounds’ composed of smaller nanoplatelets (Fig 5.21). EDX of the crystallites gave average ratios of (At% 34% Zr, 66% Se), calculation of the standard deviations ( $\sigma$ ) from five scans gave a value of  $\sigma = \pm 1.36\%$ , suggesting they are  $\text{ZrSe}_2$ . It was not possible using EDX to distinguish particles belonging to  $\text{ZrSe}_3$ . This either could be a result of interference from the underlying zirconium foil (which would diminish the overall contribution of the selenium) or that the  $\text{ZrSe}_3$  is buried beneath the

mounds of  $\text{ZrSe}_2$ , which could have formed as a result of the decomposition of  $\text{ZrSe}_3$  by a mechanism similar to that described in section (5.4.1.1)

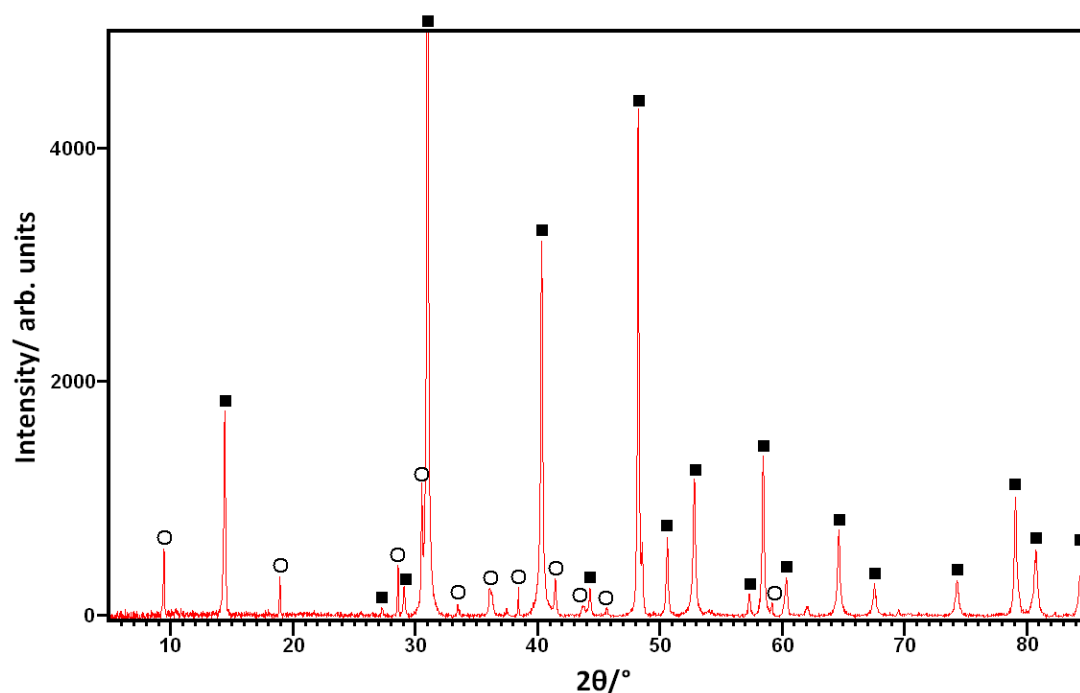


Fig 5.20 PXD pattern of sample 14, open circles represent  $\text{ZrSe}_3$  and filled squares,  $\text{ZrSe}_2$ .

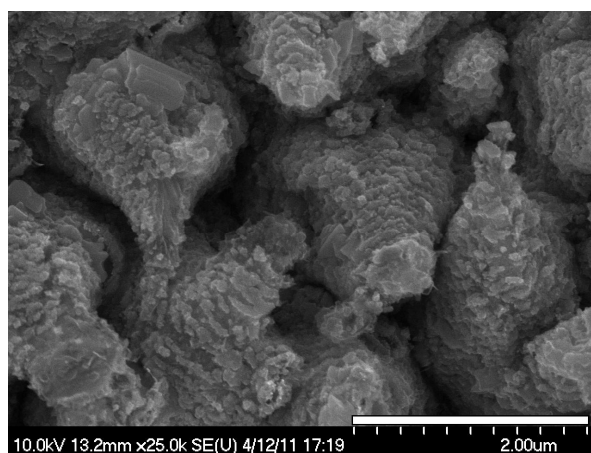


Fig 5.21 SEM Micrograph sample 14, showing the nodule formations on the foil surface.

PXD of sample 15 (900 °C) matches well to  $\text{ZrSe}_2$  (Fig 5.22a) and reflections index to hexagonal  $\text{ZrSe}_2$ , space group  $P\bar{3}m1$  with  $a = 3.75(1)$  Å and  $c = 6.112(1)$  Å, which agree well with the reported literature values ( $a = 3.771$  Å and  $c = 6.184$  Å).<sup>[228]</sup> SEM revealed clusters of oblong crystals (Fig 5.22b). EDX of these platelets using spot scans gave average values of (At% 46% Zr, 54% Se  $\pm$  1.11%). This inconsistency with  $\text{ZrSe}_2$  is likely a result of interference from the underlying zirconium foil.

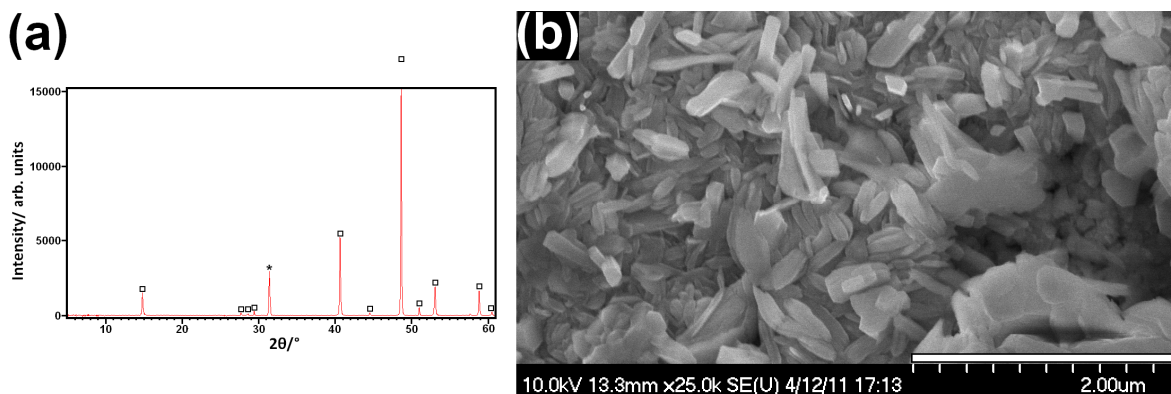


Fig 5.22 a) PXD pattern of sample 15, squares represent  $ZrSe_2$  and the asterisk corresponds to the underlying zirconium foil b) SEM Micrograph of sample 15, showing clusters of  $ZrSe_2$  crystallites.

Increasing the reaction time from 24 h to 60 h and using a reaction temperature of 650 °C, sample 16 (Table 5.1), produced a mixed phase outcome that was composed of microribbons sitting above a dense layer that covered the entire surface of the foil (Fig 5.23). EDX analysis of the microstructures revealed a 1:3 ratio of Zr to Se (At % 25.6% Zr, 74.4% Se  $\pm$  0.58%) whereas the layer beneath had a closer match to a 1:2 ratio (At% 40% Zr 60.% Se  $\pm$  1.38%).

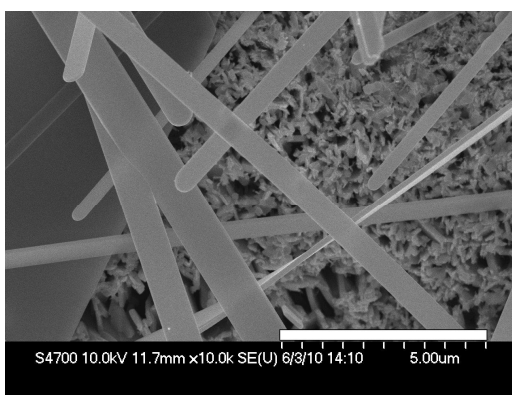


Fig 5.23 SEM micrograph of sample 16 showing  $ZrSe_3$  micro-structures

PXD of (16) reveals a match to both  $ZrSe_3$  and  $ZrSe_2$  (Fig 5.24). Indexing of reflections corresponding to  $ZrSe_3$  gave values of;  $a = 5.41(1) \text{ \AA}$ ,  $b = 3.754(6) \text{ \AA}$ ,  $c = 9.48(3) \text{ \AA}$ ,  $\beta = 96.920^\circ$  (monoclinic,  $P2_1/m$ ) which are in good agreement with the literature values ( $a = 5.410 \text{ \AA}$   $b = 3.748 \text{ \AA}$   $c = 9.444 \text{ \AA}$  and  $\beta = 97.48^\circ$  respectively).<sup>[45]</sup> Application of the Scherrer<sup>[163]</sup> equation to sample 16, (using a standard bulk sample as a comparison) calculated an average crystallite size as approximately 1.14  $\mu\text{m}$ .

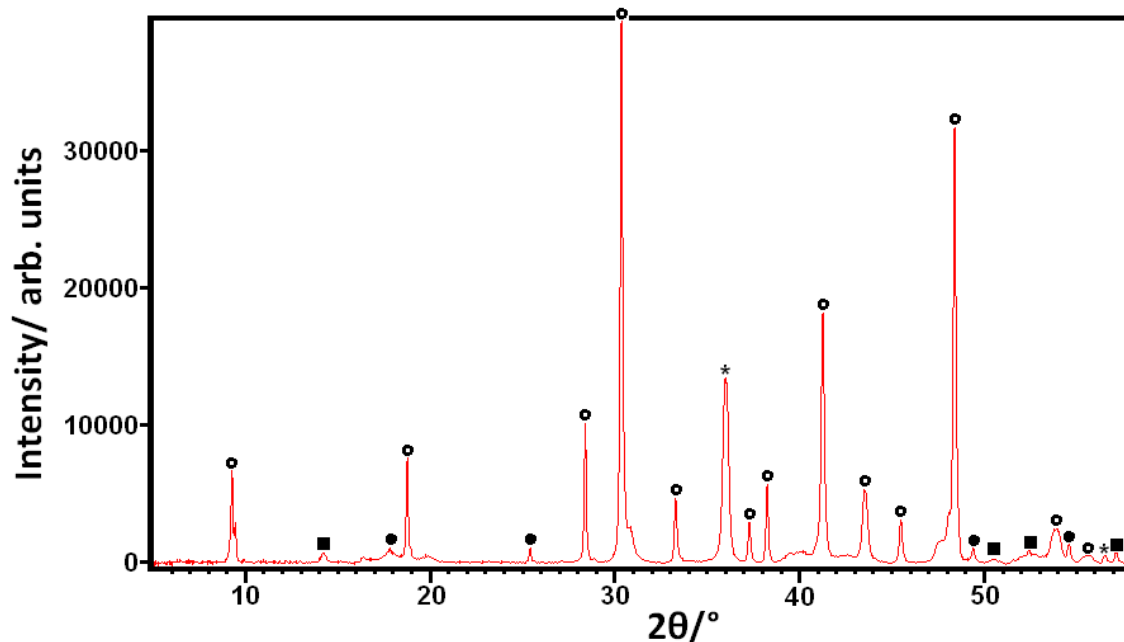


Fig 5.24 PXD pattern of sample **16**, circles represent  $ZrSe_3$  and filled squares  $ZrSe_2$ ; filled circles are unidentified peaks possibly belonging to excess selenium and asterisks represent underlying zirconium foil.

To summarise the outcomes in the Zr-Se system, at 500 °C (**13**)  $ZrSe_3$  is formed, producing tubule-like structures which originate from clusters of smaller particulates. Increasing the temperature to 700 °C (**14**) produces a mixed phase of  $ZrSe_3$  and  $ZrSe_2$  with SEM revealing mounds of small  $ZrSe_2$  particulates (Fig 5.21). A further increase to 900 °C (**15**) produces solely micro-platelets of  $ZrSe_2$ . An increase in reaction time (in respect to the previous samples) at 650 °C, (**16**) produces microribbons of  $ZrSe_3$  which sit upon a dense layer of  $ZrSe_2$ . Drawing from the analysis of crystal growth in the Zr-S system, it is likely in the case of (**13**) that the clusters are  $ZrSe_x$  particulates from the vapour condense onto the foil surface which absorb more selenium from the surrounding atmosphere to mediate growth of  $ZrSe_3$  nanotubes *via* a VS mechanism. In the case of (**16**) however, SEM micrographs suggest a different growth mechanism (Fig 5.25). From Fig 5.25 three distinct layers can be established: 1) the underlying zirconium foil, 2) a micron thick layer of  $ZrSe_2$ , 3) a surface decorated in  $ZrSe_3$  microribbons which appear to be growing from the  $ZrSe_2$  layer beneath. It suggests that the  $ZrSe_2$  forms prior to the  $ZrSe_3$  microribbons and a shorter reaction time for (**16**) would inhibit the growth of the triselenide. Tilting the substrate to approximately 45 °, an additional layer beneath the dense  $ZrSe_2$  region is found (Fig 5.26).

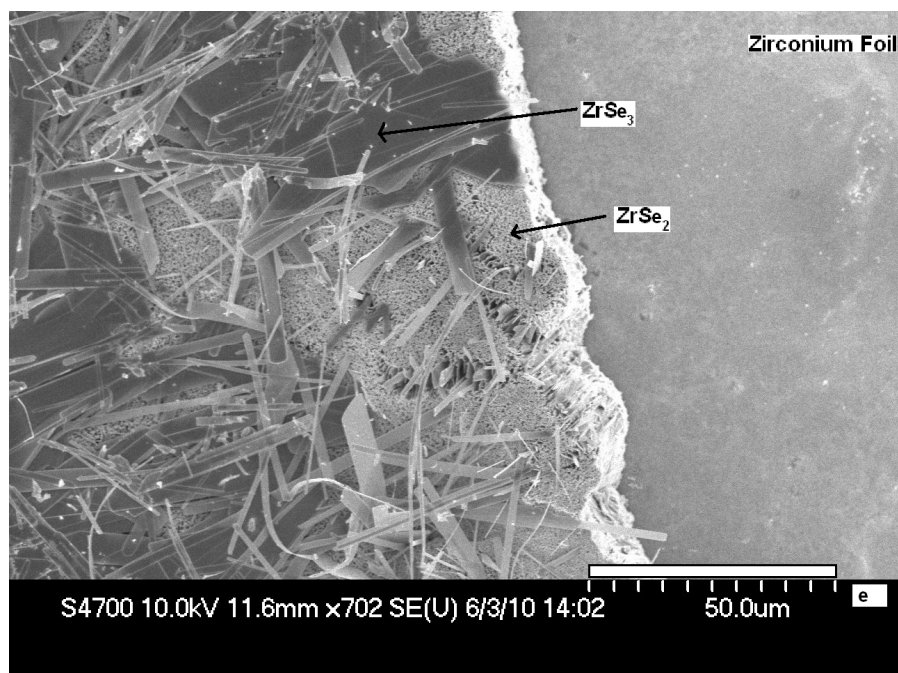


Fig 5.25 SEM micrograph showing the three layers present in sample 16; underlying zirconium foil, layer of  $ZrSe_2$  and top layer of  $ZrSe_3$ .

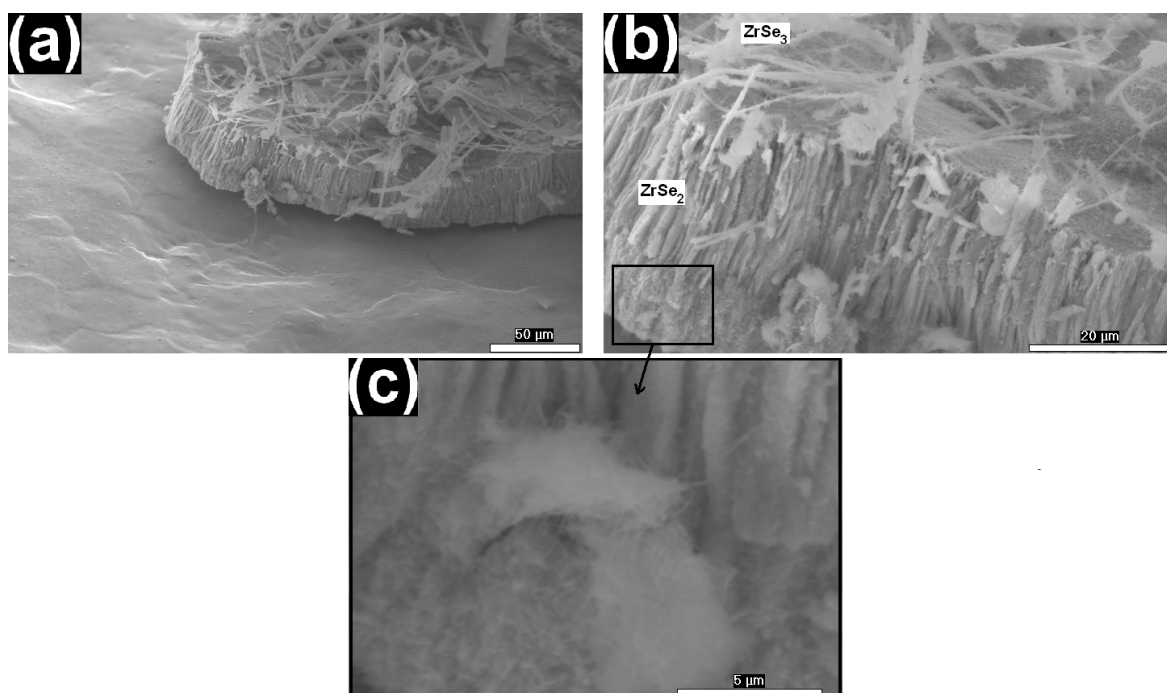


Fig 5.26 SEM micrograph showing the three layers present in sample 16 at a 45 degree tilt; a) low magnification image of micro thick layer grown on foil surface b) higher magnification of the two identified layers,  $ZrSe_2$  and  $ZrSe_3$  c) unidentified additional low-density layer beneath  $ZrSe_2$ .

The SEM micrographs presented in Fig 5.26 reveal that the micron thick  $ZrSe_2$  layer is composed of vertically aligned tubule-like structures. One could speculate that sonication of this layer may produce stand alone nanostructures. Interestingly, beneath  $ZrSe_2$  is an additional layer consisting of a low density

material. This is unfortunately a very recent discovery in the timeline of this thesis and it was not possible to conduct EDX to determine its composition. It would be curious to see if such a formation has been achieved in the foil reactions of other materials described in other sections in this chapter.

### 5.4.3 Hafnium trisulfide

Employing similar reaction conditions to sections (5.4.1) and (5.4.2), (Table 5.2), petal-like structures are obtained in the hafnium - sulfur system. PXD of sample **17** (450 ° C, 24h) revealed a multiphase outcome (Fig 5.27a). Table 5.4 gives a list of the experimental peaks and potential matches to either  $\text{HfS}_3$ ,  $\text{HfS}_2$  and/or  $\text{Hf}_{2.8}\text{S}_4$ .

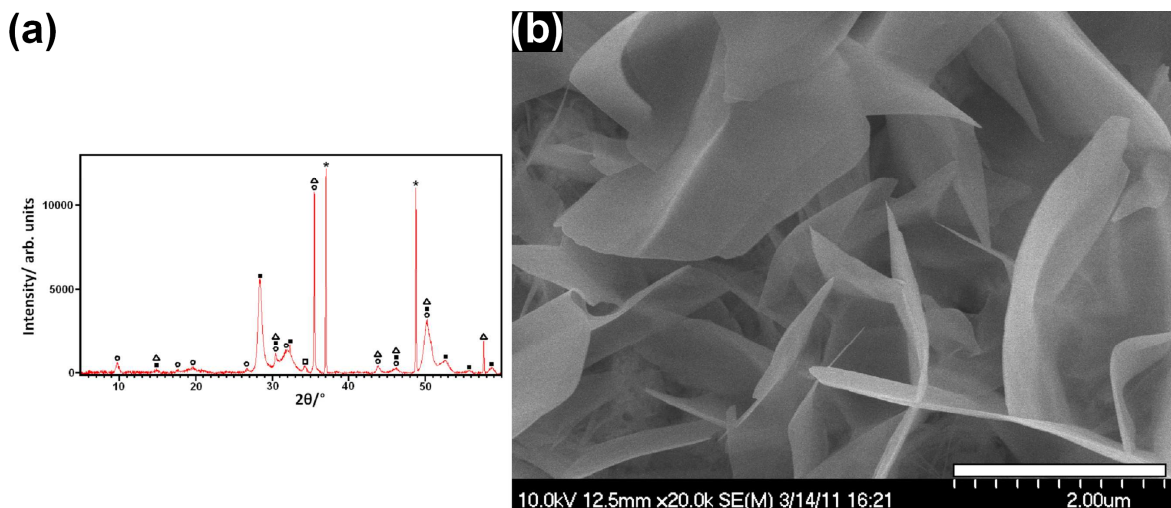


Fig 5.27 a) PXD pattern of **17**; open circles denote  $\text{HfS}_3$ , filled squares represent  $\text{HfS}_2$ , triangles correspond to  $\text{Hf}_{2.8}\text{S}_4$ . Asterisks match to the underlying Zr foil and the open square is an unidentifiable peak. b) SEM Micrograph of sample **17** showing petal-like nanostructures.

Table 5.4 Peak list for sample 17, shows phases present and the deviation in  $2\theta$  from expected values. Fields marked with a star correspond to the hafnium foil.

Sample 17 $2\theta / ^\circ$ (Rel. Int. %)	HfS <sub>3</sub> <sup>[45]</sup> $2\theta / ^\circ$	$\Delta$ $\pm 2\theta / ^\circ$	HfS <sub>2</sub> <sup>[229]</sup> $2\theta / ^\circ$	$\Delta$ $\pm 2\theta / ^\circ$	Hf <sub>2.8</sub> S <sub>4</sub> <sup>[214]</sup> $2\theta / ^\circ$	$\Delta$ $\pm 2\theta / ^\circ$
9.80 (4.70)	9.91	(-) 0.11	-	-	-	-
14.89 (1.16)	-	-	15.13	(-) 0.24	15.06	(-) 0.17
17.73 (1.07)	17.54	(+) 0.19	-	-	-	-
19.56 (1.98)	19.93	(-) 0.37	-	-	-	-
26.78 (2.22)	26.66	(+) 0.12	-	-	-	-
28.31 (46.44)	-	-	28.30	(+) 0.01	-	-
30.45 (10.35)	30.50	(-) 0.05	30.55	(-) 0.10	30.39	(+) 0.06
32.28 (15.52)	32.00	(+) 0.28	32.28	0	-	-
34.27 (4.23)	-	-	-	-	-	-
35.51 (89.26)	35.53	(-) 0.02	-	-	35.23	(+) 0.28
37.02 (100)	*	*	*	*	*	*
43.83 (3.77)	43.80	(+) 0.03	-	-	43.51	(+) 0.32
46.28 (2.35)	46.25	(+) 0.03	46.56	(+) 0.03	46.30	(-) 0.02
48.77 (90.80)	*	*	*	*	*	*
50.16 (16.12)	50.76	(-) 0.60	50.19	(-) 0.03	50.68	(-) 0.52
52.66 (6.31)	-	-	52.71	(-) 0.05	-	-
55.84 (1.08)	-	-	55.41	(+) 0.43	-	-
57.64 (16.03)	-	-	-	-	57.18	(+) 0.46
58.61 (3.46)	*	*	*	*	*	*
60.39 (2.96)	-	-	59.91	(+) 0.48	60.25	(+) 0.14

An indexing of each phase of (17) is given in Table 5.5 all of which were in good agreement the corresponding literature values. The largest deviation is an expansion in the c parameter of  $\approx 0.04 \text{ \AA}$  for the HfS<sub>2</sub> phase. <sup>[229]</sup>

Table 5.5 Indexed phases of sample 17 with the deviation from in literature values alongside in grey.

Phase	a (Å)	b (Å)	c (Å)	B (°)
	$\Delta(\pm 2\theta)$	$\Delta(\pm 2\theta)$	$\Delta(\pm 2\theta)$	$\Delta(\pm ^\circ)$
HfS <sub>3</sub> <sup>[45]</sup> (monoclinic, P2 <sub>1</sub> /m)	5.100	3.594	8.992	98.16
	5.09(1) (-0.01)	3.593(9) (-0.001)	9.02(2) (+0.02)	98.2(5) (+0.04)
HfS <sub>2</sub> <sup>[229]</sup> (hexagonal, P $\bar{3}$ m1)	3.632	-	5.847	-
	3.634(8) (+0.002)	-	5.895(4) (+0.048)	-
Hf <sub>2.8</sub> S <sub>4</sub> <sup>[214]</sup> (Cubic, Fd $\bar{3}$ m)	10.180	-	-	-
	10.16(8) (-0.02)	-	-	-

EDX of the petal-like structures gave average ratios of (At% 34.4% Hf, 65.6% S). This could be interpreted as corresponding to HfS<sub>2</sub> or the values could simply be an elemental average across the several phases. EDX was obtained by spot scans of individual petals. A calculation of the standard deviation ( $\sigma$ ) from five spot scans gave a value of  $\sigma = \pm 0.8559\%$ . The small standard deviation suggests that (17) is likely composed of HfS<sub>2</sub> petals rather than structures being a whole range of different stoichiometries.

#### 5.4.3.1 Raman spectra and reaction at 650 °C

The Raman spectrum of sample 17 revealed peaks matching to HfS<sub>3</sub>; 221 cm<sup>-1</sup>, 277 cm<sup>-1</sup>, 320 cm<sup>-1</sup> and 522 cm<sup>-1</sup>. All four peaks show a slight downshift from expected values of c.a. 5 cm<sup>-1</sup> <sup>[207]</sup> (Fig 5.28). The remaining peaks at 362, 425, 507, 582 and 729 cm<sup>-1</sup> do not match to either HfS<sub>3</sub> or HfS<sub>2</sub>. <sup>[230]</sup> This contrasts slightly with the corresponding PXD and EDX data. The reasons for which are discussed later in section 5.4.3.1.

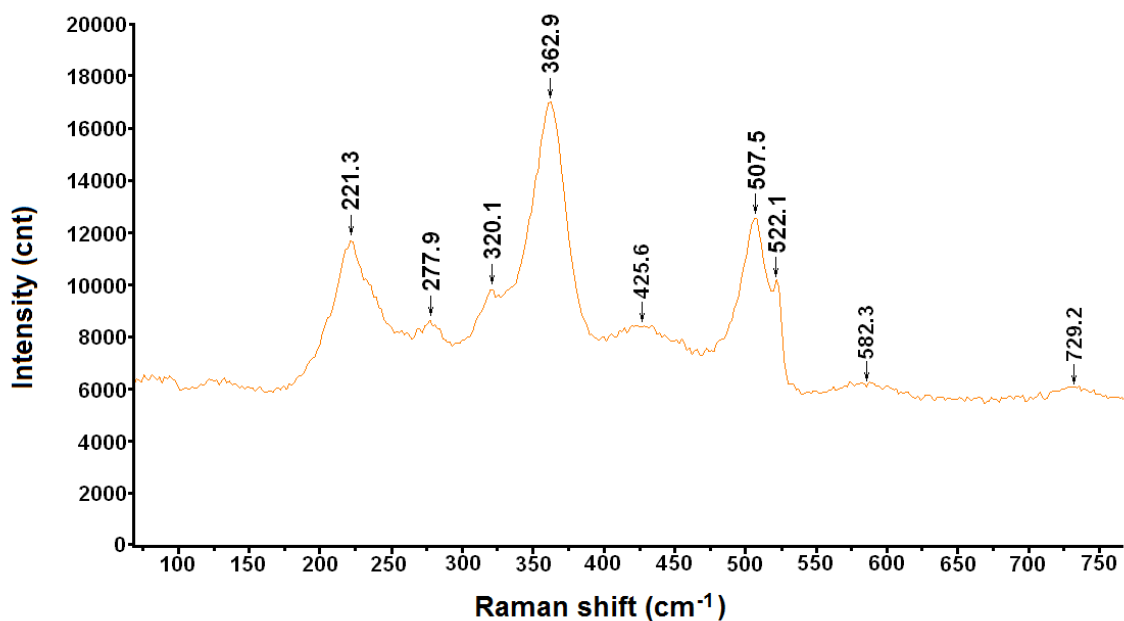


Fig 5.28 Room temperature Raman spectrum of sample 17 with a wavelength of exciting light of 532 nm.

An increase in temperature to 650 °C (**18**) (Table 5.2) produces electron transparent ribbons measuring several microns in width and tens of nanometres in thickness (Fig 5.29).

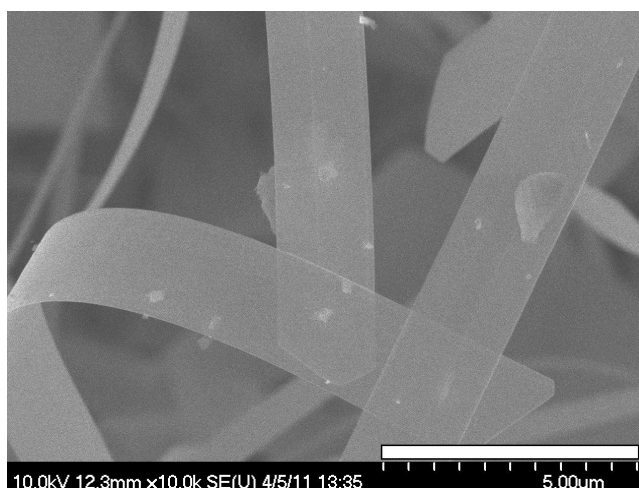


Fig 5.29 SEM micrograph of sample **18** showing the micron sized ribbons.

PXD of (**18**) reveals a sharp pattern in contrast to (**17**), suggesting that (**18**) is very crystalline. It has a good match to  $\text{HfS}_3$  (Fig 5.30). Indexing of reflections gives values of;  $a = 5.08(4) \text{ \AA}$ ,  $b = 3.582(8) \text{ \AA}$ ,  $c = 8.99(7) \text{ \AA}$  and  $\beta = 97.810^\circ$  (monoclinic, space group  $P2_1/m$ ). These agree well with the reported literature values. <sup>[92]</sup> EDX gave average values of (At % 28.05% Hf, 71.95% S  $\pm$  2.23%) which further support that the ribbons are composed of  $\text{HfS}_3$ . Application of the

Scherrer <sup>[163]</sup> equation to sample **18** (using a standard bulk sample as a comparison) calculated an average crystallite size as approximately 1.19  $\mu\text{m}$ . The Raman spectrum displayed five peaks; 125.0  $\text{cm}^{-1}$ , 210.4  $\text{cm}^{-1}$ , 251.9  $\text{cm}^{-1}$ , 314.7  $\text{cm}^{-1}$  and 519.7  $\text{cm}^{-1}$ ; all correspond to  $A_g$  phonon modes in  $\text{HfS}_3$  except for the initial peak which corresponds to a  $B_g$  mode (Fig 5.31). The peaks show a slight downshift from the reported bulk values; 130  $\text{cm}^{-1}$ , 221  $\text{cm}^{-1}$ , 262  $\text{cm}^{-1}$ , 322  $\text{cm}^{-1}$ , 527  $\text{cm}^{-1}$  (c.a. 8  $\text{cm}^{-1}$ ). <sup>[207]</sup> This could again be a reflection on the dimensions of the sample and a result of phonon confinement, like those reported for nanostructures of  $\text{ZrS}_3$ . <sup>[219]</sup>

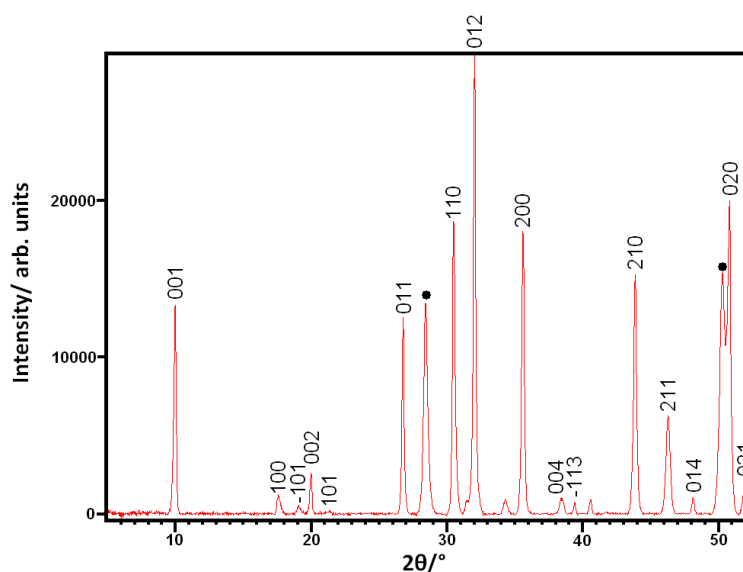


Fig 5.30 PXD pattern of sample **18**; indexed reflections correspond to  $\text{HfS}_3$ , filled circles represent  $\text{HfS}_2$ .

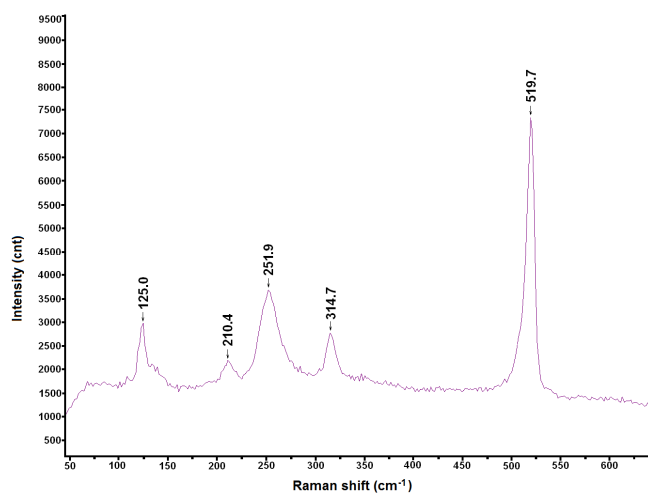


Fig 5.31 Room temperature Raman spectrum of sample **18** with a wavelength of exciting light of 532 nm.

### 5.4.3.1 TEM investigations

TEM studies have shown that **(18)** is indeed composed of micron sized  $\text{HfS}_3$  ribbons of nanometre scale thickness which yield well defined diffraction patterns that can be matched to monoclinic  $\text{HfS}_3$ . In other words, each ribbon is single crystalline, which also accounts for the very sharp peaks seen in the PXD patterns (Fig 5.30). From the diffraction pattern of a piece of ribbon, the  $a$  and  $b$  lattice parameters could be determined as  $a = 5.05(1) \text{ \AA}$  and  $b = 3.59(2) \text{ \AA}$ . These are in good agreement with the literature values ( $a = 5.0923(11) \text{ \AA}$  and  $b = 3.5952(7) \text{ \AA}$ )<sup>[92]</sup> (Fig 5.32).

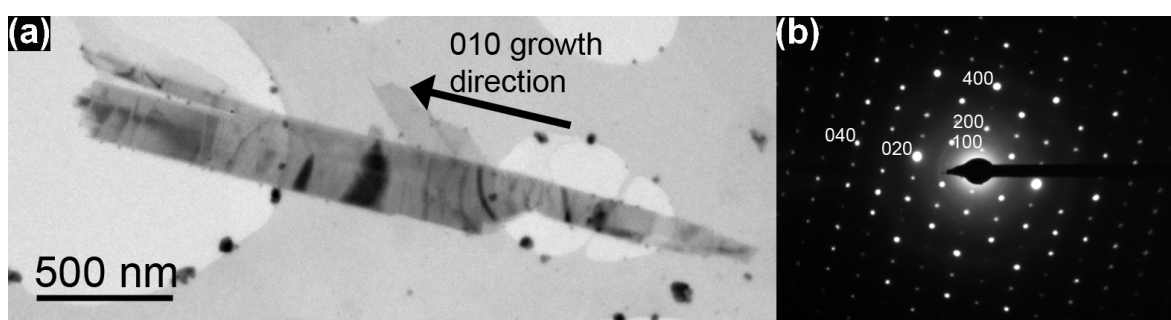


Fig 5.32 (a) Bright field TEM micrograph of a  $\text{HfS}_3$  ribbon, (b) selected area diffraction pattern. The orientation of the crystallite is in the  $ab$  plane. The image has been rotated  $90^\circ$  to be in alignment with the  $[010]$  growth direction.

TEM studies performed on another ribbon (this time in the  $b$ - $c$  plane) produced nano diffraction patterns that were used to calculate the lattice parameters as  $b = 3.59(2) \text{ \AA}$  and  $c = 8.9(1) \text{ \AA}$ , again in good agreement with the literature values ( $b = 3.5952(7) \text{ \AA}$  and  $c = 8.967(2) \text{ \AA}$ ) (Fig 5.33).<sup>[92]</sup>

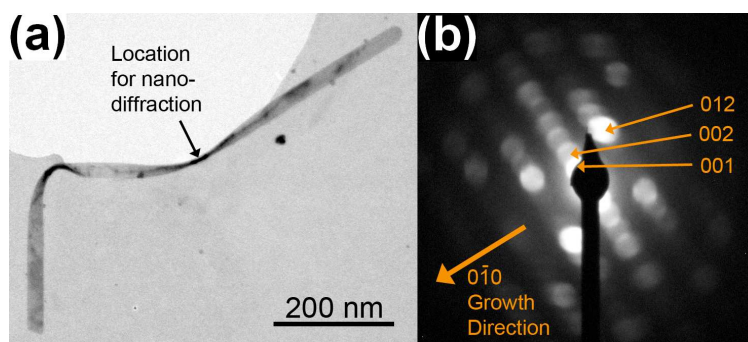


Fig 5.33 (a) Bright field TEM micrograph of a  $\text{HfS}_3$  ribbon, (b) selected area nano diffraction pattern from the same ribbon. The orientation of the crystallite is in the  $bc$  plane. The image has been rotated  $90^\circ$  to be in alignment with the  $010$  growth direction.

Like  $ZrS_3$ , it could be determined that the growth direction of the long axis of the ribbon is parallel to the (010) plane and that the thinnest direction is parallel to (001).

EELS spectra confirmed that the ribbons were composed of hafnium and sulfur with no oxide layer as seen in section 5.4.1.3 (Fig 5.34).

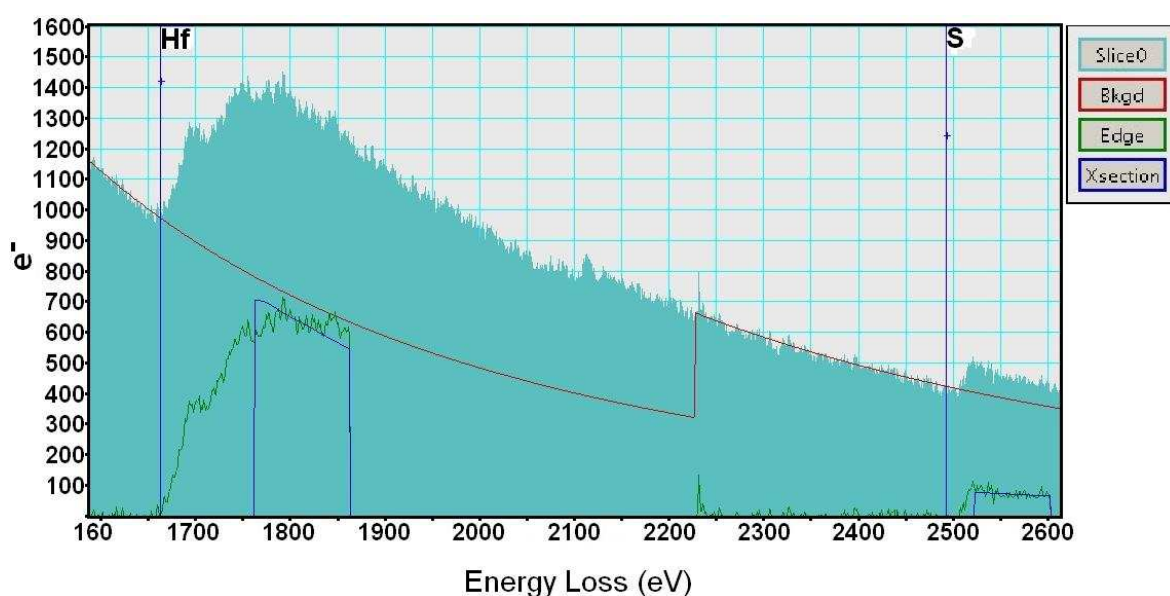


Fig 5.34 EELS spectra of sample (18) showing the presence of hafnium and sulfur.

#### 5.4.3.3 $HfS_3$ reactions with hafnium powder

In an alternative reaction, the foil was substituted with hafnium powder and reacted under the same conditions as (17), (450 °C, 24h), (19) (Table 5.2) and produces a close match to  $HfS_3$  with some peaks belonging to  $HfS_2$  (Fig 5.35a). Indexing of  $HfS_3$  reflections gave values;  $a = 5.082(4)$  Å  $b = 3.583(4)$  Å,  $c = 8.95(1)$  Å and  $\beta = 98.160^\circ$  (monoclinic, space group P21/m) which are in good agreement with previously reported literature values.<sup>[92]</sup> An SEM micrograph of (19) reveals a similar morphology to sample 17 with clusters of petal like structures (Fig 5.35b). EDX of these structures gives average values of (At % 29.1% Hf, 70.9% S). EDX was taken using spot scans of individual plates and the calculated standard deviation ( $\sigma$ ) from the values given in (Table 5.8) gave a significance of  $\sigma = \pm 0.992\%$ . The obtained EDX values lie between what would be expected for either  $HfS_2$  or  $HfS_3$ . Equally, the broadness of the peaks of the PXD pattern of (19) weaken the credibility of a clear match to  $HfS_3$  since it is

difficult to determine the exact  $2\theta$  value for each peak. Annealing of sample **19** may improve crystallinity and produce sharper peaks and make sample identification easier.

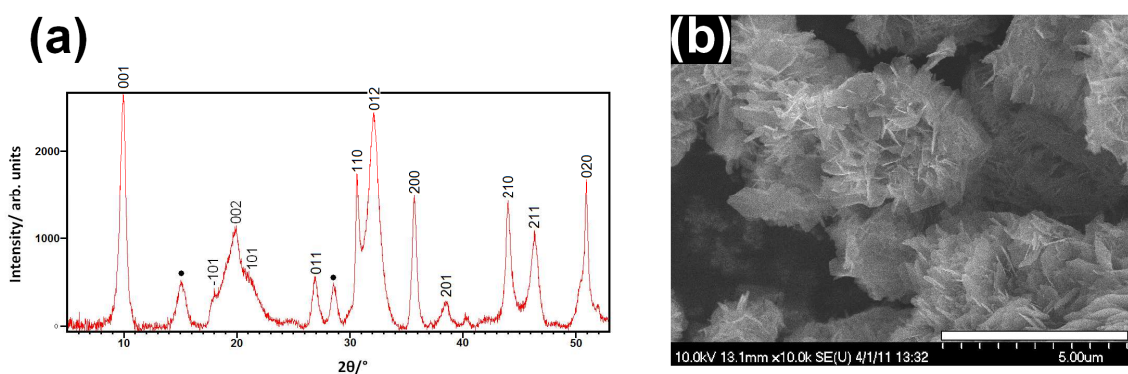


Fig 5.35 a) PXD of Sample **19**, indexed reflections refer to  $\text{HfS}_3$ , filled circles represent  $\text{HfS}_2$  b) SEM micrograph of sample **19**, showing platelet like morphology.

There is no phase diagram of the Hf-S system available to help ascertain the best synthetic conditions to obtain single phase products, but there are six reported binary stoichiometric phases;  $\text{Hf}_2\text{S}$ ,  $\text{HfS}$ ,  $\text{Hf}_3\text{S}_4$ ,  $\text{HfS}_2$  and  $\text{HfS}_3$ .<sup>[231]</sup> The latter two form at a 66.7-75 % sulfur composition and growth of  $\text{HfS}_3$  single crystals occurs between 600 °C - 800 °C.<sup>[47]</sup> In addition, in similarity to the Zr-S system, there are a number of known non-stoichiometric phases (e.g.  $\text{Hf}_{x-1}\text{S}$ , where  $x \approx 0.25$ ).<sup>[215]</sup> From the results obtained in this study, it can be determined that at 450 °C (**17**) a multiphase product possibly containing non-stoichiometric sulfides is produced. All peaks present in the PXD of (**17**) (Fig 5.27a) cannot be explained by  $\text{HfS}_3$  and  $\text{HfS}_2$  alone (although these are certainly the dominant phases) but a convincing match to  $\text{Hf}_{2.8}\text{S}_4$  is questionable. The unidentified peaks were successfully indexed to a cubic phase but there are a number of non-stoichiometric phases in the Hf-S system with a NaCl type structure, of general formula  $\text{Hf}_{x-1}\text{S}$ .<sup>[218]</sup> The unidentified peaks, therefore, can be tentatively attributed to a non-stoichiometric phase but given the current information, it cannot be stated with any certainty what the composition of this phase is. For this reason one is hesitant to associate the unidentified peaks in the Raman to surface optical phonon modes (SO) or any other nanostructure related anomalies without fully understanding the composition of sample **17** first. Raman samples

were prepared like those for TEM, by sonication of the foil in *iso*-propanol. It became clear during microscopy that the sonication of the foil had created debris (likely from the mechanical cleaving of the 2D structures plus possible mixing of other phases) which covered the surface of the nanostructures. This led to difficulty in obtaining clear diffraction patterns. It is therefore likely that the obtained Raman spectra would suffer from the same issue and that the obtained spectra would not simply be of the nanostructures but particulates present on their surface as well. By 600 °C (**18**), HfS<sub>3</sub> becomes the dominant phase. PXD of (**18**) gives a clear match to HfS<sub>3</sub> with few remaining peaks belonging to HfS<sub>2</sub> (Fig 5.30). The Raman spectrum and electron diffraction data clearly identify the major phase as HfS<sub>3</sub>, supported by the values obtained with EDX. There are no reported syntheses of HfS<sub>3</sub> nanostructures but there are reports of HfS<sub>2</sub> nanotubes, which were prepared by reaction of HfS<sub>3</sub> in an H<sub>2</sub>/Ar atmosphere. [232] Rao *et al* similarly noted an expansion in the *c*-lattice parameter [202] of HfS<sub>2</sub> nanotubes (of the order of ~1%), comparable to the 0.75% expansion for (**17**). HfS<sub>2</sub>-inorganic fullerene (IF) structures have also been synthesised via microwave-induced plasmas under a N<sub>2</sub>/H<sub>2</sub> atmosphere. [233] In both instances decomposition of HfS<sub>3</sub> has facilitated the formation of the HfS<sub>2</sub> nanostructures and it is suggested that HfS<sub>2</sub> grows from the surface of HfS<sub>3</sub> particles. Disulfide layers initially form, trapping trisulfide particles preventing them from aggregating. These then decompose to form the HfS<sub>2</sub>-tubules. [201] The dichalcogenides of group-IV transition metals generally tend to form at higher temperatures to the trichalcogenides as has been shown in the study of TiS<sub>3</sub> nanobelts [184]. It was found that annealing the TiS<sub>3</sub> nanobelts at 600 °C for two hours pseudomorphically reduced them to TiS<sub>1.7</sub>. Given the similarity of the Hf-S system to the Zr-S system, however, it is likely (**18**) forms *via* a similar mechanism described in section (5.4.1.4). If one were to anneal sample (**18**) at temperatures above 650 °C perhaps one could pseudomorphically reduce the HfS<sub>3</sub> nanoribbons to HfS<sub>2</sub> nanoribbons or another non-stoichiometric equivalent.

#### 5.4.4 Hafnium triselenide

A similar investigation to that performed in the Hf-S system was carried out in the hafnium - selenium system; samples **20-22** (Table 5.2), (450 °C; 24, 60, 120 h respectively). PXD of samples **20 - 21** give a clear match to HfSe<sub>3</sub> (Fig 5.36) and all three patterns were indexed to the monoclinic structure of HfSe<sub>3</sub>, in space group P2<sub>1</sub>/m. The specific lattice parameters are given in (Table 5.6).

Table 5.6 Indexed cell parameters for samples **20-21**, compared to HfSe<sub>3</sub>.

	a/Å	b/Å	c/Å	$\beta$ /°
HfSe <sub>3</sub> [45]	5.3880	3.7216	9.4280	97.780
Sample <b>20</b>	5.38(2)	3.719(2)	9.50(4)	97.9(1)
Sample <b>21</b>	5.375(4)	3.715(1)	9.435(8)	98.2(4)
Sample <b>22</b>	5.387(8)	3.717(2)	9.43(1)	97.6(2)

All samples are in good agreement with previous literature values with the exception of (**20**) which shows a slight increase in the c-parameter (c.a. 0.3%). An SEM micrograph of sample **20** reveals mixed morphology, with nanowire-like structures propagating from large clumps of HfSe<sub>3</sub> (Fig 5.37). The wires are on average approximately 1µm in length and ≤ 100 nm thick. EDX performed on the nanowires gives average ratios of (At % 26.75% Hf, 73.24% Se ±1.36%) corresponding to HfSe<sub>3</sub>.

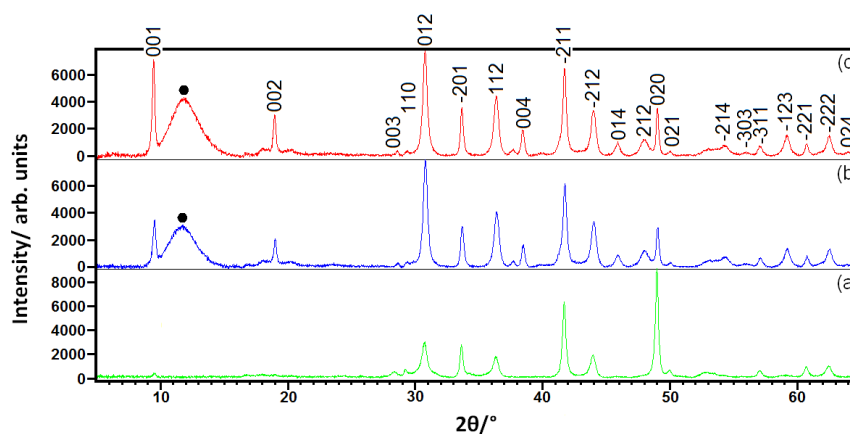


Fig 5.36 PXD patterns of samples **20-22**. Indexed reflections correspond to HfSe<sub>3</sub>: a) sample **20**, 24 h b) sample **21**, 60 h c) sample **22**, 120 h. Filled circles correspond to vacuum grease used to fix samples **20** and **21** to the flat glass plate.

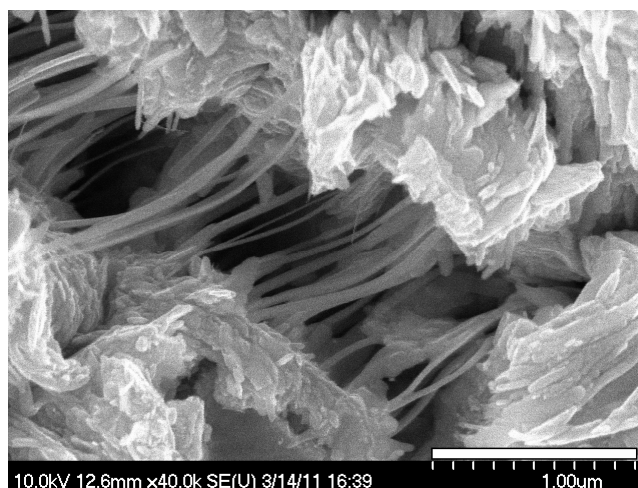


Fig 5.37 SEM Micrograph sample 20, showing mixed morphology of product

An increase in reaction time to 60 h (21) and 120 h (22) yields a more homogeneous morphology across the sample and produces an increase in the dimensions of the  $\text{HfSe}_3$  nanostructures (Fig 5.38). They are more rigid in appearance and have increased in thickness to  $\geq 100$  nm.

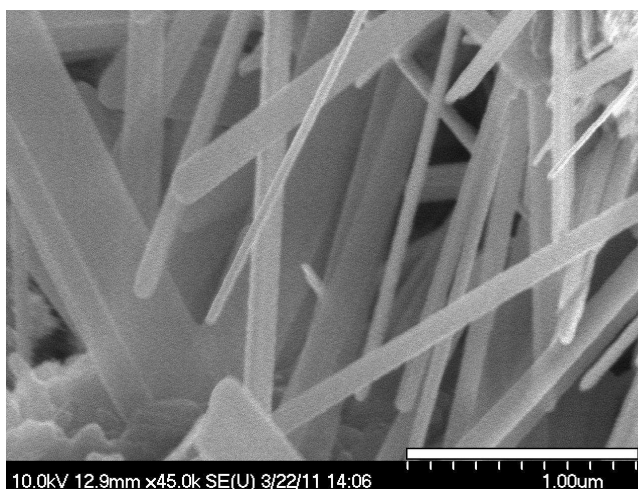


Fig 5.38 SEM Micrograph sample 21, showing the rigidity of the nanostructures

To the author's knowledge this is the first reported example of nanostructured  $\text{HfSe}_3$ . There is, in fact, little reported on  $\text{HfSe}_3$  in general. Previous studies have focused on the crystal structure <sup>[45,47,83]</sup> and optical properties <sup>[103,220]</sup> of  $\text{HfSe}_3$ -single crystals several millimetres in size. The Raman spectrum of sample 22 has seven peaks;  $62.7\text{ cm}^{-1}$ ,  $97.6\text{ cm}^{-1}$ ,  $170.5\text{ cm}^{-1}$ ,  $205\text{ cm}^{-1}$ ,  $233.9\text{ cm}^{-1}$ ,  $253.7\text{ cm}^{-1}$ ,  $291.5\text{ cm}^{-1}$  (Fig 5.39). All seven peaks display a slight downshift from previously reported literature values <sup>[220]</sup> (on average c.a.  $4.5\text{ cm}^{-1}$ ) and with the exception of the bands at  $141.3\text{ cm}^{-1}$  and  $253.7\text{ cm}^{-1}$ , peaks all correspond to  $A_g$  phonon

modes. It is noted that for single crystals, the peak at  $253.7\text{ cm}^{-1}$  does not appear with freshly cleaved crystal surfaces and is attributed to impurities or rather the presence of surface defects. These two additional peaks for sample 22 by analogy to results for  $\text{ZrS}_3$  section (5.4.1.2) could be a result of surface optical (SO) phonon modes.

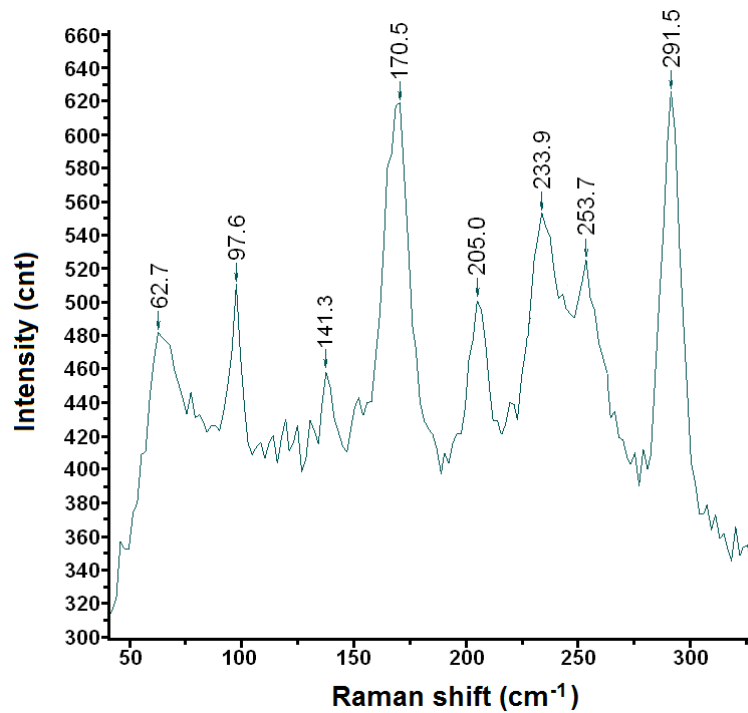


Fig 5.39 Room temperature Raman spectrum of sample 22 with a wavelength of exciting light of 532 nm.

### 5.4.5 Hafnium and zirconium tellurides

A similar investigation to sections 5.4.1, 5.4.2, 5.4.3 and 5.4.4 was carried out in the hafnium-tellurium system, samples **23-25** (450 °C; 24-120 h), (Table 5.3). The resultant foils showed a slight discolouration but PXD matched to only hafnium in all three cases. In addition, SEM experiments performed on the metal surface revealed no crystal growth. A further reaction was attempted at the slightly higher temperature of 600 °C; sample **26** (Table 5.3). The hafnium foil reacted with the tellurium vapour to produce a black powder, PXD of which matched to  $\text{HfTe}_{1.94}$  (Fig 5.40a). An indexing of the reflections gave values of  $a = 3.945(3) \text{ \AA}$ , and  $c = 6.6461(3) \text{ \AA}$  (hexagonal,  $P\bar{3}m1$ ) which are in excellent agreement with the literature values ( $a = 3.949 \text{ \AA}$ , and  $c = 6.651 \text{ \AA}$ ).<sup>[234]</sup> SEM revealed the powder to be composed of an agglomerate of nanoscaled particulates (Fig 5.40b). It is reported that  $\text{HfTe}_3$  is not stable above 600 °C<sup>[97]</sup> and therefore no further temperature increases were investigated.

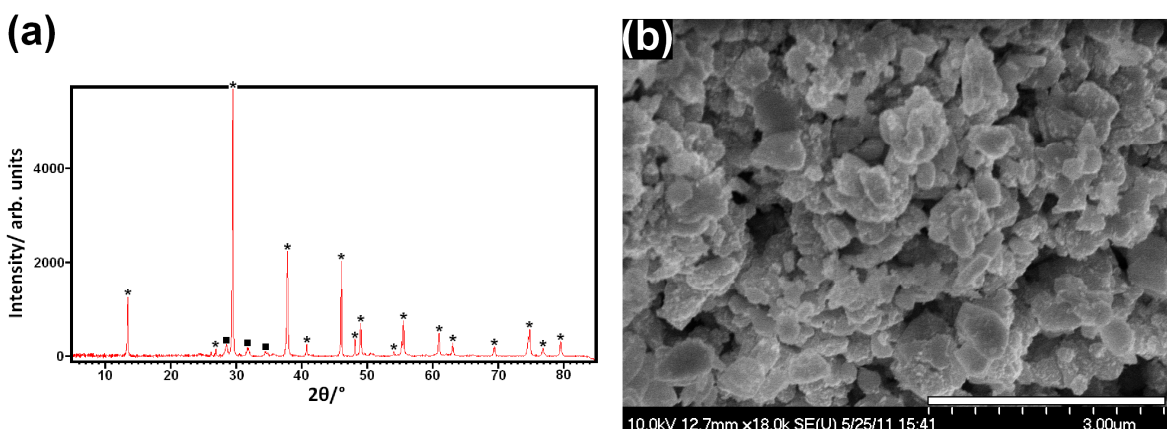


Fig 5.40 a) PXD pattern of sample **26**, asterisks correspond to  $\text{HfTe}_{1.94}$  and filled squares to excess tellurium b) SEM Micrograph of sample **26** showing agglomerated nano sized particulates

Under similar reaction conditions to the above, (Table 5.3) zirconium-tellurium samples do not exhibit any growth of nanostructures. SEM micrographs of (**27**) (450 °C, 60h) and (**28**) (450 °C, 120h) show the surface of the foil to be coated in a thick layer which is composed of multiple stacks of platelets (Fig 5.41). PXD reveals this layer to be  $\text{ZrTe}_3$  in both cases (Fig 5.42). Indexing of sample **28** gave values of;  $a = 5.88(4) \text{ \AA}$ ,  $b = 3.894(9) \text{ \AA}$ ,  $c = 10.13(9) \text{ \AA}$  and  $\beta = 97.9(3)^\circ$ .

These agree well with reported literature values ( $a = 5.8948(8) \text{ \AA}$ ,  $b = 3.9264(6) \text{ \AA}$ ,  $c = 10.104(2) \text{ \AA}$  and  $\beta = 97.93(2)^\circ$ ) although there is a decrease in the  $b$ -parameter (approximately 0.82 %).<sup>[235]</sup> Given the extreme peak broadening observed for sample (28) one is hesitant to state that this represents a true deviation from the literature values. It is difficult, for example, to determine the exact position of a peak for indexing since in some cases it is positioned over several degrees (Fig 5.42). EDX of (28) gave average values of (At% 28% Zr 72% Te  $\pm$  1.14%).

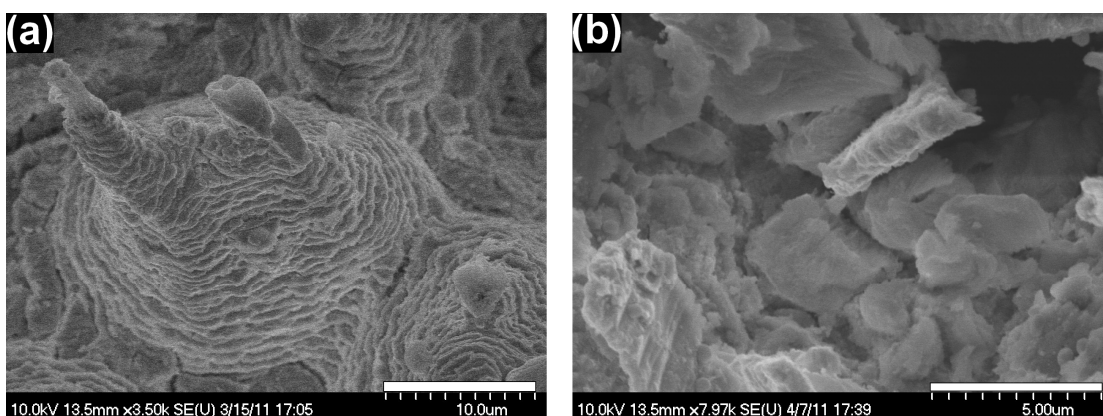


Fig 5.41 SEM Micrographs of samples a) 27 and b) 28 showing crystal growth of structures from the surface of the foil.

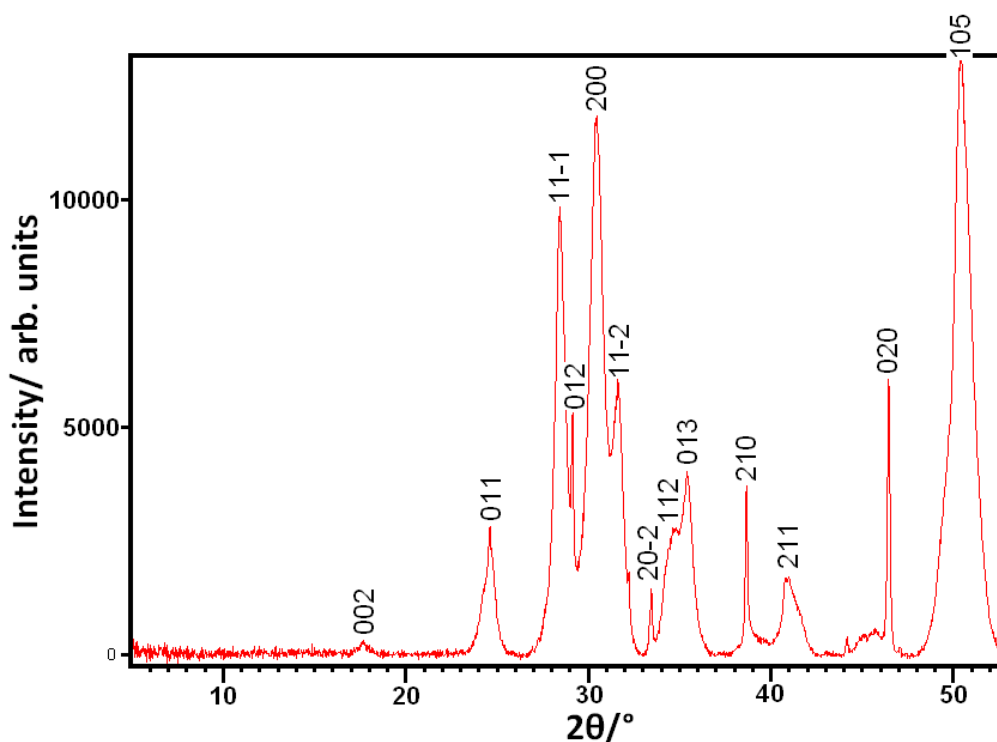


Fig 5.42, PXD pattern of sample 28; indexed reflections correspond to  $\text{ZrTe}_3$ .

According to the Zr-Te phase diagram, stoichiometric  $\text{ZrTe}_3$  is stable below 730 °C. [236] Samples **29-30** were run at 700 °C and 900 °C to discover if a slightly higher temperature would help induce the formation of nanostructures (Table 5.3). At 700 °C (**29**),  $\text{ZrTe}_2$  is produced and a further increase to 900 °C (**30**) gives mixed phases of  $\text{ZrTe}_2$ ,  $\text{ZrTe}_4$  and  $\text{Zr}_{1.45}\text{Te}_2$ . The crystal growth of samples **29 - 30** did not occur on the nanoscale with growth preferring a lattice-like layer crystal formation across the foil surface. This system was not investigated in any further detail (Fig 5.43).

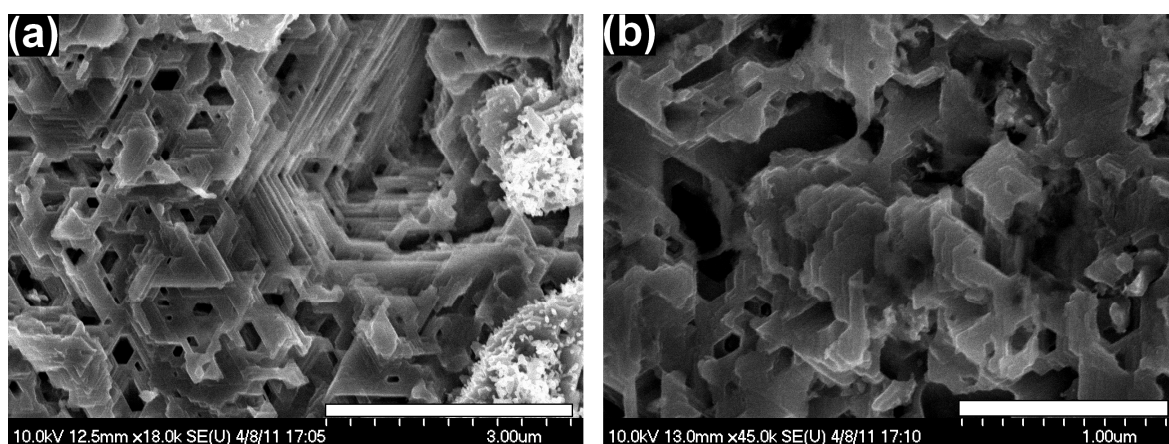


Fig 5.43 SEM micrographs of (**29**) and (**30**) showing the lattice-like crystal growth.

To briefly summarise, it has been shown that surface assisted chemical vapour transport (SACVT) can be exploited to produce nanostructures of zirconium and hafnium chalcogenides (with the exception of tellurium) by reacting metal foil with chalcogen powder in an inert atmosphere. Their structure and composition can be modified by a variation in either reaction temperature or time and using SACVT techniques it has been possible to synthesise a number of  $\text{MQ}_3$  nanostructures of the group IV transition metals zirconium and hafnium,  $\text{HfS}_3$  and  $\text{HfSe}_3$  for example. Structures can subsequently be removed from the substrate and each of these systems characterised with a variety of techniques including transmission electron microscopy (TEM), powder x-ray diffraction (PXRD), Raman spectroscopy and UV-Vis spectroscopy to see how they differ from their bulk equivalents. The technique has proved reliable to produce electron transparent sheets in a number of systems with thicknesses approaching 10 nm or less. Raman spectroscopy has shown that the reduction in crystal dimensions can affect their optical properties, which is exhibited by a downshift in the wavelength of expected peaks compared to their bulk equivalent.

## 5.5. Discussion and Conclusions

ZrS<sub>3</sub> nanobelts have been successfully synthesised via a reaction between zirconium foil and sulfur powder. It is likely a vapour-solid (VS) type mechanism is behind the growth process whereby ZrS<sub>x</sub> particles condense onto the zirconium substrate to form stable ZrS<sub>2</sub> seeding sites. This has been partially proven through a series of quenched reactions which have shown the progress of crystal growth over a period of several hours. TEM and SEM analysis has suggested that the ZrS<sub>3</sub> nanostructures grow independently of one another with an indefinite number of nanowires nucleating from a single seeding site. Raman spectroscopy showed a consistent deviation in the optical properties of ZrS<sub>3</sub> nanostructures from their bulk-counterparts. This was demonstrated by a redshift in their peak positions by several wavenumbers. In the case of ZrSe<sub>3</sub> it was possible to grow microstructures of ZrSe<sub>3</sub> upon a dense ZrSe<sub>2</sub> under layer. It was unfortunately not possible to produce single phase nano-ZrSe<sub>3</sub>. SEM micrographs revealed possible clues to the growth mechanism. It was discovered that the micron thick ZrSe<sub>2</sub> layer was comprises vertically aligned tubule-like structures. More interestingly, beneath this layer, a low density material was found. Unfortunately it was not possible to characterise this layer but it is likely an agglomeration of nanowires-like structures. Applying similar reaction conditions to the hafnium-sulfur system produced petal-like structures of what was concluded to be HfS<sub>2</sub> although an exact chemical composition was difficult to determine. As the reaction temperature is increased to 650 ° C the HfS<sub>2</sub> - nanopetals develop into micron sized ribbons of HfS<sub>3</sub> with a thickness approaching tens of nanometres. Once again these samples showed a deviation in their Raman spectra when compared to their bulk-counterparts. Given the difficulty in determining their exact stoichiometry however it was unclear if the difference in Raman spectra was a representation of the reduction in structure dimensions or simply a reflection of a non-stoichiometry or mixed phase of a Hf<sub>x</sub>S<sub>y</sub> species. TEM studies showed at least for the HfS<sub>3</sub> samples, that using the given reaction conditions it was possible to grow monocrystalline ribbons of HfS<sub>3</sub> whose lattice dimensions matched well to those of the literature. In the case of HfSe<sub>3</sub>, it was possible to grow nanostructured HfSe<sub>3</sub> which to the authors knowledge is yet to be reported in the literature. Similarly to the previous systems, the Raman spectra of HfSe<sub>3</sub> showed a downshift in their peaks of

approximately  $4.5 \text{ cm}^{-1}$ . Unfortunately in the case for tellurides of Zr and Hf it was not possible to grow  $\text{MQ}_3$  nanostructures using the applied techniques. This is not to say that growth is not possible using this method but instead that greater study is required to elude the necessary reaction conditions to prepare nanostructures of either  $\text{ZrTe}_3$  or  $\text{HfTe}_3$ .

## 6. Overall conclusions and further work

The course of this research has shown that surface assisted physical vapour transport (SAPVT) (where a chalcogen (Q) is transported as a reactive vapour) and surface assisted chemical vapour transport (SACVT) (where Metal- Q compositions are likely transported in the vapour phase), can be utilised to fabricate nanostructured chalcogenides on metal foil surfaces or metal films supported on silica substrates. The variation of reaction temperatures, reactant ratios and film thicknesses provides a means to mediate the composition, size and morphology of the nanoparticles. In Chapter 3 SAPVT was utilised to form a number of single phase, nanostructured, nickel, sulfur containing compounds. Varying reaction temperatures and Ni film thickness created a path to manipulate the size and morphology of the structures from spherical nanoparticles through nanocubes to microcubes. Nanomaterials formed by SAPVT at temperatures  $\geq 550$  °C have been confirmed as single phase, cubic, pyrite-structured, stoichiometric NiS<sub>2</sub>. The size of the NiS<sub>2</sub> cubes can be varied from below 200 nm to 1-2  $\mu\text{m}$  across and the magnetic properties were shown to be size (surface: bulk ratio) dependent. Samples grown at 650 °C (1) and 750 °C (2) exhibited a broad Curie-Weiss type profile over the investigated temperature range (0-55 K). Data collected under zero field cooled (ZFC) and field cooled (FC) conditions displayed a clear divergence in the ZFC and FC data at approximately 40 K, which resolves approaching 30 K. The nanoscaled structures of 1 exhibited a mass susceptibility higher than that of the micro structures of 2 and the antiferromagnetic transition occurs at a higher temperature. These observations support the suggestion that surface/size ratio can have an overall effect on the magnetic properties of nickel disulfide. In addition, by modifying the reactants from sulfur only, to sulfur and nickel, (using similar reaction conditions), it was possible to grow spherical nano and micro structures of trigonal Heazlewoodite (Ni<sub>3</sub>S<sub>2</sub>). It is likely that a VLS growth process is the driver behind the nanostructured formations, in the case of growth of WS<sub>2</sub> films on a Ni surface at 650 °C in the presence of NiS<sub>x</sub>, the precursor to sulfide growth is the fragmentation of a Ni substrate (typically 5-50 nm thickness) into islands. <sup>[142]</sup>

It is possible that in Chapter 3 sulfur vapour reacts with islands of NiS<sub>x</sub> liquid to form solid NiS<sub>2</sub>, which crystallises from the melt.

In Chapter 4 SACVT was exploited to produce nanostructures of titanium disulfide ( $\text{TiS}_2$ ) and titanium trisulfide ( $\text{TiS}_3$ ). Once again, systematic studies demonstrated the role of the reactant ratio and reaction temperature on the synthesis and growth process. A 1:2 ratio titanium to sulfur produced hexagonal 1T- $\text{TiS}_2$  titanium disulfide structures which could be varied from flower-like growths formed from approximately 10 nm thick nanosheets to platelets microns across in size. Increasing the proportion of sulfur to 1:4 (Ti:S) produced  $\text{TiS}_3$  flower-like structures composed of radiating nanoribbons. From the results it could be concluded that at low temperatures (300 °C), no reaction takes place whereas for intermediate temperatures (400 - 500 °C)  $\text{TiS}_2$  products were consistently obtained. At temperatures above 500 °C analysis has suggested that the product of the 1:2 ratio reactions are exclusively hexagonal  $\text{CdI}_2$ -type  $\text{TiS}_2$  and as the reaction temperature is raised so is the size of the crystalline  $\text{TiS}_2$  platelets. Additionally, at temperatures above 500 °C but with a ratio of 1:4 (Ti:S), the product become  $\text{TiS}_3$  with a variation in morphology from flower-like structures to nanoribbons radiating from a central core. Observed magnetic properties produced weak temperature independent paramagnetism for nanostructured  $\text{TiS}_2$  with a hint of Curie-Weiss like behaviour. This perceived behaviour parallels that of Ag and Cr doped  $\text{TiS}_2$  <sup>[206]</sup> adding weight to the argument that the nanostructuring of  $\text{TiS}_2$  alters its overall magnetic properties. It is proposed that nanostructures grow *via* a vapour-solid (VS) mechanism where gaseous  $\text{TiS}_x$  particles (formed by the interaction of the elemental powders) are critical to nucleation and subsequent growth on the substrate surface. Previous studies of  $\text{TiS}_3$  nanobelts grown on metal foil have reported a pseudomorphic reduction to the disulfide and non-stoichiometric  $\text{TiS}_{1.7}$ .<sup>[180]</sup> It is not obvious from the results of Chapter 4, however if  $\text{TiS}_3$  is formed *in situ* in the course of the growth of  $\text{TiS}_2$  nanostructures since, in terms of morphology, they do not resemble one another.

In Chapter 5 the use of metal foils as a growth substrate was equally successful in producing an array of nanostructures of the group IV transition metal trichalcogenides for the 4d and 5d metals zirconium and hafnium combined with both sulfur and selenium. The group IV-  $MQ_3$  nanostructures consistently showed a deviation in their optical properties with studies of their bulk counterparts, demonstrated by a redshift in their Raman spectra which has been tentatively assigned to the phonon confinement effect and surface optical phonon (SO) modes; phenomena which occur as a result of the reduced dimensions of the structure and increase in surface defects arising from the marked increase in surface area. This investigation has also established that the use of standard CVD reactions to produce nanostructures composed of sulfur and selenium were not sufficient to achieve the same outcome when employing tellurium. In the case of sulfur for example, short reaction times (24 h) coupled with relatively low reaction temperatures (450 °C) was favourable for the formation of  $ZrS_3$ ,  $HfS_3$  and  $HfS_2$  nanostructures. Tellurium on the other hand was less reactive towards the foil (perhaps due to its higher melting point) and when it did react it either produced micron sized particulates of a non-stoichiometric chalcogenide ( $MQ_x$ ) or micron thick layers of  $MQ_3$  on the foil surface. Both  $HfTe_3$  and  $ZrTe_3$  have been previously synthesised on the bulk scale from the elemental powdered reactants by means of standard chemical vapour transport (CVT).<sup>[40, 67]</sup> Using foil, under similar conditions does not, unlike in the case of sulfur and selenium, produce nanostructures. This is not to say it is not possible but rather the correct balance between reaction ratio, temperature and time to achieve the same result with metal foil is still to be elucidated.

An aspiration from Chapter 5 is to investigate the  $MQ_3$  system of zirconium and hafnium using the methodology of chapter 4 and react metal films of zirconium and hafnium with powdered chalcogen or a combination of powdered chalcogen and metal, as has been done with titanium. The structures produced in Chapter 4 by this method have proven to be markedly different in morphology from those produced by previous foil reactions of titanium with sulfur powder.<sup>[237]</sup> It is a tantalizing prospect to determine if analogous changes in morphology can be achieved by using metal films (of varying thickness) of zirconium and hafnium and if this has any reflection on their physical properties. This approach could easily be translated across the d-block metals, more specifically to tantalum and

niobium. These, reacted as elemental powders in an inert atmosphere (a standard CVT reaction), have exhibited remarkable anisotropy in their crystal growth by producing microrings of TaSe<sub>3</sub> and NbSe<sub>3</sub>. These are formations which have not been observed in other MQ<sub>3</sub> systems.<sup>[238]</sup> An even more exciting development from this study would be to pursue the preliminary studies from Chapter 3 that have shown that simple patterning of film surfaces can be exploited to produce directed, prescribed areas of nanostructures on the substrate surface. With further exploitation it could be possible to create a series of stand alone nanostructures which would maximise implementation of any potential applications they may have. Such an ability could be exploited in a number of different areas, for instance, in the case of thermoelectrics. It is widely considered that well known thermoelectric materials such as Bi<sub>2</sub>Te<sub>3</sub> could increase their thermoelectric properties by being synthesised on the nanoscale.<sup>[239, 240]</sup> To fully take advantage of their potential features however structures would need to be positioned in pre-determined locations on a substrate surface; a challenge that could be overcome by further developing the process introduced in Chapter 3. In addition, the often highly reactive surface of individual nanostructures sometimes makes their properties susceptible to the proximity of neighbouring nanostructures. For example, the ‘conductivity strengthening effect’ which has been observed in single-walled carbon nanotubes. It has been shown that when in close proximity to one another bundles of carbon nanotubes can overcome their coulomb repulsive interactions to become superconducting rather than metallic at low temperatures.<sup>[241]</sup> To grow structures in pre-determined locations could allow the easy analysis of any possible proximity effects in other nanomaterials like those produced in Chapters 3, 4 and 5.

## 7. References

- [1] R. Feynman, *Caltech Engineering and Science*, Feb 1960, Vol 23:5, 26-36.
- [2] Nanochemistry, G. A. Ozin, A. C. Arsenault, L. Cademartiri, 2009. 2<sup>nd</sup> Ed. RSC Publishing. ISBN-18-4755-895-X
- [3] M. H. Rashid and T. K. Mandal, *J. Phys. Chem. C*, 2007, **45**, 16750-16760.
- [4] S. Schimpf, M. Lucas, C. Mohra, U. Rodemerck, A. Brückner, J. Radnik, H. Hofmeister and P. Claus, *Catalysis Today*, 2002, **72**, 63-78.
- [5] Concepts of Nanochemistry, L. Cademartiri, G. A. Ozin, 2009. Wiley-VCH, Germany. Chapter 1. ISBN-35-2732-597-2
- [6] G. Schmid, B Corain, *Eur. J. Inorg. Chem* , 2003, **17**, 3081-3098.
- [7] S. Iijima, *Nature*, 1991, **354**, 56-58.
- [8] H. W. Kroto, J. R. Heath, S. C. O'Brien, R. F. Curl and R. E. Smalley, *Nature*, 1985, **318**, 162-163.
- [9] C. N. R. Rao, B. C. Satishkumar, A. Govindaraj and M. Nath, *ChemPhysChem*, 2001, **2**, 78-105.
- [10] W. Kratschmer, L. D. Lamb, K. Fostiropoulos and D. R. Huffman, *Nature*, 1990, **347**, 354-358.
- [11] Nanomaterials Chemistry, C. N. R. Rao, A. Müller and A. K. Cheetham, 2007. Wiley-VCH. ISBN-35-2731-664-7
- [12] R. Tenne, L. Margulis, M. Genut and G. Hodes, *Nature*, 1992, **360**, 444-446. L. Margulis, G. Salitra, R. Tenne and M. Talianker, *Nature*, 1993, **365**, 113-114. Y. Feldman, E. Wasserman, D. J. Srolovitz and R. Tenne, *Science*, 1995, **267**, 222-225.
- [13] M. Remskar, *Adv. Mater*, 2004, **16**, 1497-1504.
- [14] I. P. Parkin and R. G. Palgrave, *J. Mater. Chem.*, 2005, **15**, 1689-1695.
- [15] Inorganic Materials Chemistry, Oxford Primer, Mark T. Weller, 1<sup>st</sup> Ed, 1994. Oxford University Press, UK. ISBN-01-9855-798-1
- [16] Solid State Chemistry, An introduction, Smart and Moore, 1st Ed, 1992. Chapman and Hall. ISBN-04-1240-040-5
- [17] J. J. Ma, X. Y. Liu, X. J. Cao, S. H. Feng and M. E. Fleet, *European J. Inorg. Chem*, 2006, 519-522.
- [18] Y. N. Xia, P. D. Yang, Y. G. Sun, Y. Y. Wu, B. Mayers, B. Gates, Y. D. Yin, F. Kim and Y. Q. Yan, *Adv.Mater*, 2003, **15**, 353-389.

- [19] H. Moon, C. Nam, C. Kim and B. Kim, *Mater.Res.Bull*, 2006, **41**, 2013-2017.
- [20] R. S. Wagner and W. C. Ellis, *App. Phys. Lett*, 1964, **4**, 89-90.
- [21] M. Toyama, *Japanese J. App. Phys*, 1966, **5**, 1204.
- [22] S. N. Mohammad, *Nano Lett.*, 2008, **8**, 1532-1538.
- [23] S. R. Nutt, *J. Am. Ceram. Soc.*, 1984, **67**, 428-431.
- [24] W. K. Burton, N. Cabrera and F. C. Frank, *Nature*, 1949, **163**, 398-399.
- [25] Y. J. Guo, B. Y. Geng, L. Zhang, F. M. Zhan and J. H. You, *J. Phys. Chem. C*, 2008, **112**, 20307-20311.
- [26] D. Duphil, S. Bastide, J. C. Rouchaud, J. L. Pastol, B. Legendre and C. Lévy-Clément, *Nanotechnology*, 2004, **15**, 828.
- [27] Y. Dong, Y. Chu, Y. Zhuo, and W. Zhang, *Nanotechnology*, 2009, **20**, 125301.
- [28] A. Ghezelbash and B. A. Korgel, *Langmuir*, 2005, **21**, 9451.
- [29] D. S. Xu, D. P. Chen and Y. J. Xu, *Pure Appl. Chem.*, 2000, **72**, 172.
- [30] X. P. Shen, M. Han, J. M. Hong, Z. Xue and Z. Xu, *Chem. Vap. Deposition*, 2005, **11**, 250.
- [31] W. D. Shi, L. Zhou, S. Y. Song, J. H. Yang and H. J. Zhang, *Adv. Mater.*, 2008, **20**, 1892.
- [32] J. Zou, J. Zhang, B. Zhang, P. Zhao and K. X. Huang, *Mater. Lett.*, 2007, **61**, 5029.
- [33] W. Du, X. Qian, X. Ma, Q. Gong, H. Cao and Jie Yin, *Chem.-Eur.J.*, 2007, **13**, 3241.
- [34] P. P. Chin, J. Ding, J. B. Yi and B. H. Liu, *J. Alloys. Compd.*, 2005, **390**, 255.
- [35] Y. T. Didenko, W. B. McNamara III and K .S. Suslick, *J. Am. Chem. Soc.*, 1999, **121**, 5817.
- [36] M. Kristl and M. Drogenik, *Ultrason Sonoche.*, 2008, **15**, 695.
- [37] Y. Zhao, H. Pan, Y. Lou, X. Qiu, J. J. Zhu and C. Burda, *J. Am. Chem. Soc.*, 2009, **131**, 4253.
- [38] F. K. Mctaggart and A. D. Wadsley, *Aust. J. Chem*, 1958, **11**, 445-457.
- [39] J. Bear and F. K. Mctaggart, *Aust. J. Chem*, 1958, **11**, 458-470.

- [40] F. K. Mctaggart, *Aust. J. Chem*, 1958, **11**, 471-480.
- [41] J. A. Wilson and A. D. Yoffe, *Adv. Phys*, 1969, **18**, 193-335.
- [42] R. L. Withers and J. A. Wilson, *J. Solid state Phys. C-Solid State Phys*, 1986, **19**, 4809-4085.
- [43] J. F. Revelli, W. A. Phillips, *J. Solid. State. Chem*, 1974, **9**, 176-186.
- [44] B. H. Brandow, *Adv. Phys*, 1977, **26**, 651-808.
- [45] S. Furuseh, L. Brattas and A. Kjekshus, *Acta. Chem. Scand. Series a-Phys.Inorg.Chem*, 1975, **29**, 623-631.
- [46] E. Bjerkelu, A. Kjekshus, *Acta. Chem. Scand*, 1965, **19**, 701 - 710.
- [47] S. K. Srivastava and B. N. Avasthi, *J. Mater. Sci*, 1992, **27**, 3693-3705.
- [48] W. Biltz and A. Kocher, *Z. Anorg. Allg. Chem*, 1938, **238**, 81-93.
- [49] F. Jellinek, *J. Less-Common Metals*, 1962, **4**, 9-15
- [50] M. Ido, K. Tsutsumi, T. Sambongi and N. Mori, *Solid State Commun*, 1979, **29**, 399-402.
- [51] A. Meerschaut, L. Guemas and J. Rouxel, *Comptes Rendus Hebdomadaires Des Seances De L Academie Des Sciences Serie C*, 1980, **290**, 215-218.
- [52] P. Monceau, N. P. Ong, A. M. Portis, A. Meershaut, P. Molinie, J. Rouxel, *Phys. Rev. Lett*, 1976, **37**, 602-606.
- [53] M. Yamamoto, *J. Phys. Soc. Jap*, 1978, **45**, 431-438.
- [54] K. Selte and A. Kjekshus, *Acta Chemica Scandinavica*, 1964, **18**, 690-696.
- [55] F. W. Boswell, A. Prodan, J. C. Bennett, J. M. Corbett and L. G. Hiltz, *Physica Status Solidi (a) -Applied Research*, 1987, **102**, 207-220.
- [56] S. Tadaki, N. Hino, T. Sambongi, K. Nomura and F. Levy, *Synthetic Metals*, 1990, **38**, 227-234.
- [57] F. Jellinek, *Nature*, 1961, **192**, 1065-1066
- [58] W. Jaegermann and H. Tributsch, *Prog. Surf. Sci.*, 1988, **29**, 1-167.
- [59] R. H. Friend and A. D. Yoffe, *Adv. Phys*, 1987, **36**, 1-94.
- [60] E. H. Nickel, *Eur. J. Mineral*, 1993, **5**, 799-800.
- [61] D. L. Greenaway and R. Nitsche, *J. Phys. Chem. Solids*, 1965, **26**, 1445-1458.

- [62] I. Oftedal, *Zeitschrift Fur Physikalische Chemie--Stoichiometrie Und Verwandtschaftslehre*, 1928, **134**, 301-310.
- [63] Y. Arnaud and M. Chevreton, *J. Solid. State. Chem*, 1981, **39**, 230-239.
- [64] L. Brattas and A. Kjekshus, *Acta. Chem. Scand*, 1971, **25**, 2783-2784
- [65] C. N. R. Rao and M. Nath, *Dalton Transactions*, 2003, 1-24.
- [66] L. Rapoport, Y. Bilik, Y. Feldman, M. Homyonfer, S. Cohen, R. and R. Tenne, *Nature*, 1997, **387**, 791-793.
- [67] F. J. Di Salvo, D. E. Moncton and J. V. Waszczak, *Phys.Rev.B*, 1976, **14**, 4321-4328.
- [68] J. A. Wilson, F. J. Di Salvo and S. Mahajan, *Phys. Rev. Lett*, 1974, **32**, 882-885.
- [69] R. H. Friend and D. Jerome, *J. Phys. C-Solid State Phys*, 1979, **12**, 1441-1447.
- [70] R. V. Coleman, B. Giambattista, P. K. Hansma, A. Johnson, W. W. McNairy and C. G. Slough, *Adv. Phys*, 1988, **37**, 559-644.
- [71] B. Sipos, A. F. Kusmartseva, A. Akrap, H. Berger, L. Forro and E. Tutis, *Nature Materials*, 2008, **7**, 960-965.
- [72] H.W. Myron, *Physica B*, 1980, **99**, 243-249
- [73] M. Bayard and M. J. Sienko, *J. Solid. State. Chem*, 1976, **19**, 325-329.
- [74] M. Mulazzi, A. Chainani, N. Katayama, R. Eguchi, M. Matsunami, H. Ohashi, Y. Senba, M. Nohara, M. Uchida, H. Takagi and S. Shin, *Phys. Rev. B*, 2010, **82**, 075130.
- [75] C. M. Fang, C. F. van Bruggen, R. A. de Groot, G. A. Wiegers and C. Haas. *J. Phys. Condens. Matter*, 1997, **9**, 10173-10184.
- [76] C. F. Van Bruggen, R. J. Haange, G. A. Wiegers and D. K. G. De Boer, *Physica B*, 1980, **99**, 166-172.
- [77] A. Lafond, C. Deudon, A. Meerschaut and A. Sulpice, *Eur. J. Solid. State. Inorg. Chem.*, 1994, **31**, 967-978.
- [78] D. W. Bullet, *J. Phys. C: Solid State Phys*, 1982, **15**, 6163-6174.
- [79] D. Wang, M. Wu, Q. Wang, T. Wang, J. Chen, *Ionics*, 2011, **17**, 163 - 167.
- [80] Q. Wang, L. Jiao, Y. Han, H. Du, W. Peng, Q. Huan, D. Song, Y. Si, Y. Wang, H. Yuan, *J. Phys. Chem*, 2011, **115**, 8300-8304.

- [81] Solid State Chemistry, L. Smart and E. Moore 1993, 179-182 Chapman & Hall. ISBN-04-1240-040-5
- [82] J. B. Goodenough, *J. Solid State Chem*, 1971, 3, 26-38.
- [83] L. Brattas and A. Kjekshus, *Acta. Chem. Scand*, 1972, 26, 3441-3449.
- [84] Handbook of Chemistry and Physics 61<sup>st</sup> Ed 1980-1981 F216-217 CRC Press, ISBN-08-4930-461-X
- [85] D. Pacile, M. Papagno, M. Lavagnini, H. Berger, L. Degiorgi and M. Grioni, *Phys. Rev. B*, 2007, 76, 8.
- [86] R. R. Chianelli and M. B. Dines, *Inorg.Chem*, 1975, 14, 2417-2421.
- [87] H. Hahn and B. Harder, *Z. Anorg. Allg. Chem*, 1956, 288, 241-256.
- [88] W. Schairer and M. W. Shafer, *Physica Status Solidi (a) -Applied Research*, 1973, 17, 181-184.
- [89] Y. Onuki, R. Inada, S. Tanuma, S. Yamanaka and H. Kamimura, *Solid State Ion.*, 1983, 11, 195-201.
- [90] K. Endo, H. Ihara, K. Watanabe and S. I. Gonda, *J. Solid. State. Chem*, 1982, 44, 268-272.
- [91] H. G. Grimmeiss and A. Rabenau, *Zeitschrift Fur Elektrochemie*, 1961, 65, 776.
- [92] H. Haraldsen, E. Rost, A. Kjekshus and Steffens.A, *Acta. Chem.Scand*, 1963, 17, 1283-1292.
- [93] X. C. Wu, Y. R. Tao and Q. X. Gao, *Nano Research*, 2009, 2, 558-564.
- [94] J. J. Ma, X. Y. Liu, X. J. Cao, S. H. Feng and M. E. Fleet, *Eur. J. Inorg. Chem*, 2006, 519-522.
- [95] E. F. Strotzer, W. Biltz and K. Meisel, *Z. Anorg. Allg. Chem*, 1939, 242, 249.
- [96] H. Hahn, B. Harder, U. Mutschke and P. Ness, *Z. Anorg. Allg. Chem*, 1957, 292, 82-96.
- [97] S. G. Patel, S. H. Chaki and A. Agarwal, *Physica Status Solidi (a) -Applied Research*, 1993, 140, 207-212.
- [98] S. Takahashi, T. Sambongi and S. Okada, *Journal de Physique*, 1983, 44, 1733-1736.
- [99] S. Takahashi, T. Sambongi, J. W. Brill and W. Roark, *Solid State Commun*, 1984, 49, 1031-1033.

- [100] D. J. Eaglesham, J. W. Steeds and J. A. Wilson, *J.Phys.C-Solid State Phys*, 1984, **17**, L697.
- [101] H. Nakajima, K. Nomura and T. Sambongi, *Physica B & C*, 1986, **143**, 240-242.
- [102] S. Saibene, T. Butz, A. Lerf, F. Levy and W. Abriel, *Hyperfine Interactions*, 1990, **60**, 907-914.
- [103] H. Fjellvag and A. Kjekshus, *Solid State Commun*, 1986, **60**, 91-93.
- [104] S. Furusest, L. Brattas and A. Kjekshus, *Acta. Chem. Scand*, 1973, **27**, 2367-2374.
- [105] C. Felser, E. W. Finckh, H. Kleinke, F. Rucker, W. Tremel, *J. Mater. Chem*, 1998, **8**, 1787-1798
- [106] A. Prodan, V. Marinković, N. Jug, H. J . P. van Midden, H. Böhm, F. W. Boswell, J. C. Bennett, *Surface Science*, 2001, **482**, 1368-1373.
- [107] R. Yomo, K. Yamaya, M. Abliz, M. Hedo, Y. Uwatoko, *Phys. Rev. B*, 2005, **71**, 132508-1-132508-4.
- [108] Solid State Chemistry, A. Wold and K. Dwight, 1<sup>st</sup> Ed, 1993. Chapman and Hall, New York. 54-62.
- [109] D. W. G. Ballentyne, S. Wetwatana, E. A. D. White, *J. Cryst. Growth*, 1970, **7**, 79.
- [110] S. Tanda, T. Tsuneta, Y. Okajima, K. Inagaki, K. Yamaya, N. Hatakenaka, *Nature*, 2002, **417**, 397-398.
- [111] T. Matsuura, S. Tanda, K. Asada, Y. Sakai, T. Tsuneta, K. Inagaki, K. Yamaya, *Physica B-Condensed Matter*, 2003, **329**, 1550-1551.
- [112] J. Henzie, J. E. Barton, C. L. Stender, T. W. Odom, *Acc. Chem. Res*, 2006, **39**, 249-257.
- [113] C. L. Stender, E. C. Greyson, Y. Babayan, T. W. Odom, *Adv. Mater*, 2005, **17**, 2837-2841. C. L. Stender, T. W. Odom, *J. Mater. Chem*, 2007, **17**, 1866-1869.
- [114] H. Busch, *Ann. Phys.-Berlin*, 1926, **81**, 974-993.
- [115] M. Knoll, *Z. Tech. Phy*, 1935, **11**, 467-475.
- [116] V. M. Ardenne, *Z. Phys*, 1938, **109**, 553-572. V. M. Ardenne, *Z. Tech. Phys*, 1938, **19**, 407-416.
- [117] C. W. Oatley, *J. Appl. Phy*, 1982, **53**, R1-R13.

- [118] Scanning Electron Microscopy and X-ray Microanalysis 3<sup>rd</sup> Ed, J. Goldstein, D. Newbury, D. Joy, C. Lyman, P. Echlin, E. Lifshin, L. Sawyer, J. Michael 2003 *Springer Science + Business Media Inc.* ISBN-0-30-647292-9
- [119] Hitachi S-4700 SEM Training and Reference Guide - January 2007
- [120] Experimental Nuclear Physics Vol 1, H. Bethe, J. Ashkin, G. Emilio, 1953 *Wiley*. ISBN-04-7177-484-7.
- [121] H. Seiler, *J. Appl. Phys.* **1983**, 54 (11), R1-R18
- [122] Introduction to X-ray crystallography . Wooflson. 1970. Cambridge University Press.
- [123] Symmetry in molecules and crystals. M. F. C. Ladd. 1992. Ellis Horwood limited, UK. Chapter 5. ISBN-0-13-879347-6
- [124] International tables for X-ray Crystallography. 3<sup>rd</sup> Ed, 1969. Kynoch Press. ISBN-04-7068-911-0
- [125] W.L. Bragg, *Proc. Camb. Phil. Soc*, 1913, **17**, 43
- [126] Solid State Chemistry, An introduction. L. Smart and E. Moore. 2<sup>nd</sup> Ed, 1995. Chapman and Hall. ISBN-04-1262-220-3
- [127] A. Boultif., D. Louer. (2004) *J. Appl. Cryst.* Vol. 37, pp.724-731. D. Louer., M. Louer. (1972) *J. Appl. Cryst.* Vol. 5, pp.271-275. A. Boultif., D. Louer. (1991) *J. Appl. Cryst.* Vol. 24, pp.987-993.
- [128] U. D. Altermatt, I. D. Brown, *Acta. Cryst*, 2004, **43**, 125-130.
- [129] H.M. Rietveld, *Acta Cryst.* **22** 151 (1967). H.M. Rietveld, *J. Appl. Cryst.* **2** 65 (1969)
- [130] B. H. Toby, *J. Appl. Cryst*, 2001, **34**, 210-213.
- [131] G. Caglioti, A. Paoletti, F. P. Ricci, *Nucl. Instrum. Methods*, 1958, **35**, 223 - 228.
- [132] Solid State Chemistry: Techniques. A. K. Cheetham and P. Day. 2001. Oxford University Press. ISBN-0-19-855286-6
- [133] C. V. Raman, *Nature*, 1928, **121**, 619-619.
- [134] N. Lustig, R. Fainchtein, J. S. Lannin, *Phys. Rev. Lett*, 1985, **55**, 1775-1777.
- [135] Horiba scientific, Raman - frequently asked questions (pdf), 2010
- [136] R. S. Tobias, *J. Chem. Educ*, 1967, **44** , 2-8.
- [137] Molecular Spectroscopy, J. M. Brown. Oxford Chemistry Primer, Oxford Science Publications, 2003. ISBN - 01-9855-785-X

- [138] Transmission Electron Microscopy, D. B. Williams and C. B. Carter, Springer **1996**.
- [139] W. D. Shi, R. W. Hughes, S. J. Denholme and D. H. Gregory, *Crystengcomm*, 2010, **12**, 641-659.
- [140] C. W. Dunnill, H. K. Edwards, P. D. Brown and D. H. Gregory, *Angew. Chem.-Int. Edit.*, 2006, **45**, 7060-7063. C. W. Dunnill, I. MacLaren and D. H. Gregory, *Nanoscale*, 2010, **2**, 90-97.
- [141] G. Salitra, G. Hodes, E. Klein and R. Tenne, *Thin Solid Films*, 1994, **245**, 180-185.
- [142] K. Ellmer, *Phys. Status Solidi B-Basic Solid State Phys.*, 2008, **245**, 1745-1760.
- [143] S. Brunken, R. Mientus, S. Seeger and K. Ellmer, *J. Appl. Phys.*, 2008, **103**, 6.
- [144] S. Brunken, R. Mientus and K. Ellmer, *Thin Solid Films*, 2009, **517**, 3148-3151.
- [145] G. Krill, M. F. Lapiere, F. Gautier, C. Robert, G. Czjzek, J. Fink and H. Schmidt, *Journal of Physics C-Solid State Physics*, 1976, **9**, 761-782.
- [146] A. Ghezelbash, M. B. Sigman and B. A. Korgel, *Nano Lett.*, 2004, **4**, 537-542.
- [147] H. B. Li, L. L. Chai, X. Q. Wang, X. Y. Wu, G. C. Xi, Y. K. Liu and Y. T. Qian, *Cryst. Growth Des.*, 2007, **7**, 1918-1922.
- [148] Y. Hu, J. F. Chen, H. T. Zhang, T. W. Li and X. Xue, *Scr. Mater.*, 2006, **55**, 131-134.
- [149] G. Z. Shen, D. Chen, K. B. Tang, C. H. An, Q. Yang and Y. T. Qian, *Journal of Solid State Chemistry*, 2003, **173**, 227-231.
- [150] L. L. Wang, Y. C. Zhu, H. B. Li, Q. W. Li and Y. T. Qian, *Journal of Solid State Chemistry*, 2010, **183**, 223-227.
- [151] X. H. Chen and R. Fan, *Chemistry of Materials*, 2001, **13**, 802-805.
- [152] G. J. An, C. G. Liu, Y. D. Hou, X. L. Zhang and Y. Q. Liu, *Mater. Lett.*, 2008, **62**, 2643 - 2646.
- [153] S. L. Yang, H. B. Yao, M. R. Gao and S. H. Yu, *CrystEngComm*, 2009, **11**, 1383-1390.
- [154] Z. Y. Meng, Y. Y. Peng, W. H. Yu and Y. T. Qian, *Mater. Chem. Phys.*, 2002, **74**, 230-233.

- [155] X. M. Zhang, X. F. Qian, C. Wang, Y. Xie and Y. T. Qian, *Mater. Sci. Eng. B-Solid State Mater. Adv. Technol.*, 1999, **57**, 170-171.
- [156] X. F. Qian, Y. D. Li, Y. Xie and Y. T. Qian, *Mater. Chem. Phys.*, 2000, **66**, 97-99.
- [157] M. Fleet, *Can. Mineral*, 1988, **26**, 283.
- [158] E. Kulagov, T. Evstigneeva and O. Yushko-Zakharova, *Geol. Rudn. Mestorozhd*, 1969, **11**, 115.
- [159] M. Singleton, P. Nash, K. J. Lee, *Phase Diagrams of Binary Nickel Alloys* (Ed.: P. Nash), ASM international, Materials Park, OH, **1991**, pp. 227-283; T. Massalski, H. Okamoto, *Binary Alloy Phase Diagrams* (2<sup>nd</sup> ed.), ASM International, Material Parks, OH, **1990**.
- [160] S. Furuseth, A. Kjekshus and A. F. Andresen, *Acta Chemica Scandinavica*, 1969, **23**, 2325-2334.
- [161] T. Thio, J. W. Bennett and T. R. Thurston, *Physical Review B*, 1995, **52**, 3555-3560.
- [162] F. Gautier, G. Krill, M. F. Lapierre and C. Robert, *Journal of Physics C-Solid State Physics*, 1973, **6**, L320-L323.
- [163] P. Scherrer, *Nachr. Ges. Wiss. Göttingen*, 1918, **2**, 96-100.
- [164] J. B. Parise, *Acta Crystallogr., Sec. B: Struct. Crystallogr. Cryst. Chem*, 1980, **36**, 1179.
- [165] Y. H. Zhang, L. Guo, L. He, K. Liu, C. P. Chen, Q. Zhang and Z. Y. Wu, *Nanotechnology*, 2007, **18**, 8.
- [166] Y. H. Zhang, L. Guo, L. He, K. Lang, C. Chen, Q. Zhang and Z. Wu, *Chem. Eur. J.*, 2006, 2337.
- [167] I. J. Ferrer and C. Sanchez, *J. Mater. Process. Technol.*, 1999, **93**, 239-242.
- [168] U. Tanaka, T. Komori, N. Ishizawa, F. Marumo and Y. Noda, *Journal of Crystal Growth*, 1993, **129**, 683-685.
- [169] J. Chen, S. L. Li, Z. L. Tao and F. Gao, *Chem. Commun.*, 2003, **8**, 980-981.
- [170] J. J. Ma, H. Jin, X. Y. Liu, M. E. Fleet, J. X. Li, X. J. Cao and S. H. Feng, *Cryst. Growth Des.*, 2008, **8**, 4460-4464.
- [171] Y. R. Tao, X. C. Wu, Y. L. Zhang, L. Dong, J. J. Zhu and Z. Hu, *Cryst. Growth Des.*, 2008, **8**, 2990-2994.

- [172] S. Prabakar, C. W. Bumby and R. D. Tilley, *Chemistry of Materials*, 2009, **21**, 1725-1730.
- [173] Y. Zhang, Z. K. Li, H. B. Jia, X. H. Luo, J. Xu, X. H. Zhang and D. P. Yu, *Journal of Crystal Growth*, 2006, **293**, 124-127.
- [174] R. R. Chianelli, J. C. Scanlon, M. S. Whittingham and F. R. Gamble, *Inorganic Chemistry*, 1975, **14**, 1691-1696.
- [175] J. Dahn and R. R. Haering, *Mater. Res. Bull*, 1979, **14**, 1259-1262.
- [176] G. Scholz, P. Joensen, J. M. Reyes and R. F. Frindt, *Physica B & C*, 1981, **105**, 214-217.
- [177] M. Inoue and H. Negishi, *J. Phys. Soc. Jap*, 1984, **53**, 943-946.
- [178] E. W. Ong, M. J. McKelvy, G. Ouvrard and W. S. Glaunsinger, *Chem. Mater*, 1992, **4**, 14-17.
- [179] M. Remskar, A. Popovic and H. I. Starnberg, *Surface Science*, 1999, **430**, 199-205.
- [180] H. E. Brauer, H. I. Starnberg, L. J. Holleboom, H. P. Hughes and V. N. Strocov, *J. Phys-Cond. Matt*, 1999, **11**, 8957-8973.
- [181] Y. Tison, H. Martinez, I. Baraille, M. Loudet and D. Gonbeau, *Chem. Phys.*, 2003, **290**, 267-278.
- [182] J. Chen, S. L. Li, Z. L. Tao, Y. T. Shen and C. X. Cui, *J. Am. Chem. Soc.*, 2003, **125**, 5284-5285.
- [183] J. Chen, Z. L. Tho and S. L. Li, *Angew. Chem.-Int. Edit.*, 2003, **42**, 2147-2151.
- [184] X. C. Wu, Y. R. Tao and Q. X. Gao, *Nano Research*, 2009, **2**, 558-564.
- [185] J. J. Ma, X. Y. Liu, X. J. Cao, S. H. Feng and M. E. Fleet, *Euro. J. Inorg. Chem*, 2006, 519-522.
- [186] M. J. McKelvy and W. S. Glaunsinger, *J. Solid State Chem.*, 1987, **66**, 181-188.
- [187] R. R. Chianelli, J. C. Scanlon and A. H. Thompson, *Mater. Res. Bull*, 1975, **10**, 1379-1382.
- [188] W. K. Unger, J. M. Reyes, O. Singh, A. E. Curzon, J. C. Irwin and R. F. Frindt, *Solid. State. Commun*, 1978, **28**, 109-112.
- [189] S. J. Sandoval, X. K. Chen and J. C. Irwin, *Phys. Rev. B*, 1992, **45**, 14347-14353.

- [190] J. I. Meakin, P. C. Klipstein and R. H. Friend, *J. Phys. C*, 1987, **20**, 271-276.
- [191] W. A. Dollase, *J. Appl. Cryst*, 1986, **19**, 267-277. A. March, *Z. Kristallogr*, 1932, **81**, 285-297.
- [192] W. Blitz, P. Ehrlich and K. Meisel, *Z. Anorg. Chem*, 1937, **234**, 97-116.
- [193] E. Finkman and B. Fisher, *Solid State Commun*, 1984, **50**, 25-28.
- [194] D. W. Galliardt, W. R. Nieveen, R. D. Kirby, *Solid State Commun*, 1979, **34**, 37-39.
- [195] J. L. Murray, *Bull. Alloy Phase Diagr*, 1986, **7**, 156-163.
- [196] F. Tronc, M. Huber, *C.R. hebd. Seanc., Acad. Sci. Paris Ser, C*, 1969, **268**, 1771.
- [197] H. S. Chang, D. M. Schleich, *J. Solid State Chem*, 1992, **100**, 62-70.
- [198] R. Tenne, C. N. R. Rao, *Phil. Trans. R. Soc. Lond*, 2004, **362**, 2099-2125.
- [199] R. Tenne, M. Homyonfer, Y. Feldman, *Chem. Mater*, 1998, **10**, 3225-3238.
- [200] M. Nath, C. N. R. Rao, *J. Am. Chem. Soc*, 2001, **123**, 4841 - 4842
- [201] M. Nath, C. N. R. Rao, *Angew. Chem. Int. Ed*, 2002, **41**, 3451 - 3454
- [202] M. Nath, A. Govindaraj, C. N. R. Rao, *Adv. Mater*, 2001, **13**, 283-286.
- [203] M. Nath, C. N. R. Rao, *Chem. Commun*, 2001, 2336 - 2337.
- [204] R. Tenne, *Adv. Mater*, 1995, **7**, 965 - 995
- [205] M. N. Tahir, A. Yella, J. K. Sahoo, H. Annal-Therese, N. Zink, W. Tremel, *Physica Status Solidi B-Basic Solid State Phys*, 2010, **247**, 2338-2363
- [206] M. Inoue, H.P. Hughes, A.D. Yoffe, *Adv. Phys*, 1989, **38**, 565-604.
- [207] C. D. Cavellin and S. Jandl, *Solid State Communications*, 1979, **33**, 813-816.
- [208] J. Y. Harbec, C. D. Cavellin, S. Jandl, *Phys. Stat. Sol. (b)*, 1979, **96**, K117-K1120
- [209] S. Jandl, C. D. Cavellin, J. Y. Harbec, *Solid.State.Comm*, 1979, **31**, 351-353
- [210] L. Y. Huang, K. B. Tang, Q. Yang, G. Z. Shen, S. J. Jia, *Mater. Res. Bull*, 2004, **39**, 1083-1089.
- [211] G. Q. Shi, C. Li, Y. Q. Liang, *Adv. Mater*, 1999, **11**, 1145-1146.

- [212] H. Jin, D. Cheng, J. Li, X. Cao, B. Li, X. Wang, X. Liu, X. Zhao, *Solid State Sci*, 2011, **13**, 1166-1171.
- [213] R. B. Conard, H. F. Franzen, *High Temperature Science*, 1971, **3**, 49-55.
- [214] K. Stocks, G. Eulenber and H. Hahn, *Z. Anorg. Chem*, 1970, **374**, 318-324
- [215] J. K. Burdett and J. F. Mitchell, *Progress in Solid State Chemistry*, 1995, **23**, 131-170.
- [216] S. J. Kim, T. H. Nguyen and H. F. Franzen, *J. Solid. State. Chem*, 1987, **70**, 88-92.
- [217] S. G. Patel, S. H. Chaki, A. Agarwal, *Physica Status Solidi (a) -Applied Research*, 1993, **140**, 207-212.
- [218] A. R. Moodenbaugh, D. C. Johnston, R. Viswanathan, R. N. Shelton, L. E. DeLong, W. A. Fertig, *J. Low Temp. Phys*, 1978, **33**, 175-203.
- [219] C. Sourisseau, Y. Mathey, *Chemical Physics*, 1981, **63**, 143-156.
- [220] A. Zwick, M. A. Renucci, A. Kjekshus, *J. Phys. C: Solid St. Phys*, 1980, **13**, 5603 - 5614
- [221] S. Mathur, K. P. Jain, R. K. Soni, C. Julien, M. Balkanski, *Phys. Rev. B*, 1991, **43**, 3952-3958
- [222] I. H. Campbell, P. M. Fauchet, *Solid.State.Comm*, 1986, **58**, 739 - 741
- [223] Z. V. Popovic, Z. Dohcevic-Mitrovic, M. Scepanovic, M. Grujic-Brojcin, S. Askrabic, *Ann. Phys. (Berlin)*, 2011, **523**, 62 - 74
- [224] K. W. Adu, Q. Xiong, H. R. Gutierrez, G. Chen, P. C. Eklund, *Appl. Phys. A*, 2006, **85**, 287-296
- [225] S. Bhattacharya, A. Datta, S. Dhara and D. Chakravorty, *J. Raman Spectrosc*, 2011, **42**, 429-433.
- [226] Y. L. Zhang, X. C. Wu, Y. R. Tao, C. J. Mao, J. J. Zhu, *Chem. Commun*, 2008, 2683-2685.
- [227] H. Hahn, P. Ness, *Anorg. Allg. Chem*, 1959, **302**, 37 - 49
- [228] Y. Huang, J. He, Y. Zhang, Y. Dai, Y. Gu, S. Wang, C. Zhou, *J. Mater. Sci*, 2006, **41**, 3057-3062.
- [229] F. A. S. Al-Alamy, A. A. Balchin and M. White, *J. Mater. Sci*, 1977, **12**, 2037-2042.
- [230] A. Cingolani, M. Lugara, G. Scamarcio and F. Levy, *Solid State Communications*, 1987, **62**, 121-123.

- [231] Predel, B. Hf-S (Hafnium-Sulfur). Madelung, O. (ed). 1996, Springer Materials. ISBN 06-1503-046-8
- [232] M. Nath and C. N. R. Rao, *Pure Appl. Chem*, 2002, **74**, 1545-1552.
- [233] D. J. Brooks, R. E. Douthwaite, R. Brydson, C. Calvert, M. G. Measures and A. Watson, *Nanotechnology*, 2006, **17**, 1245-1250.
- [234] J. G. Smeggil, S. Bartram, *J. Solid State Chem*, 1972, **5**, 391-394.
- [235] S. Furuseth, H. Fjellvag, *Acta Chem. Scand*, 1991, **45**, 694-697.
- [236] H. Sodeck, H. Milker, K. L. Komareck, *Monatshefte für Chemie*, 1979, **110**, 1-8
- [237] J. J. Ma, X. Y. Liu, X. J. Cao, S. H. Feng and M. E. Fleet, *Euro. J. Inorg. Chem*, 2006, 519-522.
- [238] S. Tanda, T. Tsuneta, Y. Okajima, K. Inagaki, K. Yamaya, N. Hatakenaka, *Nature*, 2002, **417**, 397. T. Matsuura, S. Tanda, K. Asada, Y. Sakai, T. Tsuneta, K. Inagaki, K. Yamaya, *Phys. B*, 2003, **329-333**, 1550.
- [239] D. A. Wright, *Nature*, 1958, **181**, 834.
- [240] L. D. Hicks, M. S. Dresselhaus, *Phys. Rev. B*, 1993, **47**, 12727-12731.
- [241] M. Kociak, A. Y. Kasumov, S. Gueron, B. Reulet, I. I. Khodos, Y. B. Gorbatov, V. T. Volkov, L. Vaccarini, H. Bouchiat, *Phys. Rev. Lett*, 2001, **86**, 2416-2419.